# Mass Spectral Imaging for Chemical Analysis of Cancerous Tissues Using Time-of-Flight Secondary Ion Mass Spectrometry

Blake M. Bluestein

A dissertation

submitted in partial fulfillment of the

requirements for the degree of

Doctor of Philosophy

University of Washington

2017

Reading Committee:

Lara J. Gamble, Chair

David G. Castner

Buddy Ratner

Program Authorized to Offer Degree:

Department of Bioengineering

University of Washington

## Abstract

Mass Spectral Imaging for Chemical Analysis of Cancerous Tissues Using Time-of-Flight Secondary Ion Mass Spectrometry

Blake M. Bluestein

Chair of the Supervisory Committee:
Lara J. Gamble
Department of Bioengineering

Mass spectrometry imaging is unique as it has becoming a versatile and interdisciplinary technique; it openly crosses the boundaries between chemistry and biology as it combines detailed chemical and spatial information within biological samples. In this work, time-of-flight secondary ion mass spectrometry (ToF-SIMS) was used to analyze human breast cancer tissue and murine β cell neoplasia. ToF-SIMS for tissue sample analysis is an emerging field, so the development of characterization methods is critical to provide a framework for multiple tissue comparisons.

The work presented here demonstrates a multivariate analysis method to isolate and analyze specific tissue regions of interest by utilizing principal components analysis (PCA) of ToF-SIMS images is presented, which allowed separation of cellularized areas from stromal areas. These PCA-generated regions of interest were then used as masks to reconstruct representative spectra from specifically stromal or cellular regions. The advantage of this unsupervised selection method is a reduction in scatter in the spectral PCA results when compared to analyzing all tissue areas or analyzing areas highlighted by a pathologist. Using this method, stromal and cellular regions of breast tissue biopsies taken pre- versus post-chemotherapy demonstrate chemical separation. Fatty acids (i.e. palmitic, oleic, and stearic), monoacylglycerols, diacylglycerols and vitamin E profiles were distinctively different between the pre- and post-therapy tissues.

Utilizing this method, which provides a framework to compare a multiple tissue samples using imaging ToF-SIMS, 23 pre-treated breast cancer tissue biopsies were analyzed. Using the PCA generated masks, it was possible to compare regions with a focus on metabolic changes occurring within breast cancer tissue to reveal the chemical profile of chemoresistance. Comparing ToF-SIMS cellular and stromal region data from specific subtypes, e.g. triple negative, has shown promise in defining chemical differences between patients that respond to chemotherapy and those that do not. These differences were related primarily to fatty acids and sphingomyelin.

In another experiment, ToF-SIMS was applied to generate a high resolution *in situ* molecular analysis of Myc-induced pancreatic β cell islet tumors to investigate the tumor microenvironment. Employing PCA, we show that it is possible to chemically distinguish cancerous islets from normal tissue, in addition to intratumor heterogeneity. These heterogeneities can then be imaged and investigated using another modality such as second harmonic generation (SHG) microscopy. Using these techniques with a specialized mouse model, we found significant metabolic changes occurring within β cell tumors and the surrounding tissues. Specific alterations within the lipid, amino acid, and nucleotide metabolism were observed, demonstrating that ToF-SIMS can be utilized to identify large-scale changes that occur in generated in the tumor microenvironment and could thereby increase our understanding of tumor progression and the tumor microenvironment.

# TABLE OF CONTENTS

# LIST OF FIGURES

# LIST OF TABLES

# ACKNOWLEDGEMENTS

I would like to thank both my advisors and committee chairs, Prof. Lara Gamble and David Castner, for their mentorship and support. Thank you for providing me with the resources and encouragement to be successful.

I wish to thank my Dissertation committee, which consists of Prof. Lara Gamble, Prof. David Castner, Prof. Buddy Ratner, Prof. Colin Studholme, and Prof. Frantisek Turecek for the guidance necessary to complete this work.

Without the help of many people at the Fred Hutchinson Cancer Research Center, my research would not have been possible. Thank you, Dr. Fionnuala Morrish, your patience and willingness to discuss the biology behind much of this work was invaluable. I'd also like to thank Li Huang and Kelly Wirtala for their expertise and providing me with the best possible samples to analyze. I would also like to thank Dr. Jamie Guenthoer, Dr. David Hockenbery, and Dr. Peggy Porter for sharing their expertise and interpreting tissue samples.

I would like to thank the entire NESAC/BIO Group, both past and present, for helpful discussions and support. I would specifically like to thank Dr. Daniel Graham for teaching, training, and sharing his expertise of multivariate analysis and ToF-SIMS. I would like to thank the post-doctoral researchers, Dr. Michael Robinson, Dr. Julia Kokesch-Himmelreich, and Dr. Adam Taylor, for sharing their experience, expertise, and support. Thank you to my outstanding lab mates, Dr. Elisa Harrison, Michael Newton, and Andrew Wang, your assistance and enthusiasm has always been appreciated.

I would like to take this opportunity to thank Bob Lamm, Jason Stevens, Jonathan Tsui, Andrew Wang, and Dr. David Younger. You have been my classmates, my lab mates, but most importantly you have been my friends. Thank you for making the past 5 years unforgettable.

In addition, I would like to thank Prof. Heather Canavan, for her mentorship throughout my academic studies. You inspired my love for scientific research, encouraged me to pursue graduate school, and never doubted me. Thank you.

Finally, and most importantly, I would like to thank my family for their encouragement, love, and support. I'd like to thank my sister, Marissa Bluestein, for always reminding me of what is important and when to just breathe. Also, I'd like to thank aunt and uncle, Nancy Bluestein-Johnson and Randy Johnson, for their support and making my transition to the PNW amazing. And I'd like to thank my parents, Linda and Rick Bluestein. You have always believed in me and supported me. I could not have succeeded without you.

This work was supported by NSF GRFP (DGE-0718124), NESAC/BIO (NIH P41 EB002027), and SPORE (NIH P50 CA138293).

# Chapter 1. INTRODUCTION

## 1.1 GENERAL OVERVIEW

Exploration using molecular imaging techniques to define the complex relationship between spatial organization, structure, and function of molecules of biological systems continues to drive biological and clinical research. Molecular identification and localization within distinct regions of biological tissue samples is imperative to elucidate the functions within a biological system. While understanding how these functions operate normally is important, it becomes equally important to determine the cause of dysfunctions within the biological system. Tissue samples are typically explored using conventional imaging modalities showing structure and organization, however conventional molecular investigations require knowledge of specific targets *a priori*. In cancer research, for example, histological staining is used to determine the location, type and grade of tumors, providing high prognostic value. Histological staining is subjective to interpretation and not completely predictive of patient outcome or response to chemotherapeutics. In addition to these established methods, it is beneficial to obtain chemical information that represents the biochemical characteristics and patterns of cancerous tissues. The ability to identify and map the distribution of small, intracellular molecules, such as metabolites, within cancerous cells and tissues provides a method to ascertain chemical information not available by conventional methods. Imaging time-of-flight secondary ion mass spectroscopy (ToF-SIMS), an ultra-high vacuum (UHV) technique, which provides a label-free molecular map of a sample composed of specific secondary ions and is well suited to provide detailed chemical information with the high lateral resolution required for mapping tissue sections.

Advancements in ToF-SIMS instrumentation have made it a powerful and novel tool for biological research. Liquid metal ion guns (LMIGs) produce finely focused ion beams increasing spatial resolution in the sub-micron range for biological samples, while simultaneously increasing the yield of secondary ions, delivering crucial chemical data.[1-3] Pairing LMIGs with a time-of-flight analyzer further provides the ability to obtain

valuable chemical data as it simultaneously detects all desorbed secondary ions with a mass resolution of ($m/\Delta m$) of 10,000.[4, 5] The detection of all molecular species can provide for new hypotheses or biological conclusions by mapping and identifying previously unknown species within a tissue or cell.

These strengths have led to a considerable amount of research using ToF-SIMS for tissue analysis. However, much of this research has focused on proof of principle type studies often comparing a distinctly diseased tissue to a healthy tissue and describing the distribution of fatty acids, various lipids, and other biomolecules.[6-14] Cancerous tissues present a challenge to ToF-SIMS analysis due to their complexity and heterogeneity. To progress upon these concepts and take the next step in biochemically interpreting complex tissue samples, such as cancer biopsies, requires the improvement and development of data analysis techniques so that multiple tissues can be compared for better clinical relevancy. Improving the methods for tissue data analysis offers the capability to reveal significant metabolic events occurring within the tumor microenvironment, cancer metabolism, and aid in potential diagnosis and treatment efficacy.

## 1.2 OBJECTIVE

The primary goal of the work presented here is to relate the chemical differences obtained from ToF-SIMS spatial chemical images to metabolic pathways. The objectives of this work include: 1) the development of a ToF-SIMS data analysis method that is able to isolate and compare distinct regions, i.e., cellular to cellular, across multiple tissue samples by utilizing the chemical fingerprint of that region, and 2) develop a method to semi-quantitatively map the spatial distribution of lipids and smaller molecules (such as amino acids) present within in situ tumors. These methods are then applied to cancerous tissues to provide as an analytical tool to identify chemical variation of these specific regions between tissues. This work includes investigating human breast cancer tissue biopsies to assess metabolic mechanisms underlying chemotherapeutic resistance and spatial chemical analysis of amino acids within tumors. Method two will also be used to study the tumor microenvironment and intratumor heterogeneity using pancreatic tissue sections from a Myc-induced β-cell

neoplastic mouse model. The entirety of this work is separated into specific aims and described below.

**Specific Aim 1:** An unsupervised multivariate analysis method to compare specific regions in human breast tissue samples using ToF-SIMS.

*Objective:* Develop a method that uses multivariate analysis of ToF-SIMS image data acquired from human breast cancer tissue biopsies to identify the largest amount of variance between specific spatial and chemical regions.

*Hypothesis:* Dense cellular areas or tumors are chemically different than the surrounding connective tissue, or stroma. This difference between regions can be exploited chemically and spatially by the application of a multivariate analysis technique to ToF-SIMS data. Analyzing these regions will provide potential metabolic understandings of specific regions within pre and post chemotherapeutic treated breast cancer tissue samples.

**Specific Aim 2:** Analysis and characterization of human breast cancer tissue biopsies using ToF-SIMS to determine small biologically important molecules that affect chemotherapeutic outcomes and tumor progression.

*Objective:* Using the analysis technique developed in Specific Aim 1, isolated cellular and stromal regions within 23 human breast cancer tissues will be investigated to interpret metabolic mechanisms due to the presence of specific molecular species detected by ToF-SIMS. This will provide a new perspective of specific alterations in cancer metabolism by being able to chemically characterize distinct regions across multiple patients at micron resolution.

*Hypotheses:* Spatially mapped chemical information can be obtained from human breast cancer biopsy samples. Lipid species and small molecular fragments derived from metabolites can be identified that may aid in determining the susceptibility of a tumor to be chemoresistant when compared to other tumors.

**Sub Aim 1:** Characterize the spatial distribution of amino acids and nucleobases present within in situ tumors.

*Objective:* Identify the chemical variability of location of amino acids, nucleobases, and other low molecular weight species within ductal carcinoma in situ (DCIS) using ToF-SIMS. Spatially mapping this chemical information provides a way to corroborate genetic expression data and other ToF-SIMS data of higher mass metabolites associated within the same tissue region.

*Hypotheses:* Amino acid generation, degradation, and recycling are constantly occurring within the body. These molecules can be converted into metabolic intermediates that can be used as fuel for tumors and are also used in proteins required for cell proliferation. The location of specific amino acids at the boundary and within the tumor may aid in determining tumor malignancy and metabolic processes enhancing tumor growth.

**Specific Aim 3:** Analysis of the pancreatic β cell islet tumor microenvironment using imaging ToF-SIMS

*Objective:* Specific metabolites (e.g. amino acids and lipids) within an isolated tumor will be compared with that of control islets to elucidate metabolic changes occurring within the tumor. Further comparison of these metabolites and the surrounding tissue of the tumor to that of a control islet surrounding tissue demonstrate interactions between the tumor and the cells surrounding it.

*Hypotheses:* Myc induced β-cell islet tumors will contain higher intensities of fatty acids and amino acids than non-induced β-cell islets. Synthesis of these metabolites will be due to Myc activation of enzymes that are responsible for producing fatty acid precursors and fatty acid chain elongations and other metabolic pathways that have deregulated. Tissue surrounding the tumor will show a depletion of metabolites that the will provide the tumor to continue to progress.

# Chapter 2. BACKGROUND

As described, the aim of this project was to push the capabilities imaging time-of-flight secondary ion mass spectrometry (ToF-SIMS) as a tool to chemically and spatially identify biologically significant molecules within complex tissue samples, specifically cancerous tissues. This chapter will introduce topics that are necessary for fundamental understanding this thesis including: (1) a short introduction to mass spectrometry imaging techniques (2) an overview of the theory and governing equations of SIMS and (3) principal components analysis fundamentals (4) a short literature review of previous investigations of cells and tissues using ToF-SIMS.

## 2.1 OVERVIEW OF MASS SPECTROMETRY IMAGING TECHNIQUES

Mass spectrometry imaging (MSI) has become an interdisciplinary technique as it crosses the boundaries of physics, chemistry, and biology. MSI allows for the investigation of the spatial distributions of specific molecules at complex surfaces such as cells and tissues. There are many techniques of MSI each with its advantages, disadvantages, and methods for analysis. In this section three of the most utilized MSI techniques will be introduced: matrix assisted laser desorption ionization (MALDI), desorption electrospray ionization (DESI), and SIMS. These techniques are quite different from one another by methods of ionization, spatially resolution, and performance, as shown in Table 2.1. SIMS is well known for its superior spatial resolution down to the nanometer range and is well suited for elemental imaging and inorganic samples. SIMS is beginning to be used more frequently for biological analysis but suffers from sensitivity in the high mass range, making it difficult to identify whole proteins or biomolecules. DESI has the advantage of being performed at atmospheric pressure allowing direct analysis of living samples or thin sections of tissues without any sample preparation. However, DESI is limited in its lateral resolution and detecting high molecular weight peptides and proteins.[15, 16] MALDI has the advantage to be applied to many types of samples and has excellent sensitivity up to a mass range of 100 kDa, and lateral resolution between that of SIMS and DESI. However, MALDI requires a matrix to be applied to the sample to aid in ionization of analyte molecules, which

affects the lateral resolution and the application has been considered arduous and quality limiting.[17] This section will provide an overview of these techniques, followed by a focus on ToF-SIMS.

**Table 2.1.** Important aspects and properties of common desorption/ionization methods commonly used for mass spectrometry imaging. Adapted table combining information from van der Heide[18] and Armstalden van Hove[19]. All values provided for SIMS sources are the optimized primary ion column values.

| Source | Examples | Environment | Energy | Spot Size (d) | MW Range (*m/z*) |
|---|---|---|---|---|---|
| Liquid metal ion gun | $Ga^+$, $In^+$, $Au_n^+$, $Bi_n^{q+}$ | UHV | < 1- 40 keV | < 10 nm | 0−3000 |
| Solid-state gun | $Cs^+$ | UHV | 1-16 keV | < 50 nm | 0−3000 |
| Cluster Sources | $C_{60}^+$ | UHV | 5 eV−40 keV | 200 nm – 200 µm | 0−3000 |
| | $Ar_n^+$ | UHV | 20 −40 keV | 2−50 µm | 0−3000 |
| MALDI | Nd:YAG, N2, ND:YLF | UHV, HV, Ambient | 100-200 J/pulse | 5−300 µm | 100−500,000 |
| DESI | Solvent (e.g. $H_2O$, MeOH, DMF/ACN) | Ambient | n/a | > 150 µm | 100−66,000 |

### 2.1.1 MATRIX-ASSISTED LASER DESORPTION IONIZATION (MALDI) MASS SPECTROMETRY

As implied by the name, MALDI maging analysis requires the application of a matrix to be applied to the sample to aid in laser ionization of analyte molecules. Matrix solutions have a strong absorbance at the wavelength of the laser and must be applied on the surface of the sample. Matrix solutions consist of three major components: an organic solvent (typically methanol or acetonitrile), an organic acid (the matrix), and trifluoroacetic acid (TFA). The organic solvent extracts molecules from the tissue and quickly evaporates, allowing the matrix to form crystals from the weak organic acid.[20] The extracted molecules are then incorporated into the growing matrix crystals. Using TFA increases the availability of protons for ionization. After matrix application, a laser is fired at surface and the laser's energy is absorbed by the matrix and formed crystals causing ablation and desorption of the analyte within the matrix. Ionization of the desorbed species occurs by proton and cation transfer reactions throughout the ablated plume, allowing for detection at the mass analyzer. MALDI is a soft ionization technique, capable of desorbing large molecular species off the sample surface without

fragmentation during ionization. This includes large lipid species and entire proteins. MALDI instruments can be combined with multiple types of mass analyzers including Fourier transform ion cyclotron resonance (FT-ICR) and FT-Orbitrap for high mass resolution and high mass accuracy, but the typical mass analyzer of choice is a time-of-flight (ToF).[19] This is also the mass analyzer of choice for SIMS mass spectrometry imaging, as its speed, sensitivity and mass range detection make it attractive. However, ToF-SIMS range is typically limited to *m/z* 2000, due to extensive surface fragmentation, while MALDI can detect species up to *m/z* 200,000.[19, 21]

The spatial resolution in MALDI is limited mainly by the matrix type and application, which has an effect on the resulting crystal size, and the ability to focus the laser. The quality of the mass spectrometric image is dependent on the matrix coverage, and matrix coverage is dependent on surface parameters such as the wetness of the surface during application, and thickness of the crystal layer.[20] Therefore, the smaller the crystal sizes the higher the image resolution. For tissue imaging, the choice of matrix is extremely important for quality and validity of imaging data, as the spatial resolution can be affected by the matrix crystal size, which is typically above 10 µm.[22] The matrix choice also determines the types of species that can be analyzed (e.g. lipids or proteins). It is also possible to increase image resolution by decreasing the diameter of the laser spot but this will decrease sensitivity.

Recently, MALDI researchers have shown that it is possible to achieve 3-7 µm spatial resolutions of biological samples and single cells,[23-26] but most MALDI imaging experiments are performed with a spatial ranging from 50−200 µm.[27, 28]

MALDI has established itself as an incredibly versatile analytical technique with a high level of accuracy on tissue, one of the most heterogeneous and difficult samples to analyze. The technique has been involved in many studies to determine cancer mechanisms and biomarkers. [29-34]

As discussed previously, ToF-SIMS is able to provide higher spatial resolution but a lower mass range when compared to MALDI. Research groups have combined the two techniques to provide a complementary analysis of biological samples. Examples that of studies that have utilized both ToF-SIMS and MALDI include the analysis of Fabry disease biomarkers,[35] rat-brain sections,[11] and spinal cord.[36]

### 2.1.2 DESORPTION ELECTROSPRAY IONIZATION (DESI) MASS SPECTROMETRY

DESI is an ionization technique that uses charged solvent droplets to extract analysis from a sample surface. DESI is executed by directing electrosprayed charged droplets and ions of solvent onto the sample surface. The impact of these charged droplets/particles on the surface produces secondary microdroplets and gaseous ions of material originally present on the surface.[37] These microdroplets and ions are then drawn into the inlet of a mass spectrometer. The angle of the secondary microdroplets and the MS inlet must be optimized to allow the maximum ion volume to enter the mass spectrometer.[38] Similar to MALDI and the composition of the matrix used, solvent composition used in DESI can also provide different chemical information. Results experimenting with solvents have showed that mixtures of *N,* N – dimethylformanide (DMF) with water or methanol enhances the signal of low molecular weight compounds, when compared to mixtures of DMF with acetonitrile (ACN), which showed an increased extraction of lipids from tissue sections.[39] In addition, mixtures of DMF and ACN were deemed "morphologically friendly," meaning that there were able to extract lipids from tissue sections without damaging or causing gross changes in morphology.[39, 40] This allows for histological staining after DESI analysis.

The primary advantages of DESI are its ability to characterize samples at atmospheric pressure which enables direct analysis of samples in real time and that samples require little to no sample preparation. DESI surpasses ToF-SIMS in its ability to analyze high mass species with very high resolution and also the ability to combine analysis with MS/MS capabilities as it is compatible with many mass analyzers. Mass analyzers that have been used for DESI imaging include triple qudrupoles,[41] FT-ICR,[42] and Orbitraps.[43] DESI has the lowest spatial resolution compared to that of MALDI or SIMS. The typical resolution ranges between 180−220 μm for proteins and lipids in tissue samples,[44, 45] but for smaller compounds less than 15 μm has been demonstrated.[46]

Many studies have utilized the strengths of DESI for cancer tissue investigations, which have shown its promise as a clinical tool. Identification of tumor margins,[43, 47, 48] biomarkers in cancerous tissues,[49, 50] brain tumor classification,[45] as well as a intraoperative molecular diagnosis of brain tumors.[51]

## 2.2 SECONDARY ION MASS SPECTROMETRY (SIMS)

SIMS is an ultra-high vacuum (UHV) surface analytical tool capable of obtaining chemical information from biological samples with sub-micron spatial resolution and high chemical specificity. SIMS requires no matrix, fluorescently labeled analogs, tags, extraction, or harsh chemical treatment to samples to obtain chemically sensitive spectra or high resolution two and three-dimensional images. In a conventional SIMS experiment, an energetic primary ion beam is focused onto a sample surface. The primary ions used in this beam can consist of atomic, polyatomic, or range of clusters ($Ar^+$, $Ga^+$, $Cs^+$, $O_2^+$, $Au_n^+$, $Bi_n^{q+}$, $SF_5^+$, $C_{60}^+$, $Ar_n^+$) which, on impact of the sample surface, causes sputtering of molecular and atomic species. Some of these ejected species are charged, making them secondary ions. The impact site of the primary ion beam tends to generate atomic and small molecular fragments, but as distance is increased from the impact site large molecular compounds tend to desorb. A simplified image showing the process of the SIMS using a monatomic primary ion beam is illustrated in Figure 2.1. The majority (approximately 99%) of the ejected species are neutral and are not analyzed unless post-ionized with a secondary source, typically a laser.[52] The charged species, or secondary ions, are then extracted into a time-of-flight mass analyzer, resulting in the generation of a mass spectrum characteristic of the analyzed surface.

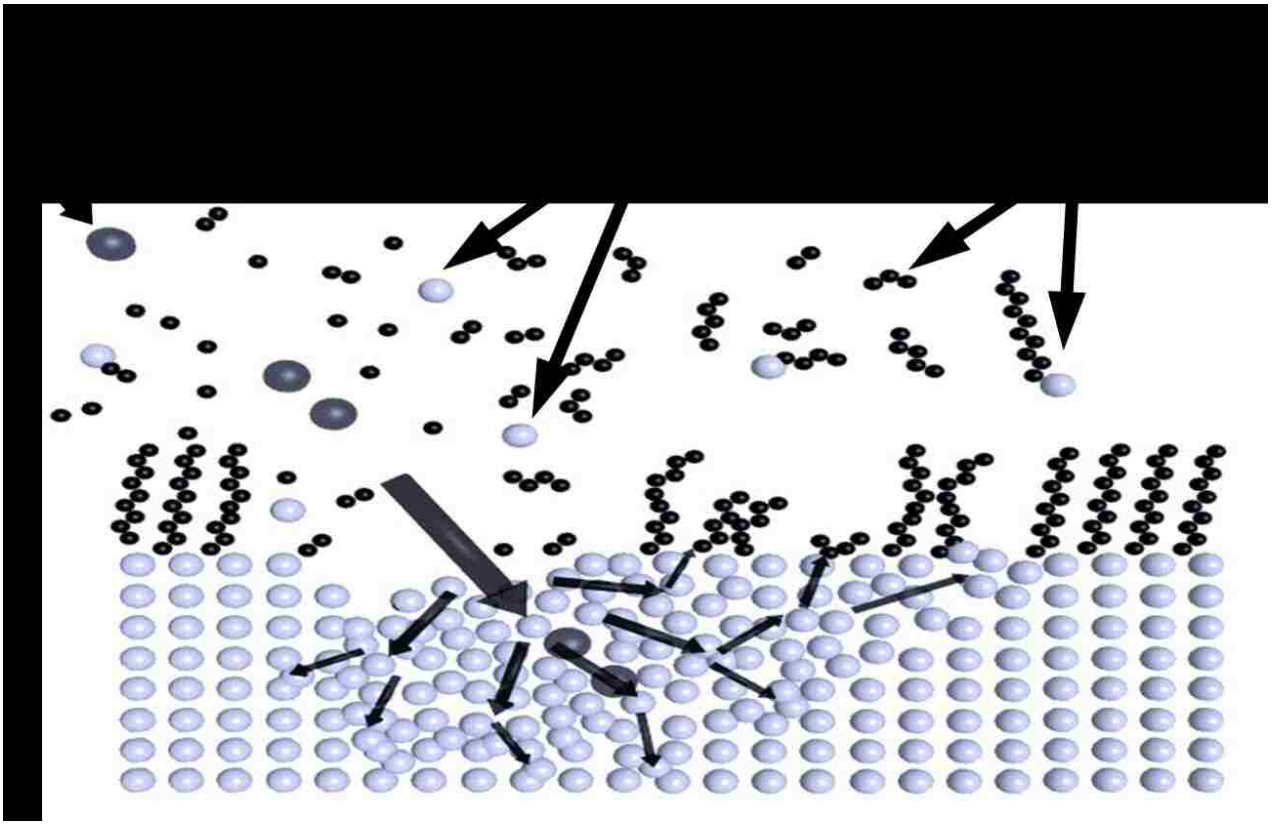

**Figure 2.1.** Simplified image of the sputtering process from a monatomic primary ion beam that occurs in secondary ion mass spectrometry. Image adapted from Daniel J. Graham.

The chemical composition of a sample can be mapped by combining a mass analyzer with a narrowly focused primary ion beam and rastering it across the sample surface. A complete mass spectrum is obtained at each point of impact of the rastered ion beam. Measurements can range from a few minutes to several hours based on the size of the analysis are and the desired mass range. After the data has been acquired, an ion of interest or a combination of ions can be selected and their surface distribution can be visualized. A major strength of SIMS imaging is the ability to identify regions of interest from the total ion image and the mass spectra from the pixels in that region can be summed, allowing for spectral investigations.

### 2.2.1 FUNDAMENTAL SIMS EQUATION

The yield of secondary ions is dependent on a number of parameters and is summarized in the essential SIMS equation below[53]:

$$I_s^m = I_p y_m \alpha_m^{\pm} \theta_m \eta \quad \textbf{(2.1)}$$

$I_s^m$: Secondary ion current of species *m*

$I_p$: Primary ion particle flux

$y_m$: Sputter yield of species *m*

$\alpha_m^{\pm}$: Ionization probability of *positive or negative* ions

$\theta_m$: Fractional concentration of *m* in the surface layer

$\eta$: Transmission of the analysis system

Secondary ions of species *m* ($I_s^m$) are sputtered from a surface, usually a solid, as a result from the bombardment of energetic primary ions from the uppermost monolayers of the surface. The secondary ion (SI) current of *m* is dependent on the two fundamental parameters, $y_m$, and $\alpha_m^{\pm}$. Where $y_m$ is the yield of sputtered particles of species *m,* neutral or ionic, per primary particle and $\alpha_m^{\pm}$ is the ionization probability of species *m*.

### 2.2.2 SPUTTERING

The sputter yield can be defined as:

$$y_m = \frac{N_m}{N_p} \quad \textbf{(2.2)}$$

$N_m$: Number of sputtered particles of species *m*

$N_p$: Number of primary ion particles that impact the analysis surface

Sputtering is a damaging process and the goal of this work is to analyze complex biological sample surfaces in their most native state. Therefore, it is crucial to know the sputter rate for organic materials like cells and tissues. However, it becomes very difficult to measure the sputter rates for heterogeneous organic materials. Thus, instead of sputter rate the concept of the disappearance cross-section, $\sigma$, was introduced with the study of organic polymers.[54] Due to the bombardment of primary ions over time, significant species from the SIMS spectrum will continually decrease in signal, $\sigma$ relates to the secondary ion intensity by the following equation:

$$I_m = I_{mo} e^{-\sigma I_p} \quad \textbf{(2.3)}$$

$I_m$: Recorded signal of species *m*

$I_{mo}$: Original surface density of species *m*

$\sigma$: Disappearance cross-section

$I_p$: Primary ion dose

The disappearance cross-section can be qualitatively related as the average surface area that is damaged during a single primary ion collision. This provides a relationship between the disappearance cross-section and can be thought of as the damage cross-section within SIMS. As previously mentioned, it is important to maintain the integrity of the biological surface to the extent that molecular signals do not begin to decrease. This requires analyzing the surface in the "static" regime.

SIMS can be separated into two distinct regimes: dynamic and static. Castaing and Slodzian initially proposed dynamic SIMS in 1962, where the authors described mass selecting secondary ions to analyze all the points of an extended area or a secondary ion microscope.[55] Dynamic SIMS analyzes ions removed from a sample by sputtering through it. Static SIMS, the method used in this research, was developed in the late 1960s and 1970s by Benninghoven and his group when they demonstrated the use of a low primary particle flux density (<1 nA $cm^{-2}$) to generate mass spectral data and is characteristic of the surface layer.[56, 57] The resulting data is considered static because statistically a single primary ion only impacts once at any point on the surface. To remain within the static SIMS regime Benninghoven calculated that this limit is reached at an ion dose of $10^{13}$ ions $cm^{-2}$. Static SIMS instruments are usually equipped with a time-of-flight (ToF) analyzer and will be the focus of the instrumentation sections.

### 2.2.3 Mechanistic Models for Sputtering

The attention on the fundamental process of sputtering has resulted in multiple theories and models based on the primary ion source and its energy when impacting the surface. One of the most common theories is the linear cascade theory which models a high energy monatomic primary ion impacting a solid surface as shown in Figure 2.1. This model assumes that sputtering occurs by particle bombardment at

small incident particle current and fluence. In the theory, the primary ion particle transfers its energy to the target atoms at the surface and initiates a series of collision cascades between the atoms in the solid. Due to the assumption on the basis of elastic collisions, some of these collision cascades return to the surface and cause the emission of sputtered particles. Fraser Reich has referred to this as a type of molecular billiards, “The cue ball goes into the material, and it sputters−it lifts off material that’s characteristic of the top surface.” [58] While this model is accurate for medium-to-high energy particle bombardment, it is less accurate for describing lower energy, polyatomic primary ions impacting complex organic surfaces such as cells and tissues.

It has been suggested that for small molecular ions used in primary ion beams ($Au_n^+$, $Bi_n^{q+}$, and $SF_5^+$), the energy transfer can proceed through various modes of electronic excitation and is best described as *kinetically assisted potential sputtering.*[18] Impinging these primary ion beams on the sample surface lead to the assumption that overlapping collision events are occurring within the lattice of the sample as a result of the same initial collision event. The linear cascade model only assumes the occurrence of individual events. The overlap of collisions results as the momentum transfer between atoms is constrained to a more localized volume and when multiple atoms from the impinging ion beam hit the same region. When these overlapping collisions occur on dense substrates additional energy loss can proceed via electronic excitation. This excitation results in a localized heat spike with thermal evaporation which produces the emission of ions and molecular fragments from the impact area.[59, 60] An illustration of this model is shown in Figure 2.2. This model better explains the assumptions that are occurring in this work, as $Bi_3^+$ was the primary ion source used for all experiments.

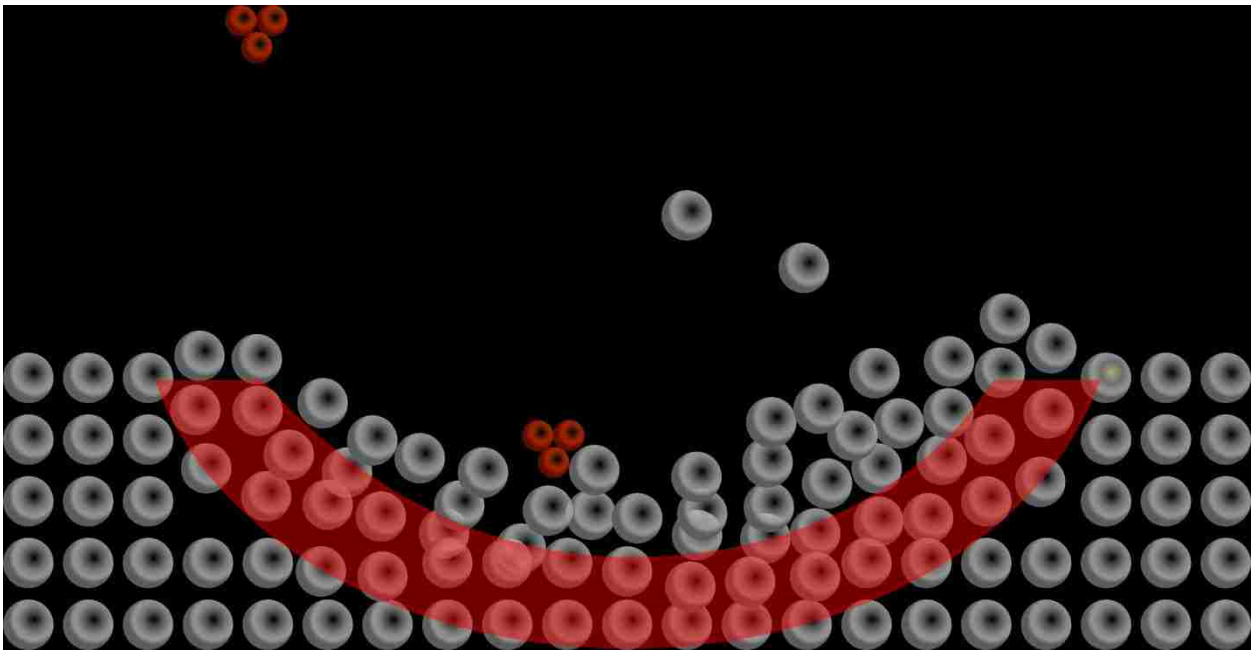

**Figure 2.2.** A simplified illustration of sputtering thought to occur during kinetically assisted potential sputtering induced on small primary ion molecular impact. The red shaded area shows the area most affected by the impact of the primary ion, with preferential ejection of atoms/ions and fragmented molecules within the central region and the ejection of intact molecules from the edges of the shaded region.

Molecular Dynamics simulations are used to provide insight and propose theories to understand the sputtering processes resulting from molecular/polyatomic/cluster ion impact. One of the leaders in modeling sputtering yields and surface roughness after bombardment of cluster primary ions, focusing on $C_{60}^+$ is Barbara Garrison.[61, 62] Garrison has shown enhanced desorption initiated by $C_{60}^+$ on multiple surfaces when compared to monoatomic ions using molecular dynamic simulations. The essential mechanism observed in the simulations show that the kinetic energy of cluster source ions is deposited closer to the surface, resulting in less penetration/deposition of the cluster ions, higher yields of secondary ions, and shallower craters.[61, 63] In summary, simulations of small molecular ion impact (e.g. $Au_n^+$, $Bi_n^{q+}$, and $SF_5^+$) demonstrate the ejection of atoms/ions and fragmented molecules near the central region of impact and the ejection of intact molecules from the halo edges of the impacted surface as shown in Figure 2.2. Simulations using large cluster ion impact (e.g. $C_{60}^+$) show the removal of surface molecules due to less sample depth penetration and the deposition of energy closer to the surface.

### 2.2.4 IONIZATION

The ionization probability ($\alpha_m^{\pm}$) is strongly influenced by the electron exchange processes between the departing species (*m)* and the surface. Therefore, the electronic state of the sample surface is critical. In general, the ionization probability for molecules in SIMS is not well understood and requires further investigation. The yields of elemental secondary ions can vary by several orders of magnitude across the Periodic Table, and are dependent of the chemical state of the surface, meaning that signal for a specific ion can be suppressed or enhanced due to its chemical environment.[53] This phenomenon is known as the *matrix effect*, further complicating the calculation of $\alpha_m^{\pm}$.

The formation of secondary ions from organic materials can occur by numerous mechanisms.[18, 53, 64] Some examples include the ejection of an electron to form an odd electron ion $M^{\bullet+}$, acid/base reactions of polar molecules form $(M+H)^+$ or $(M+H)^-$ ions, and cationization or anionization of neutral molecules. The secondary ion spectrum also shows characteristic molecular fragment peaks of lower masses which provide information of chemical structure. Ionization of these species probably occurs via a collision induced mechanism as discussed in section 2.2.3.

Matrix effects and surface charging also have an effect on secondary ion yields from organic materials. Surface charging is the build-up of positive or negative charges on the sample surface, which can cause ions of the ejection of opposite polarity ions to be slowed. This process leads to a decrease in the detection of secondary ions in the areas of the sample experiencing the charging effect. This buildup of charge on an insulating, organic sample can be remedied by irradiating the affected sample surface region (area being analyzed) with electrons. However, it should be noted that the neutralizing electron dose should be minimized, as electron flooding can cause damage to the sample over time.[65, 66]

### 2.2.5 MATRIX EFFECTS

As previously discussed the yield of secondary ions, specifically the ions' ionization probability ($\alpha_m^{\pm}$), is strongly affected by the electronic state of material being analyzed and because of this complicates the ability for quantitative analysis. This

phenomenon is termed the matrix effect. Therefore, SIMS is considered "semi-quantitative" as components at the surface or within a material usually cannot be determined as a concentration. An example of the matrix effect can be presented as the same compound in two different matrices, all other parameters being equal, may have different secondary ion yields. This difference is secondary ion yields could be due to primary ion impact-induced atomic mixing, segregation, diffusion, and surface roughness. Studies performed with rigorous standards have shown that it is possible to quantify the amount of a substance in a material, [67, 68] although this is very difficult to do accurately for a wide range of samples.

Secondary ion suppression and enhancement from matrix effects often prevent the absolute determination of concentrations of lipids, drugs or biomarkers within biological cells and tissues. This is one of the major limitations of SIMS. Relative comparisons can be made if the samples' matrices are similar, i.e. the relative amount of a particular lipid species in the plasma membranes of multiple cell types prepared the same way.

## 2.3 ToF-SIMS Instrumentation

There are a number of commercially available and custom built ToF-SIMS instruments available for materials analysis.[18] The following section will provide a brief overview of the major components within a commonly operated ToF-SIMS instrument.

### 2.3.1 Primary Ion Sources

Most commercially available ToF-SIMS instruments are equipped with more than one ion source and an electron source. In organic analyses, the typical primary ion sources used are liquid metal ion guns and electron impact sources, due to the ability to provide high spatial resolution and less damage to the surface.

#### 2.3.1.1 *Liquid metal ion gun (LMIG)*

The liquid metal ion gun (LMIG) sources are used for producing small spot ion beams. Sources found in SIMS instrumentation are $Ga^+$, $In^+$, $Au_n^+$ or $Bi_n^{q+}$, where the *n*

(typically 1 through 7) and *q* (limited to 1 through 3) are integer values representing the number of atoms and charge, respectively. $Au_n^+$ and $Bi_n^{q+}$ sources are currently the best primary ion sources for obtaining high spatial resolution (HSR) molecular information from samples.[69] LMIGs produce an ion beam by applying a large electric field directly to a thin wire tip that has been heated to create a liquid metal. Ion are then extracted from the resulting Taylor cone and focused down the column to the sample. Polyatomic ions have been shown to have medium to shallow penetration into the sample, high secondary ion yield, and lower residual sample damage when compared to high-energy monoatomic sources making them useful for the analysis of biological/organic samples. $Bi_n^+$ sources have also been shown to have a higher current than that of $Au_n^+$ sources, making it the preferred source for authors performing biological tissue imaging experiments.[2] For organic materials, spatial resolution is on the order of 100-200 nm.[1, 2, 69]

#### 2.3.1.2 *ELECTRON IMPACT SOURCES*

Electron impact (EI) sources are using for producing inert gas ion beams. $Ar^+$ is the most common beam used, but EI sources can also generate $O_2^+$ and $SF_5^+$ beams. Current technology and modifications have been able to produce beams such as $C_{60}^+$ and $Ar_n^+$, where *n* can equal up to several thousand.[18, 69-73] These sources consist of a chamber in which the gas of interest is introduced and then irradiated by electrons. These energetic electrons interact with the gas atoms/molecules and induce the emission of electrons from these atoms/molecules which results in the formation of positively charged ions. These positive ions can then be extracted and used to impact the surface with energies ranging from <1−40 keV.

The production of larger cluster sources such as $C_{60}^+$ and $Ar_n^+$ requires additional hardware within the instrument. A sublimation chamber is used to generate organic vapors, which are then irradiated by electrons. These sources are capable of producing beams of up to 40 keV and multiples for doubly and triply charged ion ($C_{60}^{2+}$ and $C_{60}^{3+}$). $C_{60}^+$ ion beams. Until recently, these sources have not been as useful for high spatial resolution imaging as LMIG sources and are typically utilized for their low damage sputtering and analysis of organic samples using high primary ion doses. $Ar^+$ cluster

ions are produced in a gas cluster ion beam (GCIB) source. The source condenses individual atoms into neutral clusters by cooling in a supersonic jet. These clusters are then ionized using electron impact. While these large cluster sources are becoming more popular in organic and biological analysis due to their ability to provide large molecular ions (*m/z* 500-2000) and less fragmentation, their major drawback is their inability to be focused much below ~5 μm.[74, 75] Fletcher et al. has shown that it is possible to achieve 1 μm resolution with a $C_{60}^+$ primary ion beam on organic samples using a research-based ToF-SIMS instrument.[76]

### 2.3.2 TIME-OF-FLIGHT ANALYZER

A time-of-flight (ToF) analyzer is installed on the ION-TOF V, the instrument used in all experiments described in this work. The ToF system analyzes pulses of secondary ions that have been accelerated to fixed potential so that all ions possess the same kinetic energy. Once accelerated to the same energy, the ions are then allowed to drift through a field free space before hitting a detector. As the masses travel through the field free region, heavier masses will travel more slowly than lighter masses. A diagram of a ToF analyzer is shown in Figure 2.3. As masses impact the detector an ion's travel time can be related to its mass by the following equation[53]:

$$t = L\left(\frac{m}{2zV}\right)^{\frac{1}{2}} \quad \textbf{(2.4)}$$

$t$: Measured ion flight time

$L$: Flight path length, length of flight tube

$m$: Mass of ion

$z$: Charge of ion

$V$: Accelerating potential

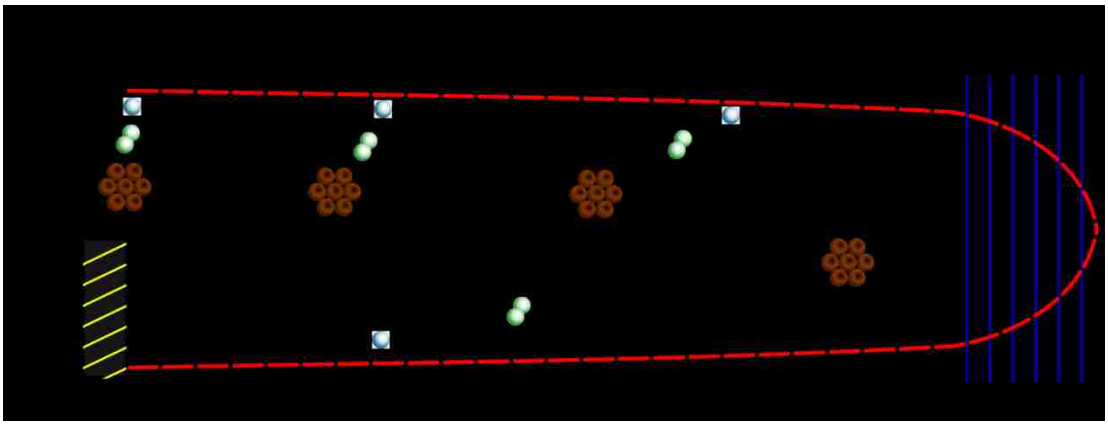

**Figure 2.3.** Diagram displaying a time-of-flight analyzer. Secondary ions are extracted and accelerated at the entrance of the analyzer, where they enter a field free drift region. The drift path is shown in a dashed red line. Smaller fragment ions travel faster than larger fragments, impacting the detector first, producing a mass spectrum as a function of time. The reflectron improves mass resolution by correcting the flight distance of ions of the same mass that enter the analyzer with slightly different energies.

The ToF analyzer is equipped with a reflectron, which uses a time dependent electric field in the ion mirror to reverse the directions of the ions entering it. The use of a reflectron improves mass resolution by correcting the flight times of ions with the same mass that have an initial energy spread when entering the mass analyzer.

Advantages of a ToF analyzer are its ability to detect all collected secondary ions in parallel, at a high mass resolution ($m/\Delta m$ ~10,000) and a dynamic mass range of $0<m/z<$ 10,000.[4, 5] This is incredibly important when analyzing biological samples, as not all molecules of interest may be known prior to analysis.

### 2.3.3 Other ToF-SIMS Instruments Used for Biological Sample Analysis

As imaging ToF-SIMS is being utilized more frequently to examine biological samples such as cells and tissues, developments within the instrumentation have been introduced to accommodate this. The design of the research-based J105-3D Chemical Imager instrument by Ionoptika was aimed to provide molecular distributions in three dimensions from organic materials with high spatial resolution (~1 µm).[76] The J105 also provides a glove box so that biological samples may be prepped for frozen hydrated analysis and also can utilize a stage capable of freeze-fracturing of frozen cells under vacuum.[77, 78] As a dynamic SIMS instrument, it pulses the secondary ions into the analyzer instead of pulsing the beam which is common on most other ToF-SIMS instruments. Due to its modified geometry, this instrument was one of the first with the

ability to perform MS/MS imaging experiments.[76, 79] MS/MS offers the ability for detailed elucidation of biomolecules within cell and tissue sample increasing the confidence in the interpretation. Recently, commercial producers of ToF-SIMS instrumentation have developed MS/MS capabilities by adding collision cells for selected ions, as demonstrated by the PHI *nanoTOF* II,[80] or the addition of a second analyzer, as demonstrated by IONTOF's Hybrid SIMS.[81, 82] These developments demonstrate the plethora of ToF-SIMS instrumentation dedicated to analysis of biological samples.

## 2.4 DATA ANALYSIS USING PRINCIPAL COMPONENTS ANALYSIS (PCA)

ToF-SIMS generates large complex data sets, especially in organic materials. A typical tissue image data set comprised of 1280x1280 pixels, a typical image size in this work, accounts for more than 1.6 million spectra. Within each spectrum, there can be hundreds of peaks. This presents the challenge of how to process and analyze these large data sets accurately. Due to the complexity of the data and challenging nature of biological samples, multivariate analysis methods are frequently employed to aid in analyzing the data. A method frequently used is principal components analysis (PCA).

### 2.4.1 FUNDAMENTALS OF PCA

PCA is both a supervised and unsupervised multivariate analysis technique that determines the greatest sources of variance within a data set. The input to PCA is a matrix where the rows are samples (i.e., spectra) and the columns are variables (i.e., peak intensities). It can be considered unsupervised because no other inputs other than all peak intensities from a mass spectrum are used to define the correlation. It can also be considered supervised if only specific peaks are selected before PCA is applied. PCA describes the variance within this input data matrix by determining the directions of greatest variation within the data. In this way, PCA acts to rotate the data set onto a new coordinate system that better describes the variance within the data set, as seen in Figure 2.4.[83] The new axes, termed principal components, have been formed by this transform are linear combinations of the original variables (ToF-SIMS peak intensities). The first principal component (PC1) captures the largest amount of variance in the dataset followed by decreasing amounts of variance in following PCs. The two outputs

of PCA are the scores, which relate the samples to one another, and the loadings, which relate the variables (the peaks) to the data points.

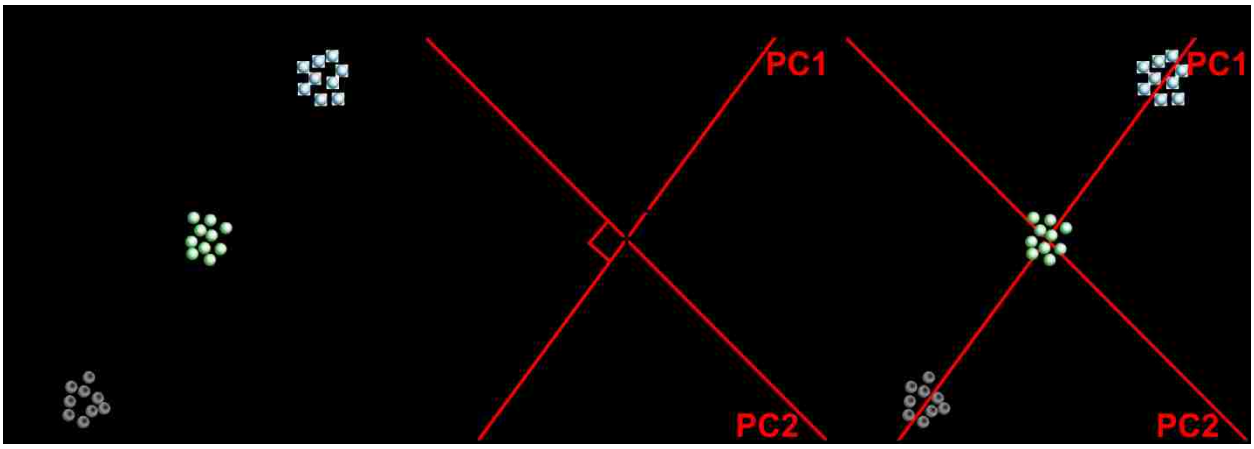


**Figure 2.4.** Graphical representation of principal components analysis. PCA can be visualized as an axis rotation. The PC axes are rotated **(B)** to capture the greatest directions of variations in the original data **(A)**. An overlay of the PC axes and the original axes is shown in **(C)**. This figure adapted from https://www.nb.uw.edu/mvsa/general-intro-pca, provided by Daniel Graham.

Sample scores indicate how each sample or individual mass spectrum correlates with other mass spectra within the dataset. Similar scores indicate mass spectral similarities and can be displayed in a plot or image depending on the original input of the sample data. An example of a scores plot showing two data sets, red and blue, with 88% total variance captured within the first PC is shown in Figure 2.5 (left). It can be seen that red samples with positive scores complete separate from the blue samples with negative scores across the y-axis. This can be interpreted as the sample sets being completely different from each other. The scores also indicate the reproducibility within each sample set. The red samples are tightly grouped together and the 95% confidence limits, the red bar above and below the samples, are also narrow. This suggests that the samples are spectrally similar. The blue samples show more spread between samples and have a wide 95% confidence limit. This suggests more spectral variability across this sample set.

Loadings indicate the specific chemical differences observed in the samples within each PC. The loadings show the peaks that are correlated with scores plots/images, and demonstrate how peaks within the mass spectrum correlate with each other. An example of the loadings plot is shown in Figure 2.5 (right). The positive loadings (red) in Figure 2.5 correlate with the positive scores (red samples, Figure 2.5,

right). The mass 58.1 shows a high loadings value for the red samples and is associated with being one of the large differences between the red and blue samples. The negative loadings correlate with the blue samples. The masses 577.5 and 601.5 which are present in the blue samples show the largest chemical difference between the red and blue sample sets.

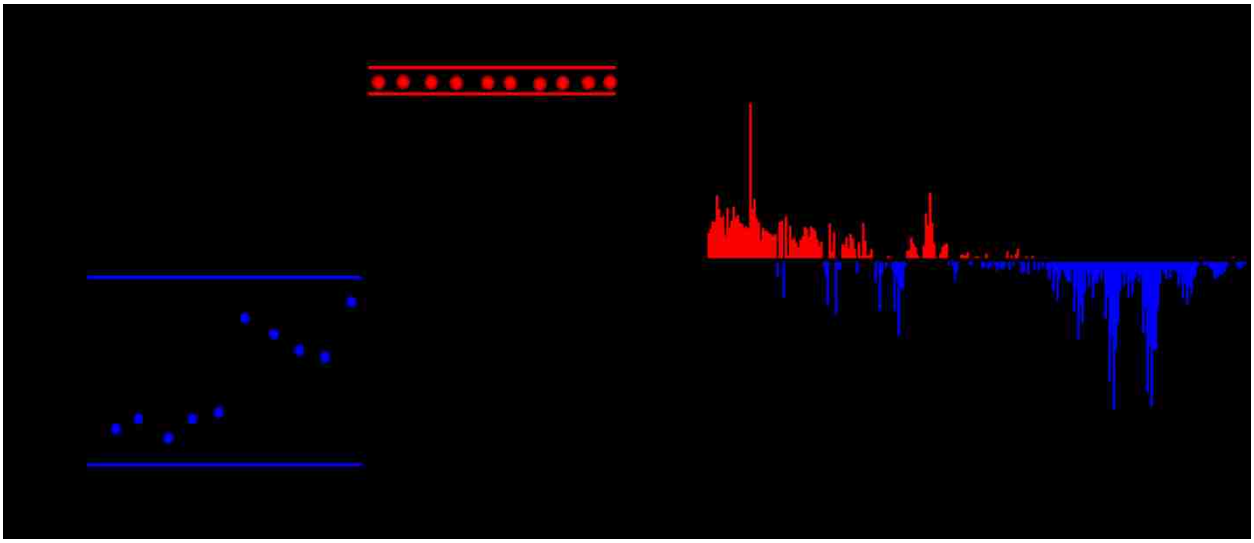

**Figure 2.5.** Example of PCA scores (left) and loadings (right). Red samples are observed with positive scores (left, y > 0) and correlate to positive loadings (right, y > 0) also colored red. Blue samples are observed with negative scores (left, y < 0) and correlate with negative loadings (right, y < 0) also colored blue. Colored lines above below samples in scores plot represent the 95% confidence interval.

Typically data is pre-processed by applying scaling, centering, and non-linear transformations. In this work, all data is Poisson scaled before any type of PCA is applied, either imaging or spectral, as this scales the data to the noise structure of ToF-SIMS. PCA has found many applications with ToF-SIMS data; however, it is a complex analysis technique. Daniel J. Graham, Matthew S. Wagner and David Castner have shown many of these applications but have also described many ways to appropriately apply this technique to ToF-SIMS data and complex samples.[83-85]

## 2.5 SUMMARY AND APPLICATIONS OF SIMS STUDIES OF CELLS AND TISSUES

The first secondary ion images of a biological cell were obtained in the dynamic regime, generally using a magnetic sector mass analyzer. At the time only one secondary ion species could be analyzed at a time and the process was limited to

atomic species. However, Chandra and Morrison used the technique to intracellular distributions of ions (i.e. $K^+$, $Na^+$, $Mg^+$, $Ca^+$).[86, 87] Chandra and coworkers went on to be the first to describe frozen hydrated protocols for SIMS analysis of cells, which has been one of the primary methods for cell-based studies.[88] Early publications relating to cellular and tissue investigations were centered on mapping atomic elements relevant to biological activities,[89] visualizing the distribution of isotopically labeled additives,[90] and intracellular drug distributions of cancer drugs containing a characteristic atomic marker (e.g. boron).[91, 92]

Static SIMS allows for the detection of intact molecular-type ions from top monolayers of the cell. This surface sensitivity makes static SIMS advantageous for the analysis of lipids and the lipid membranes of cells. The first study using ToF-SIMS to examine biological cells was performed by Colliver et al. in 1997 on a *Paramecium*.[93] The authors proposed a frozen-hydrated sample preparation technique specifically for ToF-SIMS analysis. Even though the secondary ion (SI) yield was low mainly due to the use of $Ga^+$ primary ion beam, this work proved the practicality of obtaining molecular information from a single biological cell with ToF-SIMS. After this report, studies have been published that investigated lipid systems,[94, 95] cellular membrane model systems,[96, 97] and components of cellular plasma membranes.[98, 99]

As the development of preparation techniques for cells and LMIGs improved SI yield, publications using ToF-SIMS to image biological samples began increase. In 2004, Ostrowski *et al.* used ToF-SIMS to image the changes in the lipid composition during the mating of *Tetrahymena*, a protozoan.[100] Using a freeze-fracturing method, the authors showed a reduction in the low-curvature lipid phosphatidylcholine (PC) in the membrane regions between fusing *Tetrahymena* and that the fusing region contained an elevated signal of a high-curvature lipid, 2-aminoethylphosphonolipid. The first attempt to probe the three-dimensional (3D) chemistry of a single cell was performed by Fletcher *et al.* in 2007. The authors used a large cell system, *Xenopus laevis* oocyte, using a 40 keV $C_{60}^+$ ion beam for sputtering and analysis, identifying multiple lipid species and their distribution throughout the cell.[101] Studies using smaller cells, such as rat kidney and HeLa cells were used to continue pushing the capabilities of ToF-SIMS in both 2D and 3D. Breitenstein *et al.* demonstrated that as each layer was

sputtered from the cells using a cluster beam ($C_{60}^+$) and subsequently analyzed using a LMIG ($Bi_3^+$) that the distribution observed in the *xz* was the vertical inverse of the actual distribution.[102, 103] This was the introduction to mathematical transformations to correct and mirror the real distribution. This was further improved upon by Robinson *et al.*, who investigated the sputter rate of individual cells, and designed the ZCorrectorGUI, which provided the *z*-axis correction and 3D visualization within a graphical user interface.[104]

Other applications utilizing ToF-SIMS high sensitivity were used to study cancer and characterize metabolic changes in cells. Kulp *et al.* provided a studying showing the practicality of using ToF-SIMS imaging to identify subtle chemical differences to differentiate three breast cancer cell lines using multivariate analysis techniques.[29] The authors also demonstrated that using ToF-SIMS and PCA could identify cellular compartments (e.g. cytosol, nuclear, and membrane) from cellular homogenate. Many other research groups studied multiple cancer cell lines treated with a variety of substances, ranging from drugs to heavy metals.[33-35] Other research used multivariate analysis techniques to discriminate the chemical differences between malignant and non-malignant,[31, 32] as well as the lipid metabolism associated with metastatic potential.[30]

Cellular studies using ToF-SIMS demonstrates the complexity of data analysis. Expanding the technique to tissue analysis increases both the complexity and the amount of data to be analyzed. The majority of ToF-SIMS research conducted on biological tissues has also been focused on lipids, as these provide high SI yields. Rat brain sections have become a well-established model system for ToF-SIMS investigations.[9, 105-107] Recently, developments in have shown that subjecting rodent brains to trifluoracetic acid vapor provides an increased signal and chemical species previously unobserved.[36] Further investigations have been conducted in lipid-related diseases such as Duchenne muscular dystrophy,[10, 108] nonalcoholic fatty liver disease,[109] atherosclerosis,[110] and cystic fibrosis.[111, 112] The comparison of chemical images across healthy and diseased tissue exposes areas of abnormal chemistry and can identify the presence or absence of a specific biomarker. For example, Cillero-Pastor *et al.* showed that alterations in the localization of cholesterol-related peaks provided for a way to distinguish the difference between healthy and osteoarthritic

cartilage.[11] ToF-SIMS analysis of tissues treated with drugs to observe localization or the metabolic changes in tissue after drug administration demonstrate the use of the technique for drug discovery.[107] Phan *et al.* found that the distribution and abundance of lipids within a common fruit fly's brain change significantly after the administration of methylphenidate, a common treatment for attention deficit/hyperactivity disorder.[37]

Cancer tissue studies using ToF-SIMS are also increasing; however, the difficulty of acquiring human tissues for viable clinical data is a limiting factor. Prostate cancer,[113] colon cancer,[7] and recently breast cancer tissues have been investigated. Angerer *et al.* found evidence of lipids related to inflammatory cell signaling outside of tumors and cancerous areas to be dominated by nonessential fatty acids.[114] The tissue studies presented here show that ToF-SIMS has the potential applicability to study a wide range of disease types and provide a new perspective in metabolic analysis.

# Chapter 3. MATERIALS AND METHODS

## 3.1 SUBSTRATES

Silicon wafers were used as substrates breast cancer tissue experiments. Silicon wafers (Silicon Quest Intl., Santa Clara, CA) were diced using a diamond saw into 2 $cm^2$ chips.

Indium tin oxide (ITO) coated glass slides were used as substrates for mouse pancreatic tissue experiments after the initial MYC experiments Chapter 6 were conducted. ITO coated glass provides a substrate that can be analyzed by ToF-SIMS and subsequently stained for microscopy studies. Boro-aluminosilicate glass slides with ITO coated on one surface were purchased from Delta Technologies, Ltd. (Loveland, CO) with a surface resistivity of 4-10Ω and a size of 2.5 $cm^2$. All ITO slides were cleaned using the protocol detailed within the methods section below.

## 3.2 BIOLOGICAL TISSUE SPECIMENS

Tissue specimens were immediately embedded in Tissue-Tek® (Fisher Scientific, Pittsburgh, PA) optimum cutting temperature (OCT) compound cryopreserved using liquid nitrogen and stored in a -80 °C freezer. Frozen tissue blocks were sectioned in a cryostat-microtome held at -23°C at the Fred Hutchinson Cancer Research Center (FHCRC). Each tissue sample was serially sectioned three times and each section ranged from ~5-7 µm in thickness. Tissue sections were obtained from the Fred Hutchinson Cancer Research Facility and cryosectioned onto clean 2 $cm^2$ silicon wafer chips or 2 $cm^2$ ITO glass substrates. Human breast cancer tissues were cryosectioned by Kelly Wirtila and murine pancreatic tissues were cryosectioned by Li Huang. Detailed explanations of tissue acquisition and procedures are explained in detail within each chapter.

## 3.3 SILICON SUBSTRATE PREPARATION

2 cm x 2 cm chips were immersed in deionized water overnight to remove salts from the dicing process followed by 2x five minute sonications in dichloromethane,

acetone and methanol (all purchased from Sigma Aldrich, St. Louis, MO) for removal of organic contaminants. Wafer chips were then dried with $N_2$, placed in a petri dish backfilled with $N_2$ and sealed with Parafilm® (VWR International), and stored in a laminar hood until use.

## 3.4 ITO SUBSTRATE PREPARATION

ITO glass slides were cleaned using a 20% by weight solution of ethanolamine (≥99%, purchased from Sigma Aldrich, St. Louis, MO) in deionized water, heated to 80 °C in an ultrasonic bath. Immersion ITO in this solution with ultrasonic agitation for a period of 15 minutes will provide for the removal of any fingerprints, body oils or similar residual organic contaminants. Following the immersion cycle, the substrates should be removed and rinsed several times with MilliQ ultrapure water (18.2 MΩ cm), and blown dry $N_2$. ITO slides were then placed in a petri dish backfilled with $N_2$ and sealed with stored in a laminar hood until use.

## 3.5 BIOLOGICAL TRANSPORTATION

The samples were then placed in a petri dish, sealed with Parafilm® (VWR International), and transported to the University of Washington for immediate ToF-SIMS analysis. Each tissue section was introduced to vacuum within 90 minutes of the tissue being cryosectioned.

## 3.6 TOF-SIMS ANALYSIS

Detailed ToF-SIMS experimental procedures are presented within each chapter. The information below details the typical instrument settings used for tissue experiments.

ToF-SIMS analysis was performed at room temperature. Positive and negative secondary ion spectra were collected with an ION-TOF TOF SIMS 5-100 instrument (ION-TOF, Münster, Germany), using a pulsed 25 keV $Bi_3^+$ primary ion beam. The $Bi_n^+$ LMIG is oriented at 45° to the surface normal. The spectra were calibrated using peaks

of known mass, and these peaks are presented in each chapter. Low energy electrons were flooded onto the sample to compensate for charge buildup on the surface.

High mass resolution (HMR) spectra were acquired using $Bi_3^+$. The $Bi_3^+$ current was typically 0.15 pA to avoid saturation of salts, phophotidylcholine ($C_5H_{15}NPO_4^+$, *m/z* 184.07), $PO_3^-$ (*m/z* 78.95), and low mass peaks (<*m/z* 96). This provides the highest mass resolution, typically >5500 at $C_2H_3^+$ (*m/*z 27.02), however, the spatial resolution is typically ≥5 μm. The high spatial resolution (HSR) mode was used to collect high spatial resolution images using $Bi_3^+$. The current was between 0.03-0.06 pA. In this mode, the spectra have nominal mass resolution (masses resolved are analogous to step functions) but spatial resolution is much higher than in HMR, typically ≤ 1 μm. All data was collected using the IONTOF SurfaceLab 6 software.

Before all tissue experiments large area images of the entire tissue were created by manually stitching individual optical images of 800 μm × 800 μm from the video camera within the ToF-SIMS before analysis of each tissue. Each individual optical image was obtained by moving the ToF-SIMS stage with 800 μm steps. Typically 3-4 large patches (approximately 1 mm × 1 mm) were selected for ToF-SIMS analysis rather than the entire tissue sample due to the time intensiveness required to analyze such large samples, which would lead to degradation during analysis or lipid migration.

Regions of interest (ROIs) were selected and used for comparison between specific tissue regions. These areas were typically selected using principal components analysis on ToF-SIMS images. Details of how these regions were selected are discussed within their subsequent chapters and heavily in Chapter 4. ROIs were also chosen in tissue experiments, but this was based on the distribution of a specific secondary ion or a summed set of secondary ions.

## 3.7 PRINCIPAL COMPONENTS ANALYSIS (PCA)

Detailed PCA experimental procedures are presented within each chapter. The information provided below is the general application and procedures that were similar for all experiments.

All PCA analysis was performed using the SpectraGUI and ImageGUI software (Daniel J. Graham, NESAC/BIO, University of Washington) within MATLAB (Mathworks,

Natick, MA). Data used were pre-processed to an appropriate format for the use of PCA. Specifically, ToF-SIMS image data were Poisson scaled and mean centered, and summed spectral data from individual tile images were normalized to the sum of the intensities of all of the peaks in the peak list, square-root transformed, and mean centered.

Regions of exposed silicon or ITO substrate and OCT (e.g. holes or tears from cutting tissue and embedding medium surrounding tissue) were excluded from all analyses by applying a threshold to the pixels with a $Si^+$ signal, where *m/z* 27.9 was used to detect silicon, *m/z* 114.9 for $In^+$, and *m/z* 332.2 ($C_{14}H_{29}^+$, a fragment of the benzalkonium additive in OCT)[13] is used to detect OCT areas. Peaks were chosen whose maximum intensity was twice or more than that of the average background intensity. The spectra from all tissues were overlaid and then peaks were manually selected and integrated to full width half max.

PCA, using the ImageGUI, is first applied to image data formatted as .bif6 files from SurfaceLab 6. No peaks are excluded from this data except salts, substrate (Si, Si and In containing peaks), and embedding medium (OCT). Normalization was not applied to imported image patches; image data were pre-processed by Poisson scaling and mean centering before PCA.

Spectral PCA of tissue data is composed of multiple steps using SurfaceLab 6 and both the ImageGUI and SpectraGUI (Daniel Graham, NESAC/BIO, University of Washington). The data collected as 1 mm × 1 mm stitched image (termed “patches”), contains 25 200 × 200 $\mu m^2$ “tiles.” Using the SurfaceLab 6 Spectra Program, a mass interval list will be created by manually integrating the mass peaks desired for analysis, followed by a data reconstruction in the format of .ita to allow for visualization of the selected masses. Then, using the SurfaceLab 6 Images Program, all the images can be exported in a .bif6 file. The .bif6 files can then be imported into the ImageGUI program in MATLAB. When the tile resolution (*e.g.* 256 × 256 pixels) is input into the ImageGUI’s cut up stage raster option, the patch will be diced into is 25 independent tiles. A .txt file is generated of the mass intensities within each tile. The .txt from multiple patches and samples can be combined for future spectral PCA. If individual tile data is not required

and only the intensities of a specific ROI are needed, it is more efficient to use the "statistics" option within the SurfaceLab6 Spectra Program.

## 3.8 SECOND HARMONIC GENERATION (SHG) MICROSCOPY

SHG was used to determine if there were any ordered structures (*e.g.* vasculature) and to confirm signals related to collagen observed with ToF-SIMS within tissue samples. SHG is restricted to molecules with a non-centrosymmetric organization and provides for detailed optical images of fibrillary collagen and has been shown to image mixtures of collagens I and III around blood vessels.[115] The multiphoton excitation fluorescence (MPEF) and SHG images were acquired with a scanning confocal multiphoton microscope (Olympus, FV1000 MPE BX61) with a 20x objective. The light source was a tunable laser (Spectra-Physics Mai Tai) with $\lambda_{exc}$ at 910 nm and with bandpass filters at 495–540 nm for the MPEF channel and 420–460 nm for the SHG channel. The detectors were photon multipliers, located so that the SHG captures in back-scattering mode and the MPEF in epifluorescence mode. All SHG experiments were performed on H&E stained slides. Image data acquired was processed using ImageJ software.

# Chapter 4. An Unsupervised MVA Method to Compare Specific Regions in Human Breast Tissue Samples Using ToF-SIMS

Blake M. Bluestein[a], Fionnuala Morrish[b], Daniel J. Graham[a], Jamie Guenthoer[b], David Hockenbery[b], Peggy Porter[b], and Lara J. Gamble[a,§]

[a] University of Washington, Dept. of Bioengineering, MolES Building, Box 351653, Seattle, WA 98195-1653

[b] Fred Hutchinson Cancer Research Center, Seattle, WA 98109

*Analyst,* 2016, Volume 141, Issue 6, Pages 1947-1957

[§] Corresponding Author

Lara Gamble

University of Washington

Department of Bioengineering

Box 351653

Seattle, WA 98195

1-206-543-8094 (phone)

1-206-543-3778 (fax)

lgamble@uw.edu (e-mail)

## 4.1 ABSTRACT

Imaging time-of-flight secondary ion mass spectrometry (ToF-SIMS) and principal component analysis (PCA) were used to investigate two sets of pre- and post-chemotherapy human breast tumor tissue sections to characterize lipids associated with tumor metabolic flexibility and response to treatment. The micron spatial resolution imaging capability of ToF-SIMS provides a powerful approach to attain spatially-resolved molecular and cellular data from cancerous tissues not available with conventional imaging techniques. Three ca. 1 $mm^2$ areas per tissue section were analyzed by stitching together 200 μm × 200 μm raster area scans. A method to isolate and analyze specific tissue regions of interest by utilizing PCA of ToF-SIMS images is presented, which allowed separation of cellularized areas from stromal areas. These PCA-generated regions of interest were then used as masks to reconstruct representative spectra from specifically stromal or cellular regions. The advantage of this unsupervised selection method is a reduction in scatter in the spectral PCA results when compared to analyzing all tissue areas or analyzing areas highlighted by a pathologist. Utilizing this method, stromal and cellular regions of breast tissue biopsies taken pre- versus post-chemotherapy demonstrate chemical separation using negatively-charged ion species. In this sample set, the cellular regions were predominantly all cancer cells. Fatty acids (i.e. palmitic, oleic, and stearic), monoacylglycerols, diacylglycerols and vitamin E profiles were distinctively different between the pre- and post-therapy tissues. These results validate a new unsupervised method to isolate and interpret biochemically distinct regions in cancer tissues using imaging ToF-SIMS data. In addition, the method developed here can provide a framework to compare a variety of tissue samples using imaging ToF-SIMS, especially where there is section-to-section variability that makes it difficult to use a serial hematoxylin and eosin (H&E) stained section to direct the SIMS analysis.

## 4.2 INTRODUCTION

Mass spectrometry imaging (MSI) is quickly emerging as a key research tool in biological research areas such as neuroscience, drug delivery, and cancer.[49, 106, 116, 117] The combination of MS chemical and molecular specificity with imaging capabilities has provided a new perspective for biological sample analysis including localization and interactions of drugs in cells and tissues,[81, 118-121] proteomics,[122, 123] and lipidomics.[49, 124, 125] Specifically, the MS imaging technique time-of-flight secondary ion mass spectrometry (ToF-SIMS) is a label-free method with micron resolution imaging capabilities making it well suited for imaging of cells,[33, 104] and key tissue regions.[11, 126] Utilizing the micron lateral resolution of SIMS can be crucial in the process of separating regions of interest within tumor microenvironments for cancer research. These microenvironments can regulate anticancer activities but can also promote cancer progression and provide biological protection which limits therapeutic efficacy and delivery.[127] By combining micron resolution imaging with molecular information, it is possible to observe and begin to interpret potential immune response related metabolic events that may associate with cancer progression or regression within the tumor.

Breast cancer biopsies can vary cellular density as well as percent of cancer cell and stroma (connective tissue composed of fat and fibrous tissue) content. Pathological assessment is typically performed with histological staining to determine the location, type and grade of tumors, but does not always predict patient outcome or response to chemotherapeutics.[128-133] Stromal heterogeneity and tumor-stroma interactions provide prognostic indicators for invasive growth and metastasis.[134-137] Previous studies indicate that stromal-cancer cell metabolite interchange aids tumor growth and progression.[138, 139] It is hypothesized that the stromal biochemical state may dictate sensitivity to chemotherapy.[140] However, it is difficult to acquire metabolic data specifically from cellular and stromal regions, as these regions can be difficult to isolate for metabolic profiling due to the complexity of their spatial distribution. Separating out chemical information specifically from the stromal or cellular region can be useful to compare chemistries from different tissue areas that contain varying amounts of these specific regions.

In this study, a combination of ToF-SIMS and multivariate imaging analysis techniques are used as an analytical tool to identify chemical variation of specific cellular and stromal regions from breast cancer specimens and to compare the chemical variation between pre- and post- chemotherapy. We describe different analysis methods to isolate and interpret metabolic features of cancer cell regions within tissues including pathologist-driven selection of regions of interest (ROIs) using hematoxylin and eosin (H&E) stained tissue sections as well as the use of an unsupervised imaging MVA method to separate out stromal regions in the SIMS images. Herein unsupervised refers both to the fact that principal component analysis (PCA) is an unsupervised MVA method (meaning no input other than peak intensities are used), and to the fact that by using PCA to select ROIs we demonstrate that one can isolate cellular and stromal areas within breast tissue sections and reduce scatter within the resulting scores without introducing human bias through hand-selected regions. This method further provides improvement to isolate and analyze complex regions that consist of either cellular/tumor or stromal regions that cannot be selected by hand or the threshold of just one mass spectrometric image. The MVA method of PLS-DA has been successfully used to with InfraRed (IR) imaging data to discern different regions in breast cancer tissue and identify tumor and non-tumor areas within a set of samples.[141] However, to our knowledge, the method of using PCA to select ROIs for comparing different regions has not yet been applied to ToF-SIMS imaging data. ToF-SIMS has been used previously to study diseased tissues and cells with a major focus on lipids,[6, 11, 32, 108] which are known to contribute and also regulate a range of metabolic and biochemical processes within cells. Furthermore alterations in lipid metabolism are an indication of carcinogenesis.[142] The imaging data in this study is specifically used to assess how lipid molecules relate to the differences found between tissue samples. One major distinction, however, is that here we compare similar regions (*e.g.* cellular regions) of four different tissue samples to investigate chemical differences between untreated tumors and those that have been exposed to chemotherapy treatments.[33] In addition, the method developed here can provide a framework to compare multiple tissue samples using imaging ToF-SIMS when there is difficulty using a region of interest marked on a serial (consecutive) section to direct the SIMS analysis

due to section-to-section variability. This novel approach utilizes the high lateral resolution capability of imaging ToF-SIMS to compare highly specific regions (*e.g.* just tumor cells) from one tissue to another and use spectral PCA to highlight chemical differences between those tissue specimens.

## 4.3 METHODS

### 4.3.1 TISSUE SAMPLE PREPARATION

Paired pre- and post- chemotherapy biopsy specimens were obtained from patients consented according to institutional review board protocols. Both patients received standard pre-operative chemotherapy with doxorubicin at 60 mg/m$^2$ IV and cyclophosphamide 600 mg/m$^2$ IV on day 1 every 14 days for 4 cycles and paclitaxel 80 mg/m$^2$ IV weekly x 12 weeks. The patient with 'Basal Like' breast cancer received the paclitaxel first while the patient with Luminal A breast cancer received the Doxorubicin and cyclophosphamide combination first, but the order of therapy is known to not substantially affect treatment efficacy. Specimens were immediately embedded in Tissue-Tek® (Fisher Scientific) optimum cutting temperature (OCT) compound, cryopreserved using liquid nitrogen and stored in a -80 °C freezer. Frozen tissue blocks were sectioned in a cryostat-microtome held at -23°C at the Fred Hutchinson Cancer Research Center (FHCRC). Each of the four tissue samples was serially sectioned three times and each section was ~5 µm in thickness. The first and third sections were stained for optical imaging using hematoxylin and eosin (H&E), while the second section was analyzed by ToF-SIMS. The second slice of tissue was placed directly on a 2 cm$^2$ silicon wafer that was previously cleaned with two successive sonications in dichloromethane, acetone, and methanol.[13] The samples were then placed in a petri dish, sealed with Parafilm® (VWR International), and transported to the University of Washington for immediate ToF-SIMS analysis. Each tissue was sectioned on a different day and the time from tissue cutting to analysis was less than 90 minutes for any sample.

### 4.3.2 GENE EXPRESSION SUBTYPE IDENTIFICATION

Six to nine tissue sections were macrodissected to select regions containing the highest proportion of invasive tumor cells to reduce contamination from non-tumor cells. RNA was isolated using the AllPrep DNA/RNA Mini Kit (Qiagen Inc., Valencia, CA) and gene/transcript expression was assessed using the WG-DASL® *(HumanHT-12 v4)* Assay (Illumina, Inc., San Diego, CA). Data processing and analysis were done in the R environment (v3.0.3). The raw expression data were pre-processed and median normalized using the Bioconductor lumi package,[143] and gene expression intrinsic subtypes (Luminal A and Basal-like) were determined using the 50-gene panel described by Parker et al.[144] with the software Bioconductor genefu package.[145]

### 4.3.3 TOF-SIMS

ToF-SIMS experiments were performed using an ION-TOF TOF.SIMS 5-100 (ION-TOF GmbH, Münster, Germany) equipped with a liquid metal ion gun (LMIG) for analysis and an electron flood gun for charge neutralization. The LMIG was used to generate a pulsed 25 keV $Bi_3^+$ beam impacting the target at an angle of 45°. The $Bi_3^+$ beam was set in spectroscopy mode for high mass resolution (HMR) to acquire spectra in both polarities and fast imaging mode to acquire high spatial resolution (HSR) negative polarity images. The $Bi_3^+$ current was typically 0.13-0.15 pA for HMR and 0.05 pA for HSR. Target currents were measured before each data set using a Faraday cup. HSR mode images with micron spatial resolution were acquired and compared to features found in ToF-SIMS to H&E images. Large area images of the entire tissue biopsy were created by manually stitching individual optical images of 800 µm × 800 µm from the video camera within the ToF-SIMS before analysis of each tissue. These large optical stitched images were then aligned to H&E images using the tissue borders to aid in selecting areas where analysis patches were to be acquired. For all data collection, HMR positive ion data was acquired followed immediately by HMR negative ion data on the same area. X and Y sample stage coordinates were saved in the software to ensure data acquired was from the same region in both polarities. HSR images were obtained from each sample region after all HMR spectra were completed. In HMR mode, mass

resolution ($m/\Delta m$) for the $C_2H_3^+$ ion was greater than 4500. Positive ion spectra were calibrated to $CH_3^+$, $C_2H_3^+$, and $C_4H_5^+$. Negative ion spectra were calibrated to $CH^-$, $OH^-$, and $C_2H^-$.Spectra were acquired from 1 mm × 1mm or 1.6 mm × 0.6 mm "patches" comprising of 25 or 24 200 µm × 200 µm "tiles" on each tissue, an example of positions is shown in Figure 4.1. Each tile contains 256 ×256 pixels, giving the patches a total pixel count of 1280 × 1280. Selecting to analyze three large patches rather than the entire tissue biopsy sample was chosen due to the time intensiveness required to analyze the samples. Long analysis times can lead to degradation of lipid signals or lipid migration.[9, 13] Thus, analyzing three patches results in a timely analysis, providing the most relevant and reproducible data of the tissue's native chemical composition. The $Bi_3^+$ dose was limited to ≤$5.0\times10^{11}$ ions/cm$^2$ for each tile in both positive and negative ion modes, resulting in a total $Bi_3^+$ dose ≤$1.0\times 10^{12}$ ions/cm$^2$ per tile. SurfaceLab 6 software (ION-TOF GmbH, Münster, Germany) was used for all analyses.

### 4.3.4 Principal Component Analysis

Principal component analysis (PCA) was applied to ToF-SIMS images acquired from the tissues using all pixels in the data set (herein referred to as image data and displayed as images) and to summed spectral data from individual patches (herein referred to as spectral data and displayed as individual data points).

Data used in this study were pre-processed for PCA as follows: 1) ToF-SIMS image data were Poisson scaled and mean centered, and 2) summed spectral data from individual tile images were normalized to the sum of the intensities of all of the peaks in the peak list, square-root transformed, and mean centered. Regions of exposed silicon substrate and OCT (e.g. holes or tears from cutting tissue and embedding medium surrounding tissue) were excluded from all analyses by applying a threshold to the pixels with a $Si^+$ signal, where *m/z* 27.9 was used to detect silicon and *m/z* 332.2 ($C_{14}H_{29}^+$, a fragment of the benzalkonium additive in OCT)[13] is used to detect OCT areas. All PCA was performed using the NBToolbox SpectraGUI and ImageGUI (Daniel Graham Ph.D., NESAC/BIO, University of Washington), that operate within MATLAB (MathWorks, Natick, MA). Peaks were chosen whose maximum intensity was twice or more than that of the average background intensity. The spectra from all

tissues were overlaid and then peaks were manually selected and integrated to full width half max. All peaks below *m/z* 920 were selected, excluding known salt, salt adduct, substrate and inorganic peaks. A total peak list of 846 and 807 peaks were chosen from the positive and negative ion modes, respectively. All peaks in the list were used for image PCA analysis while spectral PCA was limited to peaks with *m/z* above 200 resulting in 391 and 329 peaks for the positive and negative ions peak lists, respectively.

PCA, using the ImageGUI, is first applied to image data formatted as .bif6 files from SurfaceLab 6. No peaks are excluded from this data except salts, substrate (Si and Si containing peaks), and embedding medium (OCT). Normalization was not applied to imported image patches; image data were pre-processed by Poisson scaling and mean centering before PCA.

The presence of large fatty acid droplets, observed as well defined high intensity areas of C16:1 ($C_{16}H_{29}O_2^-$, palmitoleic acid, *m/z* 253.2),[14, 109] C16:0 ($C_{16}H_{31}O_2^-$, palmitic acid, *m/*z 255.2),[109, 146] C18:2 ($C_{18}H_{29}O_2^-$, linoleic acid, *m/z* 279.2),[10, 109] C18:1 ($C_{18}H_{33}O_2^-$, oleic acid, *m/z* 281.2),[109, 146] and C18:0 ($C_{18}H_{35}O_2^-$, stearic acid, *m/z* 283.2),[30, 109, 125, 146] were occasionally observed in different tissue sections. The strong signal from the fatty acid droplets would dominate PCA and the main variability between the samples would then be related to fatty acid droplets present in that particular tissue slice. Therefore, the fatty acid droplets were removed prior to PCA as manually selected ROIs of the tissue image data, using the polyline function within SurfaceLab 6, so sample comparison could be focused on specific tissue regions. Droplets were easily identified in images as localized areas with characteristic fatty acid peak intensities at least 5 times that of the fatty acids distributed within the remaining tissue section. It is important to note that breast tissue is a fatty tissue, therefore the prevalence of fatty acid droplets within tissue sections can vary. Analysis of other types of tissues (i.e. brain, heart, and liver) may or may not contain these droplets.[105, 109, 146, 147] When analyzing chemical variances between patients or within one patient, including the fatty acid droplets present in breast tissue could cause misinterpretation data due to the variability of droplet presence (i.e. if there happened to be a droplet in that particular biopsy sample and/or section).

Scores images that corresponded to cellular and stromal areas from serial H&E images were selected to be used as masks. Using SurfaceLab 6, scores images were imported and spectra reconstructed by applying a 10% minimum, 90% maximum signal threshold to the pixels within the selected score image. The resulting data, in .bif6 format, were imported back into ImageGUI and the patch parsed into individual 200 µm × 200 µm tiles, shown in Figure 4.1C, where each tile represents one data point in the spectral PCA plots. The parsed data was then imported in .xlsx format into SpectraGUI for spectral analysis, where each individual tile represents one data point in the PCA scores plots. Imported data were normalized to the sum of the intensities of all of the peaks in the peak list, square-root transformed, and mean centered prior to spectral PCA.


**Figure 4.1. (A)** Chart of H&E stained images for pre and post chemotherapeutic treated tissues of Luminal A type and Basal-like from two patients **(B)** An increased magnification optical H&E stained image of a selected analysis region. **(C)** Summed $CN^-$ and $CNO^-$ ion image from the ToF-SIMS analysis region corresponding to **(B)** showing the 25 200 × 200 µm tiles comprising of one stitched patch. White regions seen in the tissue slices can indicate either tears or (most typically when round) fatty acid droplets. All scale bars represent 1 mm.

## 4.4 RESULTS AND DISCUSSION

Paired pre- and post- chemotherapy tissue samples from two patients were acquired for a total of 4 tissue samples. The hematoxylin and eosin (H&E) stained sections for the 4 tissue samples are shown in Figure 4.1A and Figure 4.1B. The hematoxylin stain, blue color, indicates the cellular nuclei while eosin stains the stromal or connective tissue in a lighter pink color. Three stitched patches (as described in Figure 4.1) were taken per tissue for a total of 12 stitched patches. Each of the breast cancer specimens were classified into gene expression intrinsic subtypes.[144] The first pre/post-therapy specimen pair was classified as a Luminal A breast cancer, characterized by having genetic expression patterns similar to the luminal epithelial component of the normal breast.[128, 148] Generally, the Luminal A cancers are estrogen receptor (ER) and progesterone receptor (PgR) positive, and human epidermal growth factor receptor 2 (HER2) negative with lower expression of proliferative genes. The second pre/post-therapy tissue pair was classified as a Basal-like breast cancer. The Basal-like subtype typically lacks expression of ER, PgR, and shows low or no HER2 expression. Basal-like tumors are characterized by an expression pattern corresponding to that of the basal epithelial cells in the normal breast and body and highly express proliferation genes.[128, 148]

In order to ascertain chemical differences between pre- and post- chemotherapy tissues, PCA was used to analyze ToF-SIMS spectral and image data. Three different methods are used to acquire information from different ROIs from different tissue slices. Specifically, (1) using the spectral data from all patches within the region imaged from a given tissue, (2) using regions indicated by pathologist on a H&E stained slice image and (3) using the spectral data from all patches after generating ROIs using imaging PCA. The negative polarity ion data showed the best correlation between the pre and post chemotherapy treatment samples and thus is used to compare the spectral PCA results generated from the three different ROI methods. The positive ion PCA results did not show separation that correlated with pre- and post-chemotherapy treatment regardless of the method used. The positive polarity data are presented and discussed using the last method only.

### 4.4.1 MVA OF ALL PATCHES

As detailed in the methods section, each analysis patch was separated into individual tiles after removal of substrate, embedding medium, and large fatty acid deposits, followed by the application of PCA. The spectral PCA results from the negative ion polarity data with peaks above *m/z* 200 (key *m/z* values, deviations, and proposed biological molecule are shown in (Supplemental Table S.4.1) of the entire stitched patches (both pre and post for both tissue types) are shown in Figure 4.2. The lines above and below the data points indicate 95% confidence intervals. PC1 data (not shown) indicates slight separation between tissues from the two patients, rather than by pre- and post-therapy possibly identifying person-to-person chemical variation. In PC2, it is noticeable that the post-therapy tissues do indicate a trend with higher scores, which correspond to a high loading value of fatty acid C16:0 ($C_{16}H_{31}O_2^-$, palmitic acid, *m/z* 255.2), while the pre-therapy tissues trend with lower score values, corresponding to the strongest negative loading peak of Vitamin E ($C_{29}H_{49}O_2^-$, *m/z* 429.3)[10] and fatty acid C18:1 ($C_{18}H_{33}O_2^-$, oleic acid, *m/z* 281.2). Using the entire patch as a region of interest, the scores exhibit a large spread between the 95% confidence intervals signifying a high amount of variability within each patch as well as for different patches within the tissue. It is possible that the large variability may be due to comparison of the entire tissue areas rather than comparison of specific tumor features within the analysis patch.

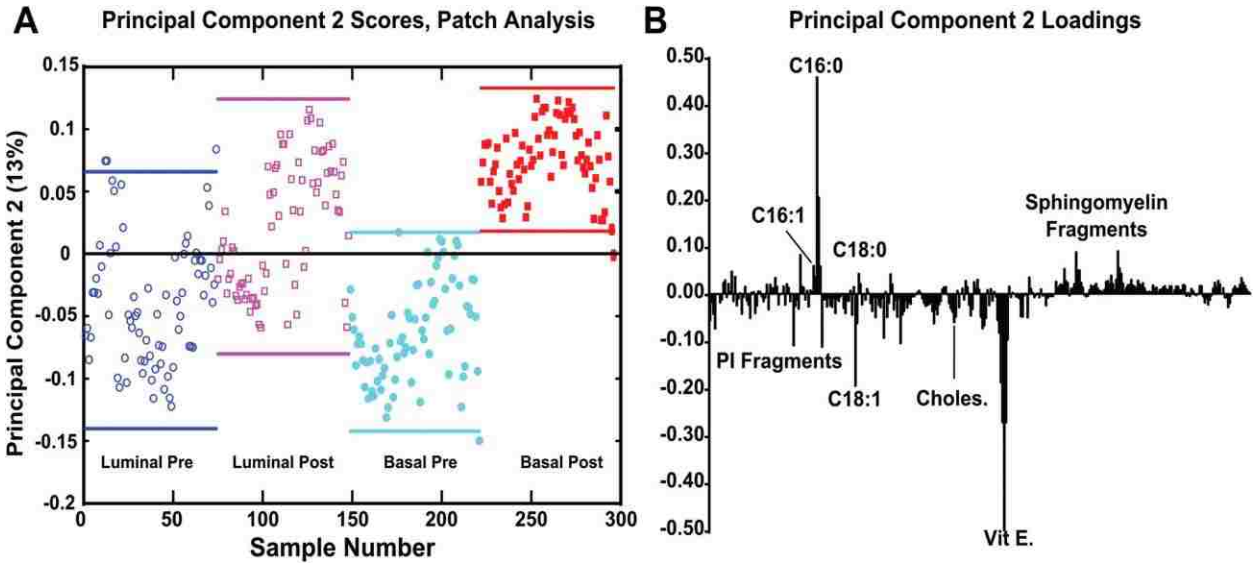


**Figure 4.2 (A)** PC2 scores plot generated from whole patch data using the negative ions m/z > 200. **(B)** PC2 shows an overall variance of 13%. Pre chemotherapeutic tissues shown as blue colored and cyan ●, post chemotherapeutic tissues shown as colored magenta and red. The lines above and below the data points indicate 95% confidence intervals.

### 4.4.2 MVA ANALYSIS OF H&E DRIVEN ROI SELECTIONS

Due to the heterogeneity and complexity of the sample, a second type of ROI selection was performed to focus on pathologist-recommended regions, e.g. high density of cancer cells, from the serial H&E slice. These regions are outlined in light blue in the H&E and black in the ToF-SIMS summed image of $CN^-$ and $CNO^-$ (Figure 4.3A and Figure 4.3B), to provide a guide for a more accurate ToF-SIMS spectral comparison between cancer cell regions or “cancer cell nests” and stromal regions. Supplemental Figure S.4.1 shows the pathologist-selected areas on the H&E images for all four tissues.

It can be noted (in Figure 4.3) that the H&E image of the tissue that was examined by the pathologist is not identical to the ToF-SIMS image. This is not surprising since there is at least a 5 µm difference between these serial sections (including the section thickness and frost buildup on the tissue sample prior to the slicing of the next section).

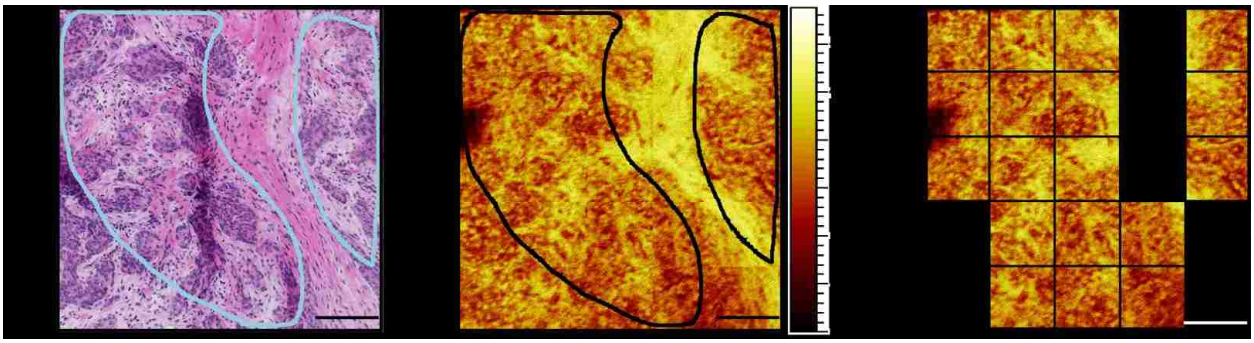

**Figure 4.3. (A)** An example of an analysis patch at higher magnification with pathologist selected areas on the H&E (blue) **(B)** Pathologist selected areas (black lines) projected onto sum ion image of $CN^-$ and $CNO^-$ (m/z 26.0 and 42.0) **(C)** Representative ion image of tiles removed, shown in black, prior to PCA. All scale bars are 200 µm.

In an effort to develop a minimally time consuming process, a rough estimate of the pathologist-selected areas were used, meaning that only tiles that primarily corresponded with pathologist-selected areas were selected for the analysis (Figure 4.3C). The results using PCA on this more selective region of interest are shown in Supplemental Figure S.4.2. Comparing the method of a selective region to whole spot analysis (Figure 4.2), it can be seen that the percentage of variance of PC2 as well as the loadings peaks look similar for both types of ROI analyses. However, the scores separation between the pre- and post-therapy specimens from the Basal-like cancer are no longer observed while the pre and post specimens from the Luminal A cancer now show a clearer separation. While a hand drawn ROI to attempt to directly select the regions selected by the pathologist may have slightly improved these results, the section-to-section variability noted during the analysis likely plays the major role in incorrectly selecting the ROIs on the ToF-SIMS image(since the regions of interest on the pathology section may not match those on the ToF-SIMS section). For example, the image shown in Figure 4.3 has a large, obvious stromal feature (large pink region), while other tissue sections such as the Basal-like post chemotherapy tissue (Supplemental Figure S.4.1) had very small, well separate regions that were difficult to correlate and identify on the ToF-SIMS image. This difference in separation could be due the following; (1) large stromal areas excluded by the pathologist in the Basal-like post-chemotherapy tissue, (2) small distributed cellular areas included by the pathologist within the Basal-like pre-chemotherapy tissue, (3) lowering the number of

tiles used in PCA, and (4) larger cellular areas comprised of more tiles included by the pathologist within the Luminal A cancer tissues.

### 4.4.3 VARIATIONS IN SERIAL TISSUE SLICES

Composition and localization of cellular areas within a tumor vary as you move serially through a tissue block. This variability increases the complexity of choosing the ToF-SIMS analysis region of a tissue section by comparing to a region from a serial section. Figure 4.4 illustrates an example of the heterogeneity between the three serial 5 µm sections. For accurate spot location on each section, images were aligned by overlay at the same magnification and approximate spot location boxed. In Figure 4.4A and Figure 4.4D, the initial H&E section reviewed by the pathologist, a circular structure, noted by a black arrow, is present within the 1 mm x 1 mm analysis area. It can also be seen that in Figure 4.4A there is not a substantial amount of cell nuclei (blue stain) populating the region. Figure 4.4B and Figure 4.4E shows the ToF-SIMS stitched microscope camera image and the summed $CN^-$ and $CNO^-$ HSR image acquired. Figure 4.4C is the serial section cut after the ToF-SIMS section. The higher intensity region in the center of the ion image (Figure 4.4E) is indicative of the stromal region whereas the lower intensity regions indicate cellular regions (with the exception of the area with no signal in the lower left area of the image which is due to fatty acid droplets). Comparing all the images in Figure 4.4 it can be seen that the ToF-SIMS image in Figure 4.4E is more similar to the H&E image in Figure 4.4F, but still has some differences highlighting the difficulties in using serial sections to choose analysis regions as certain structures vary in depth.

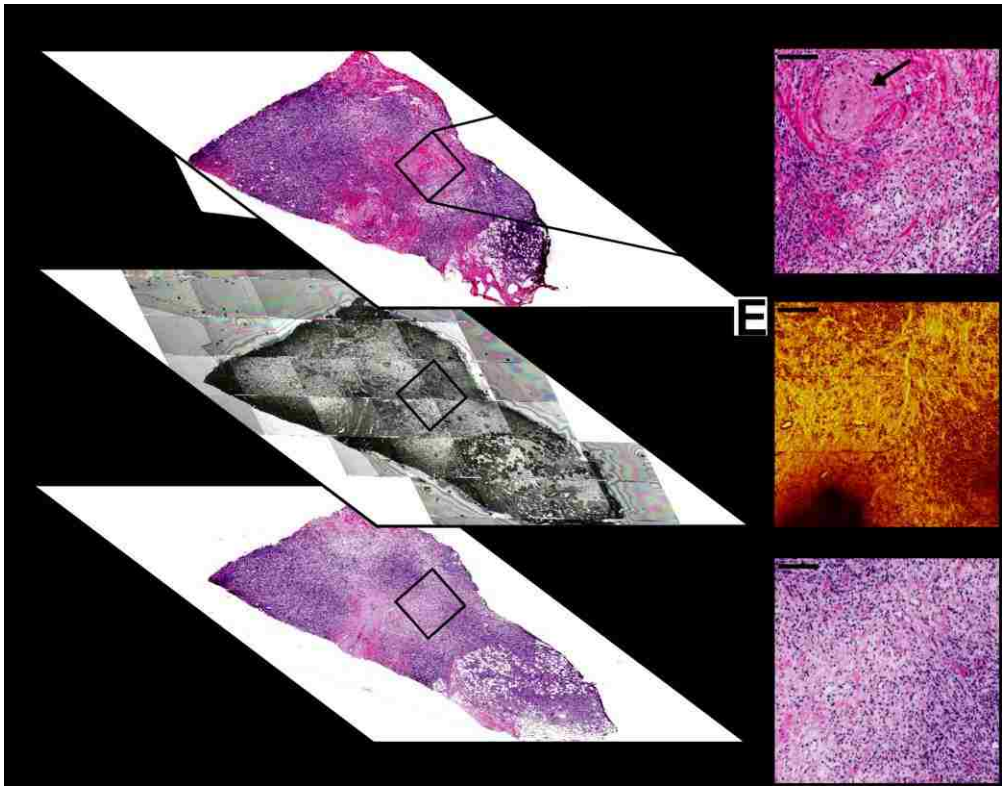

**Figure 4.4.** Optical and ToF-SIMS camera and ion images showing the heterogeneity between serially cut tissue sections for the entire section and at a specific 1mm × 1mm analysis area, outlined in black. **(A)** Initial Section 1, an optical H&E stained section before the ToF-SIMS section. **(D)** H&E optical image at an increased magnification of a selected analysis region. Black arrow shows circular structure that becomes absent after this section. **(B)** Section 2, used for ToF-SIMS analysis. ToF-SIMS microscope stitch. **(E)** Summed ion image of $CN^-$ and $CNO^-$ does not display similar structure as observed in **(D)**. **(C)** Section 3, H&E made directly after the ToF-SIMS section. **(F)** Increased magnification optical H&E stained section of selected region displaying a more analogous structure to **(E)**. Scale bar in **D-F** represents 200 µm.

### 4.4.4 MVA USING UNSUPERVISED SELECTION OF REGION SPECIFIC ROIS BY PCA

H&E-stained serial tissue sections do not necessarily show the same areas of interest as the ToF-SIMS analysis section and, as shown in the previous two methods, the amount of cellular and stromal area in the analysis area may dominate the PCA separation. Therefore, a different method must be developed to focus on tissue areas of interest that can provide tissue to tissue slice comparisons. Additionally, there is interest in comparing specific regions from different tissue samples (for example comparing only cellular regions from two different patient biopsies). While the tissue shown in Figure 4.3 had a rather prominent stromal feature, making it relatively simple to separate out major stromal areas from the cellular areas, many of the tissue sections had less prominent

stromal features making it more difficult to use a coarse method to precisely separate out the stromal and cellular areas. In order to more precisely separate the stromal and cellular areas of the tissue, PCA was applied to the image data of each patch with an *m/z* 0 –920 peak list. The low mass peaks, such as $CN^-$ and $CNO^-$, were previously shown to be indicative of stromal regions (e.g. Figure 4.3B) and would aid in separation of these areas.

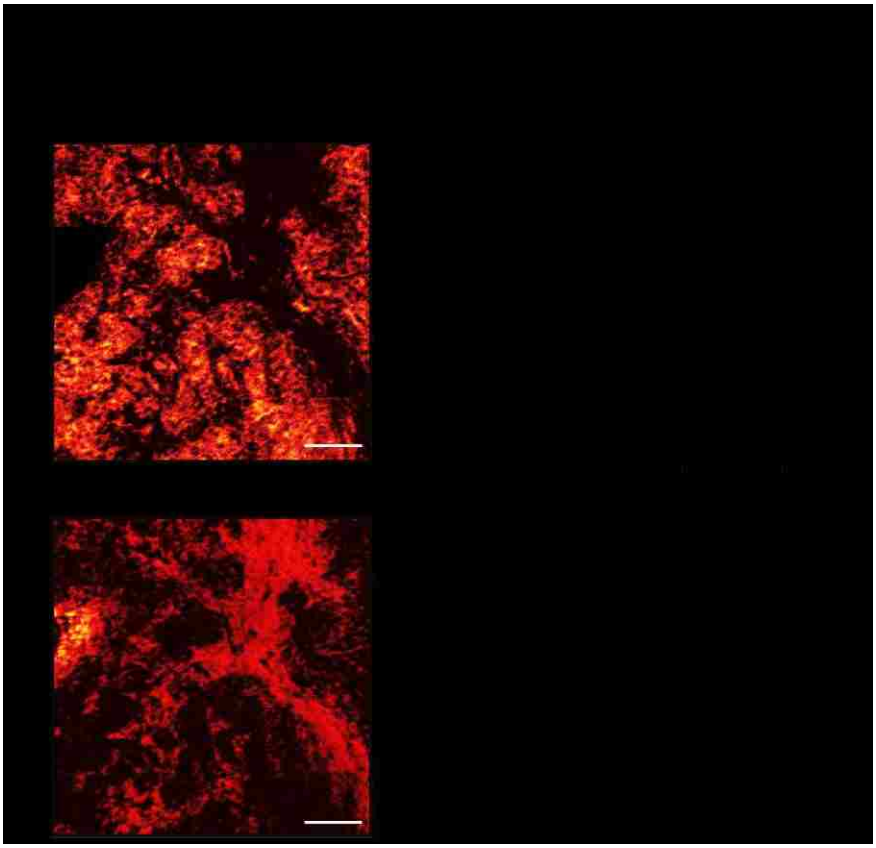

**Figure 4.5.** Negative ion image PCA results with a variance of 0.66% from an example patch. **(A)** Positive scores image showing the isolation of cellular regions. **(B)** Positive loadings that display the chemical species identified within (A) the cellular scores image. **(C)** Negative scores image or the stromal region. **(D)** Negative loadings showing the chemical species identified within the stromal region. The cellular and stromal regions can be distinguished from the H&E stained image presented in Figure 4.3A. Image contrast was enhanced for clearer presentation for publication. Scale bars represent 200 µm.

In Figure 4.5, principal component 2 image scores (Figure 4.5A and Figure 4.5C) and loadings (Figure 4.5B and Figure 4.5D) produced from image PCA demonstrate the separation between cellular (Figure 4.5A and Figure 4.5B) and stromal regions (Figure 4.5C and Figure 4.5D), which can be visually seen to correspond with the cellular and stromal structures visible in adjacent H&E-stained sections as seen in Figure 4.3A.

Again, the tissue section with the most prominent stromal feature is chosen to demonstrate the utility of this method to separate out stromal features. In this particular sample, PC1 separates the presence of a fatty acid droplet and regions exhibiting vitamin E (shown in Figure 6C) from the remainder of the image, which is dominated by high loading peaks of $CN^-$ and $CNO^-$ and other low mass fragments (not shown). In tissue samples where fatty acid droplets are not present, the separation between cellular and stromal is found in PC1.

The PC2 loadings plot for this patch exhibit high negative loadings for $CN^-$ , $CNO^-$, and the fatty acids C18:2 ($C_{18}H_{29}O_2^-$, linoleic acid, *m/z* 279.2) and C18:1 ($C_{18}H_{33}O_2^-$, oleic acid, *m/z* 281.2). These negative loading masses can be associated with the negative PC2 scores image analogous to the stromal region of the tissue. The high negative loading of the fatty acid peaks could be due to the fatty acid droplet located at the left edge of the patch, visible as a high intensity region in the negative PC2 scores image. The composition of these fatty acid droplet regions, which appear as white (un-stained) 'holes' in the histology image, are easily identified with ToF-SIMS imaging. Consistent trends generated by image PCA observed from the loadings plot show $CN^-$, $CNO^-$, and $PO_3H^-$ (*m/z* 79.9) loading in the direction of the stromal region scores.

The positive loading masses can be associated with the positive PC2 scores image, which is indicative of the cellular regions within the tissue sample. General trends observed while using image PCA indicated that cellular areas consistently had higher relative intensities of fragments related to vitamin E ($C_{10}H_{11}O_2^-$, *m/z* 163.1 and $C_{29}H_{49}O_2^-$) and phosphoinositol ($C_9H_{16}PO_9^-$, *m/z* 299.05).[149] Due to the section-to-section variability in the samples, several cellular domains were revealed in the imaging PCA analysis of the tissues that were not visible in the histology images.

The scores images that were representative of cellular and stromal areas were used to create an ROI threshold "mask", to extract the imaging mass spectral information specifically from stromal and cellular regions. Figure 4.6 demonstrates the process used to create specific cellular and stromal ROIs using the image PCA scores as masks. First, the representative cellular and stromal scores images are scaled to equal the same number of pixels acquired in the ToF-SIMS image (Figure 4.6A and

Figure 4.6B). As previously discussed in the methods section, breast tissue is a fatty tissue and the presence of fatty acid droplets may vary section-to-section and between patient specimens. When comparing the chemical variance between one patient or many, it is important that the data is not misinterpreted by the presence or absence of fatty acid droplets in a particular specimen. Before the mask is applied, fatty acid droplets must be removed from the scores image or the results from spectral PCA will be heavily influenced by their presence or absence when comparing sample chemistries. The droplet can be verified by viewing the raw data images. Fatty acid droplets generally separated from the tissue sample and are typically visible in PC1 scores (Figure 4.6C, white arrow). In order to remove the fatty acid droplets from these data sets, PC2 can be overlaid with PC1 and the fatty acid droplet area can be subtracted from the PC2 scores image. Once the droplet area has been removed new cellular or stromal images can be generated. These new images can then be applied as ROI masks as previously described. An example of completed masks is shown in teal in Figure 4.6D and Figure 4.6E.

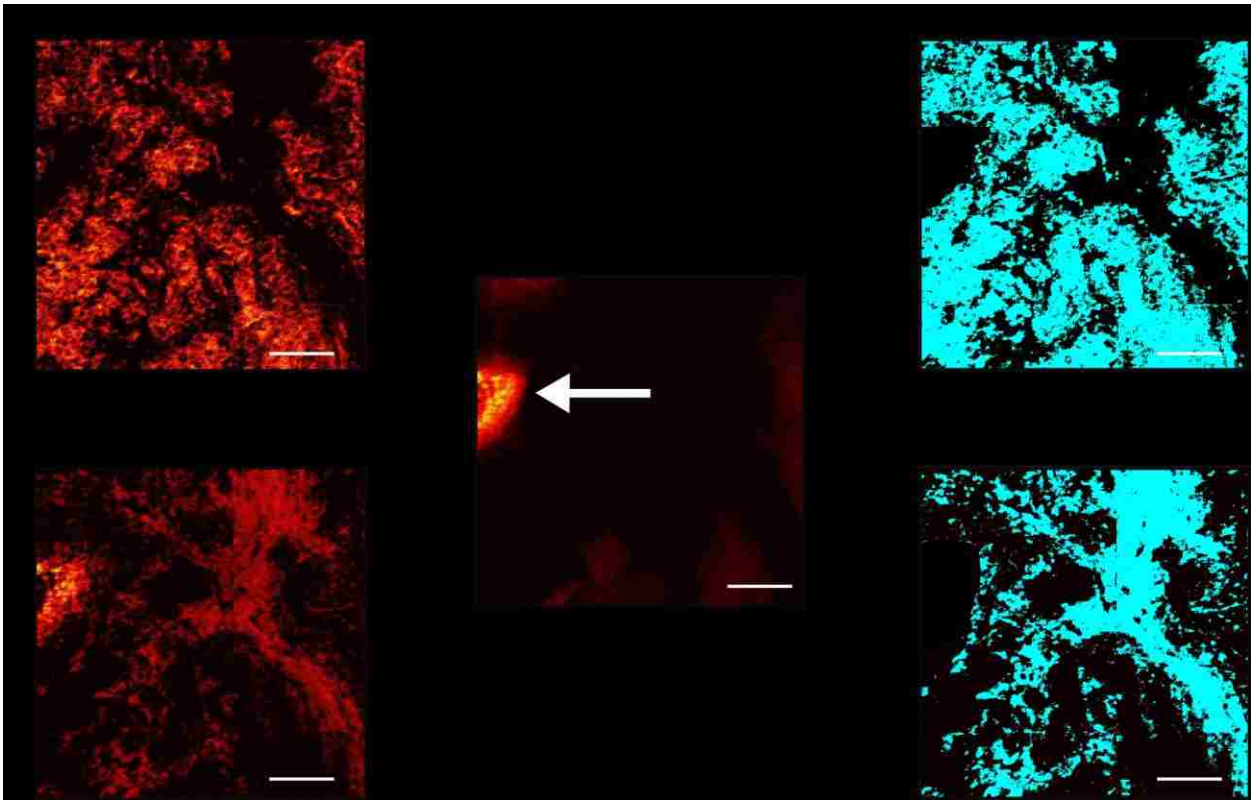

**Figure 4.6.** Image PCA mask workflow. Using the scores images that isolate the cellular **(A)** and stromal **(B)** areas and subtracting fatty acid (FA) droplets **(C),** if present within the sample, region specific threshold masks **(D and E)** can be generated. Images can then be reconstructed to contain only spectra representative of the **(D)** cellular or **(E)** stromal regions. All scale bars are 200µm.

After spectra were reconstructed using either the cellular or stromal ROI masks, the ROI patch areas were subjected to the same process, parsing the patch into tiles for individual data points and followed by spectral PCA of the tiles as was done in the previous datasets. Figure 4.7 shows the resulting spectral PCA scores and corresponding loadings plots for PC2 of the reconstructed tiles of the cellular regions identified by image PCA. The scores trends are similar to those seen in PC2 scores of the pathologist-selected areas (Supplemental Figure S.4.2A) as well as the analysis of the entire patch (Figure 4.2).

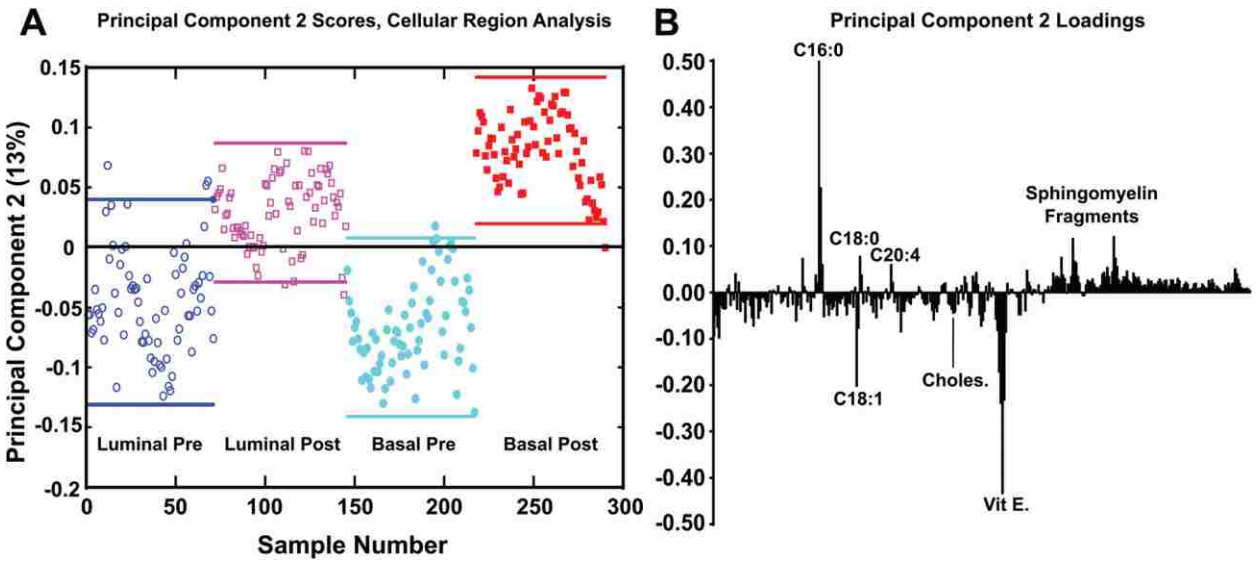


**Figure 4.7.** Spectral PCA results of cellular/tumor areas between tissue samples using image PCA masks to reconstruct only cellular/tumor regions for each tissue. **(A)** PC2 scores generated using PCA masks using the negative ions *m/z* > 200. **(B)** Loadings plot displaying the chemical species that correspond to PCA mask analysis scores. This method provides the best separation between the samples when compared to the previous methods, capturing 13% of the total variance. Pre-chemotherapy tissues shown as blue colored ○ and cyan ●, post-chemotherapy tissues shown as colored magenta □ and red ■.

As with the previous analysis methods, the post-therapy tissues have positive scores values and the pre-therapy tissues have negative scores. However, when data specifically from the cellular regions of the images are compared, the spread of the data between the confidence intervals is reduced. The loadings plots for PC2 in Figure 4.2B and Supplemental Figure S.4.2B are also similar to the loadings plot seen in Figure 4.7B, where saturated fatty acids C16:0, C18:0 ($C_{18}H_{35}O_2^-$, stearic acid, *m/z* 283.2) and fragments of possible sphingomyelin ($C_{34}H_{67}NO_6P^-$, $C_{36}H_{69}NO_6P^-$, $C_{38}H_{76}N_2O_6P^-$, SM(34:1), *m/z* 616.5, 642.5, 687.6 respectively)[109] have positive loadings, while vitamin E and the unsaturated fatty acid C18:1 load negatively, indicating different chemical profiles for cellular regions within pre/post-therapy tissues. Key differences, however, include little to no contribution from PI fragments or C14. The PC1 vs PC2 scores plot and corresponding loading plots (Figure 4.8) for the cellular specific ROIs shows both the separation between pre- and post-chemotherapy tissues on PC2 as well as some separation between the Basal-like subtype and Luminal A subtype tissues across PC1. There is large variability in the Luminal A pre-chemotherapy tumor tissue, where the confidence interval slightly overlaps both post-chemotherapy tissues. However, both the pre and post-chemotherapy Luminal tissues have largely negative scores on PC1, while

the Basal-like tissues have largely positive scores. Phosphoinositol fragments ($C_6H_1$-$PO_8^-$, *m/z* 241.01, and $C_6H_{12}PO_9^-$, *m/z* 259.02) and C18:0 trend with Luminal type tissues while C14:0 ($C_{14}H_{27}O_2^-$, *m/z* 227.2), C16:0, and C18:1 fragments are correlated with the Basal-like type tissues.

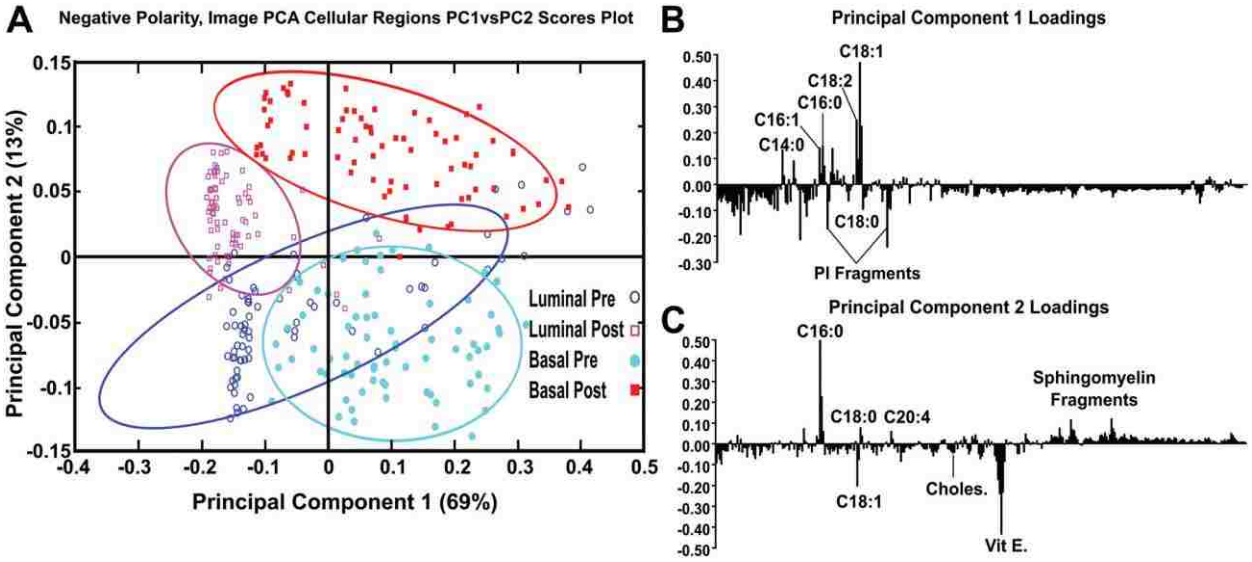


**Figure 4.8. (A)** PC1 vs PC2 scores using image PCA masks to reconstruct the cellular/tumor regions using negative ions *m/z* > 200. **(B)** PC1 loadings plot displaying the chemical species that correspond to PC1 scores (x-axis) **(C)** PC2 loadings plot displaying the chemical species that correspond to PC2 scores (y-axis). Pre-chemotherapeutic tissues shown as blue colored ○ and cyan ●, post-chemotherapeutic tissues shown as colored magenta □ and red ■.

Supplemental Figure S.4.3 shows the PCA scores and corresponding loadings plots of PC2 comparing the stromal regions of the samples in the negative polarity. Phosphoinositol fragments, C18:1, and vitamin E trend to be associated with the pre-chemotherapy samples. Where C14:0, C16:0, C18:0, and sphingomyelin fragments are correlated with the post-chemotherapy samples. The 95% confidence intervals have a wider spread for stromal region data than was seen for the cellular region data, however, a trend is still noticeable within the stroma data indicating that differences between pre- and post-chemotherapy samples can be found in the stromal as well cellular regions.

As was noted previously for ToF-SIMS investigation of breast cancer cells, the negative polarity ions provide the ability to observe distributional changes of fatty acids and intact lipids, while the positive data has been shown to provide the ability to observe changes in mono and diacylglycerides.[30] While PCA analysis of the pre- and post-

chemotherapy tissues using negative polarity ions similarly shows a trend in the scores related to fatty acids and lipids, the positive ion data results in more overlap of the scores 95% confidence intervals than found for the negative ion data. This is best shown in Supplemental Figure S.4.4 where PC2 vs PC4 scores and corresponding loadings are shown for the positive ion data. There is near separation between the pre/post Basal-like samples in PC2, but separation between the Luminal A pre/post samples is not observed until PC4. In summary, there does not appear to be a trend in the loadings peaks for the pre- and post-therapy tissues using positive ions, indicating that any changes in the mono and diacylglyceride content as a result of chemotherapy are not consistent across tissue types.

## 4.5 CONCLUSIONS

Current cancer research has indicated, primarily through gene expression data, that specific microenvironments in breast tumors may provide signals and nutrients to promote cancer cell survival and/or chemoresistance.[135, 136, 150] However, due to the heterogeneity of human breast cancer tissues, it remains difficult to acquire supportive metabolic data to aid in understanding tumor gro wth and treatment efficacy. The regions of interest (ROIs) selected for such molecular characterization require micron-level lateral resolution. Here we show that imaging ToF-SIMS can be used to chemically identify distinct tissue regions in tumors with high lateral resolution. In this work, we have presented an unsupervised methodology for isolating and analyzing specific tissue regions providing a way to compare similar regions in multiple tissue slices. These results demonstrate that the combination of imaging ToF-SIMS and image principal component analysis (PCA) can be used as an unsupervised method to select distinct ROIs within tissues. Comparisons are made using the entire analysis regions as well as hand-selected ROIs. When different tissue samples are compared using imaging PCA-driven ROIs there is less spread in the PCA scores. An advantage of using the imaging PCA-directed method is that it allows for like regions to be compared in spectral PCA and thereby improves chemical separation when multiple tissue samples are compared. Here four different tissue sections from two different patients before and after chemotherapy were compared using the negative ion ToF-SIMS data and PCA-driven

ROI selection. Trends are found for tissues breast cancer specimens that were taken before chemotherapy treatment (pre) and those taken from the same patient after treatment (post). From the spectral PCA results it is seen that the unsaturated fatty acids C16:0 and C18:0 and sphingomyelin correspond with the post-chemotherapy tissues. Deficiency of sphingomyelin is thought to be related to the disruption of apoptosis in highly invasive cancer cells,[151] therefore an increase in intensity in the post-treated samples compared to the pre-treated may correlate with treatment response of the patient. C16:0 has been shown to generate apoptotic signals, some related to sphingolipids.[152] Conversely, overexpression of fatty acid synthase in breast cancer, which is responsible for the synthesis of C16:0, has been shown to contribute to drug resistance.[153]

Vitamin E and the unsaturated fatty acid C18:1 correspond with the pre-chemotherapy tissues in the PCA analysis. Vitamin E may provide strong antioxidant protection of cancer cells from lipid peroxidation, facilitating tumor growth when in the presence of reactive oxygen species (ROS).[154] That the vitamin E signal corresponds to the pre-treated and not the post-treated tissues is consistent with several studies that have shown that chemotherapy and radiation therapy are associated with increased formation of reactive oxygen species and depletion of critical plasma and tissue antioxidants.[155, 156] The C18:1 oleic acid is known to prevent cytotoxicity and decrease mitochondrial superoxide production induced by C16:0 palmitate.[157] This provides a possible explanation for the trends seen within the pre-chemotherapy treated tissues for both C18:1 and vitamin E. While these findings require further experimental investigation to gain a concrete understanding in cancer biology, the results demonstrate the utility of PCA-driven ROI selection of ToF-SIMS data to compare metabolic trends of specific regions across multiple patients and tissue sections.

## 4.6 ACKNOWLEDGEMENTS

We would like to thank Kelly Wirtala at FHCRC for expert sectioning of tissue samples and helping with the development of sample preparation protocols. We would also like to thank Michael Robinson for scientific discussions and data acquisition. We would also like to acknowledge our funding sources: NESACBIO NIH P41 EB002027, SPORE NIH P50 CA138293, and NSF-GRFP DGE-0718124/1256082.

## 4.7 SUPPORTING INFORMATION

## AN UNSUPERVISED MVA METHOD TO COMPARE SPECIFIC REGIONS IN HUMAN BREAST TISSUE SAMPLES USING TOF-SIMS

Blake M. Bluestein[a], Fionnuala Morrish[b], Daniel J. Graham[a], Jamie Guenthoer[b], David Hockenbery[b], Peggy Porter[b], and Lara J. Gamble[a,§]

[a] University of Washington, Dept. of Bioengineering, MolES Building, Box 351653, Seattle, WA 98195-1653

[b] Fred Hutchinson Cancer Research Center, Seattle, WA 98109

*Analyst,* 2016, Volume 141, Issue 6, Pages 1947-1957

[§] Corresponding Author

Lara Gamble

University of Washington

Department of Bioengineering

Box 351653

Seattle, WA 98195

1-206-543-8094 (phone)

1-206-543-3778 (fax)

lgamble@uw.edu (e-mail)

**Supplemental Table S.4.1**. Key negative and positive ion *m/z* fragment identification for peaks observed in PCA.

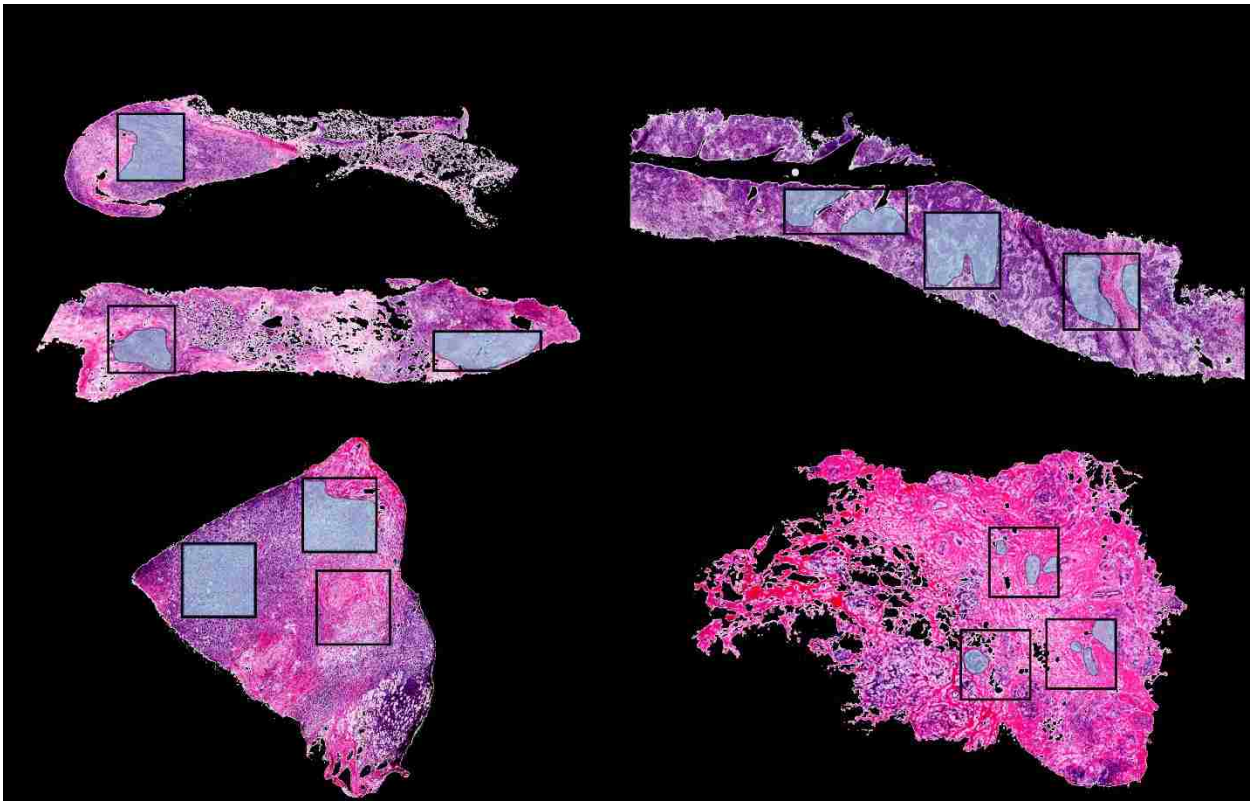

**Supplemental Figure S.4.1.**Optical H&E images showing the pathologist directed ROIs in blue. These regions were reconstructed and compared using spectral PCA for the results presented in Supplemental Figure S.4.2. All scale bars represent 1 mm.

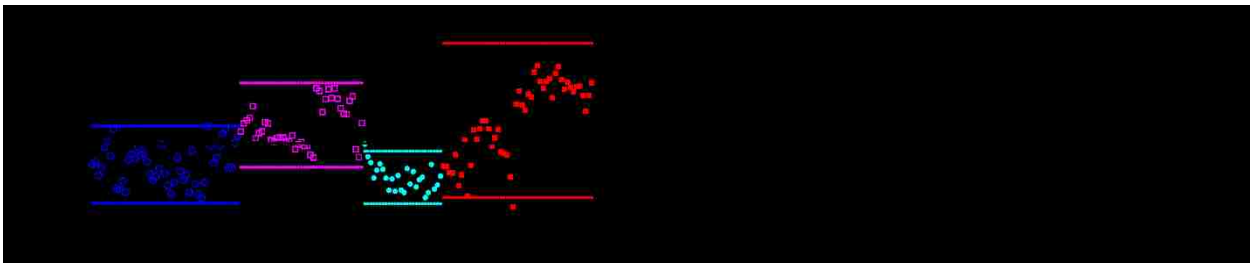

**Supplemental Figure S.4.2. (A)** PC2 scores generated from pathology driven analysis by tile removal for ion *m/z* > 200. PC2 shows an overall variance of 13%. **(B)** PC2 loadings displaying chemical species that correspond to scores from pathology driven analysis. Pre-chemotherapeutic tissues shown as blue colored ○ and cyan ●, post-chemotherapeutic tissues shown as colored magenta □ and red ■.

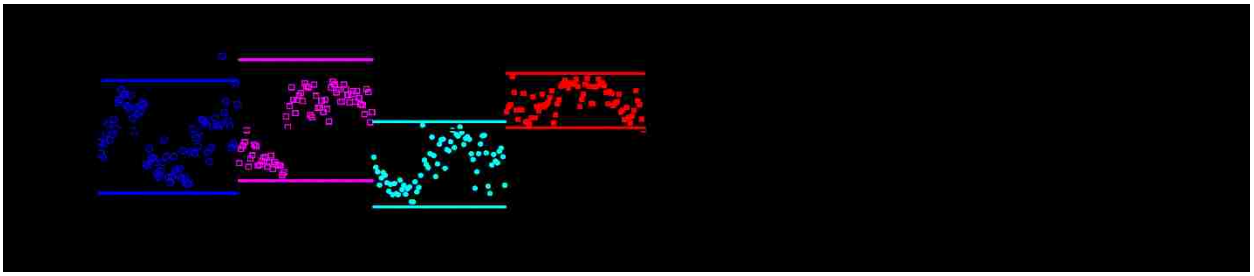

**Supplemental Figure S.4.3**.Spectral PCA results of negative polarity stromal areas between tissue samples using image PCA masks to reconstruct only stromal regions for each tissue. **(A)** PC2 scores generated from PCA masks using negative ions *m/z* > 200. **(B)** Loadings plot displaying the chemical species that correspond to scores from PCA mask analysis. The heterogeneity of the stromal regions can be seen within the figure, possibly denoting that stromal regions can change when located near dense tumor regions. Pre-chemotherapeutic tissues shown as blue colored ○ and cyan ●, post-chemotherapeutic tissues shown as colored magenta □ and red ■.

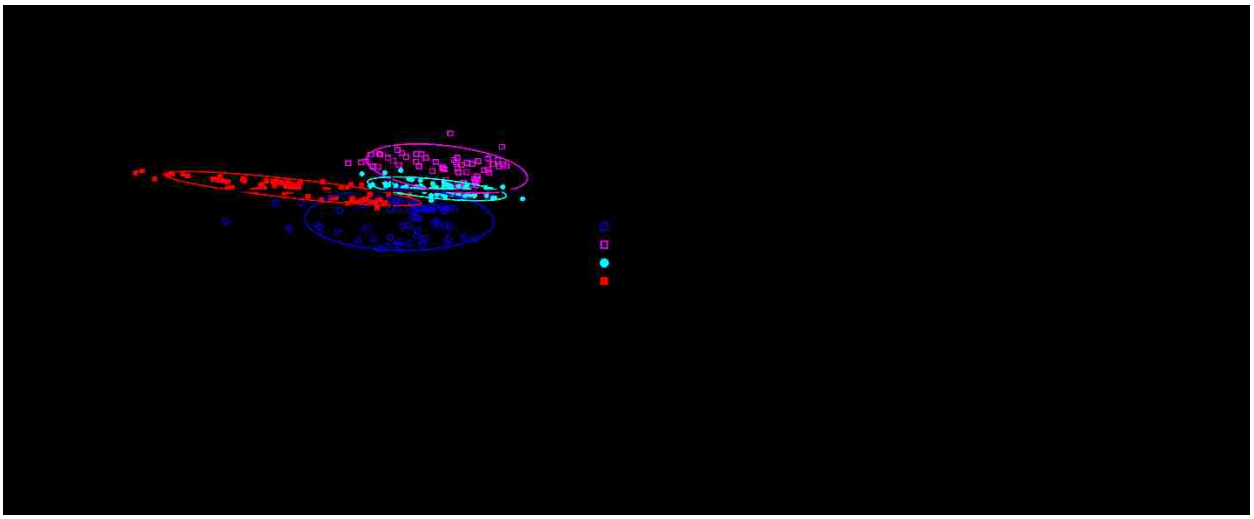

**Supplemental Figure S.4.4.** Spectral PCA results of positive polarity cellular/tumor areas between tissue samples using image PCA masks to reconstruct only cellular/tumor regions for each tissue. **(A)** PC2 vs PC4 scores using image PCA masks to reconstruct the cellular/tumor regions using positive ions *m/z* > 200. **(B)** PC2 loadings plot displaying the chemical species that correspond to PC2 scores(x-axis) **(C)** PC4 loadings plot displaying the chemical species that correspond to PC4 scores (y-axis). Pre-chemotherapeutic tissues shown as blue colored ○ and cyan ●, post-chemotherapeutic tissues shown as colored magenta □ and red ■.

# Chapter 5. Chemical Analysis of Cellular and Stromal Regions from Human Breast Cancer Tissues Using Imaging Time-of-Flight Secondary Ion Mass Spectrometry

Blake M. Bluestein[a], Fionnuala Morrish[b], Daniel J. Graham[a], Jamie Guenthoer[b], David Hockenbery[b], Peggy Porter[b], and Lara J. Gamble[a,§]

[a] University of Washington, Dept. of Bioengineering, MolES Building, Box 351653, Seattle, WA 98195-1653

[b] Fred Hutchinson Cancer Research Center, Seattle, WA 98109

[§] Corresponding Author

Lara Gamble

University of Washington

Department of Bioengineering

Box 351653

Seattle, WA 98195

1-206-543-8094 (phone)

1-206-543-3778 (fax)

lgamble@uw.edu (e-mail)

## 5.1 ABSTRACT

Breast cancer is a complex and heterogeneous malignancy, encompassing multiple tumor forms associated with varying histological types and clinical outcomes. Profiling breast cancer with expression arrays is common, which can reveal biomarkers that potentially aid patient treatment efficacy. However, the positive predictive capability is limited, as many patients possess *de novo* resistance or acquire resistance to certain chemotherapeutics. Therefore, investigating the metabolic changes within breast cancer tissue could potentially lead to new therapeutic targets and revealing the chemical profile of chemoresistance. In this work, imaging time-of-flight secondary ion mass spectrometry (ToF-SIMS) was used to acquire chemical image data from 23 pre-treated breast cancer tissue biopsies. Principle components analysis (PCA) was applied to both ToF-SIMS images to isolate cellular and stromal regions within patient samples. Using these PCA generated masks, it is possible to compare specific regions across many patients, identifying key chemical differences these clearly defined regions. Comparing ToF-SIMS cellular and stromal region data from specific subtypes, e.g. triple negative, has shown promise in defining chemical differences between patients that respond to chemotherapy and those that do not. Characterization of ductal carcinoma in situ (DCIS) tumor containing tissues using ToF-SIMS and PCA determined the spatial distribution of specific amino acids and nucleobases within the tumor and collagen structures surrounding tumors.

## 5.2 INTRODUCTION

Breast cancer is a complex and heterogeneous malignancy, encompassing multiple tumor forms and subtypes, some of which are very aggressive, difficult to detect, and do not respond to treatment.[158] Pathological assessment is typically performed with histological staining to determine the location, type and grade of tumors, but does not always predict patient outcome or response to chemotherapeutics. Genetic profiling breast cancer with expression arrays is common, which can reveal biomarkers that potentially aid patient treatment efficacy.[159] However, the positive predictive capability is limited, as many patients possess *de novo* resistance or acquire resistance to certain chemotherapeutics.[160] Stromal heterogeneity and tumor-stroma interactions provide prognostic indicators for invasive growth and metastasis.[134-137] Previous studies indicate that stromal-cancer cell metabolite interchange aids tumor growth and progression.[138, 139] It is hypothesized that the stromal biochemical state may dictate sensitivity to chemotherapy.[140] However, it is difficult to acquire metabolic data specifically from cellular and stromal regions, as these regions can be difficult to isolate for metabolic profiling due to the complexity of their spatial distribution.

Using an unsupervised method multivariate analysis technique applied to time-of-flight secondary ion mass spectrometry (ToF-SIMS)[161] images, selecting chemical information specifically from the cellular or stromal regions of tumor tissue samples can be achieved with micron-level lateral. This method has been utilized to compare the chemistries different tissue slices.

ToF-SIMS has been previously used to study diseased tissues and cells with a major focus on lipids, such as Duchenne muscular dystrophy[10], osteoarthritic cartilage tissue[11], and Alzheimer brain tissues[12]. In each of these studies unique lipid profiles were determined which distinguished the diseased from the healthy tissue. Alterations within the lipid metabolism are also known as a hallmark of carcinogenesis.[162, 163] Recent research using ToF-SIMS imaging to analyze breast cancer sections demonstrated its potential in analyzing the lipids in the cancerous microenvironment.[114]

This work focuses on utilizing distinct cellular and stromal regions of interest (ROIs) generated from principle components analysis (PCA) of ToF-SIMS images to

compare multiple human breast cancer biopsies. PCA was then be applied to the specific ROIs providing the chemical variance between breast cancer biopsy samples, which potentially offers insight into breast cancer metabolism. This approach combined with genetic expression profiles and known patient outcomes provides a perspective rich in both chemical and genetic information that can aid in understanding the link between chemoresistance and metabolism found in breast cancer patients. Further analyses of breast cancer tissues exhibiting ductal carcinoma in situ tumors observed significant changes in metabolites and their distribution.

## 5.3 METHODS

### 5.3.1 TISSUE SAMPLE PREPARATION

Breast biopsy specimens were obtained from patients consented according to institutional review board protocols. Specimens were immediately embedded in Tissue-Tek® (Fisher Scientific) optimum cutting temperature (OCT) compound, cryopreserved using liquid nitrogen and stored in a -80 °C freezer. Frozen tissue blocks were sectioned in a cryostat-microtome held at -23°C at the Fred Hutchinson Cancer Research Center (FHCRC). Each of the four tissue samples was serially sectioned three times and each section was ~5 µm in thickness. The first and third sections were stained for optical imaging using hematoxylin and eosin (H&E), while the second section was analyzed by ToF-SIMS. The second slice of tissue was placed directly on a 2 $cm^2$ silicon wafer that was previously cleaned with two successive sonications in dichloromethane, acetone, and methanol. The samples were then placed in a petri dish, sealed with Parafilm® (VWR International), and transported to the University of Washington for immediate ToF-SIMS analysis. Each tissue was sectioned on a different day and the time from tissue cutting to analysis was less than 90 minutes for any sample.

### 5.3.2 GENE EXPRESSION SUBTYPE IDENTIFICATION

Tissue sections were macrodissected to select regions containing the highest proportion of invasive tumor cells to reduce contamination from non-tumor cells. RNA was isolated using the AllPrep DNA/RNA Mini Kit (Qiagen Inc., Valencia, CA) and

gene/transcript expression was assessed using the WG-DASL® *(HumanHT-12 v4)* Assay (Illumina, Inc., San Diego, CA). Data processing and analysis were done in the R environment (v3.0.3). The raw expression data were pre-processed and median normalized using the Bioconductor lumi package[143], and gene expression intrinsic subtypes (Luminal A, Luminal B, HER2-enriched, and TN) were determined using the 50-gene panel described by Parker et al.[144] with the software Bioconductor genefu package[145]. A table of all tissues and their subtype designation is shown in Table 5.1.

### 5.3.3 ToF-SIMS

ToF-SIMS experiments were performed using an ION-TOF TOF.SIMS 5-100 (ION-TOF GmbH, Münster, Germany) equipped with a liquid metal ion gun (LMIG) for analysis and an electron flood gun for charge neutralization. The LMIG was used to generate a pulsed 25 keV $Bi_3^+$ beam impacting the target at an angle of 45°. The $Bi_3^+$ beam was set in spectroscopy mode for high mass resolution (HMR) to acquire spectra in both polarities and fast imaging mode to acquire high spatial resolution (HSR) negative polarity images. The $Bi_3^+$ current was typically 0.13-0.15 pA for HMR and 0.05 pA for HSR. Target currents were measured before each data set using a Faraday cup. HSR mode images with micron spatial resolution were acquired and compared to features found in ToF-SIMS to H&E images. Large area images of the entire tissue biopsy were created by manually stitching individual optical images of 800 µm × 800 µm from the video camera within the ToF-SIMS before analysis of each tissue. These large optical stitched images were then aligned to H&E images using the tissue borders to aid in selecting areas where analysis patches were to be acquired. For all data collection, HMR positive ion data was acquired followed immediately by HMR negative ion data on the same area. X and Y sample stage coordinates were saved in the software to ensure data acquired was from the same region in both polarities. HSR images were obtained from each sample region after all HMR spectra were completed. In HMR mode, mass resolution ($m/\Delta m$) for the $C_2H_3^+$ ion was greater than 4500. Positive ion spectra were calibrated to $CH_3^+$, $C_2H_3^+$, and $C_4H_5^+$. Negative ion spectra were calibrated to $CH^-$, $OH^-$, and $C_2H^-$. Spectra were acquired from 1 mm × 1mm, 1.6 mm × 0.6 mm, and 1.2 mm × 0.8 mm “patches” comprising of 25 or 24 200 µm × 200 µm “tiles” on each tissue, an

example of positions is shown in Figure 5.1. Each tile contains 256 ×256 pixels, giving the patches a total pixel count of 1280 × 1280. Selecting to analyze three large patches rather than the entire tissue biopsy sample was chosen due to the time intensiveness required to analyze such large samples, which would lead to degradation during analysis or lipid migration. Thus, analyzing three patches would provide a timely analysis, providing the most relevant data of the tissue's native chemical composition. The $Bi_3^+$ dose was limited to ≤$5.0\times10^{11}$ ions/$cm^2$ for each tile in both positive and negative ion modes, resulting in a total $Bi_3^+$ dose ≤$1.0\times 10^{12}$ ions/$cm^2$ per tile. SurfaceLab 6 software (ION-TOF GmbH, Münster, Germany) was used for all analyses. A table of all tissues where data has been acquired and analyzed is shown in Table 5.1. Reference data including H&E stained images, ToF-SIMS camera stitched images, high spatial resolution ToF-SIMS images, and tables containing genetic and pathological designation can be found in Appendix A. Supplemental Table S.5.2 provides key masses and their biological molecule identified within PCA.

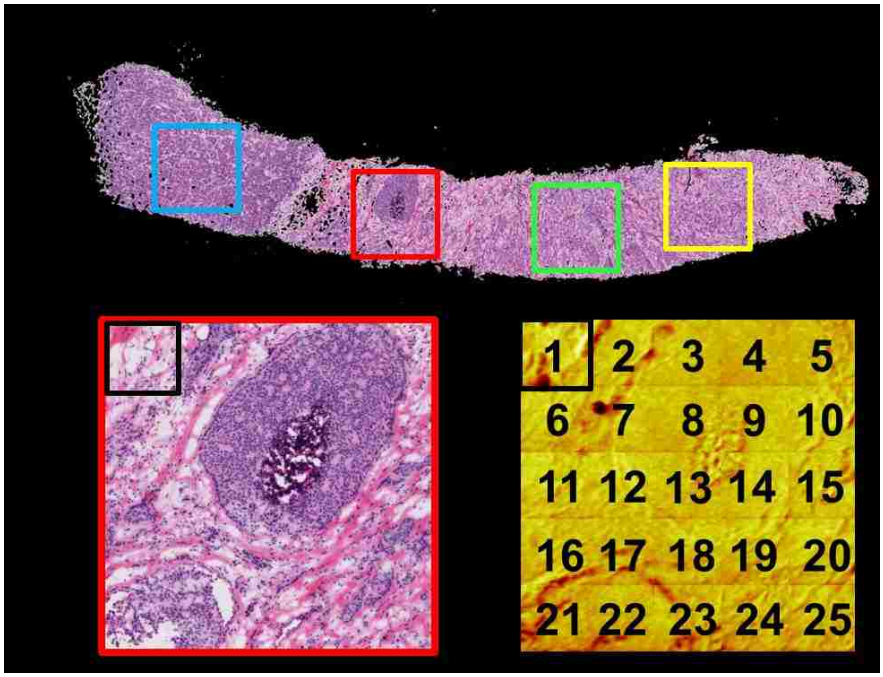


**Figure 5.1.** Example of ToF-SIMS data acquisition from breast tissue biopsy. **(A)** H&E stained image of breast cancer tissue biopsy. Colored boxes represent 1 mm × 1 mm patches where ToF-SIMS data was acquired. **(B)** An increased magnification optical H&E image of a selected analysis region showing the 200 × 200 µm tile outlined in black. **(C)** A total counts ion image from the ToF-SIMS analysis region corresponding to **(B)** showing the 25 200 × 200 µm tiles comprising of one stitched patch. White regions seen in the tissue slices can indicate either tears or fatty acid droplets.

### 5.3.4 PRINCIPAL COMPONENT ANALYSIS

Principal component analysis (PCA) was applied to ToF-SIMS images acquired from the tissues using all pixels in the data set (herein referred to as image data and displayed as images) and to summed spectral data from individual patches (herein referred to as spectral data and displayed as individual data points).

Data used in this study were pre-processed for PCA as follows: 1) ToF-SIMS image data were Poisson scaled and mean centered, and 2) summed spectral data from individual tile images were normalized to the sum of the intensities of all of the peaks in the peak list, square-root transformed, and mean centered. Regions of exposed silicon substrate and OCT (e.g. holes or tears from cutting tissue and embedding medium surrounding tissue) were excluded from all analyses by applying a threshold to the pixels with a $Si^+$ signal, where *m/z* 27.9 was used to detect silicon and *m/z* 332.2 ($C_{14}H_{29}^+$, a fragment of the benzalkonium additive in OCT)[13] is used to detect OCT areas. All PCA was performed using the NBToolbox SpectraGUI and ImageGUI (Daniel Graham Ph.D., NESAC/BIO, University of Washington), that operate within MATLAB (MathWorks, Natick, MA). Peaks were chosen whose maximum intensity was twice or more than that of the average background intensity. The spectra from all tissues were overlaid and then peaks were manually selected and integrated to full width half max. All peaks below *m/z* 920 were selected, excluding known salt, salt adduct, substrate and inorganic peaks. A total peak list of 846 and 807 peaks were chosen from the positive and negative ion modes, respectively. All peaks in the list were used for image PCA analysis while spectral PCA was limited to peaks with *m/z* above 200 resulting in 391 and 329 peaks for the positive and negative ions peak lists, respectively.

PCA, using the ImageGUI, is first applied to image data formatted as .bif6 files from SurfaceLab 6. No peaks are excluded from this data except salts, substrate (Si and Si containing peaks), and embedding medium (OCT). Normalization was not applied to imported image patches; image data were pre-processed by Poisson scaling and mean centering before PCA.

The presence of large fatty acid droplets were occasionally observed in some of the tissue sections. It is important to note that breast tissue is a fatty tissue, therefore

the prevalence of fatty acid droplets within tissue sections can vary from none to many depending on the biopsy. As shown in Figure 4.5 and Figure 4.6C, the strong signal from the fatty acid droplets dominates the PCA scores resulting in the main variability between the samples being the presence or absence fatty acid droplets in a particular tissue slice. Following the protocol developed in Chapter 4, the fatty acid droplets were removed prior to PCA as so sample comparison could be focused on cellular and/or stromal tissue regions.

Scores images that corresponded to cellular and stromal areas from serial H&E images were selected to be used as masks. Using SurfaceLab 6, scores images were imported and spectra reconstructed by applying a 10% minimum, 90% maximum signal threshold to the pixels within the selected score image. The resulting data, in .bif6 format, were imported back into ImageGUI and the patch parsed into individual 200 µm × 200 µm tiles where each tile represents one data point in the spectral PCA plots. The parsed data was then imported in .xlsx format into SpectraGUI for spectral analysis, where each individual tile represents one data point in the PCA scores plots. Imported data were normalized to the sum of the intensities of all of the peaks in the peak list, square-root transformed, and mean centered prior to spectral PCA. Further spectral PCA was done by separating data sets by their defined cancer subtypes for comparison.

### 5.3.5 Ductal Carcinoma In Situ Principal Component Analysis

Four patches from three separate tissues (patient numbers: 4, 7, 8) had pathologist identified ductal carcinoma in situ (DCIS). PCA was applied ToF-SIMS data to these four specific patches using two modified peak lists in the positive polarity. The first containing signature amino acid fragments from Canavan et. al[164] and May et. al.[165] However, the peak at *m/z* 86.1 was excluded as this peak could not be differentiated from the choline head group from the phosphotidylcholine lipid due to the mass resolution of the instrument and saturation of the detector by phosphotidylcholine fragment. This peak list contained a total of 45 peaks. The second list combined both nucleobases and the previous 45 peaks from the amino acid peak list for a total of 68

peaks. All other parameters discussed previously using the positive polarity and peak selection was applied in the same manner to generate the image PCA data.

### 5.3.6 SECOND HARMONIC GENERATION (SHG)

The multiphoton excitation fluorescence (MPEF) and SHG images were acquired with a scanning confocal multiphoton microscope (Olympus, FV1000 MPE BX61) with a 20x objective. The light source was a tunable laser (Spectra-Physics Mai Tai) with $\lambda_{exc}$ at 910 nm and with bandpass filters at 495-540 nm for the MPEF channel and 420-460 nm for the SHG channel. The detectors were photon multipliers, located so that the SHG was captures in back-scattering mode and the MPEF in epifluorescence mode. All SHG experiments were performed on H&E stained slides obtained from the Fred Hutchinson Cancer Research Center.

**Table 5.1.** List of patient breast cancer biopsies analyzed in this study, their receptor status (estrogen (ER), progesterone (PR), human epidermal growth factor receptor 2 (HER2)), cytokeratin 5/6 status, epidermal growth factor receptor (EGFR) status, tumor grade, pathological response (pCR), and immunohistochemistry (IHC) (triple negative, TN and HER2 enriched, HER2) and gene expression subtype. All breast cancer biopsies were analyzed before any treatment was administered with the exception of Patient 23.

| Patient No. | ER | PR | HER2 | CK5/6 | EGFR | KI67 | Grade | pCR | IHC subtype | Gene Expression Subtype |
|---|---|---|---|---|---|---|---|---|---|---|
| 2 | POS | POS | NEG | NEG | NEG | 5 | 1 | non-pCR | Luminal A | Luminal A |
| 4 | POS | POS | POS | NEG | NEG | 71 | 3 | non-pCR | Luminal B | Luminal B |
| 6 | POS | NEG | POS | NEG | NEG | 44 | 3 | pCR | Luminal B | Luminal B |
| 8 | POS | POS | POS | NEG | NEG | 20 | 2 | non-pCR | Luminal B | Luminal A |
| 10 | POS | POS | NEG | NA | NA | 57 | 3 | non-pCR | Luminal B | Luminal B |
| 12 | POS | POS | NEG | NA | NA | 19 | 3 | non-pCR | Luminal B | Luminal A |
| 14 | POS | NEG | NEG | NA | NA | 69 | 3 | pCR | Luminal B | Luminal B |
| 16 | NEG | NEG | NEG | POS | NEG | 95 | 3 | pCR | TN | Basal-like |
| 18 | NEG | NEG | NEG | POS | NEG | 69 | 3 | non-pCR | TN | Basal-like |
| 20 | NEG | NEG | NEG | POS | POS | 57 | 3 | pCR | TN | Basal-like |
| 22 | NEG | NEG | NEG | POS | NEG | 93 | 3 | pCR | TN | Basal-like |

## 5.4 RESULTS AND DISCUSSION

To simplify the complexity and aid in the interpretation of such a large ToF-SIMS data set, principal components analysis (PCA) was applied to both ToF-SIMS image and spectral data to reduce the dimensionality of the data. Using the method developed in Chapter 3, PCA was applied to a total of 75 patches from 22 pre-treated breast cancer biopsies and one post-treated biopsy that contained normal stromal structures only. Briefly summarizing the method presented in Chapter 3, regions of interest (ROIs), specifically cellular and stromal regions were generated from the use of PCA of ToF-SIMS image data for all tissue samples. The scores images that were representative of cellular and stromal areas were then used to reconstruct and extract the mass spectral information from the ToF-SIMS images. The reconstructed spectral information specific

to cellular or stromal regions was subjected to PCA to compare across all patients respectively (e.g. cellular vs. cellular and stromal vs. stromal). Using this method identifies the largest amount of variance between highly specific areas within patients providing a way to determine chemical differences between patient response that may be linked to lipid metabolism.

### 5.4.1 PCA Application to ToF-SIMS Spectra of Cellular Regions

Figure 5.2 shows the results from spectral PCA of the isolated cellular regions in the negative polarity with an *m/z* ≥ 200 using all 22 samples and 72 analysis patches. PC2 scores, with an overall variance of 9%, exhibited the most separation between samples. The loadings plot presented in Figure 5.2C shows chemical species that correlate to Figure 5.2A and Figure 5.2B. PC2 positive loadings (Figure 5.2C, y > 0) show fatty acids C14:0, C16:1, C16:0, C18:0, C20:4, and C20:3 ($C_{14}H_{27}O_2^-$, $C_{16}H_{30}O_2^-$, $C_{16}H_{31}O_2^-$, $C_{18}H_{35}O_2^-$, $C_{20}H_{31}O_2^-$, $C_{20}H_{33}O_2^-$, *m/z* 227.20, 253.22, 255.24, 283.26, 303.24, 305.25, respectively), phosphoinsitol (PI) fragments ($C_6H_{10}PO_8^-$, *m/z* 241.01 and $C_9H_{16}PO_9^-$, *m/z* 299.05), cholesterol sulfate ($C_{27}H_{45}O_4S^-$, *m/z* 465.30), and two sphingomyelin (SM) (34:1) fragments ($C_{36}H_{69}NO_6P^-$, $C_{38}H_{76}N_2O_6P^-$, *m/z* 642.51, 687.56) having high positive loadings. C18:2, C18:1($C_{18}H_{31}O_2^-$, $C_{18}H_{33}O_2^-$, *m/z* 279.23, 281.25 respectively), a fragment of C18:2 or C20:1 at *m/z* 261.24 ($C_{18}H_{31}O_2^-$ or $C_{19}H_{33}^-$), C20:1 ($C_{20}H_{37}O_2^-$, m/z 309.28), cholesterol ($C_{27}H_{45}O^-$, *m/z* 385.35), and vitamin E ($C_{29}H_{49}O_2^-$, m/z 429.37) dominate the negative loadings (Figure 5.2C, y < 0). While PC2 did show some separation between samples, the data set did not result in a discernable trend when related to either pathological response (pCR) or by breast cancer subtype shown in Figure 5.2A and Figure 5.2B, respectively.

It is worth mentioning that PC1 (not shown), encompassed more of the chemical variance at 53%, but showed a large standard deviation for many of the samples resulting in little to no separation in the PCA scores plot for PC1. This could be due to the variable presence of fatty acids and cholesterol across a single tissue, showing higher intensity in some tiles of the analysis patch compared to others within the same analysis patch and tissue section. The loadings for PC1 consisted specifically of fatty acids and cholesterol.

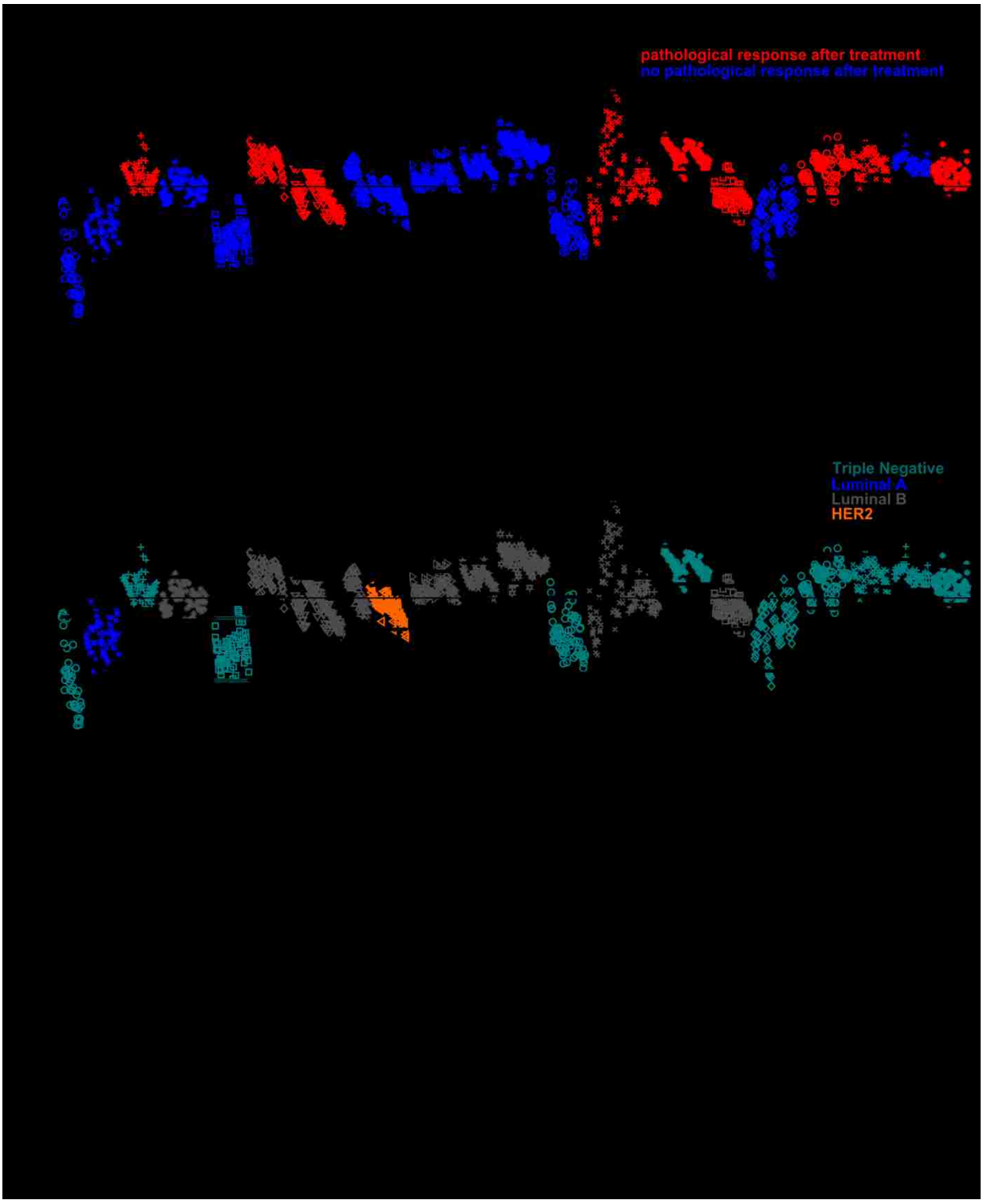


**Figure 5.2. (A)** PC2 scores generated from using cellular ROIs using the negative ions *m/z* >200. PC2 shows an overall variance of 9%. The lines above and below the individual sample data points demonstrate the 95% confidence interval. Patient data is presented as pathologically responding (red) and non-responding (blue). **(B)** PC2 scores colored to show breast cancer subtypes, triple negative (teal), luminal A (blue), luminal B (gray), and HER2 enriched (orange). **(C)** Loadings plot displaying the chemical species that correspond to the cellular regions.

### 5.4.2 PCA Application to ToF-SIMS Spectra of Stromal Regions

The same method using PCA on isolated ToF-SIMS spectral regions described above was also applied to all 22 samples and 72 analysis patches of the reconstructed stromal regions. Figure 5.3A and Figure 5.3B show the results from spectral PCA of the isolated stromal regions in the negative polarity with an $m/z \geq 200$. As with the cellular spectral analysis using PCA, there was no distinct separation trend by pCR (Figure 5.3A) or by breast cancer subtype exhibited by any PCs. Similarly to the PC1 scores of the cellular region data, the PC1 scores (57% of the variance) of the stromal regions (not shown) also showed large confidence intervals and overlap of score. PC2 scores of the stromal data (Figure 5.3A and Figure 5.3B) captured an overall variance of 9% and as with the cellular data PC2 showed less variability within each tissue sample. However, there was no apparent overall trend related to pCR or tumor subtype. PC2 scores from the stromal regions (Figure 5.3A and Figure 5.3B), show more variability or spread within each tissue sample when compared to the PC2 scores of the cellular data (Figure 5.2). This may be due to the fact that the stromal tissue is more heterogeneous than that of the cellular regions, as the cells associated with the stroma can remodel the extracellular matrix and are known to readily mutate in the tumor microenvironment.[166] Some of the tiles within these stromal regions may be closer to the cellular/tumor regions and are different than that of the other stromal tiles further away from the cellular/tumor regions exhibiting more variability. Examining the loadings in Figure 5.3C of the stromal regions also shows similar chemicals species to what was observed in cellular regions, with the exception of a high loading of vitamin E in the positive loadings.

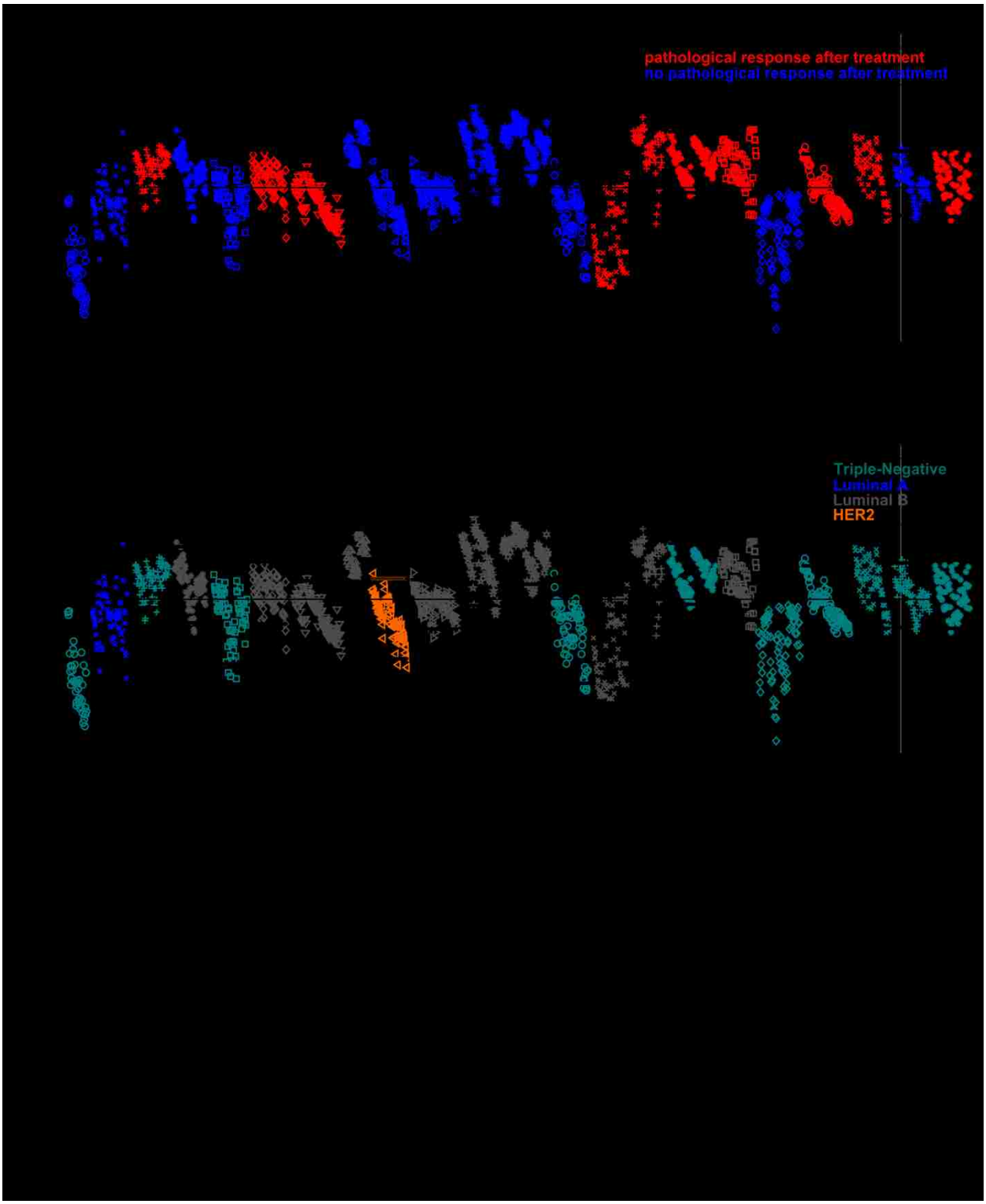


**Figure 5.3. (A)** PC2 scores generated from using stromal ROIs using the negative ions *m/z* >200. PC2 shows an overall variance of 9%. The lines above and below the individual sample data points demonstrate the 95% confidence interval. Patient data is presented as pathologically responding (red) and non-responding (blue). **(B)** PC2 scores colored to show breast cancer subtypes, triple negative (teal), luminal A (blue), luminal B (gray), and HER2 enriched (orange). **(C)** Loadings plot displaying the chemical species that correspond to the stromal regions.

The biopsy obtained from Patient 23 showed completely normal breast tissue. The biopsy was taken after Patient 23 had been treated with chemotherapeutics but it is possible that the biopsy missed the cancerous region, as only normal stromal structures were visible. This sample provided a “healthy” or normal stromal sample to compare with the other stromal samples. When this sample was added to the other stromal samples, there was not a significant shift in the scores of any PC of any samples and little change in the loadings plot. Thus, the addition of the normal stromal tissue did not provide any further separation aiding in the identification of chemical differences between pCR and non-pCR tissues. As observed in the previous two previous spectral PCA analyses of cellular and stromal regions, PC2 scores (Figure 5.4A) showed the best separation of the samples. The overall variance of 9% captured by PC2 with the addition of the normal stromal tissue data is equal to the amount of variance captured by PC2 without the addition of the normal stromal tissue as shown in Figure 5.3. The loadings plot including the normal stromal tissue shown in Figure 5.4B, also did not show any significant differences when compared to the loadings plot in Figure 5.3C. The normal stromal tissue did exhibit a general trend of positive scores which correlated to fatty acids C14:0, C16:0, C18:1, C18:0, vitamin E, cholesterol sulfate, and SM (34:1) and PI fragments.

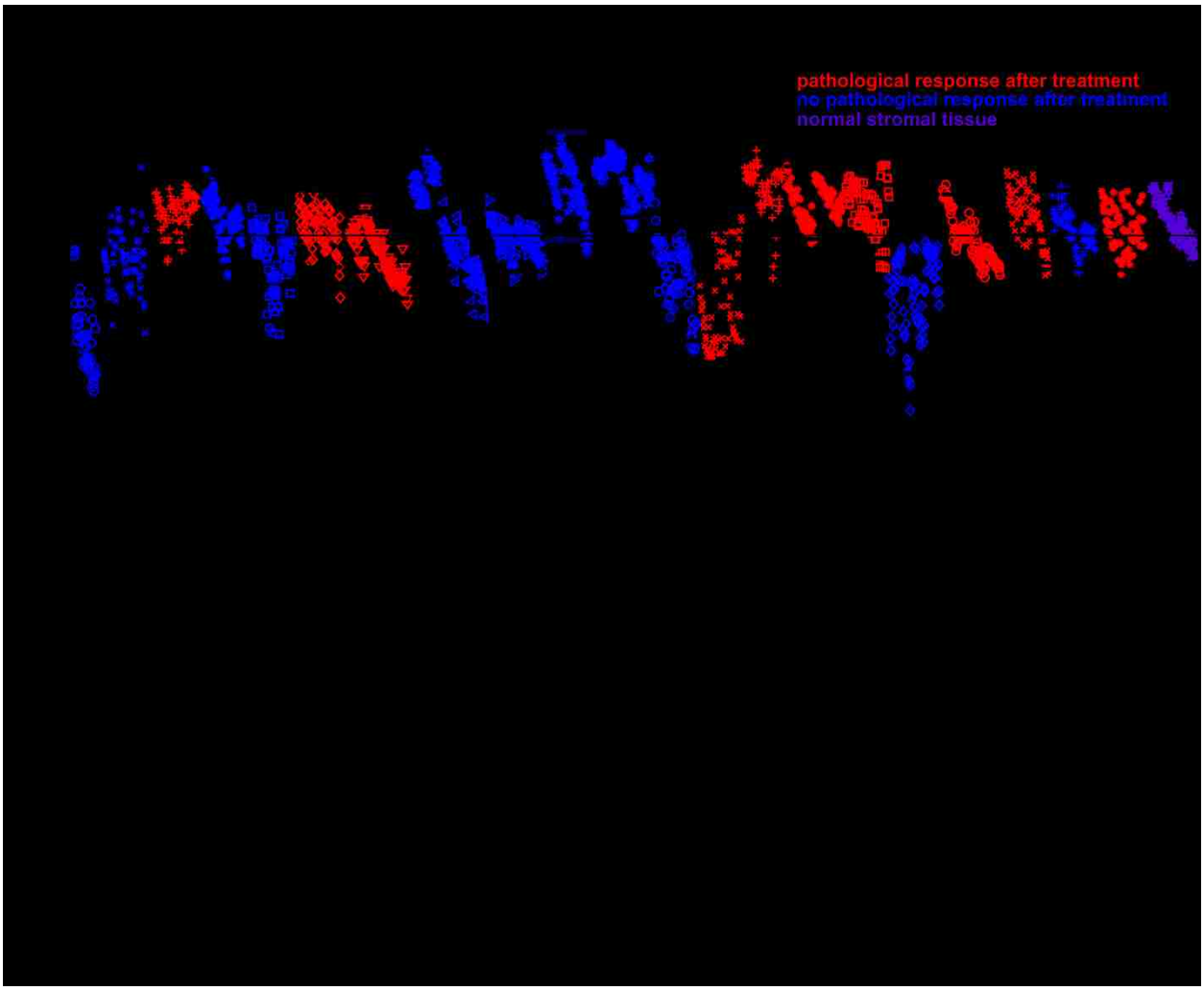


**Figure 5.4. (A)** PC2 scores generated from using stromal ROIs using the negative ions *m/z* >200. PC2 shows an overall variance of 9%. The lines above and below the individual sample data points demonstrate the 95% confidence interval. Patient data is presented as pathologically responding (red), non-responding (blue), and normal stromal tissue (purple). **(B)** Loadings plot displaying the chemical species that correspond to the stromal regions.

### 5.4.3 Application of PCA to Specific Breast Cancer Subtypes

To test if specific cancer tissue subtypes exhibited distinct chemical information pertaining to pathological response (pCR), the samples from subtypes TN (triple negative) and Luminal B types were individually compared using spectral PCA according to the immunohistochemistry designation. The aim was to utilize specific regions (e.g. cellular and stromal) within subtypes to identify potential molecular species involved with chemoresistance. The TN subtype showed separation of pCR and non-pCR patient tissue samples, demonstrating that lipid metabolism variability has the

potential to distinguish treatment/patient outcome for TN type tumors. Luminal B showed significantly more variability than the TN samples without an apparent separation between pCR and non-pCR tissues.

#### 5.4.3.1 *TRIPLE NEGATIVE TISSUES*

The results from PC2 of the cellular regions of the TN subtype are shown in Figure 5.5A. PC2 (12% variance) exhibited the best sample separation between patient tissue samples and shows a clear pattern of separation between complete pCR (Figure 5.5A, red) and non-pCR (Figure 5.5A, blue). The tissues with positive scores, patient numbers 3, 16, 19, 20, and 22 are classified as pCR patients and separated across PC2, where fatty acids C14:0, C16:0, C18:0, C20:4, C20:3, and SM fragments are observed in the positive loadings (Figure 5.5B, $y > 0$). C18:2, C18:1, and cholesterol all have negative loadings and correlate with the non-pCR patient tissues 1, 5, 13, and 18. Patient number 21, a non-pCR case, exhibited positive scores which align with pCR patient tissues. A potential explanation for the tissue biopsy from patient 21 to follow the pCR tissue trend is that while not readily apparent in the serial H&E sections, the biopsy may contain cellular areas undergoing necrosis. Tumor tissues showing necrotic cellular areas have shown to be rich with SM and are associated with a higher mortality rate and are more aggressive.[27, 167] It is also known that SM is a precursor to signal for cell apoptosis[168], where during apoptosis SM goes from the outer leaflet of the cell membrane into the cytosol where it begins the cell death signaling pathway. However, SM is also a precursor for a sphingosine-1-phospahte (S1P) which is an inducer for cell growth.[169] Since SM is a precursor for both cell death and proliferation this makes interpretation of the data more difficult. One potential explanation for TN pCR patients exhibiting a higher presence SM in their cellular regions is that the SM has not been internalized for either proliferation or apoptotic signaling and that their membrane and SM metabolism has not been significantly altered. For future studies, the examination of biopsies for necrosis may aid in understanding the presence of SM.

Also of note, are PI fragments ($C_6H_{10}PO_8^-$, *m/z* 241.01 and $C_9H_{16}PO_9^-$, *m/z* 299.05) and fatty acids C16:0, C18:0, and C20:4 in the positive loadings. It has been discussed that PI (38:4) which consists of two fatty acid chains, C18:0 and C20:4, is

significantly increased in non-malignant breast cancer cells.[170] While the entire mass of PI(38:4) cannot be observed at a high intensity at *m/z* 885.55, its fragmentation pattern is quite apparent within the loadings plot with C20:4 and C18:0. It is also possible that C16:0 is a fragment from SM(34:1) or multiple higher mass lipids and is therefore more difficult to assign a proper biological function to its presence.

Non-pCR patients correlated with fatty acids C18:2, C18:1, and C20:1. It has been suggested that when oxygen is restricted to cells that fatty acid desaturases (FADS), commonly used for both fatty acid synthesis and pro-inflammatory conditions, are not functional.[114] For example, an inactive FADS2 in non-pCR patients would result in an accumulation of C20:1 and C18:1. Furthermore, an inactive FADS2 would also explain the presence of C18:2, as this the substrate used by FADS2 in the fatty acid synthesis pathway using essential fatty acids to generate long chain polyunsaturated fatty acids.

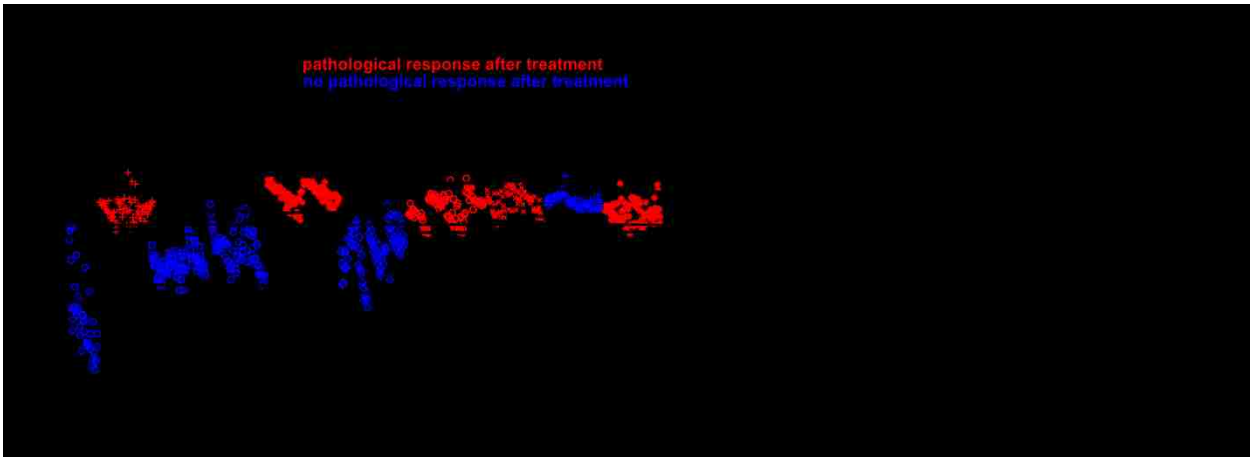


**Figure 5.5. (A)** PC2 scores generated by using cellular ROIs of TN patients using negative ions *m/z* > 200. The lines above and below the individual sample data points demonstrate the 95% confidence interval. Patient data is presented as pathologically responding (red) and non-responding (blue). **(B)** PC2 loadings plot displaying the chemical species that correspond to the TN cellular regions scores. PC2 captures a total of 12% of the total variance.

Further examination of the TN samples demonstrated that the stromal regions of the TN tissues also exhibit a similar trend as the cellular regions. These results are shown in Figure 5.6. The PC2 scores of the isolated stromal regions from the TN group (Figure 5.6A) were similar to that of the TN cellular group (Figure 5.5A), where the pCR patients separated from the non-pCR patients with the exception of Patient 21. The scores of the stromal components exhibit slightly more variation within samples, which

can be seen by the increased spread of data points between the 95% confidence intervals.

Comparing the scores and loadings of the stromal to cellular regions shows one key difference. The negative loadings (Figure 5.6B) of the stromal regions (associated with non-pCR tissues) does not show the fatty acid C18:2. This may indicate that the cellular or tumor regions are actively transporting C18:2 for fatty acid synthesis resulting in less, or depleted, C18:2 in the surrounding environment. Other fatty acids such as C20:1 and C18:1 and its $[M\text{-}H_2O]^-$ ($C_{18}H_{32}O^-$) fragment at *m/z* 263.24, and cholesterol are consistent with the cellular plot.

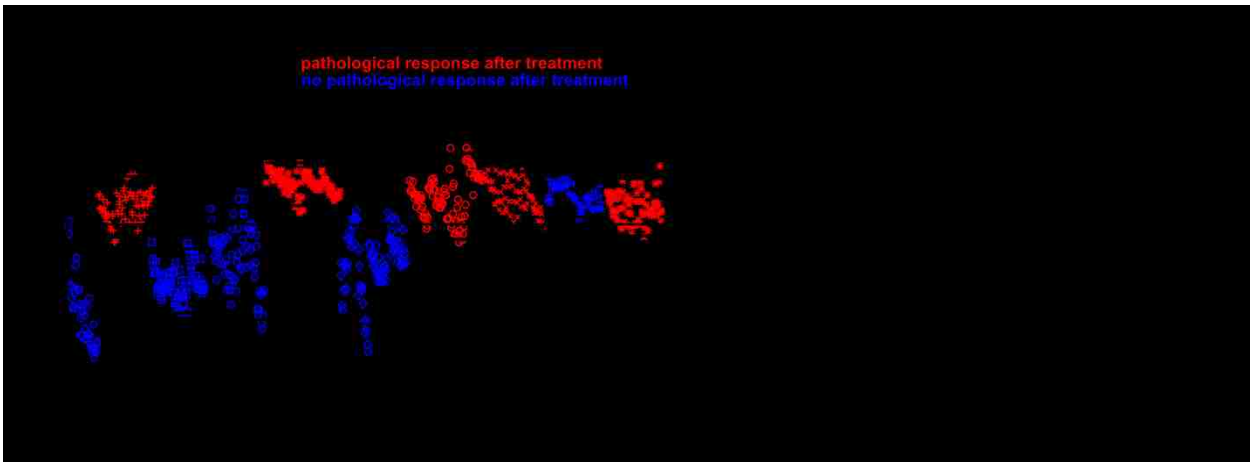


**Figure 5.6. (A)** PC2 scores generated by using stromal ROIs of TN patients using negative ions *m/z* > 200. The lines above and below the individual sample data points demonstrate the 95% confidence interval. Patient data is presented as pathologically responding (red) and non-responding (blue). **(B)** PC2 loadings plot displaying the chemical species that correspond to the TN stromal regions scores. PC2 captures a total of 10% of the total variance.

Using the normal stromal tissue biopsy acquired from Patient 23, the TN stromal tissues could be "challenged" to test the robustness of the separation of pCR and non-pCR observed by PCA. The resulting scores from PC2 are shown in Figure 5.7A. There was nearly no change observed in scores after the addition of the normal stromal tissue data. The overall variance captured remained equal to 10% and the loadings plot (Supplemental Figure S.5.1) did not show any significant changes. The normal stromal tissue data exhibited positive scores along with all pCR tissues and the one non-pCR tissue, Patient 21. This could be interpreted that the pCR stromal tissues are also more similar to that of the normal stromal tissue than that of the non-pCR tissue.

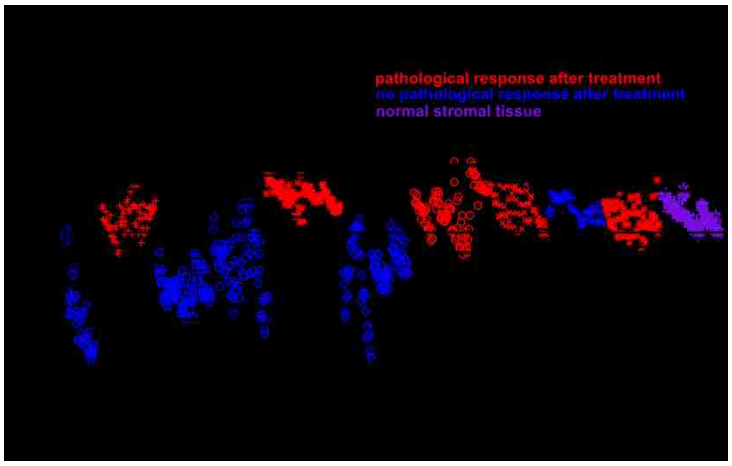


**Figure 5.7.** PC2 scores generated using stromal ROIs of TN patients using negative ions *m/z* > 200. Patient data is presented as pathologically responding (red), non-responding (blue), and normal stromal tissue (purple). The lines above and below the individual sample data points demonstrate the 95% confidence interval. PC2 captures a total of 10% of the variance between all samples.

#### 5.4.3.2 *LUMINAL B TISSUES*

PCA was used to explore the chemical variance between 10 patients with the Luminal B subtype and identify potential molecular species involved with chemoresistance. PC2 offered the best separation between patient tissues, however unlike the TN dataset, no PCs for the Luminal B set showed a clear separation between pCR and non-pCR tissues. PC2 of the cellular regions is shown in Figure 5.8A with pCR samples in red and non-pCR samples in blue. The lack of trend between pCR and non-pCR tissues could be due to the variability of receptor types on the Luminal B tissues or potentially even the subtype itself (showing different types for IHC and gene expression). For example, all of the TN tissues were negative for all receptors, meaning that there was no overexpression of estrogen (ER), progesterone (PR), and human epidermal growth factor 2 (HER2). The Luminal B subtype data compared here has variable overexpression of both PR and HER2, which could influence the spread of the data in samples. This is reflected in Table 5.1 showing the receptor status of all the tissues studied.

The cellular loadings plots of the Luminal B tissues (Figure 5.8B) shows other fatty acid species not observed in the TN loadings (Figure 5.5B). In the positive loadings longer chain fatty acids C24:1 ($C_{24}H_{45}O_2^-$, *m/z* 365.34) and C24:0 ($C_{24}H_{47}O_2^-$, *m/z* 367.36) are observed. These fatty acids have been documented to be located in

necrotic areas.[114] It has been shown that in mammalian tissues C24:0 and C24:1 are the most common very long chain fatty acids (VLCFAs) and that sphingolipids are common carriers of the C24 chain.[171] It has also been shown that elongating enzymes, specifically ELOVL1, produces a C24 with acetyl coenzyme A (CoA) which is a substrate for sphingolipid and ceramide synthesis.[171, 172] Ceramides are the lipids known to be produced by the hydrolysis of sphingolipids (e.g. sphingomyelin) that are intracellular signals for cell apoptosis.[173] While it is unknown if the C24 fatty acids observed here are related to ceramide or sphingolipid synthesis it can be said that the fatty acid profile when using PCA to compare Luminal B cellular regions is much different than that of the TN tissues. It is also possible that PC2 is separating the tissues by their fatty acid enzymatic processes. Following this assumption it would explain the accumulation of fatty acids C18:0 and its fragment $C_{18}H_{33}O^-$ at *m/z* 265.25, C20:3, and C20:2 as these are all products of mammalian fatty acid synthesis. The presence of C20:4 is contradictory, as it is an essential fatty acid unable to be synthesized and can be associated with inflammation, apoptosis, and tumor promotion.[174] Also, the fragment at *m/z* 269.25, possibly $C_{17}H_{33}O^-$ , has no literature significance and is li a fragment from a higher mass lipid.

The negative loadings that correlate show far fewer metabolites that correlate to Patient tissues 4, 8, 11, 15, and 17. The negative loadings are dominated by C18:1 and vitamin E. While it has been shown that vitamin E analogs can trigger apoptosis in some breast cancer cells types,[175, 176] which may explain why pCR Patients 15 and 17 exhibit negative scores, however, this does not provide an explanation for the other 3 non-pCR patients.

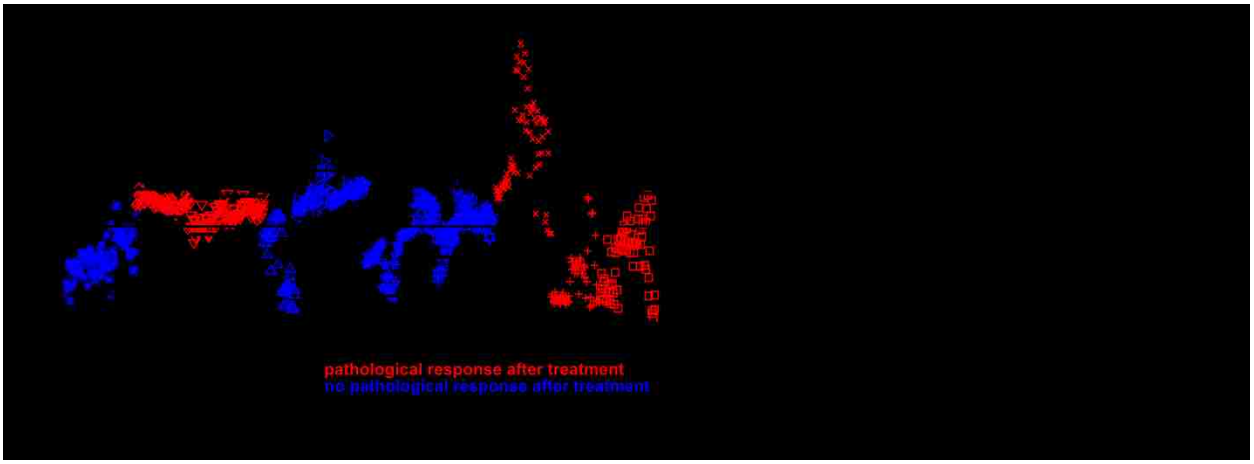


**Figure 5.8. (A)** PC2 scores generated by using cellular ROIs of Luminal B patients using negative ions *m/z* > 200. The lines above and below the individual sample data points demonstrate the 95% confidence interval. Patient data is presented as pathologically responding (red) and non-responding (blue). **(B)** PC2 loadings plot displaying the chemical species that correspond to the of Luminal B cellular scores. PC2 captures a total of 14% of the total variance.

Examining the stromal components of the Luminal B subtype, also did not result in any discernable trend between pCR and non-pCR patients. Again PC2 (14% of total variance) demonstrated the best separation between samples Figure 5.9A. The loadings (Figure 5.9B) that corresponded to these scores show C16:0, C18:2, C18:1, PI fragments (*m/z* 241.04 and 299.07) vitamin E, and SM fragments (*m/z* 642.51and 687.56) for positive loadings while the negative loadings corresponded to C18:0, C20:4, C20:3, C24:1, and cholesterol. Patient tissue 4 appears to have scores that are more neutral as data is spread between positive and negative scores across the y=0 axis. This is different than what was observed in the Luminal B cellular scores, as only Patient tissue 12 exhibited neutral scores.

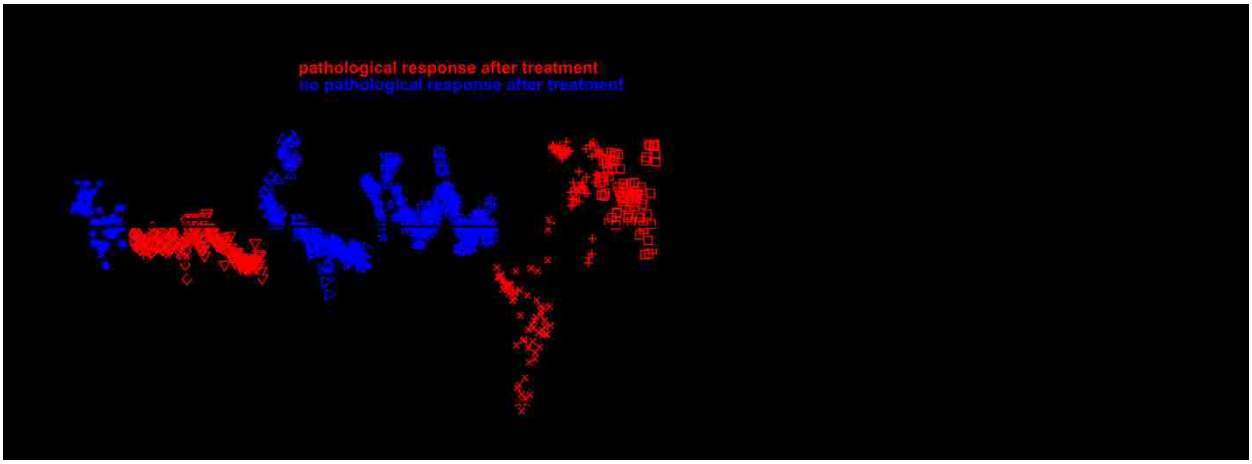


**Figure 5.9. (A)** PC2 scores generated by using stromal ROIs of Luminal B patients using negative ions *m/z* > 200. The lines above and below the individual sample data points demonstrate the 95% confidence interval. Patient data is presented as pathologically responding (red) and non-responding (blue). **(B)** PC2 loadings plot displaying the chemical species that correspond to the of Luminal B stromal scores. PC2 captures a total of 14% of the total variance.

The normal stromal tissue data set from Patient 23 was also included in the Luminal B stromal regions as a separate analysis. The scores resulting from this analysis can be seen in Figure 5.10 and the loadings in Supplemental Figure S.5.2. The scores and loadings of the Luminal B stromal data set were not significantly changed with the addition of the normal tissue. The normal stromal tissue resulted with a majority of positive scores. This is of note, as this relates to less pCR tissues, Patients 6, 7 and 14 exhibited negative scores, and more to non-pCR tissues like Patients 8, 11, and 12.

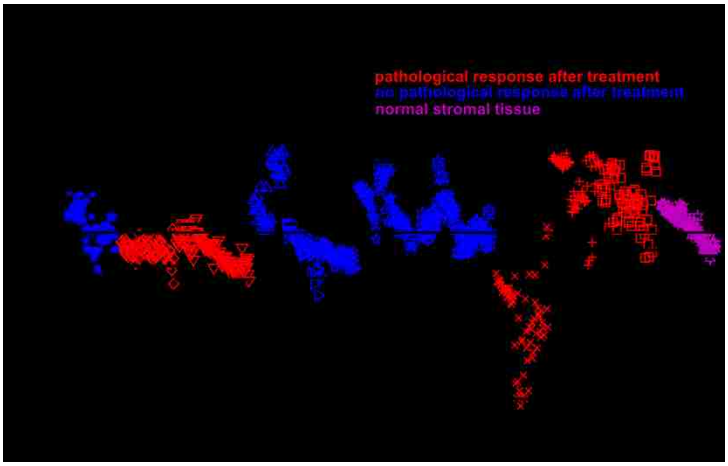


**Figure 5.10.** PC2 scores generated using stromal ROIs of Luminal B patients using negative ions *m/z* > 200. Patient data is presented as pathologically responding (red), non-responding (blue), and normal stromal tissue (purple). The lines above and below the individual sample data points demonstrate the 95% confidence interval. PC2 captures a total of 14% of the variance between all samples.

Comparing the stromal and cellular components of the Luminal B subtype it is noticeable that SM fragments are observed to have more variance within the stromal regions than the cellular. Comparing the TN and Luminal B subtypes, it can be seen that the TN subtype does not demonstrate variability of vitamin E. Vitamin E variability is only observed in both cellular and stromal regions loadings of the Luminal B subtype.

### 5.4.4 Characterization of Amino Acids and Nucelobases within In Situ Tumors

Along with various subtypes and different receptor status, the different biopsy samples had different tumor designations (e.g. infiltrating and in situ). In particular, malignant cells contained within the ductal basement membrane of the breast can be diagnosed as ductal carcinoma in situ (DCIS). These ducts and the lobules may be filled by malignant cells, which may also undergo central necrosis.[177] The College of American Pathologists released that DCIS is “the earliest possible and most treatable diagnosis of breast cancer” as it is the most common form of non-invasive breast cancer.[178] However, if DCIS goes untreated, it can develop into invasive breast cancer. Therefore, acquiring as much information as possible about DCIS tumors could aid in further understanding invasive breast cancer mechanisms.

Amino acid generation, degradation, and recycling are constantly occurring within the body. These molecules can then be converted into metabolic intermediates that can be used as fuel for tumors and also used in proteins required for cell proliferation.[179, 180] Considering that DCIS tumors have not become invasive, ToF-SIMS provides a unique way in observing the spatial location of amino acids and other nucleobases within or at the boundary of the DCIS tumor. Furthermore, ToF-SIMS is especially suited for lower molecular weight species in the positive polarity which are not constantly discussed within the SIMS community.

Four patches from three separate tissues 4, 7, 8 analyzed by ToF-SIMS had pathologist identified DCIS tumors. These patches were then analyzed using a modified amino acid peak list from Canavan et al.[164] DCIS tumors varied in number and size within each analysis patch. Patient 4 showed the largest DCIS tumor (approximately 0.5 mm × 0.68 mm), which contained a necrotic core at the center of the tumor. This analysis area will be used as an example as the tumor and surrounding tissue is easily

observed. Patient 7 contained two analysis areas with DCIS tumors. One area contained only one DCIS tumor with a necrotic core, but was much smaller (approximately 0.27 mm ✕0.25 mm) when compared to DCIS tumor from Patient 4. The second DCIS analysis area from Patient 7 had multiple DCIS tumors, ranging in size from 0.18 mm ✕ 0.08 mm to 0.58 mm ✕ 0.28 mm, without any necrotic areas and is shown in both Figure 5.13E-H and Supplemental Figure S.5.3. Patient 8 had one analysis patch containing one DCIS tumor (approximately 0.3 mm ✕ 0.28 mm). This tumor did not contain a necrotic core. PCA of the DCIS patches showed similar separation of the DCIS/cellularized areas and stromal regions in both the scores and loadings.

**Figure 5.11.** PCA of ToF-SIMS amino acid image data of a tissue biopsy containing DCIS tumors. **(A)** PC1 positive scores displaying the DCIS tumors and cellular areas. **(B)** PC1 negative scores displaying the connective tissue around and at the interface of the DCIS tumors and cellular areas. **(C)** Loadings plot displaying the amino acids that correspond to the scores images shown in **(A and B)**. All scale bars represent 200 µm.

Using the amino acid peak list, PCA was applied to the DCIS tumor image acquired from Patient 4. The results are shown in Figure 5.11. PC1 scores images show a distinct separation of the tumor and cellular dense areas (Figure 5.11A) and the stromal or connective tissue regions (Figure 5.11B). These images can be correlated with Figure 5.1B and Figure 5.13A, which displays the H&E stained optical image of this region. It can be seen in positive values on the loadings plot (Figure 5.11C) that the

cellular dense areas and the majority of the tumor correlate to alanine (Ala), tyrosine (Tyr), lysine (Lys), valine (Val), glycine (Gly), methionine (Met), and tryptophan (Trp).

The negative scores display the stromal or connective tissue regions (Figure 5.11B) also show the necrotic region located at the center of the tumor. These regions correlate with the negative loadings (Figure 5.11C) showing a range of amino acids.

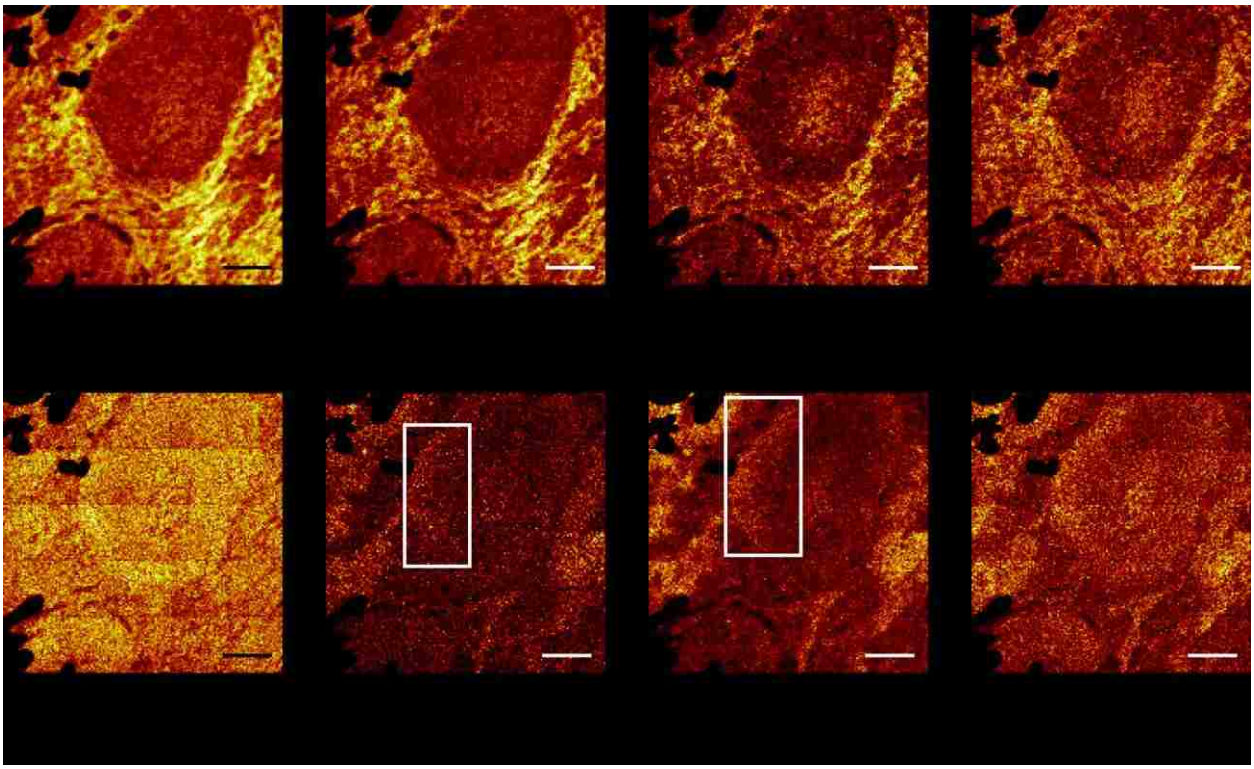

**Figure 5.12.** ToF-SIMS ion images of amino acids and nucleotides from a tissue section containing a DCIS tumor. All scale bars represent 200 µm.

Examining ion images of some of the highest loading peaks is shown in Figure 5.12. It can be seen that key glycine ($CH_4N^+$, *m/z* 30.03) and proline ($C_4H_6N^+$, *m/z* 68.05) fragments are located primarily outside of the tumor, pertaining to the collagen containing stromal tissue. Both arginine ($C_2H_7N_3^+$, *m/z* 73.06) and histidine fragments ($C_5H_8N_3^+$, *m/z* 110.07) are observed to be localized in the same areas as glycine and proline and are also exhibit signal with the necrotic tumor core. It can be observed in the ion image of the methionine fragment ($C_5H_9OS^+$, *m/z* 117.04) that there is an increased signal within the tumor and cellularized areas compared to the stromal region. The spatial distribution of guanine ($C_5H_3N_4O^+$, *m/z* 135.03) exhibits a higher signal in the infiltrating cellular areas outside of the DCIS tumor. It can also be observed in the ion

image of guanine, that there is signal present at the edge of the DCIS tumor indicated by the boxed area. The tyrosine fragment ion ($C_{10}H_{10}NO^+$, *m/z* 136.08) image shows a similar distribution to guanine but with an increased intensity in the cellularized regions outside of the DCIS tumor. Signal can also be seen in the tyrosine ion image along the same edge of the DCIS tumor where guanine was present but extends further than guanine as indicated by the boxed region. An identifying fragment of tryptophan ($C_{10}H_{11}N_2^+$, *m/z* 159.09) also has a similar distribution to that of guanine and tyrosine within the tumor and the cellular regions outside of the tumor, but with a higher intensity. It can also be observed in the tryptophan image that there is intensity within the necrotic tumor core. Interestingly, the ion fragments from guanine, tyrosine, and tryptophan do not appear have a similar intensity within the other DCIS tumor, which is located in the lower left hand corner of all ion images.

The correlation of tryptophan with the cellular areas could be related to an altered metabolism of tryptophan. It has been shown that high-grade breast cancer tumors at an advanced stage overexpress enzymes whose key substrate is tryptophan and could explain the increase of tryptophan in the tumor/cellular areas.[181] The higher signal intensity of methionine within the tumor and cellularized areas is consistent with an altered metabolism and is associated with rapid growth in liver cells.[182, 183] The presence of tyrosine in the cellular regions potentially corresponds to an overexpression of tyrosine kinases at the cell membrane, as they are commonly overexpressed in many human cancers.[184] Signals generated with the phosphorylation of tyrosine by these kinases have been shown to be increased, contributing to tumorigenesis and promoting the Warburg effect.[185] It is expected that the highest loadings associated with the stromal or connective tissue would be glycine and proline, as collagen is a major component of connective tissue and is comprised of proline and glycine. However, the glycine fragment ($C_4H_7N_2O_2^+$, *m/z* 115.05) is contradictory to what is expected as it exhibits a high positive loadings value. It is possible that this mass contains fragments from other molecules, particularly phosphatidylcholine, the most common cellular membrane component. This is most likely the case as all other glycine fragments have negative loadings and are associated with the collagenous regions.

The highest negative loadings show glycine, proline (Pro), arginine (Arg), and arginine/histidine (Arg/His). The high negative loadings for glycine and proline is due to their prevalence in collagen fibers. Collagen is the main structural protein in mammalian connective tissues.[186] The presence of arginine could be linked to multiple sources, such as collagen but is also the precursor for nitric oxide (NO). NO is suggested to be responsible for tumor-induced immunosuppression.[54] The remaining amino acids are likely due to the breakdown and release of intracellular components associated with the necrotic core of the tumor.

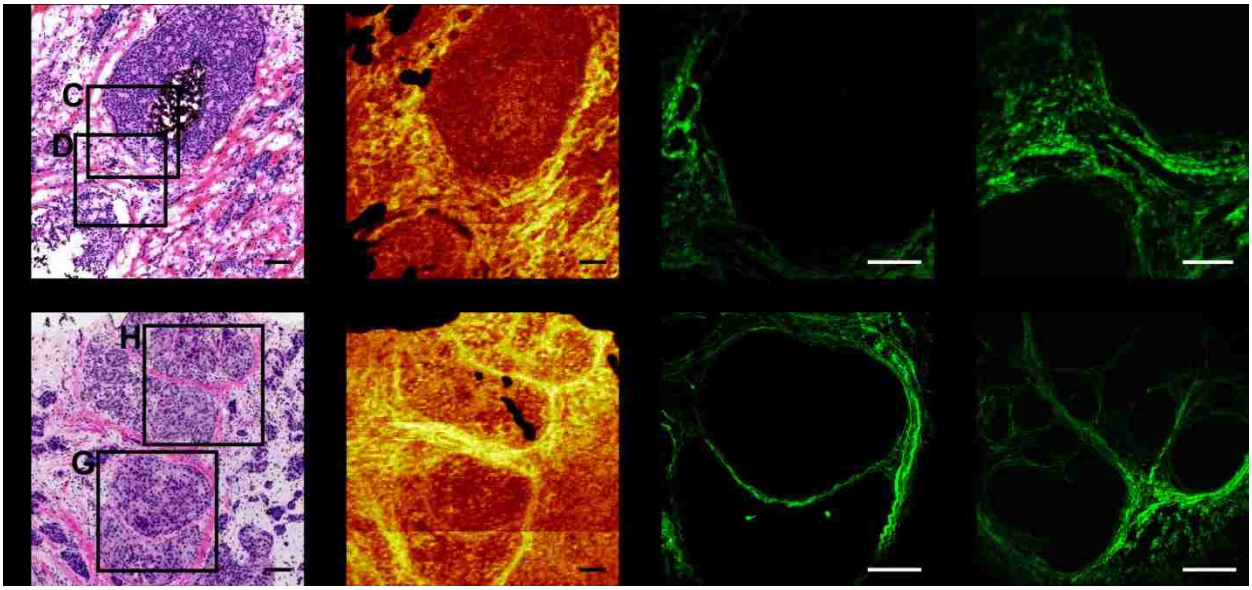


**Figure 5.13.** Images of collagenous regions from tissues containing DCIS tumors using H&E, ToF-SIMS, and SHG. **(A & E)** Shows the adjacent H&E stained region analyzed by ToF-SIMS. DCIS tumors shown are from Patient 4 (A) and Patient 7 (E). Labeled boxes correspond to SHG imaged areas. **(B & F)** Adjacent DCIS containing tissue section analyzed by ToF-SIMS and summed glycine ($CH_4N^+$, *m/z* 30.03) and proline ($C_4H_6N^+$, *m/z* 68.04) fragments corresponding to collagen. **(C,D,G, & H)** show green colored fluorescence images of fibrillary collagen acquired from SHG. All scale bars represent 100 µm.

Further investigation using second harmonic generation (SHG) on adjacent H&E stained tissue sections was used to corroborate that the negative scores and loadings pertained to collagen. These results are shown in Figure 5.13. Briefly, SHG is a powerful non-linear microscopy technique that can image cellular autofluorescence and extracellular matrix structures in intact tissues. SHG has been used a powerful modality for imaging fibrillar collagen in a large range of tissues.[187, 188] SHG images (Figure 5.13C, Figure 5.13D, Figure 5.13G, and Figure 5.13H) can be directly correlated to the collagenous connective tissue structures shown in the H&E stained optical image

(Figure 5.13A and Figure 5.13E, pink regions), and the summed ion images of glycine and proline (Figure 5.13B and Figure 5.13F). This indicates that the ToF-SIMS can be used to interpret the chemical structures that surround tumors and possibly that it can provide similar predictive capability as SHG using key fragments from collagen.

To test whether it was possible to extract spatial locations of nucleobases from DCIS tumors, 23 distinct nucleobases peaks previously identified[165] were added to the amino acid peak list, followed by the application of PCA to ToF-SIMS image data. The results are shown in Figure 5.14. PC1 successfully separated the tumor (Figure 5.14A) from the connective tissue (Figure 5.14B). The scores in Figure 5.14 are similar to the scores images presented in Figure 5.11. This is not surprising as the majority of the same peaks have been used. Examining the loadings plot (Figure 5.14C) shows that almost all nucleobases have positive loadings, which can be correlated to the DCIS tumor and cellularized regions observed by positive scores (Figure 5.14C). This is expected as these are the densest cell areas within the tissue sample. The negative scores shown in Figure 5.14B and negative loadings show the same trend as observed with the amino acid peak list in Figure 5.11. The consistent high negative loadings of glycine and proline are indicative of the collagenous regions outside of the tumor. These results were consistent using the amino acid and nucleotide peak list on the DCIS tumor shown in Figure 5.13E-H and can be found in Supplemental Figure S.5.3.

**Figure 5.14.** PCA of ToF-SIMS amino acid and nucleotide image data of a tissue biopsy containing DCIS tumors. **(A)** PC1 positive scores displaying the DCIS tumors and cellular areas. **(B)** PC1 negative scores displaying the connective tissue around and at the interface of the DCIS tumors and cellular areas. **(C)** Loadings plot displaying the amino acids and nucleotides that correspond to the scores images shown in **(A and B)**. All scale bars represent 200 µm.

## 5.5 CONCLUSIONS

Isolated cellular and stromal regions of breast cancer biopsies (before treatment) were analyzed using imaging ToF-SIMS and PCA. Using the entirety of the sample pool in spectral PCA did not show any discernable trend between samples when related to tumor subtype or patient pCR. By separating the samples into their specific subtype (e.g. TN and Luminal B), spectral PCA demonstrated a trend separating TN pCR and non-pCR patients based on the fatty acids present in specific regions. However, there was more variability in the Luminal B subtype and this subtype did not appear to follow the same trend. This could be due to the variability of the Luminal B subtype and using a more specific peak list may make provide clearer separation between pCR and non-pCR.

PCA of ToF-SIMS image data revealed the separation of DCIS tumors and the stromal tissue surrounding it using only amino acids and nucleobases. SHG investigations agree that ToF-SIMS and imaging PCA can distinctly identify the structure of the stromal tissue based on its chemical information. This shows that there is an opportunity supplement the isolated cellular and stromal regions chemical data

with ToF-SIMS ability to recognize specific structures, such as collagen, which has been previously used to predict breast cancer patient data.[186]

## 5.6 ACKNOWLEDGEMENTS

We would like to thank Kelly Wirtala at FHCRC for expert sectioning of tissue samples and helping with the development of sample preparation protocols. We would like to thank Michael Robinson for scientific discussions and ToF-SIMS data acquisition. We would also like to thank Patrik Johansson for SHG data acquisition. We would also like to acknowledge our funding sources: NESACBIO NIH P41 EB002027, SPORE NIH P50 CA138293, and NSF-GRFP DGE-0718124/1256082.

## 5.7 SUPPORTING INFORMATION

## CHEMICAL ANALYSIS OF CELLULAR AND STROMAL REGIONS FROM HUMAN BREAST CANCER TISSUES USING IMAGING TIME-OF-FLIGHT SECONDARY ION MASS SPECTROMETRY

Blake M. Bluestein[a], Fionnuala Morrish[b], Daniel J. Graham[a], Jamie Guenthoer[b], David Hockenbery[b], Peggy Porter[b], and Lara J. Gamble[a,§]

[a] University of Washington, Dept. of Bioengineering, MolES Building, Box 351653, Seattle, WA 98195-1653

[b] Fred Hutchinson Cancer Research Center, Seattle, WA 98109

[§] Corresponding Author

Lara Gamble

University of Washington

Department of Bioengineering

Box 351653

Seattle, WA 98195

1-206-543-8094 (phone)

1-206-543-3778 (fax)

lgamble@uw.edu (e-mail)

**Supplemental Figure S.5.1.** PC2 loadings plot displaying the chemical species that correspond to the of TN stromal scores in Figure 5.7 including the normal stromal tissue biopsy (Patient 23).

**Supplemental Figure S.5.2.** PC2 loadings plot displaying the chemical species that correspond to the of Luminal B stromal scores in Figure 5.10 including the normal stromal tissue biopsy (Patient 23).

**Supplemental Figure S.5.3. (A)** PC1 positive scores displaying the DCIS tumors and cellular areas from Patient 7. **(B)** PC1 negative scores displaying the connective tissue around and at the interface of the DCIS tumors and cellular areas. **(C)** Loadings plot displaying the amino acids that correspond to the scores images shown in (A & B). All scale bars represent 200 µm.

**Supplemental Table S.5.2.** Key ions and fragment identification for peaks observed in PCA loadings plots.

| Mass (m/z) | Composition | Possible Biomolecule | Mass (m/z) | Composition | Full Amino Acid Name | Abbreviation |
|---|---|---|---|---|---|---|

# Chapter 6. Analysis of the Tumor Microenvironment Using Imaging Time-of-Flight Secondary Ion Mass Spectrometry

Blake M. Bluestein[a], Fionnuala Morrish[b], Daniel J. Graham[a], Li Huang[b], David Hockenbery[b], Lara J. Gamble[a,§]

[a] University of Washington, Dept. of Bioengineering, MolES Building, Box 351653, Seattle, WA 98195-1653

[b] Fred Hutchinson Cancer Research Center, Seattle, WA 98109

[§] Corresponding Author

Lara Gamble

University of Washington

Department of Bioengineering

Box 351653

Seattle, WA 98195

1-206-543-8094 (phone)

1-206-543-3778 (fax)

lgamble@uw.edu (e-mail)

## 6.1 ABSTRACT

Solid tumors are a structurally complex system, composed of many different cell types. The tumor microenvironment includes non-malignant cell types that participate in complex interactions with tumor cells. The cross-talk between tumor and normal cells is implicated in regulating cell growth, metastatic potential, and chemotherapeutic drug resistance. A new approach is required to interrogate and quantitatively characterize cell to cell interactions in this complex environment.

Here, we have applied time-of-flight secondary ion mass spectrometry (ToF-SIMS) to generate a high resolution *in situ* molecular analysis of Myc-induced pancreatic β cell islet tumors. The high mass resolution and micron spatial resolution of ToF-SIMS allows detection of metabolic intermediates such as lipids and amino acids. Employing multivariate analysis, specifically principal components analysis (PCA), we show that it is possible to chemically distinguish cancerous islets from normal tissue, in addition to intratumor heterogeneity. These heterogeneities can then be imaged and investigated using another modality such as second harmonic generation (SHG) microscopy.

Using these techniques with a specialized mouse model, we found significant metabolic changes occurring within β cell tumors and the surrounding tissues. Specific alterations within the lipid, amino acid, and nucleotide metabolism were observed, demonstrating that ToF-SIMS can be utilized to identify large-scale changes that occur in generated in the tumor microenvironment and could thereby increase our understanding of tumor progression and the tumor microenvironment.

## 6.2 INTRODUCTION

Solid tumors are a structurally complex system consisting of tumor cells, infiltrating immune cells and non-malignant stromal cells. The physical and chemical interactions between malignant cells and non-transformed cells create the tumor microenvironment. This environment has been implicated in the regulation of cell growth, determining metastatic potential, and impacting the outcome of chemotherapy.[189, 190] Tumor growth depends on the conversion of nutrients into biochemical and biosynthetic precursors especially within lipid pathways, as lipids are used for cell membrane formation, signaling, and energy. However, these metabolic requirements are impacted by the tumor microenvironment, which determines the availability of nutrients such as glucose and glutamine, and oxygen supplied to the tumor.[191]

The use of an inducible *c-Myc* oncogene in a well-established model of pancreatic β cell tumorogenesis provides a controlled system in which to observe β cell tumorigenesis and investigate the role of the tumor microenvironment in tumor growth[192]. Myc, a transcription factor, is one of the most frequently deregulated oncogenes in human cancers.[193] Deregulation of Myc is responsible for many of the metabolic changes that induce malignancy. Myc deregulation alters glucose, glutamine, and lipid metabolism and significantly modifies mitochondrial function.[194-199] While it is known that Myc is frequently deregulated in many cancers, it is unknown how Myc-activated tumor metabolism is impacted by an adjacent cellular environment that has the potential to either assist or restrict the tumor growth. Many biochemical processes that contribute to tumor initiation and growth could be affected by the synthesis or degradation of specific metabolites ranging from nucleotides, lipids, to amino acids within the tumor microenvironment. Chemical imaging of Myc pancreatic tissues with micron resolution would permit the assessment of endogenous cellular metabolic products within specific β cell tumor regions and surrounding tissue (made up of acinar cells). Harnessing the capabilities of high resolution chemical imaging allows for the development of methods to evaluate how these distinct tissue regions affect each other's metabolism, further aiding our understanding the tumor microenvironment.

Metabolic analyses require sensitivity, specificity, selectively and speed, which are strengths of utilizing mass spectrometry imaging (MSI) as an optimal technique to detect and identify biologically relevant metabolites.[17, 27, 30, 49, 81] Imaging time-of-flight secondary ion mass spectrometry (ToF-SIMS) provides detailed spatial (5–20 μm) and chemical information providing a new perspective to biological tissue analysis that has not been available using techniques commonly used for clinically relevant samples, such as high-performance liquid chromatography (HPLC), fluorescent microscopy, and immunohistochemistry.[11, 33] Recent chemical imaging research using a Myc-driven mouse model of renal cell carcinoma demonstrated that glutamine derived lipids and metabolites drive tumor progression.[200] Further chemical imaging research using a Myc model of lung adenocarcinoma also showed that tumors have distinct lipid signatures compared with normal tissue.[201] These studies were conducted using entire cancerous kidney or lung sections, but individual Myc-induced pancreatic islet tumors have yet to be explored in this manner. In this work, we provide evidence of significant metabolic changes occurring within Myc driven β cell tumors and the surrounding tissue by combining sophisticated animal models with imaging ToF-SIMS. We also demonstrate the application of ToF-SIMS and second harmonic generation (SHG) microscopy to address heterogeneity within tumors and the microenvironment to determine the presence of blood vessels.

## 6.3 Materials and Methods

### 6.3.1 Mouse Tissue Samples and Preparation

The *pIns-c-mycER$^{TAM}$/p53$^{-/-}$* Myc-inducible mouse model was used to generate pancreatic β cell tumors.[202] In this model the *c-Myc* gene (hereafter referred to as Myc), is regulated by an insulin promoter and generates a chimeric mutant estrogen receptor fused to the C-terminus of the Myc protein.[203] The presence of this fusion allows for -Myc induction using tamoxifen injection, and the insulin promoter provides tissue specific expression in pancreatic β-cells.[192, 202] On induction of Myc , hyperplasia and vascularization of β-cell islets was evident by 6 days. After 6 days of Myc activation, pancreatic tissues were harvested and frozen in optimal cutting temperature (OCT)

compound. Control pancreas samples were harvested from $p53^{-/-}$ mice, which had also been injected with tamoxifen for 6 days.[202] 4-µm thick cryosections were used for hematoxylin and eosin (H&E) staining or for ToF-SIMS analysis. Since the cryosection analyzed by ToF-SIMS is mounted directly onto a silicon wafer, H&E images of the tissue sections provide a reference to guide identification and selection of neoplastic islets within the tissue.

### 6.3.2 MASS SPECTROMETRY IMAGING

All ToF-SIMS experiments were performed with an ION-TOF TOF.SIMS 5-100 instrument (ION-TOF GmbH, Münster, Germany) equipped with a liquid metal ion gun (LMIG) for analysis and an electron flood gun for charge neutralization. The LMIG was used to generate a pulsed 25 keV $Bi_3^+$ beam impacting the target at an angle of 45°. The $Bi_3^+$ beam was set in spectroscopy mode for high mass resolution to acquire spectra and images in both polarities. The $Bi_3^+$ current was typically 0.13–0.15 pA. Target currents were measured before each data set using a Faraday cup. Large optical stitches of all tissues were produced by manually stitching images from the video camera within the ToF-SIMS before analysis. Optical stitch images were then aligned to H&E images using the tissue borders to aid in selecting areas where analysis patches were to be acquired. For all data collection, HMR positive ion data was acquired followed immediately by HMR negative ion data on the same area. X and Y sample stage coordinates were saved in the software to ensure data acquired was from the same region in both polarities. Mass resolution (m/Δm) for the $C_2H_3^+$ ion was greater than 4500. Positive ion spectra were calibrated to $CH_3^+$, $C_2H_3^+$, and $C_4H_5^+$. Negative ion spectra were calibrated to $CH^-$, $OH^-$, and $C_2H^-$.Spectra were acquired from 1 mm x 1 mm “patches” comprising of 25 or 24 200 µm x 200 µm “tiles” on each tissue. Each tile contains 256 x 256 pixels, giving the patches a total pixel count of 1280 x 1280 and a pixel size of 781 nm x 781 nm. The purpose of analyzing smaller areas is to capture the localized areas of the islet tumors and to image the entire sample, which can undergo sample degradation or lipid migration over time.[9] The $Bi_3^+$ dose was limited to $\leq 5.0\times10^{11}$ ions/$cm^2$ for each tile in both positive and negative ion modes, resulting in a total $Bi_3^+$ dose $\leq 1.0\times 10^{12}$ ions/$cm^2$ per tile so the static limit would not be surpassed. SurfaceLab

6 software (ION-TOF GmbH, Münster, Germany) was used for all analyses. A total of three Myc and four control tissue sections were analyzed with each tissue having a minimum of three selected patches.

### 6.3.3 SECOND HARMONIC GENERATION (SHG)

The multiphoton excitation fluorescence (MPEF) and SHG images were acquired with a scanning confocal multiphoton microscope (Olympus, FV1000 MPE BX61) with a 20x objective. The light source was a tunable laser (Spectra-Physics Mai Tai) with $\lambda_{exc}$ at 910 nm and with bandpass filters at 495–540 nm for the MPEF channel and 420–460 nm for the SHG channel. The detectors were photon multipliers, located so that the SHG captures in back-scattering mode and the MPEF in epifluorescence mode. All SHG experiments were performed on H&E stained slides.

### 6.3.4 DATA ANALYSIS

Principal component analysis (PCA) was applied to ToF-SIMS images and spectra data acquired from the tissues. PCA is applied to ToF-SIMS images to determine the largest sources of chemical variance within the ToF-SIMS image. The scores images correspond to the loadings, which provide the distinct molecular species responsible for the variance within the scores images, thus providing a method to spatially identify correlated masses/molecules for further investigation.

Regions of exposed silicon substrate and OCT (e.g. holes or tears from cutting tissue and embedding medium surrounding the tissue section) were excluded from all analyses by applying a threshold to the pixels with a $Si^+$ signal, where *m/z* 27.9 was used to detect silicon and *m/z* 332.2 ($C_{14}H_{29}^+$, a fragment of the benzalkonium additive in OCT)[13] is used to detect OCT areas. PCA was performed using the NBToolbox ImageGUI (Daniel Graham, NESAC/BIO, University of Washington), that operate within MATLAB (MathWorks, Natick, MA). Peaks were chosen that had a maximum intensity two times or more than that of the average background intensity. The spectra from all tissues were overlaid and then peaks were manually selected and integrated to full width half max. A total peak list of 1017 and 1349 peaks were chosen from the positive and negative ion modes, respectively. Normalization was not applied to imported image

patches; image data were preprocessed by Poisson scaling and mean centering before PCA.

A comparison of relative intensities was achieved by first selecting regions of interest (ROIs) of either islets or acinar tissue without vascularized areas and normalizing ions to the total ion counts. This resulted in a total of 23 Myc and 12 control islets. The acinar ROIs resulted in 9 regions for Myc and 10 for the control. Normalized ion counts from these ROIs were then compared using Welch's unpaired t-tests with P-value < 0.05 chosen as statistically significant.

## 6.4 RESULTS

The objective of this work was to use ToF-SIMS to map and identify molecules associated with the metabolic changes induced by Myc overexpression in pancreatic β cells tumors and the adjacent cellular environment, in the *pIns-MycER$^{TAM}$;p53$^{-/-}$* mouse model with Myc-inducible pancreatic β cell tumorigenesis. In this model, the induction of Myc promotes rapid tumorigenesis, with tumors occupying the majority of the pancreas within 12 days, for this reason we chose to study the 6 day stage where there is evident hyperplasia and a distinct exocrine tissue available for analysis. Imaging ToF-SIMS and PCA were used to identify, map, and compare chemical differences within Myc-induced islet tumors and surrounding acinar cells t after 6 days of Myc activation with tamoxifen in the *pIns-MycER$^{TAM}$;p53$^{-/-}$* mouse model (referred to hereafter as Myc tissues) and pancreatic islets from p53$^{-/-}$ mice, also treated with tamoxifen, were used as controls (hereafter referred to as control tissue).

### 6.4.1 DISTINGUISHING TUMOR ISLETS FROM THE ACINAR TISSUE USING IMAGING PCA

Determining the spatial distribution of distinct lipids and metabolic intermediates within Myc induced β cell tumors and the acinar tissue surrounding these tumors can identify metabolic abnormalities related to Myc-induced cellular proliferation and signaling. This information may also provide insight into the metabolic cross-talk occurring between these two environments.

PCA of ToF-SIMS image data resulted in a separation between the Myc-induced tumor and acinar tissue in both polarities in PC1, demonstrating that the largest amount

of chemical variance was between these regions. Figure 6.1 shows positive polarity PCA data, which exhibits separation of tumor from the surrounding acinar tissue within the first principal component scores images for the Myc tissue. The PC1 scores and loadings reveal the major differences in chemistries between the tumor (Figure 6.1a) and acinar tissue (Figure 6.1b). PC1 positive loadings relating to the tumor are dominated by the salt or salt containing peaks, such as the potassium isotope at *m/z* 40.96 ($^{41}K^+$), $CNKNa^+$ (*m/z* 87.96), and $CNK_2^+$ (*m/z* 103.93). Molecular peaks of metabolic interest also found in the positive loadings were $Fe^+$ (*m/z* 55.94), histidine fragments ($C_5H_8N_3^+$, *m/z* 110.07), phenylalanine fragments ($C_8H_{10}N^+$, *m/z* 120.08), phosphatidylcholine fragments $C_6H_{17}NPO_4^+$, $C_5H_{14}NPO_4Na^+$, and $C_5H_{14}NPO_4K^+$ (*m/z* 198.10, 206.06, 222.03), and heme fragments ($C_{29}H_{21}FeN_4^+$, $C_{29}H_{23}FeN_4^+$, $C_{30}H_{25}FeN_4^+$, $C_{34}H_{32}FeN_4O_4^+$, *m/z* 481.05, 483.08, 497.10, 616.18) [204, 205] (Figure 6.1a). PC1 negative loadings indicated that the acinar tissue surrounding the tumor correlated with $Mg^+$ (*m/z* 23.98), small hydrocarbon fragments ($C_3H_5^+$, $C_4H_6^+$, $C_5H_7^+$, *m/z* 41.04, 54.05, 67.05), and choline ($C_5H_{14}NO^+$, *m/z* 104.11) (Figure 6.1b).

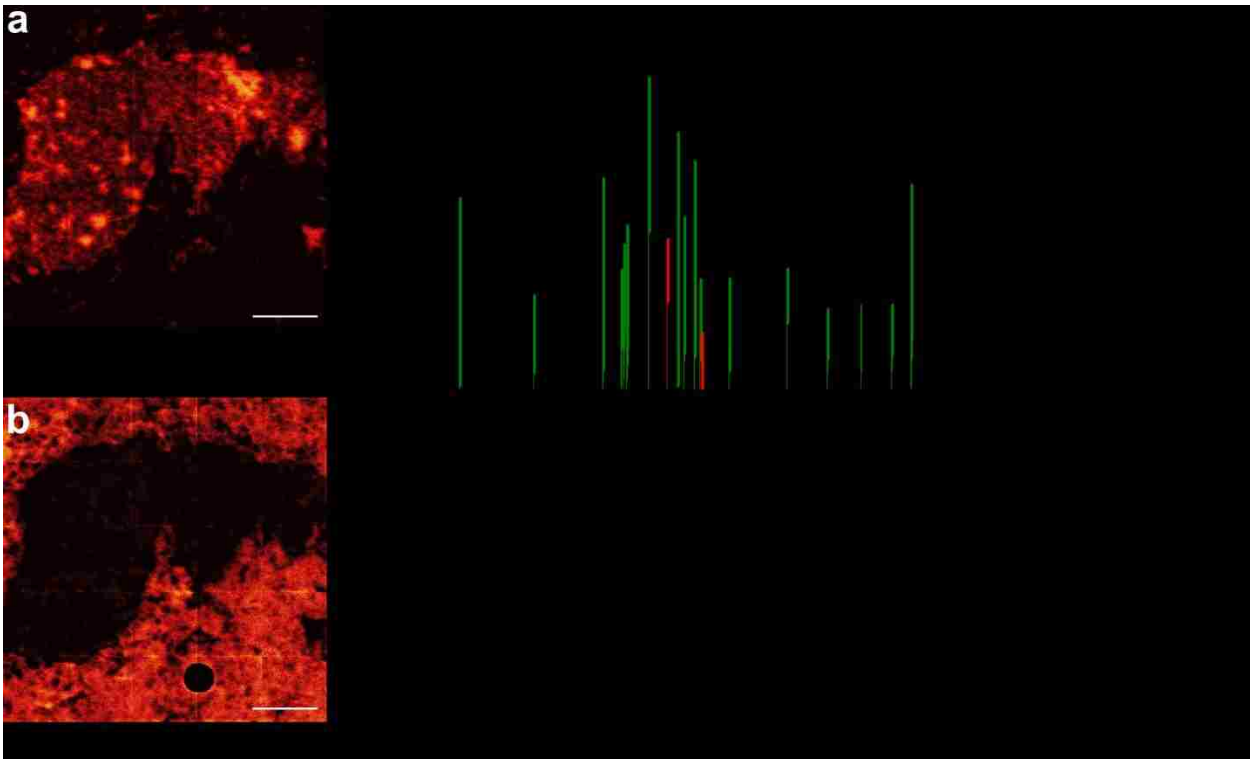


**Figure 6.1.** Positive polarity PCA of ToF-SIMS image of Myc tissue region after removal of substrate/embedding medium signal. **(a)** PC1 positive scores image displaying the Myc islet tumor. (b) PC1 negative scores image displaying the acinar tissues. **(c)** PC1 loadings plot displaying the chemical species that correspond to scores images. Key potassiated masses are colored green, histidine and phenylalanine colored red, masses corresponding to heme fragments is labeled. Scale bar is 200 µm.

Recent work using matrix assisted laser desorption mass spectrometry imaging (MALDI-MSI) to investigated how Myc overexpression affects lipid metabolism in lung cancer observed an increased $K^+$ associated with tumors and a higher proportion of potassiated lipids in tumor regions.[201] Calcium and ATP-sensitive K+ ion channels at the cell surface membrane of pancreatic β cells control insulin secretion. In healthy β cells, the potassium ion channels are normally open allowing potassium to diffuse out of the cell, but when the metabolism of glucose produces ATP, the ATP-sensitive potassium ion channels close.[206] Deregulation of this channel as well as an increased extracellular $K^+$ associated with the tumor may account for the $K^+$ adducts observed in loadings that correlate to the tumor.

In contrast to the Myc pancreatic tissue, where differences between islet and acinar tissue were evident in the first PC scores, there was no evident difference for this first PC in the PCA scores of image data in controls. Instead, the control islet was typically observed in PC2 to PC3 scores and associated with collagenous and

vasculature structures. This indicates that the chemical variance between the islet and the acinar tissue was much lower than what is exhibited in the Myc tissue.

Individual ToF-SIMS images of key fragments for both Myc and control are illustrated in Figure 6.2. $Fe^+$, histidine and heme fragments were all observed in localized spots within the tumor (Figure 6.2d-f). The presence of these ions is indicative of blood or vasculature present within the tumor, as histidine is known to be found on hemoglobin and *pIns-c-mycER$^{TAM}$/p53$^{-/-}$* islet tumors[202] produce highly hemorrhagic vasculature[192]. Unlike the Myc islet tumors, the control islets did not exhibit increased signals of $Fe^+$, histidine, phenylalanine, or heme fragments within the islet (Figure 6.2j-l). However, the acinar tissue of the control islet correlated with $Mg^+$ as was observed in the Myc tissue, and this is illustrated in Figure 6.2b & h.

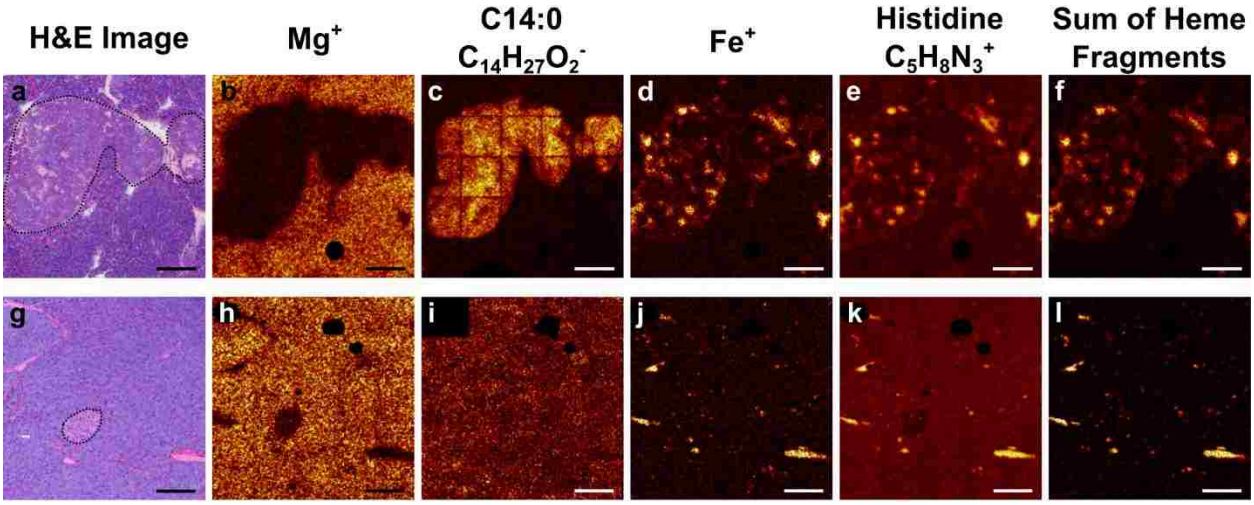


**Figure 6.2.** ToF-SIMS images of metabolites observed in PCA across mouse pancreatic tissue sections. Top (letters **a-f**), show Myc tissues; bottom (letters **g-l**) show control pancreatic tissues. Observed masses $Mg^+$ (*m/z* 23.98), C14:0, $C_{14}H_{27}O_2^-$ (*m/z* 227.20), $Fe^+$ (m/z 55.93), histidine, $C_5H_8N_3^+$ (*m/z* 110.07), sum of heme fragments $C_{29}H_{21}FeN_4^+$, $C_{29}H_{23}FeN_4^+$, $C_{30}H_{25}FeN_4^+$, $C_{34}H_{32}FeN_4O_4^+$ (*m/z* 481.05, 483.08, 497.10, 616.18). Signal from substrate and embedding medium were removed from images and can be seen as areas that are black and show no signal. Scale bar is 200 µm.

PCA of ToF-SIMS negative polarity image data also distinctly separated the Myc islet tumor from the remaining acinar tissue within the first PC (Supplemental Figure S.6.3). The positive loadings associated with the tumor are dominated by ions $CN^-$ and $CNO^-$, $Cl^-$, and C14:0 (*m/z* 26.00, 42.00, 34.96, and $C_{14}H_{27}O_2^-$, *m/z* 227.20), but higher mass lipid fragments, such as vitamin E ($C_{29}H_{49}O_2^-$, *m/z* 429.38) and fragments of sphingomyelin (SM) (34:1) ($C_{36}H_{69}NO_6P^-$, $C_{38}H_{76}N_2O_6P^-$, *m/z* 642.51, 687.56) are also observed. The presence of myristic acid (C14:0, *m/z* 227.20) localized within the tumor,

not previously documented in Myc-induced tumor lipid imaging work to date, shows a clear alteration in the lipid metabolism of Myc β cell tumors that is restricted to the tumor and does not arise in the surrounding acinar tissue. SM has been shown as a marker for the surface of β cells, but is also an indicator of the functionality of the cells. Previous investigations observed that there is a correlation between insulin secretory capacity and the presence of SM in islets, where a higher level of SM correlates with a higher expression of insulin.[207] SM (34:1) and its fragments were also localized within the control islets (Supplemental Figure S.6.2).

In Myc tissues the PC1 negative scores in the negative polarity were indicative of the acinar tissue around the tumor. The majority of the negative loadings in PC1 that are correlated with acinar tissue are consistent with salt adducts as indicated by masses ending with 0.8 to 0.9. However, linoleic acid (C18:2, $C_{18}H_{31}O_2^-$, *m/z* 279.23) and a phosphoinositol fragment ($C_9H_{16}PO_9^-$, *m/z* 299.06) also had distinguishable negative loadings values. The presence of linoleic acid outside of the islets can be explained by previous investigations showing stimulatory effects on insulin secretion from β cells.[208] The presence of linoleic acid was also observed in the tissue surrounding the control islets (Supplemental Figure S.6.2) and thus this is not a distinguishing feature of acinar tissue adjacent to Myc-induced β cell tumors.

Similarly to positive polarity PCA results, PCA of the negative polarity image data could not separate the control islets from the surrounding acinar tissue. Overall, the most distinct difference between Myc-induced islet tumors and control islet in the negative data was the absence of C14:0 within the control islet (Figure 6.2c & i). Key ToF-SIMS images of masses observed in PCA can be seen in Supplemental Figure S.6.1 and Supplemental Figure S.6.2.

### 6.4.2 TUMOR HETEROGENEITY

Tumor heterogeneity is known to affect multiple properties such as responses to therapy, proliferation, and invasion.[209] Therefore, using ToF-SIMS to spatially characterize molecular intratumor heterogeneities may lead to the deconvolution of metabolic mechanisms occurring during tumor progression. The PCA scores image shown in Figure 6.1a and ToF-SIMS images in Figure 6.2d-f, indicate areas of

intratumor heterogeneity within the tumor. Using a method we previously developed and applied to breast tissue,[210] we separate out the tumor islet region by applying PCA to the PC1 scores image shown in Figure 6.1a. Utilizing this method provides a direct characterization of the chemical variation occurring spatially within the tumor observed in both Figure 6.1 and Figure 6.2. These results are shown in Figure 6.3 for the positive polarity and in Supplemental Figure S.6.4 for the negative polarity.

The positive polarity results separated the high intensity regions within the tumor in PC1 positive scores as shown in Figure 6.3a. The positive loadings (Figure 6.3c) associated with the high intensity regions showed loadings of $Fe^+$, histidine fragments ($C_4H_6N_2^+$, $C_5H_8N_3^+$, $C_6H_5N_2O^+$, *m/z* $82.05^+$, $110.07^+$, $121.04^+$) and heme fragments.[204, 205] These fragments observed by PCA of these regions of interest (ROIs) further provided chemical identification of these spatial locations and identified fragments that may potentially be related to vasculature and providing interior tumor characterization. As described above, masses that are associated with blood were present within the tumor, which may be providing visualization of early angiogenesis or blood vessel leakiness occurring within and around the tumor. Both angiogenesis and blood vessel leakiness occur frequently in tumors and provide both nutrients and oxygen that facilitate rapid tumor growth.[211, 212]

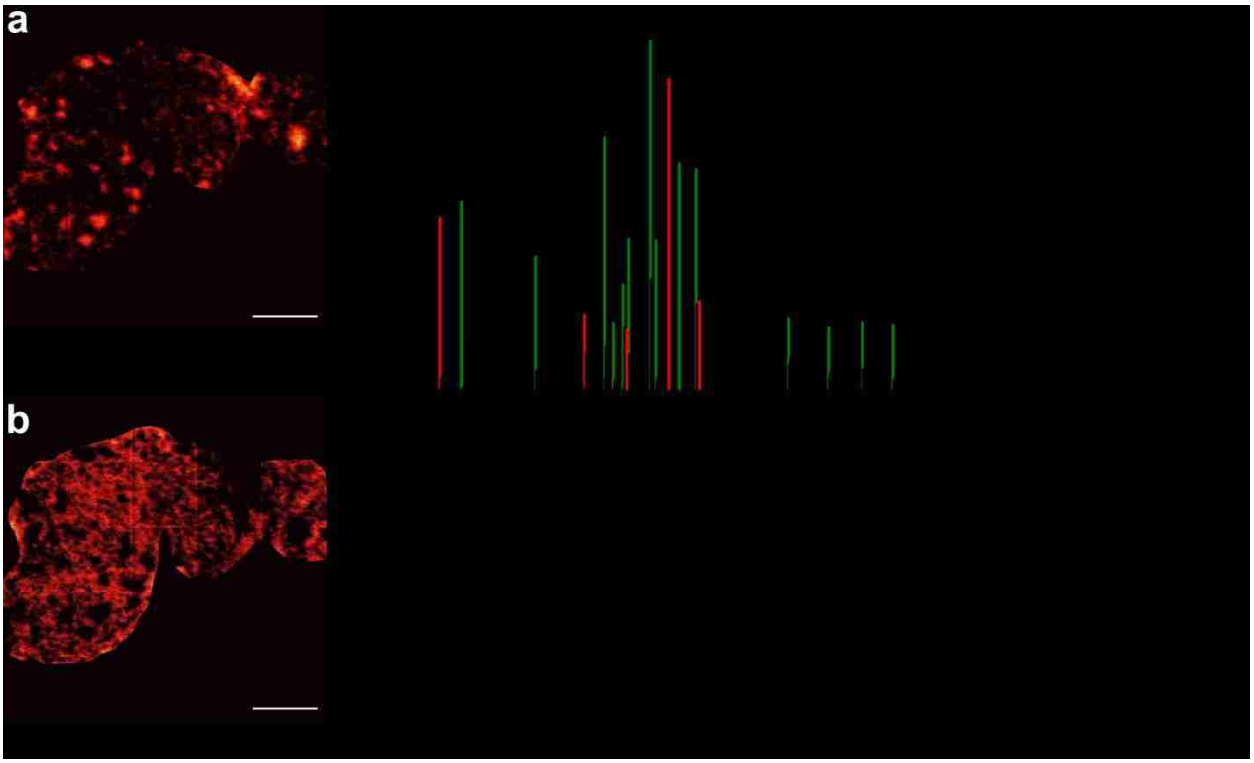


**Figure 6.3.** Positive polarity PCA of ToF-SIMS image of the Myc islet tumor ROI. **(a)** PC1 positive scores image displaying the high intensity regions within the Myc islet tumor. **(b)** PC1 negative scores image displaying the tumor interior. **(c)** PC1 loadings plot displaying the chemical species that correspond to scores images. Key potassiated masses are colored green, histidine fragments are colored red, and masses corresponding to heme fragments is labeled. Scale bar is 200 µm.

The PC1 negative scores seen in Figure 6.3b displayed the interior of the tumor and the corresponding negative loadings exhibited short chain hydrocarbon fragments, with most fragments associated with phosphatidylcholine, known to be the main lipid component within the cellular membrane. These chemical species are to be expected in the remaining areas of the tumor as these lipids make up the cellular components and membrane of the cells present in the islet.

The negative polarity PCA results also displayed separation of the high intensity regions from the remainder of the tumor in PC1 (Supplemental Figure S.6.4a). The positive scores displayed the tumor interior and the positive loadings exhibited fatty acids (C14:0, C16:0, $C_{16}H_{31}O_2^-$, C18:1, $C_{18}H_{33}O_2^-$, and C18:0, $C_{18}H_{35}O_2^-$, *m/z* 227.20, 255.23, 281.25, 283.26 respectively). All the fatty acids present within the islet tumor, besides C14:0, have been shown to be fragments of larger lipids in viable tumors and tumor tissues.[27, 201, 213]

The negative polarity PC1 negative scores, which correlate to the high intensity areas, displayed high loadings of $CN^-$ and $CNO^-$. These molecular fragments are typically indicative of proteins or amino acids. These data agree with what was observed in the positive polarity, as the heme and histidine fragments both contain $CN^-$ and $CNO^-$.

### 6.4.3 Second Harmonic Generation Microscopy of Tumors and Blood Vessels

Using second harmonic generation (SHG) we sought to determine if there was any ordered structure similar to vasculature at these high intensity regions observed with ToF-SIMS within tumor areas. SHG is restricted to molecules with a non-centrosymmetric organization and provides for detailed optical images of fibrillary collagen and has been shown to image mixtures of collagens I and III around blood vessels.[115] Figure 6.4 shows images of a Myc tissue area that has both a tumor with the high intensity regions and a blood vessel next to a tumor. The molecular signals associated with both what appear to be blood and vasculature are shown in the ToF-SIMS images (Figure 6.4b-d) and are localized in the same areas as seen in the H&E image (Figure 6.4a). The chemistry of the blood vessel region at a higher magnification with a ToF-SIMS overlay image is shown in Figure 6.4f, where $Fe^+$, histidine and heme fragments in green exhibit signal from the blood vessel, while phosphocholine shown in red represents the islet tumor boundary, and $Mg^+$ in blue shows the acinar tissue outside the tumor. The blood vessel from Figure 6.4a & e imaged by SHG can be seen in Figure 6.4g. The structure of collagen within the blood vessel can be observed in the SHG image represented by a falsely colored green. Merging the SHG fluorescence (green) with autofluorescence (red) from the tissue (Figure 6.4h) provides contrast, showing red in the cellular regions and the yellow overlay where the blood vessel structure is located. The suspected blood or vasculature areas can easily be observed in the H&E image of the Myc islet tumor in Figure 6.4i. Comparing these areas from Figure 6.4i to the ToF-SIMS overlay image of an adjacent section (Figure 6.4j), it can be seen that $Fe^+$, histidine and heme fragments (green) show similar localizations. It is evident by the SHG image in Figure 6.4k that there is no collagen present that would suggest blood vessel structure within the tumor islet, the small circular areas of

fluorescence are tissue debris trapped within the H&E mounting medium resulting in the scattering of photons. This combination of techniques provides evidence that these high signal regions are not vasculature.

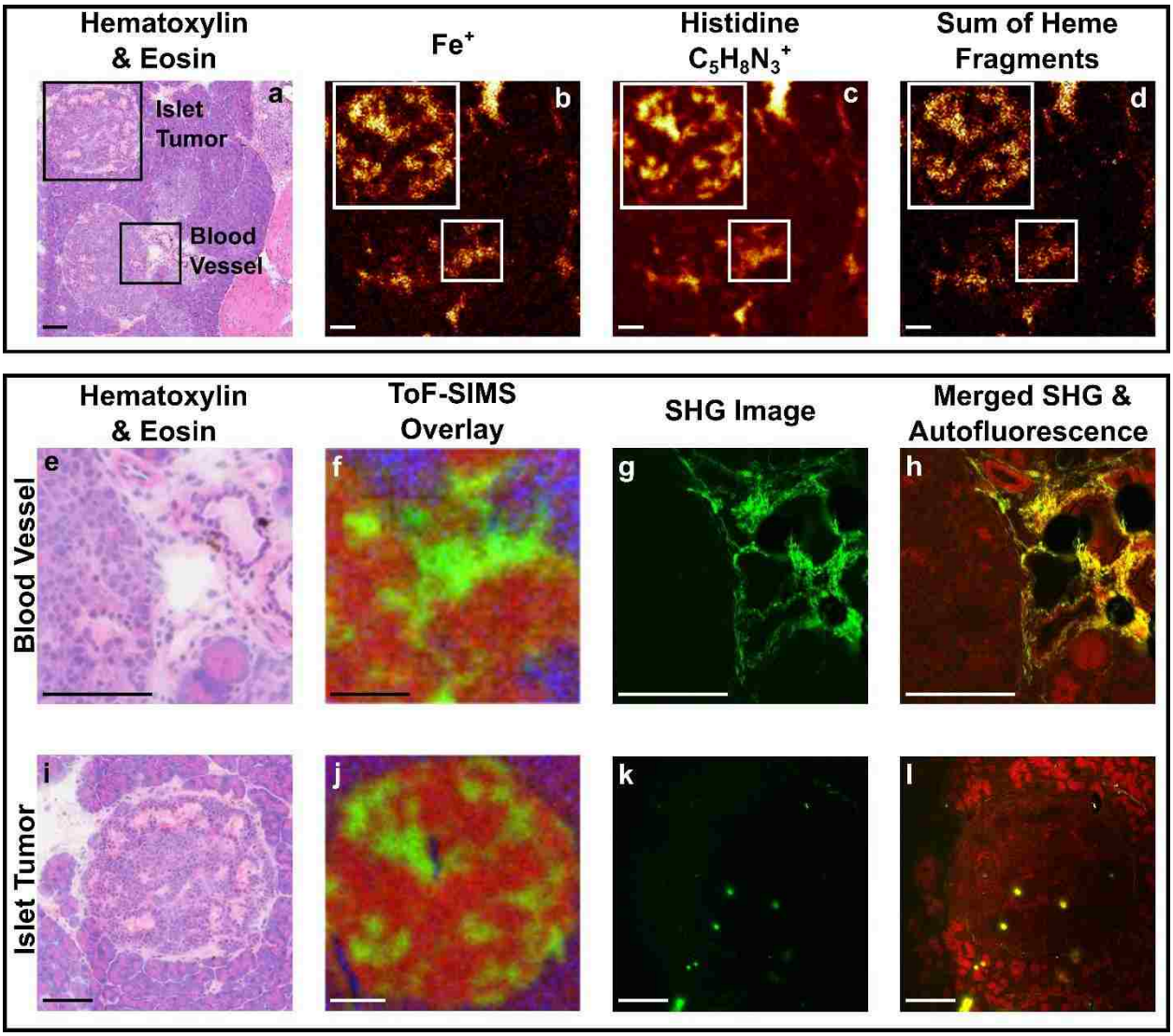


**Figure 6.4.** Images of vasculature and blood lakes using a combination of H&E, ToF-SIMS, and SHG. Top row; **(a)** shows the adjacent H&E Myc tissue section region containing both a tumor with blood lakes and blood vessels, **(b-d)** show the adjacent tissue section analyzed by ToF-SIMS and corresponding fragments related to blood lakes and vasculature. Heme fragments used for summed ToF-SIMS image shown in **(d)** $C_{29}H_{21}FeN_4^+$, $C_{29}H_{23}FeN_4^+$, $C_{30}H_{25}FeN_4^+$, $C_{34}H_{32}FeN_4O_4^+$ (*m/z* 481.05, 483.08, 497.10, 616.18). Middle row; letters **(e-h)** show the blood vessel region magnified. Bottom row; (letters **i-l**) show the islet tumor region magnified. **(i,j)** show a ToF-SIMS RGB overlay of red denoting the tumor (phosphocholine fragment, $C_5H_{14}NPO_4Na^+$, *m/z* 206.06) green denoting blood lakes or vasculature (sum of $Fe^+$, histidine and heme fragments listed above), and blue denoting surrounding tissue ($Mg^+$, *m/z* 23.98). **(g,k)** show green colored fluorescence images acquired from SHG, where **(g)** shows the structure of the collagen lining the blood vessel and (k) shows scattering from debris but no SHG signal within the tumor. **(h,j)** show the merged SHG and autofluorescence acquired using SHG, where the red represents autofluorescence occurring from the surrounding H&E stained cells. Scale bar is 100 µm.

These data are consistent with previous results which showed that erythrocytes remained present in pancreatic islet tumors after the vascular system was emptied and perfused with fixative solution due to defective blood vessel linings.[212] Some of these remaining red blood cells would form discrete blood lakes, but further examination of the blood lakes showed no evidence in being directly connected to the blood stream and were lined with tumor cells. Further H&E and SHG images of blood lakes can be observed in Supplemental Figure S.6.5.

### 6.4.4 Molecular Differences Between Myc Tumor and Control Pancreatic Tissue

To accurately associate changes occurring between the tumor microenvironment present in the Myc tissues, vasculature was removed from the dataset and all peaks within the whole mass range were used for a complete comparison against the control tissues. The tissues were separated into two regions of interest (ROIs), the islets and the surrounding acinar tissue, and the peak intensities in the spectra for each region were compared between the Myc and control pancreatic sections. Using Welch's *t* test all peaks were tested and compared and it was found that there were significant changes to the amino acid, nucleotides, and lipid content between the tissues. Table 6.1,Table 6.2, and Table 6.3 show the percentage change of biomolecules present in Myc and control islets and surrounding acinar tissue in both positive and negative polarities.

Amino acids and carnitines were found to have an increased normalized intensity while monoacylglycerides (MAGs) and diacylglycerides (DAGs) decreased within the Myc islets compared with the control. The largest changes were observed in the histidine fragment $C_5H_8N_3^+$ (*m/z* 110.07) with a 2-fold increase in intensity, heme fragments with an approximately 2.5-3 fold increase in intensity, and $Fe^+$ with a 1.5 fold increase in intensity in the Myc islets due to the presence of blood lakes. Serine ($C_2H_6NO^+$, *m/z* 60.05) exhibited an approximate 40% increase in intensity of in the Myc islets. Other key amino acid fragments such as methionine ($C_2H_5S^+$, *m/z* 61.01), phenylalanine ($C_9H_8O^+$, *m/z* 132.05), and tryptophan ($C_{11}H_8NO^+$, *m/z* 170.07) showed an approximate increase of 20–25%. Many other amino acids exhibited a small increase between approximately 10% and 18% and are listed in Table 1. There was a decrease

of monoacylglycerides (MAGs) and diacylglycerides (DAGs) within Myc islets as seen with MAG (18:2), MAG (18:1), MAG (18:0) (*m/z* 337.29, 339.29, 341.31), DAG (36:2) and DAG (36:1) (*m/z* 603.59 and 605.63), yet long chain fully saturated PC (30:0) (*m/z* 706.55) and PC (32:1) (*m/z* 732.55) were elevated by 105% and 44% respectively. However, PC (34:1) (*m/z* 760.59) and its potiassiated (PC (34:1) + K, *m/z* 798.55) adduct decreased by approximately 40%. Palmitoylcarnitine (*m/z* 400.35), which facilitates the transfer of long-chain fatty acids from the cytoplasm into the mitochondria during the oxidation of fatty acids, showed an increase of nearly 50% within Myc islets.

**Table 6.1.** Comparison of biomolecules identified in positive polarity for Myc islets and control islets. All results are statistically significant with a value of $p<0.05$ according to *t* test with Welch's correction.

| **Description** | **Formula** | **Measured *m/z*** | **Myc Islets Mean (x $10^{-4}$)** | **Control Islets Mean (x $10^{-4}$)** | **Percent Difference** |
|---|---|---|---|---|---|
| Heme Fragment | $C_{29}H_{21}FeN_4$ | 481.05 | 0.18 ± 0.09 | 0.05 ± 0.02 | 291.2 |
| Heme Fragment | $C_{29}H_{23}FeN_4$ | 483.08 | 0.21 ± 0.11 | 0.05 ± 0.03 | 287.0 |
| Heme Fragment | $C_{30}H_{25}FeN_4$ | 497.10 | 0.18 ± 0.09 | 0.05 ± 0.02 | 250.7 |
| Iron | Fe | 55.93 | 0.40 ± 0.15 | 0.16 ± 0.03 | 147.5 |
| PC(30:0) | $C_{38}H_{77}NO_8P$ | 706.53 | 0.04 ± 0.01 | 0.02 ± 0.01 | 104.8 |
| Histidine | $C_5H_8N_3$ | 110.07 | 6.1 ± 1.8 | 3.1 ± 1.0 | 96.8 |
| Palmitoylcarnitine | $C_{23}H_{46}NO_4$ | 400.35 | 0.08 ± 0.02 | 0.05 ± 0.03 | 47.5 |
| PC(32:1) | $C_{40}H_{79}NO_8P$ | 732.55 | 0.04 ± 0.01 | 0.02 ± 0.01 | 43.7 |
| Serine | $C_2H_6NO$ | 60.045 | 3.5 ± 0.56 | 2.5 ± 0.61 | 38.8 |
| PC(30:0)+K | $C_{38}H_{77}NO_8PK$ | 744.50 | 0.06 ± 0.02 | 0.04 ± 0.02 | 30.2 |
| Phenylalanine | $C_9H_8O$ | 132.05 | 0.57 ± 0.07 | 0.45 ± 0.05 | 26.9 |
| Carnitine | $C_7H_{16}NO_3$ | 162.11 | 0.23 ± 0.02 | 0.18 ± 0.02 | 24.5 |
| Tryptophan | $C_{11}H_8NO$ | 170.06 | 0.67 ± 0.08 | 0.55 ± 0.09 | 20.7 |
| Methionine | $C_2H_5S$ | 61.01 | 1.7 ± 0.33 | 1.4 ± 0.39 | 20.6 |
| Glycine | $C_3H_6NO$ | 72.04 | 3.2 ± 0.24 | 2.7 ± 0.29 | 17.3 |
| Glycine | $CH_4N$ | 30.03 | 37 ± 5.1 | 32 ± 4.8 | 15.6 |
| Arginine | $CH_5N_3$ | 59.05 | 8.6 ± 1.6 | 7.5 ± 1.3 | 15.2 |
| Arginine | $C_4H_{10}N_3$ | 100.09 | 2.4 ± 0.30 | 2.1 ± 0.34 | 14.7 |
| Tyrosine | $C_8H_{10}NO$ | 136.08 | 1.4 ± 0.17 | 1.2 ± 0.21 | 13.2 |
| Glutamine | $C_4H_6NO$ | 84.05 | 6.0 ± 0.88 | 5.3 ± 1.0 | 13.1 |
| Threonine | $C_4H_5O$ | 69.04 | 9.5 ± 1.1 | 8.4 ± 1.1 | 13.0 |
| Valine | $C_5H_7O$ | 83.05 | 7.5 ± 0.54 | 6.7 ± 0.50 | 12.0 |
| Tyrosine | $C_7H_7O$ | 107.05 | 2.8 ± 0.27 | 2.5 ± 0.25 | 10.5 |
| DAG (36:1) | $C_{39}H_{73}O_4$ | 605.55 | 0.04 ± 0.01 | 0.05 ± 0.02 | -26.8 |
| DAG (36:2) | $C_{39}H_{71}O_4$ | 603.54 | 0.03 ± 0.01 | 0.05 ± 0.02 | -29.7 |
| MAG(18:0) | $C_{21}H_{41}O_3$ | 341.30 | 0.06 ± 0.01 | 0.09 ± 0.02 | -31.5 |
| MAG(18:2) | $C_{21}H_{37}O_3$ | 337.27 | 0.05 ± 0.01 | 0.08 ± 0.02 | -34.0 |
| MAG(18:1) | $C_{21}H_{39}O_3$ | 339.29 | 0.06 ± 0.01 | 0.09 ± 0.03 | -34.7 |
| PC(34:1)+K | $C_{42}H_{82}NO_8PK$ | 798.54 | 0.06 ± 0.03 | 0.11 ± 0.06 | -39.5 |
| PC(34:1) | $C_{42}H_{83}NO_8P$ | 760.57 | 0.08 ± 0.04 | 0.13 ± 0.09 | -40.1 |

Myc islets showed over a 3-fold increase in myristic acid (C14:0, *m/z* 227.20) as shown in Table 2. Increases of approximately 30% and 20% were observed in adenine ($C_5H_4N_5^-$, *m/z* 134.048) and guanine ($C_5H_3N_5^-$, *m/z* 133.04), respectively and likely reflect nucleotide biosynthesis within the tumor. Myc islets showed an 85% decrease in cholesterol sulfate compared to control islets. Phophatidylethanolamine (PE) (38:4) and PE (38:3) (*m/z* 750.55, 752.60) also exhibited a decrease in Myc islets of more than half of the intensity observed in the control. Fatty acids such as arachidonic acid (C20:4, *m/z* 303.24), linolenic acid (C18:3, *m/z* 277.23), oleic acid (C18:1, *m/z* 281.25), stearic acid (C18:0, *m/z* 283.26), eicosapentaenoic acid (C20:5, *m/z* 301.22), eicosatrienoic acid (C20:3, *m/z* 305.26), and eicosadienoic acid (C20:2, *m/z* 307.27) were all decreased in the Myc islets compared with the control with decreases ranging from approximately 40% to 55%. SM (34:1) characteristic fragments were also decreased by 20–25% in Myc islets.

**Table 6.2.** Comparison of biomolecules identified in the negative polarity for Myc islets and control islets. All results are statistically significant with a value of p<0.05 according to *t* test with Welch's correction.

| Description | Formula | Measured *m/z* | Myc Islets Mean (x $10^{-4}$) | Control Islets Mean (x $10^{-4}$) | Percent Difference |
|---|---|---|---|---|---|
| Myristic Acid, 14:0 | $C_{14}H_{27}O_2$ | 227.20 | 2.5 ± 0.76 | 0.58 ± 0.13 | 341.0 |
| Adenine | $C_5H_4N_5$ | 134.05 | 7.1 ± 2.2 | 5.4 ± 1.5 | 32.3 |
| Guanine | $C_5H_3N_5$ | 133.04 | 1.6 ± 0.42 | 1.3 ± 0.29 | 22.6 |
| Thymine | $C_5H_5N_2O_2$ | 125.03 | 7.7 ± 0.81 | 7.0 ± 0.96 | 9.4 |
| Pyruvic Acid | $C_3H_4O_3$ | 87.01 | 9.8 ± 0.33 | 11 ± 0.97 | -7.9 |
| Palmitic acid; 16:0 | $C_{16}H_{31}O_2$ | 255.23 | 22 ± 3.7 | 25 ± 4.6 | -12.7 |
| FA(24:0) | $C_{24}H_{47}O_2$ | 367.35 | 0.05 ± 0.01 | 0.06 ± 0.01 | -14.1 |
| FA(C22:4) | $C_{22}H_{35}O_2$ | 331.26 | 0.13 ± 0.02 | 0.15 ± 0.02 | -17.3 |
| Eicosenoic Acid; 20:1 | $C_{20}H_{37}O_2$ | 309.28 | 0.27 ± 0.04 | 0.33 ± 0.05 | -18.4 |
| FA(C24:1) | $C_{24}H_{45}O_2$ | 365.34 | 0.08 ± 0.01 | 0.09 ± 0.01 | -19.3 |
| SM (34:1) | $C_{37}H_{75}N_2O_6P$ | 673.51 | 0.10 ± 0.02 | 0.12 ± 0.03 | -21.3 |
| SM (34:1) | $C_{40}H_{80}N_2O_6P$ | 715.58 | 0.07 ± 0.02 | 0.09 ± 0.03 | -24.0 |
| SM (34:1) | $C_{36}H_{69}NO_6P$ | 642.50 | 0.44 ± 0.12 | 0.58 ± 0.18 | -24.6 |
| SM (34:1) | $C_{34}H_{67}NO_6P$ | 616.48 | 0.26 ± 0.06 | 0.35 ± 0.11 | -25.4 |
| FA(C22:5) | $C_{22}H_{33}O_2$ | 329.24 | 0.12 ± 0.02 | 0.18 ± 0.03 | -29.6 |
| FA(C22:6) | $C_{22}H_{31}O_2$ | 327.23 | 0.11 ± 0.01 | 0.16 ± 0.03 | -32.3 |
| Eicosapentaenoic Acid; 20:5 | $C_{20}H_{29}O_2$ | 301.22 | 0.15 ± 0.03 | 0.24 ± 0.06 | -38.8 |
| Eicosadienoic Acid; 20:2 | $C_{20}H_{35}O_2$ | 307.26 | 0.29 ± 0.05 | 0.52 ± 0.13 | -44.9 |
| Stearic Acid; 18:0 | $C_{18}H_{35}O_2$ | 283.26 | 8.3 ± 1.6 | 15 ± 2.5 | -45.0 |
| Vitamin E | $C_{29}H_{49}O_2$ | 429.37 | 0.39 ± 0.13 | 0.72 ± 0.23 | -45.4 |
| Eicosatrienoic Acid; 20:3 | $C_{20}H_{33}O_2$ | 305.25 | 0.41 ± 0.08 | 0.78 ± 0.16 | -46.6 |
| C18:3 | $C_{18}H_{39}O_2$ | 277.22 | 0.28 ± 0.04 | 0.54 ± 0.11 | -49.0 |
| Oleic Acid; 18:1 | $C_{18}H_{33}O_2$ | 281.25 | 6.1 ± 1.5 | 12 ± 3.1 | -50.6 |
| PE(38:4) | $C_{43}H_{77}NO_8P$ | 766.55 | 0.03 ± 0.01 | 0.06 ± 0.02 | -53.8 |
| Arachidonic Acid; 20:4 | $C_{20}H_{31}O_2$ | 303.23 | 0.58 ± 0.16 | 1.3 ± 0.47 | -56.1 |
| PE(38:4) | $C_{43}H_{77}NO_7P$ | 750.54 | 0.03 ± 0.01 | 0.07 ± 0.03 | -56.6 |
| PE(38:3) | $C_{43}H_{79}NO_7P$ | 752.57 | 0.03 ± 0.01 | 0.09 ± 0.03 | -65.9 |
| Linoleic Acid; 18:2 | $C_{18}H_{31}O_2$ | 279.23 | 1.8 ± 0.46 | 5.8 ± 1.9 | -69.5 |

The acinar tissue surrounding the islets in both the Myc and control tissues presented less variation of biomolecules between tissue types than what was observed between islets. In the positive polarity, the largest changes were observed in palmitoylcarnitine which had a 37% increase in in Myc tissue and iron with a 20% increase. In contrast methionine (fragment $C_2H_5S^+$, *m/z* 61.01) was decreased by 19% in the Myc versus control acinar. All other amino acids that showed a statistically significant difference ($p \leq 0.05$) between the normalized intensity means in the acinar tissue, exhibiting decreases ranging from 8% to 14%, are listed in Table 6.3.

The Myc acinar tissue showed decreased intensities in all major biomolecules when compared with the control acinar tissue, with large decreases observed in all lipids except C14:0. PE (38:4) and PE (38:3) exhibited the largest decreases of 37% and 39%, respectively, within the Myc surrounding acinar tissue. SM (34:1) fragments all showed a consistent decrease ranging from 26–35%. In addition, smaller fatty acid fragments such as eicosadienoic acid (20:2) and palmitic acid (C16:0, *m/z* 255.23) demonstrated a decrease of 25–27%. Adenosine monophosphate (AMP) ($C_{10}H_{13}N_5O7P^-$, *m/z* 346.06), a possible metabolite from the cyclic-AMP or hydrolysis of adenosine-diphosphate (ADP), was found to be 25% lower in Myc surrounding acinar tissue. Other nucleotides such as thymine and guanine were also found to be slightly decreased in the Myc surrounding acinar tissue by 11–15%.

**Table 6.3.** Comparison of biomolecules identified in both negative and positive polarity for the surrounding acinar tissue of Myc and control. All results are statistically significant with a value of $p<0.05$ according to *t* test with Welch's correction.

| Description | Formula | Measured *m/z* | Myc Acinar Mean (x $10^{-4}$) | Control Acinar Mean (x $10^{-4}$) | Percent Difference |
|---|---|---|---|---|---|
| **Positive Polarity** | | | | | |
| Palmitoylcarnitine | $C_{23}H_{46}NO_4$ | 400.35 | 0.06 ± 0.01 | 0.05 ± 0.01 | 36.6 |
| Iron | Fe | 55.93 | 0.17 ± 0.02 | 0.14 ± 0.01 | 20.2 |
| Alanine/cysteine | $C_2H_6N$ | 44.05 | 86 ± 3.0 | 94 ± 7.0 | -8.6 |
| Tryptophan | $C_{11}H_8NO$ | 170.06 | 0.71 ± 0.04 | 0.81 ± 0.10 | -11.7 |
| Arginine | $C_4H_{10}N_3$ | 100.09 | 2.5 ± 0.29 | 2.9 ± 0.43 | -14.0 |
| Glutamine | $C_4H_6NO$ | 84.05 | 6.1 ± 0.92 | 7.1 ± 1.1 | -14.1 |
| Methionine | $C_2H_5S$ | 61.01 | 1.9 ± 0.34 | 2.3 ± 0.47 | -18.5 |
| **Negative Polarity** | | | | | |
| Thymine | $C_5H_5N_2O_2$ | 125.04 | 6.3 ± 0.61 | 6.3 ± 0.72 | -11.0 |
| Guanine | $C_5H_4N_5O$ | 150.04 | 3.7 ± 0.55 | 3.7 ± 0.66 | -14.9 |
| GPGro headgroup | $C_6H_{12}O_6P$ | 211.04 | 0.51 ± 0.03 | 0.51 ± 0.06 | -12.2 |
| Palmitic acid; 16:0 | $C_{16}H_{31}O_2$ | 255.23 | 21 ± 5.8 | 21 ± 7.1 | -24.5 |
| Adenosine-5-phosphate | $C_{10}H_{13}N_5O_7P$ | 346.06 | 0.38 ± 0.08 | 0.10 ± 0.03 | -24.7 |
| SM (34:1) | $C_{38}H_{76}N_2O_6P$ | 687.55 | 0.10 ± 0.01 | 0.12 ± 0.05 | -26.0 |
| Eicosadienoic acid; 20:2 | $C_{20}H_{35}O_2$ | 307.26 | 0.09 ± 0.02 | 0.38 ± 0.15 | -27.2 |
| SM (34:1) | $C_{34}H_{67}NO_6P$ | 616.48 | 0.06 ± 0.02 | 0.09 ± 0.04 | -28.0 |
| SM (34:1) | $C_{38}H_{74}N_2O_6P$ | 673.51 | 0.12 ± 0.03 | 0.06 ± 0.02 | -33.4 |
| SM (34:1) | $C_{40}H_{80}N_2O_6P$ | 715.58 | 0.03 ± 0.01 | 0.03 ± 0.02 | -34.9 |
| PE(38:4) | $C_{43}H_{77}NO_7P$ | 750.54 | 0.03 ± 0.01 | 0.03 ± 0.02 | -36.5 |
| PE(38:3) | $C_{43}H_{79}NO_7P$ | 752.57 | 0.03 ± 0.01 | 0.03 ± 0.02 | -38.7 |

## 6.5 DISCUSSION

Our analyses provide evidence of significant metabolic changes occurring within Myc driven β cell tumors and the surrounding tissue, which demonstrates a proof-of-

concept for utilizing ToF-SIMS to identify large scale changes that occur in tumor and stromal cell metabolism during tumorigenesis. The specific alterations of significance include, the *de novo* synthesis of fatty acids such as C14:0 and PC30:0, the increase in palmitoylcarnitine in the tumor and acinar tissue surrounding it, the increase in nucleotides and the increase in amino acids within the tumor but depletion of amino acids within the acinar tissue.

Metabolites with high signal intensity within tumors included carnitine and palmitoylcarnintine and suggest increased fatty acid oxidation, as both are involved in transporting fatty acids across the mitochondrial membrane for oxidation and energy generation. The increase in palmitoylcarnintine and decrease in palmitate (C16:0) in Myc acinar tissue suggests the tumor may also engage mechanisms to deplete palmitate from the surrounding environment to satisfy the high metabolic demands of tumor growth.

Metabolites increased in Myc-acinar tissue include AMP and these levels may be influenced by Myc expression in the islet tumor. Myc overexpression is reported to deplete ATP, resulting in the activation of AMP-activated protein kinase (AMPK), a key protein for regulating cellular energy.[214] AMPK is switched on by the rise in the AMP:ATP ratio, which can either result from cellular stresses occurring with depletion of ATP (e.g. hypoxia or glucose deprivation) or stresses that increase ATP consumption (e.g. excessive cell growth), which are common occurrences in tumor cells.[180] AMPK activation inhibits biosynthetic pathways related to fatty acid and cholesterol synthesis while increasing catabolism.[215] This would agree with our data as we observed an increase in palmitoylcarnitine, which facilitates fatty acid oxidation, in both the Myc islets and acinar tissue surrounding the tumor. Together these data further supports the hypothesis that the high energy demands of the Myc β cell tumor impacts the metabolism of the surrounding cells and tissue, thereby providing a conducive tumor promoting microenvironment.

The observed decrease in SM within the Myc islets is an indicator that the β cells are losing their capacity to produce insulin as there is a direct correlation between insulin secretory capacity and SM presence in islets.[207] SM synthase 1 and 2 have critical roles in allowing insulin vesicles release from Golgi cisterna and their inhibition

repressed insulin secretion.[216] The decrease in β cell function could also be indicative of cellular dedifferentiation. According to Ischenko et. al, Myc is crucial for inducing the transformation from tumor cells to cancer stem cells.[217] Furthermore, activation of Myc in pancreatic β cells precipitates an acute loss of insulin production capacity with genes related to insulin production and other β cell lineage markers reduced significantly after 72 hours, indicating a loss of β cell differentiation.[218] In addition, other research has shown that genome reprogramming and dedifferentiation are important early steps in pancreatic ductal adenocarcinoma tumor initiation and progression.[219-221] The decrease in SM found in the Myc acinar tissue may, in contrast, possibly be linked to AMPK activation and the inhibition of complex fatty acid synthesis resulting in shuttling of fatty acids to the tumor.

Lipids altered in Myc β cell tumors include increases in the short chain, fully saturated fatty acid, C14:0, and is likely a product of Myc-induced *de novo* fatty acid synthesis from glucose and/or possibly from glutamine via reverse carboxylation.[222] This would require overriding the AMPK block on synthesis outlined above but is consistent with previous studies demonstrating that Myc increases the gene expression profile for fatty acid synthesis and can also increase the profile of certain lipids in different cell types.[199, 213, 223, 224] Evaluating the status of other lipids entities, the decreased intensity of arachidonic acid (20:4; AA) in the Myc islets is notable, as other groups have found its levels to be increased in Myc-activated tissues, such as the lung and lymphoma tissue.[201, 213] In these models increased AA is likely linked to production of eicosanoids, which regulate the inflammatory response and are implicated in cancer progression.[225, 226] However, in pancreatic β cells arachidonic acid stimulates insulin secretion and its production requires DAG and MAG lipases[227] and a supply of MAG and DAG. In the Myc β cell tumors the drop in AA is correlated with reduction in MAG and DAG fragments with similar decreases ranging from 27–35% and providing further evidence of loss of function and the potential dedifferentiation of β cells.

Phospholipids PC (30:0) and PC (30:0) + $K^+$ were increased in the Myc islets and this is consistent with the high demand for membrane lipids generated in a rapidly growing tumor and possibly facilitated by the p53-/- status of these tumors.[228] These PC

increases could explain the potential fate of the highly increased short chain fatty acid, C14:0, as the composition of PC (30:0) is most likely C14:0 and C16:0.

The increase in a wide array of amino acids within the Myc islets is a potential marker of enhanced cellular growth and proliferation, as growing tumors require large amounts of energy and building blocks for the construction of new cellular components.[180, 229] The approximate 39% increase in serine observed in the Myc islets compared with the control islets is in agreement with prior investigations of cancer metabolism, as the serine biosynthetic pathway represents a critical change in glucose metabolism contributing to tumor growth and cellular reprogramming.[230-232] 3-phosphoglycerate, a glycolytic intermediate, is converted to serine through a series of enzymes, a number of which are upregulated in Myc-induced liver tumors (PHGDH, PSAT1 and PSPH),[233] and Myc activation of serine biosynthesis aids cancer progression under nutrient deprived conditions.[234] Further serine metabolism by serine hydroxymethyltransferase, also Myc regulated,[235] leads to the production of glycine, which also increased by approximately 17% within MYC islets. Serine and glycine are precursors used in the folate cycle, which in turn provides precursors to generate methionine[236] and methionine was increased within the Myc islets and decreased in the surrounding acinar tissue. Methionine adenosyltransferase (MAT), an enzyme that catalyzes the first step in methionine metabolism, has been associated with rapid growth in cells and dedifferentiation of cells within the liver[182, 183] and methionine metabolism is deregulated in Myc-driven liver cancer.[234] The role of methionine provides possible insight into the metabolic contribution to physiological changes occurring in our model, as the β cells within the Myc islets are showing signs of dedifferentiation as discussed above and are in a state of rapid growth. The depletion of methionine in the acinar tissue around the Myc islet is likely due to the high requirement of methionine needed for MAT and subsequent methyl donation within the tumor facilitating epigenetic changes associated with dedifferentiation, which requires gene silencing of dedicated tissue lineage markers.[237] Other amino acids increased in Myc islets include the essential amino acids phenylalanine and tyrosine. Previous studies have demonstrated that these two essential amino acids, both potentially transported by the Myc regulated transporter Slc7a5,[238] are key contributors to primary tumor growth and metastasis.[239]

These studies by Elstad et al. demonstrated that a diet that restricts phenylalanine and tyrosine resulted in longer survival and inhibition of primary tumor growth and metastasis in mice. Additional amino acids increased by 10-15% in Myc β cell tumors include arginine a provider of pivotal metabolic intermediates and essential for cancer cell growth,[240] valine an essential amino acid with increased uptake in cancer cells[241] and also threonine, which if combined with induction of threonine dehydrogenase would supplement tumor cell pools of glycine and acetyl CoA, contributing to S-adenosylmethionine synthesis the abundance of which regulates histone methylation and cell fate.[242]

Finally, a counterintuitive finding was the increase in glutamine observed in the Myc islets, as other groups have noted that Myc overexpression drives glutamine catabolism rather than synthesis.[200, 243] This increase in glutamine in the tumor may be derived from a combination of *de novo* synthesis and transport of glutamine from the surrounding cells as there is depletion of glutamine in Myc acinar cells. Glutamine is highly concentrated in the blood lakes present in Myc β-cell tumors and these may act as a fuel source sink providing metabolites to the tumor.

## 6.6 CONCLUSION

Imaging ToF-SIMS provides a new approach for imaging the tumor microenvironment and tumor heterogeneity and our results demonstrate s the potential to differentiate altered metabolic processes occurring within cancerous tissues. PCA of ToF-SIMS image data of pancreatic tissue containing β cell tumors revealed distinct chemical differences between the lipid and amino acid content within the tumor and surrounding tissue. Characterization of intratumor heterogeneity was successfully accomplished by selecting regions of interest (ROIs) to separate the tumor region from the surrounding tissue and applying PCA to the ROI data. PCA of the tumor region allowed for chemical identification of spatial heterogeneity occurring within the tumor, showing the composition of blood lakes in discrete areas and the remaining biomolecules present within the tumor. The combination of ToF-SIMS images and SHG demonstrated that two imaging modalities can correlate with each other in defining the biological structures within tissue, such as blood vessels. Lastly, data interpretation

using ROIs of ToF-SIMS images, peak intensity comparisons, and SHG, provides a method to observe significant changes occurring within pancreatic β cell tumors and the surrounding tissue. Together these data collection and analysis methods demonstrate that imaging ToF-SIMS can provide biologically valuable chemical characterization of metabolites in tissues comprising the tumor and microenvironment at a high lateral resolution with low mass capabilities.

## 6.7 ACKNOWLEDGEMENTS

We would also like to acknowledge our funding sources: NESACBIO NIH P41 EB002027, NSF-GRFP DGE-0718124/1256082 and RO1CA158921-01A1 (F.M., L.H and D.H.).

## 6.8 SUPPORTING INFORMATION

# ANALYSIS OF THE TUMOR MICROENVIRONMENT USING IMAGING TIME-OF-FLIGHT SECONDARY ION MASS SPECTROMETRY

Blake M. Bluestein[a], Fionnuala Morrish[b], Daniel J. Graham[a], Li Huang[b], David Hockenbery[b], Lara J. Gamble[a,§]

[a] University of Washington, Dept. of Bioengineering, MolES Building, Box 351653, Seattle, WA 98195-1653

[b] Fred Hutchinson Cancer Research Center, Seattle, WA 98109

[§] Corresponding Author

Lara Gamble

University of Washington

Department of Bioengineering

Box 351653

Seattle, WA 98195

1-206-543-8094 (phone)

1-206-543-3778 (fax)

lgamble@uw.edu (e-mail)

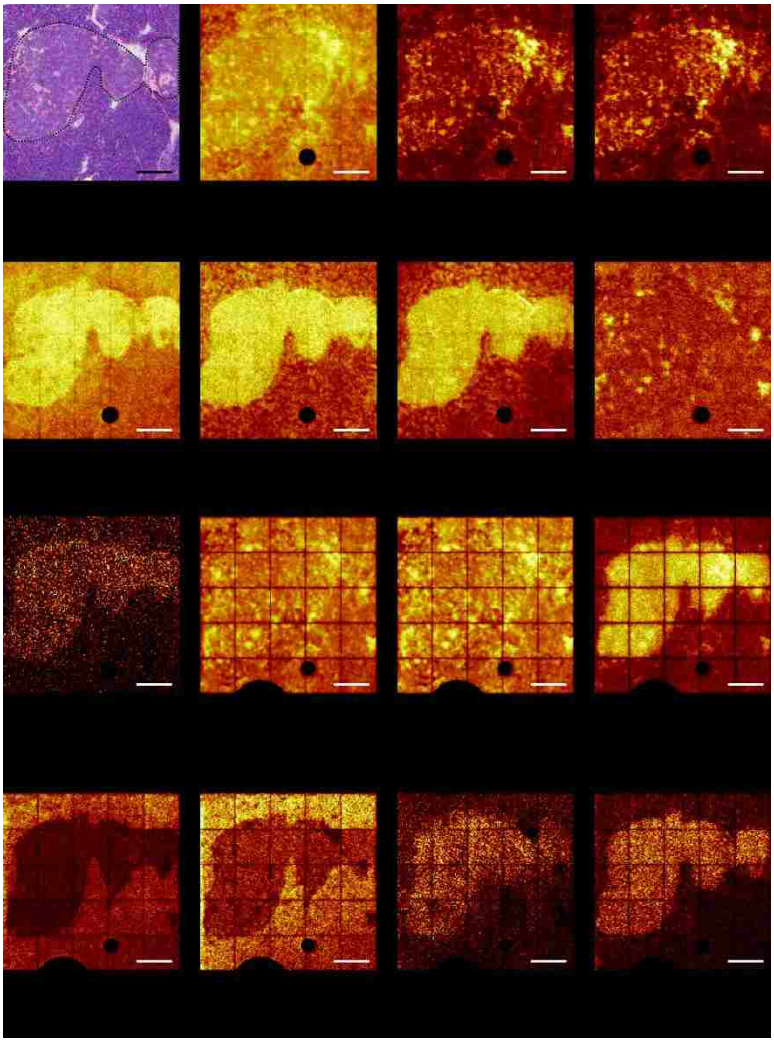

**Supplemental Figure S.6.1.** Key masses identified from Myc tissues. Scale bars represent 200 µm.

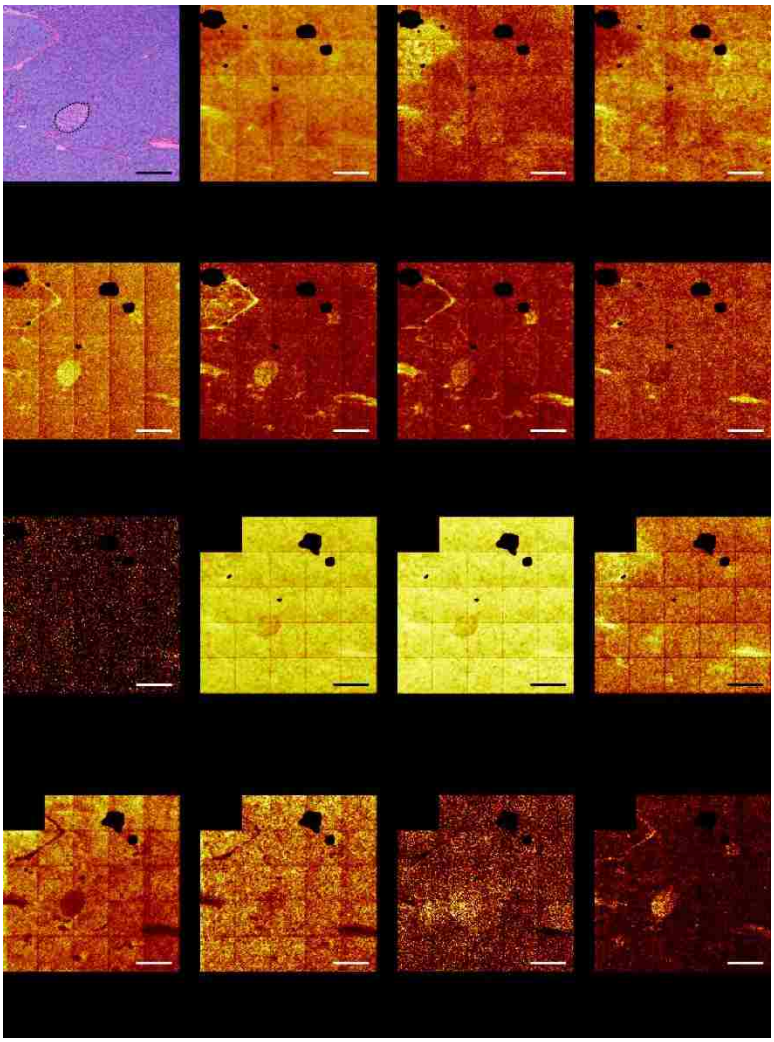

**Supplemental Figure S.6.2.** Key masses identified from control tissues. Scale bars represent 200 µm.

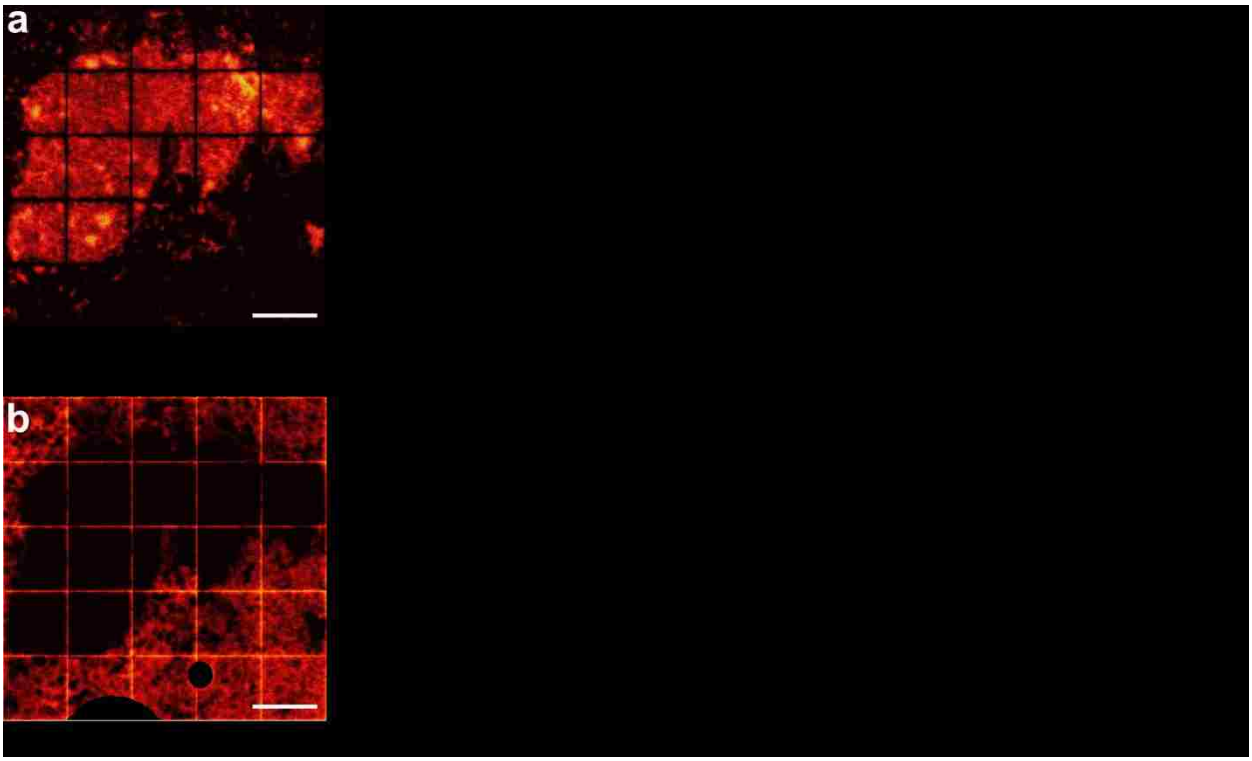


**Supplemental Figure S.6.3.** Negative polarity PCA of ToF-SIMS image of Myc tissue region after removal of substrate/embedding medium signal. **(a)** PC1 positive scores image displaying the Myc islet tumor. **(b)** PC1 negative scores image displaying the acinar tissues. **(c)** PC1 loadings plot displaying the chemical species that correspond to scores images. The edges of the individual raster tiles can be seen in the negative scores image due to a charging/saturation effect within the instrument from $PO_3^-$ (*m/z* 78.97), which is observed directly in the negative loadings. Scale bar is 200 µm.

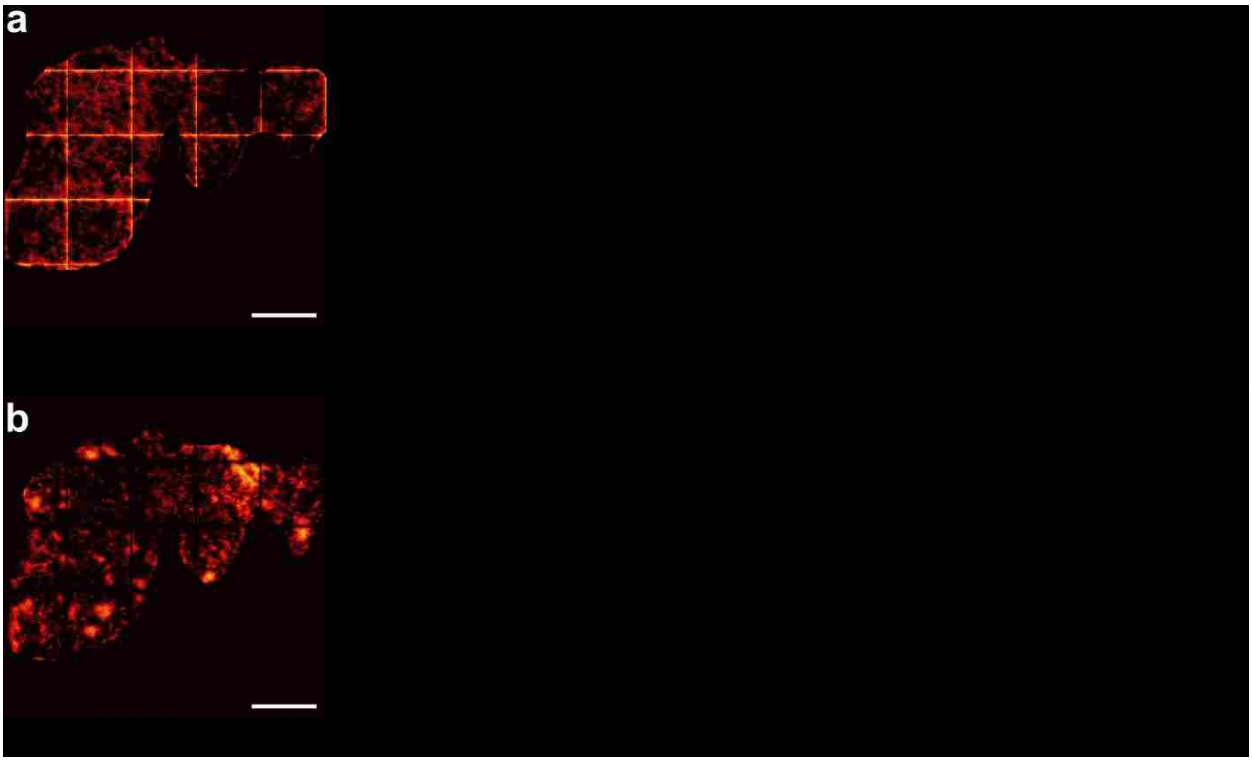


**Supplemental Figure S.6.4.** Negative polarity PCA of ToF-SIMS image of the Myc islet tumor ROI. **(a)** PC1 positive scores image displaying the tumor interior. **(b)** PC1 negative scores image displaying the high intensity regions within the Myc islet tumor. **(c)** PC1 loadings plot displaying the chemical species that correspond to scores images. The positive loadings are dominated by $PO_3^-$, most which is consistent to the charging observed around the individual tiles edges seen in the positive scores image **(a)**. Scale bar is 200 µm.

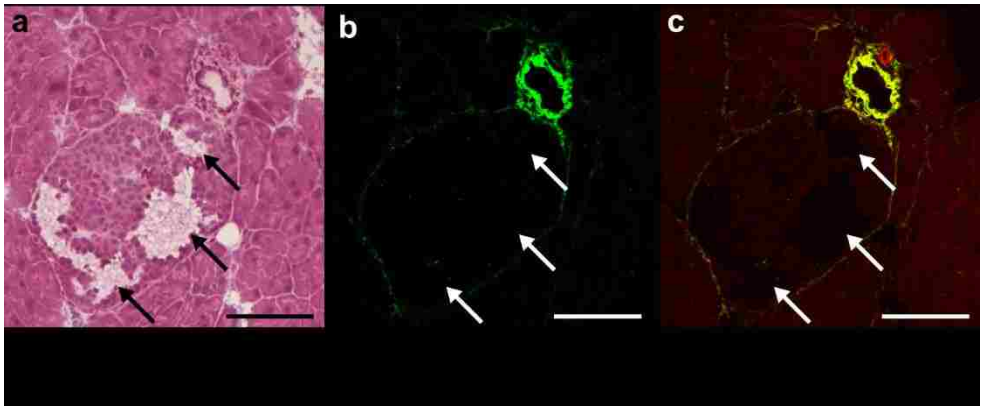


**Supplemental Figure S.6.5.** Images of vasculature and blood lakes using a combination of H&E and SHG. Arrows point to blood lakes. **(a)** Hematoxylin and eosin stained section displaying the Myc islet tumor in the center and blood vessel located to its upper right. **(b)** SHG image demonstrating collagen structure at a high intensity signal (green) around the blood vessel and surrounding the tumor. **(c)** merged image of autofluorescence and SHG providing contrast of the tissue section and blood lakes. Scale bars represent 200 µm.

# Chapter 7. CONCLUSIONS AND FUTURE DIRECTIONS

## 7.1 CONCLUSIONS

The overarching goal of this dissertation was the continued development of tissue analysis using imaging time-of-flight secondary ion mass spectrometry (ToF-SIMS). The work presented here has successfully demonstrated that ToF-SIMS is a powerful analytical tool capable providing detailed and spatially precise molecular signatures of tumors and tumor microenvironments, presenting a new perspective for investigating cancerous tissues.

A percentage of this work was focused on developing a methodology that would allow for the comparison of specific regions across many tissues. This work provided a method to identify and compare specific regions (e.g. cellular and stromal) within tissue samples using an unsupervised multivariate analysis technique. This resulted in the ability to consistently isolate regions from tissue sections that varied significantly per section. This work was seminal for further investigations into human breast cancer tissue analyses.

With this newly developed model, multiple human breast cancer tissue biopsies were compared to one another in order to determine what metabolic factors contribute to chemotherapeutic resistance. Comparing the isolated regions using principal component analysis (PCA) resulted in a large amount of variability between all samples without a clear separation of subtype (e.g. triple negative, luminal B, etc.) or patient response to chemotherapy. However, when separating tissue biopsies into their respective subtypes resulted in observable trends between patients who were responsive or non-responsive to chemotherapeutics.

In the final chapter, the focus was switched from patient response to interpreting the tumor microenvironment in a mouse pancreatic cancer model. This work showed that combining ToF-SIMS imaging and non-linear optical imaging methods, such as second harmonic generation (SHG), can correlate with each other in defining biological structures, such as blood vessels, within tissue. Also, using regions of interest (ROIs) of ToF-SIMS images was successful in observing significant metabolic changes occurring

within the tumors and surrounding tissue related to fatty acid synthesis and amino acid metabolism.

Together these data collection and analysis methods demonstrate that imaging ToF-SIMS can provide biologically valuable chemical characterization of metabolites in cancerous tissues.

## 7.2 FUTURE DIRECTIONS

There is an enormous amount of data that has been collected and can be expanded upon from the work presented here. However, there are many factors to consider when analyzing tissue data after it has been collected. Here I present alternative methods to analyze this data and future investigations.

### 7.2.1 HUMAN BREAST CANCER PATIENT DATA ANALYSIS

PCA was primarily used in Chapter 5 to observe the major chemical variance between breast cancer patients and their response to chemotherapy. PCA is useful tool as an initial analysis to help reduce the dimensionality of the data, but it is examining the raw data will be crucial to understanding metabolic mechanisms occurring during chemotherapeutic resistance. One approach would be to focus on subtypes (e.g. triple negative or luminal B) and create groups of all the pathological responding and non-responding patients and compare specific mass intensities against each other. A preliminary approach of this can be seen in Table A.4. However, even though these mean intensities are observed to be statistically significant ($p \leq 0.05$), the standard deviation can be very large, which may render the comparison ineffective. Therefore, each mass intensity comparison should be examined and proved valid instead of accepting only from statistical significance. Furthermore, once major differences have been found in the tissues the large impact will come from the biological interpretation. This can be done by combining the ToF-SIMS data with gene expression data available from the Fred Hutchinson Cancer Research Facility.

Another approach would be to compare specific pathological areas to each other. As shown in Table A.3, pathologist indicated regions (e.g. infiltrating ductal carcinoma and tumor with lymphocytes) could be compared to each other.

Lastly, the positive data remains to be analyzed for the majority of the patient data. ToF-SIMS can provide a way to observe changes that are occurring within the amino acid metabolism of cancerous tissues, as shown in Chapter 6. However, the PCA of images and the compiling of a dataset this large is both computationally and labor intensive.

### 7.2.2 MYC PANCREATIC CANCER INVESTIGATIONS

A major advantage to the mouse model used in Chapter 6, is that it is an inducible and regressible β cell neoplasia model. This means that the tumors can be induced, or grow, for a period of time and then allowed to regress, or shrink. For example, the data presented in Chapter 6 shows a mouse model that had tumor induction for 6 days. In future experiments it would be possible to perform ToF-SIMS of pancreas tissues that had 6 days of induction with 6 days regression. This also provides for the opportunity to do multiple durations of inductions and regressions within the mouse model to analyze. Utilizing the method and analysis shown in Chapter 6 on multiple models or time durations of induction and regression could provide a way to observe major metabolic changes occurring at different tumor stages, including progression, regression, and how the surrounding tissue responds to these changes. Furthermore, with a genetic mouse model it would be possible to obtain genetic information to corroborate what is observed in ToF-SIMS data.

# APPENDIX

# APPENDIX A. ADDITIONAL HUMAN BREAST CANCER SAMPLE DATA

This appendix is to aid in further understanding the breast cancer patient data presented in Chapters 4 & 5. It is also provided to allow for future investigations using the data set.

## Appendix A.1 REFERENCE TABLES FOR BREAST CANCER BIOPSIES

**Table A.1.** Reference table of breast cancer patient data. Includes study identification number, Porter lab number, pre/post treatment designation, and number related to patient numbers in Chapter 5. Receptor status (estrogen (ER), progesterone (PR), human epidermal growth factor receptor 2 (HER2)), cytokeratin 5/6 status, epidermal growth factor receptor (EGFR) status, tumor grade, and immunohistochemistry (IHC) (triple negative, TN and HER2 enriched, HER2) gene expression subtype, and pathological response (pCR) are shown here.

| Study ID | Porter Lab Number (pre/post) | Patient No. in Chap. 5 | ER | PR | HER2 | CK5/6 | EGFR | KI67 | Grade | IHC subtype | Gene Expression Subtype | Pathological Response |
|---|---|---|---|---|---|---|---|---|---|---|---|---|
| 7587-01 | 120803 | 1 | NEG | NEG | NEG | POS | POS | 35 | 3 | TN | HER2-enriched | non-pCR |
| 7587-03 | 120804/120924 | 2 | POS | POS | NEG | NEG | NEG | 5 | 1 | Luminal A | Luminal A | non-pCR |
| 7587-04 | 120805 | 3 | NEG | NEG | NEG | POS | POS | 91 | 3 | TN | Basal-like | near pcr |
| 7587-05 | 120876 | 4 | POS | POS | POS | NEG | NEG | 71 | 3 | Luminal B | Luminal B | non-pCR |
| 7587-07 | 120926/130314 | 5 | NEG | NEG | NEG | POS | NEG | 85 | 2 | TN | Basal-like | non-pCR |
| 7587-08 | 130162 | 6 | POS | NEG | POS | NEG | NEG | 44 | 3 | Luminal B | Luminal B | pCR |
| 7587-09 | 130163 | 7 | POS | POS | POS | NEG | NEG | 63 | 3 | Luminal B | Luminal B | pCR |
| 7587-11 | 130200 | 8 | POS | POS | POS | NEG | NEG | 20 | 2 | Luminal B | Luminal A | non-pCR |
| 7587-12 | 130199 | 9 | NEG | NEG | POS | POS | POS | 30 | 3 | HER2 | HER2-enriched | near pCR |
| 7587-13 | 130250 | 10 | POS | POS | NEG | NA | NA | 57 | 3 | Luminal B | Luminal B | non-pCR |
| 7587-14 | 130315 | 11 | POS | POS | NEG | NEG | NEG | 35 | 2 | Luminal B | Luminal B | non-pCR |
| 7587-15 | 130415 | 12 | POS | POS | NEG | NA | NA | 19 | 3 | Luminal B | Luminal A | non-pCR |
| 7587-20 | 130495 | 13 | NEG | NEG | NEG | POS | POS | 80 | 3 | TN | Basal-like | non-pCR |
| 7587-21 | 130496 | 14 | POS | NEG | NEG | NA | NA | 69 | 3 | Luminal B | Luminal B | pCR |
| 7587-22 | 130698 | 15 | POS | POS | POS | NEG | NEG | 9 | 2 | Luminal B | Luminal B | partial responder |
| 7587-23 | 130528/140276 | 16 | NEG | NEG | NEG | POS | NEG | 95 | 3 | TN | Basal-like | pCR |
| 7587-24 | 130804 | 17 | POS | POS | POS | POS | NEG | 21 | 2 | Luminal B | Luminal B | pCR |
| 7587-25 | 130802 | 18 | NEG | NEG | NEG | POS | NEG | 69 | 3 | TN | Basal-like | non-pCR |
| 7587-27 | 130801 | 19 | NEG | NEG | NEG | POS | POS | 83 | 3 | TN | Basal-like | pCR |
| 7587-28 | 0/140396 | 23 | POS | POS | POS | POS | NEG | 30 | 3 | Luminal B | Luminal B | non-pCR |
| 7587-29 | 140159 | 20 | NEG | NEG | NEG | POS | POS | 57 | 3 | TN | Basal-like | pCR |
| 7587-30 | 140207 | 21 | NEG | NEG | NEG | POS | NEG | 60 | 3 | TN | Basal-like | non-pCR |
| 7587-33 | 140586 | 22 | NEG | NEG | NEG | POS | NEG | 93 | 3 | TN | Basal-like | pCR |

**Table A.2.** Reference table of breast cancer patient data including study identification number, Porter lab number, pre/post treatment designation, ToF-SIMS analysis date, and number of ToF-SIMS analysis spots on each respective tissue.

| | | | | |
|---|---|---|---|---|
| 7587-01 | 120803 | pre | 9/17/2013 | 3 |
| 7587-03 | 120924 | post | 8/5/2013 | 3 |
| 7587-05 | 120876 | pre | 10/3/2013 | 4 |
| 7587-07 | 130314 | post | 8/7/2013 | 3 |
| 7587-09 | 130163 | pre | 10/24/2013 | 4 |
| 7587-12 | 130199 | pre | 7/16/2013 | 4 |
| 7587-14 | 130315 | pre | 8/14/2013 | 3 |
| 7587-20 | 130495 | pre | 12/10/2013 | 3 |
| 7587-22 | 130698 | pre | 8/20/2015 | 3 |
| 7587-23 | 140276 | post | 11/19/2014 | 3 |
| 7587-25 | 130802 | pre | 10/23/2014 | 4 |
| 7587-28 | 140396 | post | 9/29/2014 | 4 |
| 7587-30 | 140207 | pre | 7/29/2015 | 3 |

**Table A.3.** Reference table of breast cancer patient data displaying each ToF-SIMS analysis sots with pathologist interpretation.

| | | | | |
|---|---|---|---|---|
| **120803** | Tumor | Unranked | Tumor | n/a |
| **120924** | Tumor | Do not use | Tumor | n/a |
| **120876** | Infiltrating tumor | No tumor | DCIS | Tumor |
| **130314** | Infiltrating ductal carcinoma | Norm duct | Norm duct | n/a |
| **130163** | Infiltrating tumor | Ductal carcinoma in situ | Ductal carcinoma in situ | Infiltrating tumor |
| **130199** | Tumor | Tumor | Tumor | No tumor |
| **130315** | Tumor | Tumor | Tumor | n/a |
| **130495** | Unranked | Unranked | Unranked | Unranked |
| **130698** | Ductal carcinoma in situ | Lymphocytes | Infilrating ductal carcinoma | n/a |
| **140276** | Norm Eplithelum plus lymphocityes | Loose fibrous tissue | Loose fibrous tissue | n/a |
| **130802** | Invasive ductal carcinoma | Normal lobule plus lymphocytes | Invasive ductal carcinoma | Tumor plus lymphocytes |
| **140396** | Normal stroma | Normal stroma | Normal stroma | Normal stroma |
| **140207** | Infilrating ductal carcinoma | Infiltrating ductal carcinoma plus lymphocytes | Infiltrating ductal carcinoma | n/a |

**Table A.4.** Preliminary analysis comparing metabolites observed in the PC2 loadings of the cellular regions of the triple negative (TN) pathologically responding (pCR) patients to the non-pathologically responding (non-pCR) patients as seen in Figure 5.5.

| | | | | | | | |
|---|---|---|---|---|---|---|---|
| 227.20 | $C_{14}H_{27}O_2^-$ | Myristic acid, 14:0 | 4.75E-04 | 4.09E-04 | 2.94E-04 | 3.32E-04 | 1.81E-04 |
| 253.22 | $C_{16}H_{29}O_2^-$ | Palmitoleic acid; 16:1 | 9.50E-04 | 8.48E-04 | 6.41E-04 | 5.90E-04 | 3.09E-04 |
| 259.02 | $C_6H_{12}PO_9^-$ | Phosphoinositol fragment | 2.46E-04 | 9.94E-05 | 1.48E-04 | 8.42E-05 | 9.88E-05 |
| 303.24 | $C_{20}H_{31}O_2^-$ | Arachidonic acid; 20:4 | 2.37E-04 | 4.06E-04 | 8.79E-05 | 1.23E-04 | 1.49E-04 |
| 307.26 | $C_{20}H_{35}O_2^-$ | 20:2 | 1.70E-04 | 2.55E-04 | 1.11E-04 | 8.75E-05 | 5.85E-05 |
| 385.35 | $C_{27}H_{45}O^-$ | Cholesterol | 6.96E-05 | 3.30E-05 | 5.90E-05 | 3.42E-05 | 1.06E-05 |
| 616.47 | $C_{34}H_{67}NO_6P^-$ | SM(34:1) | 1.73E-05 | 9.74E-06 | 6.19E-06 | 5.11E-06 | 1.11E-05 |
| 687.56 | $C_{38}H_{76}N_2O_6P^-$ | SM(34:1) | 2.91E-05 | 1.86E-05 | 7.83E-06 | 8.08E-06 | 2.13E-05 |

# Appendix A.2 Analysis Area References: Hematoxylin and Eosin (H&E) Stained Breast Cancer Tissue Sections and Summed $CN^-$ and $CNO^-$ ToF-SIMS Images of Respective Analysis Spots

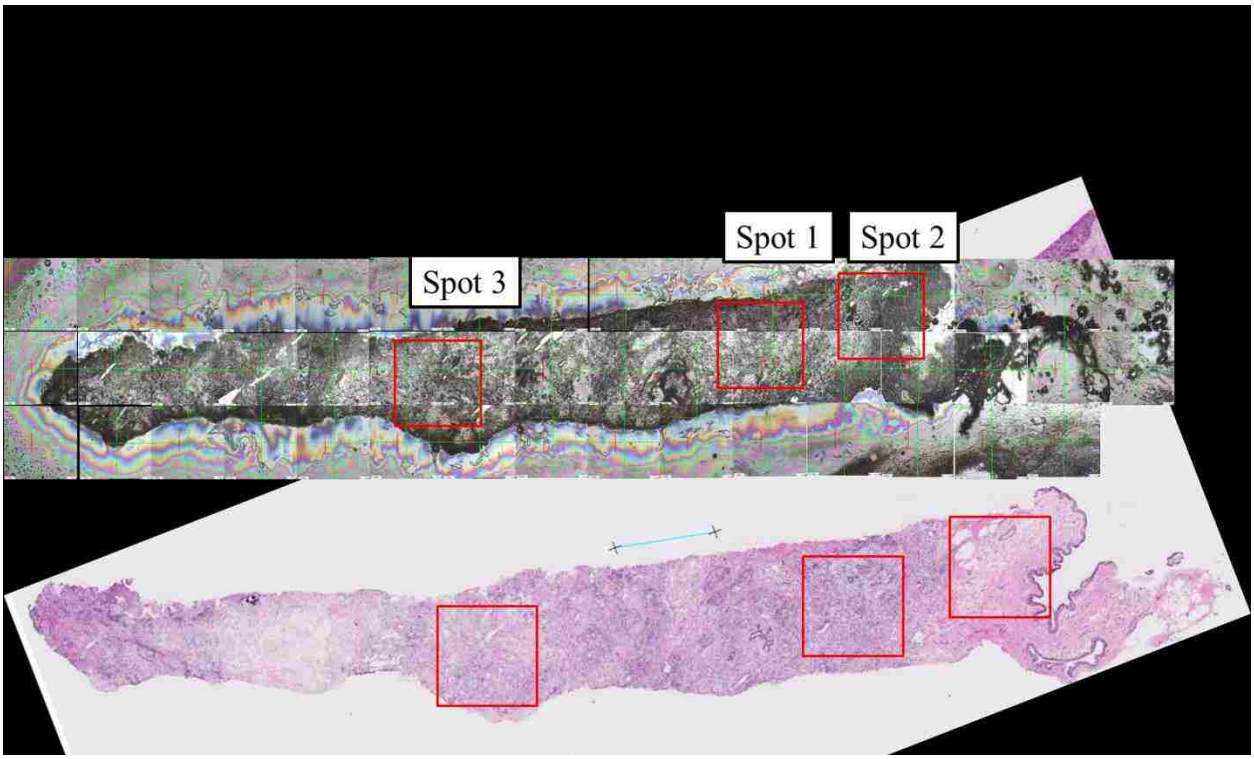


**Figure A.1.** H&E and corresponding ToF-SIMS camera stitch of tissue 120803 analysis areas.

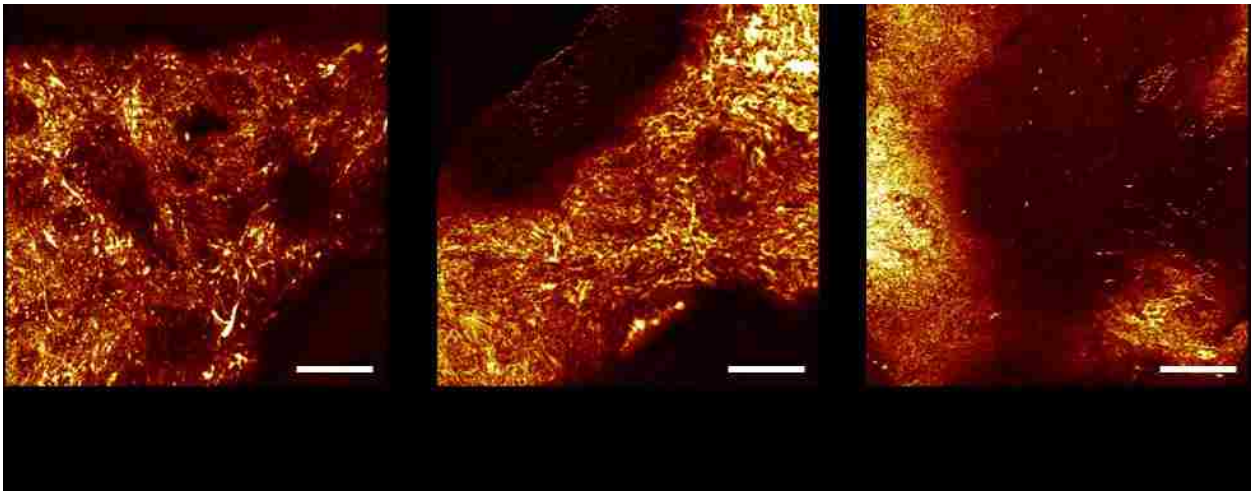

**Figure A.2.** High spatial resolution ToF-SIMS images of summed $CN^-$ and $CNO^-$ analysis areas from tissue 120803. Scale bars are 200 µm.

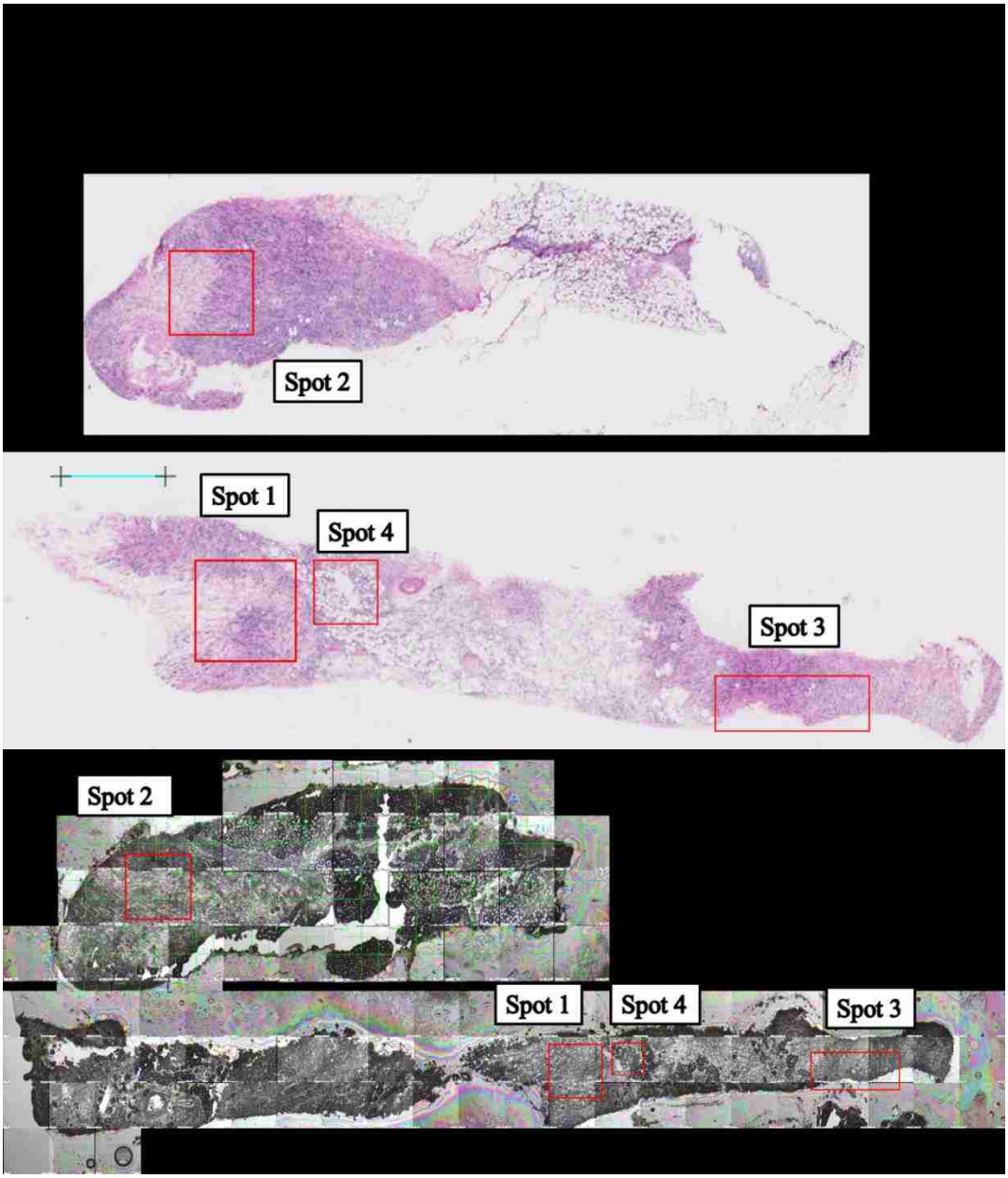


**Figure A.3.** H&E and corresponding ToF-SIMS camera stitch of tissue 120804 analysis areas.

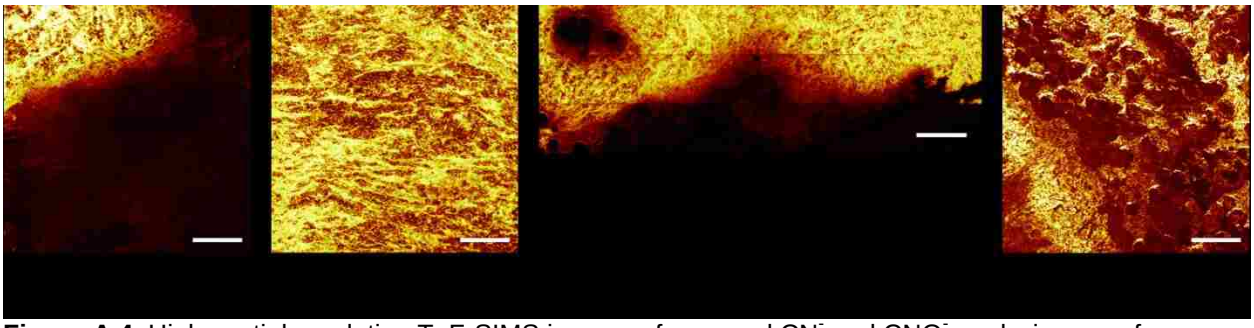

**Figure A.4.** High spatial resolution ToF-SIMS images of summed $CN^-$ and $CNO^-$ analysis areas from tissue 120804. Scale bars are 200 µm.

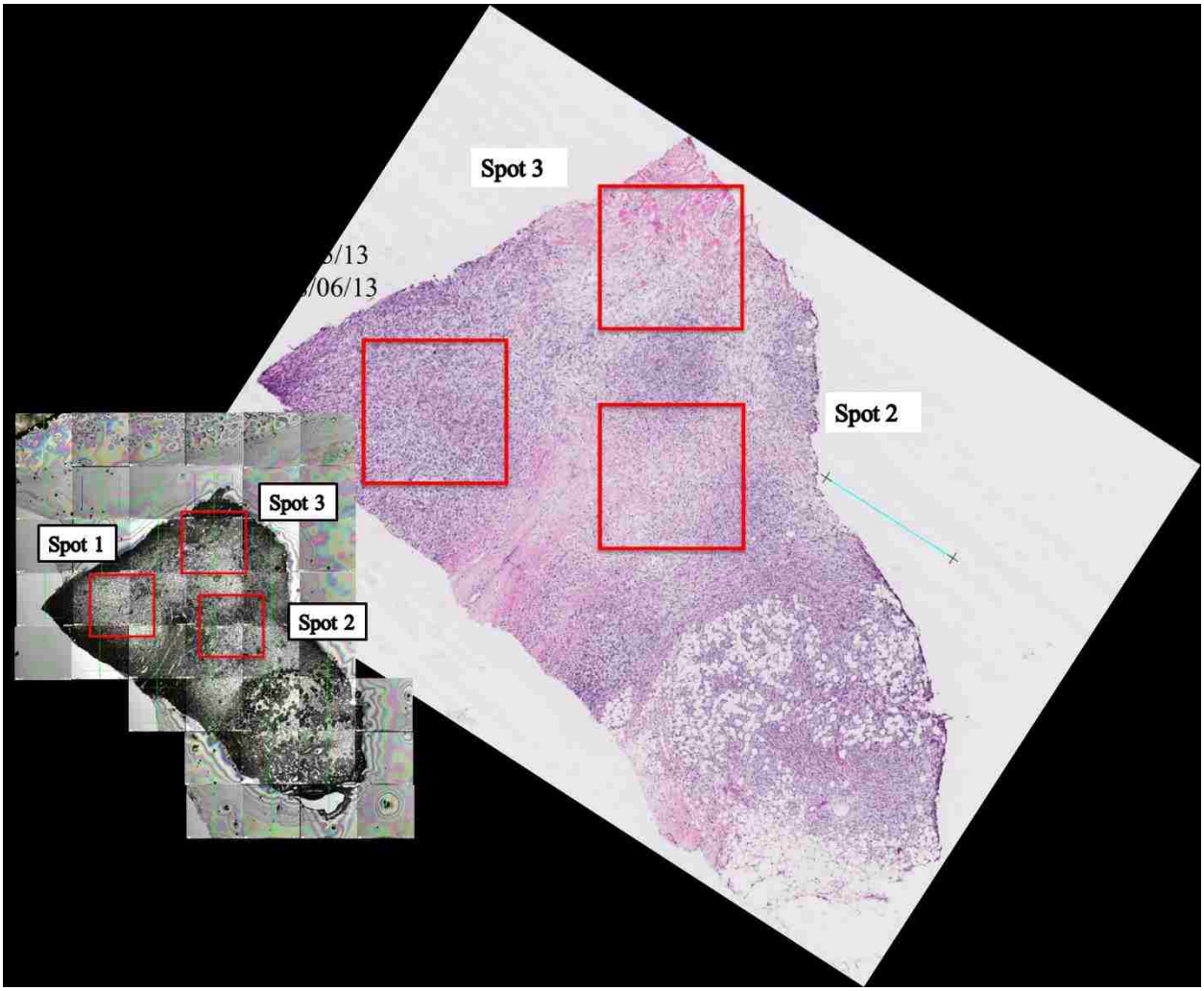


**Figure A.5.** H&E and corresponding ToF-SIMS camera stitch of tissue 120924 analysis areas.

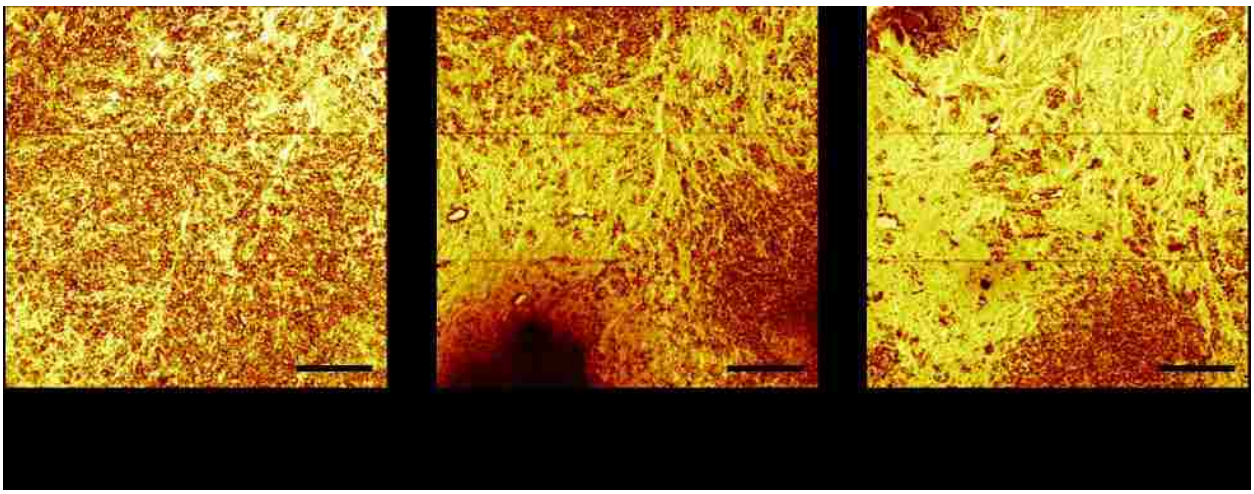

**Figure A.6.** High spatial resolution ToF-SIMS images of summed $CN^-$ and $CNO^-$ analysis areas from tissue 120924. Scale bars are 200 µm.

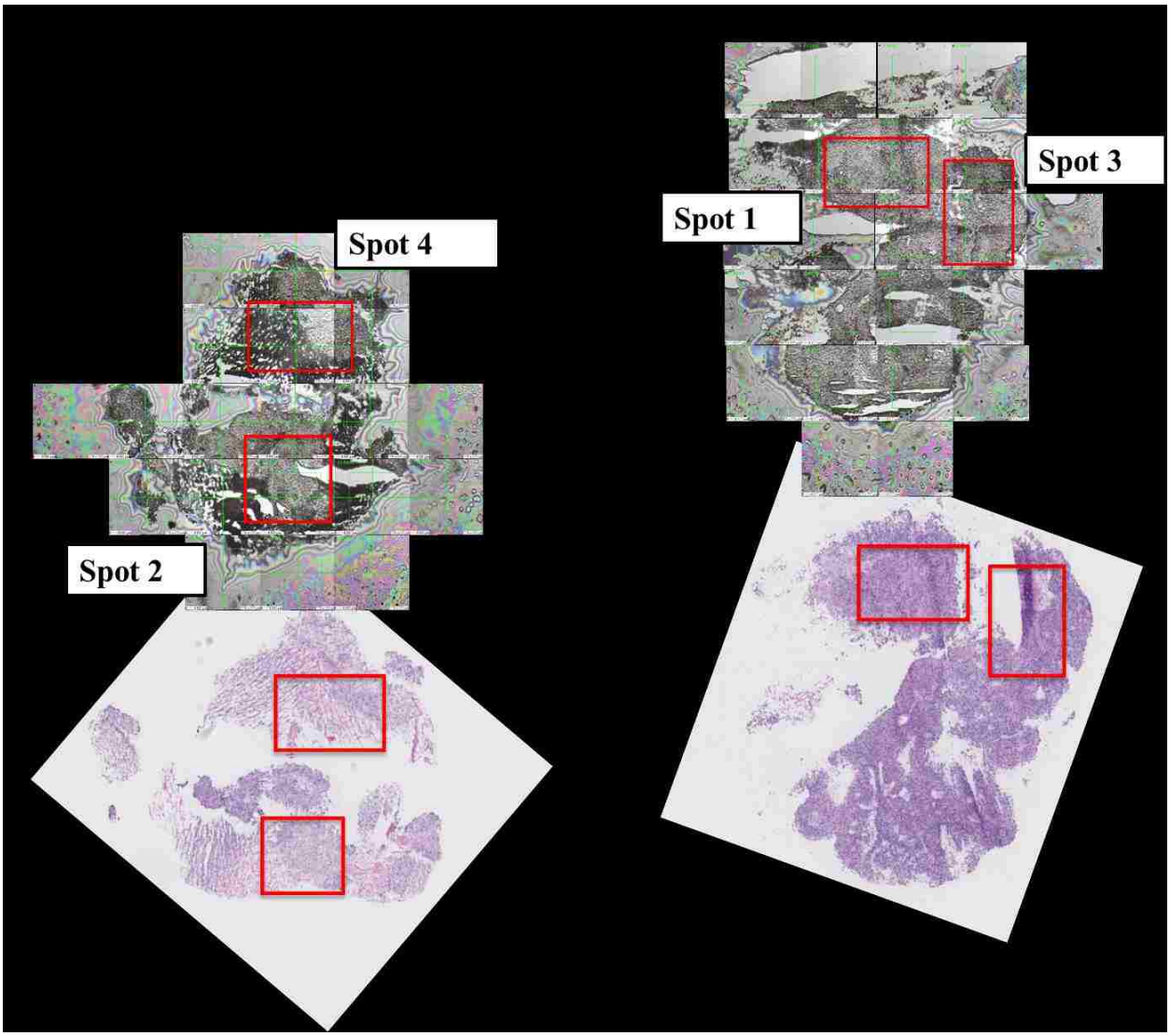


**Figure A.7.** H&E and corresponding ToF-SIMS camera stitch of tissue 120805 analysis areas.

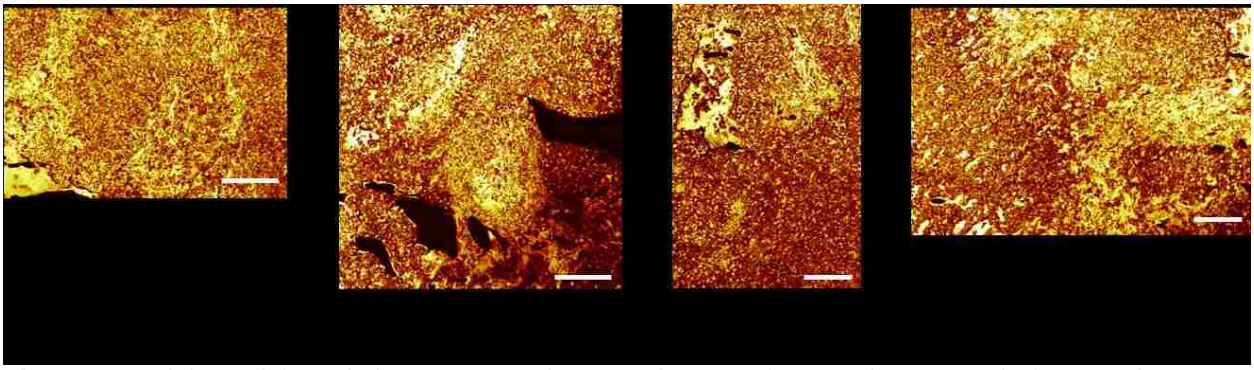

**Figure A.8.** High spatial resolution ToF-SIMS images of summed $CN^-$ and $CNO^-$ analysis areas from tissue 120805. Scale bars are 200 µm.

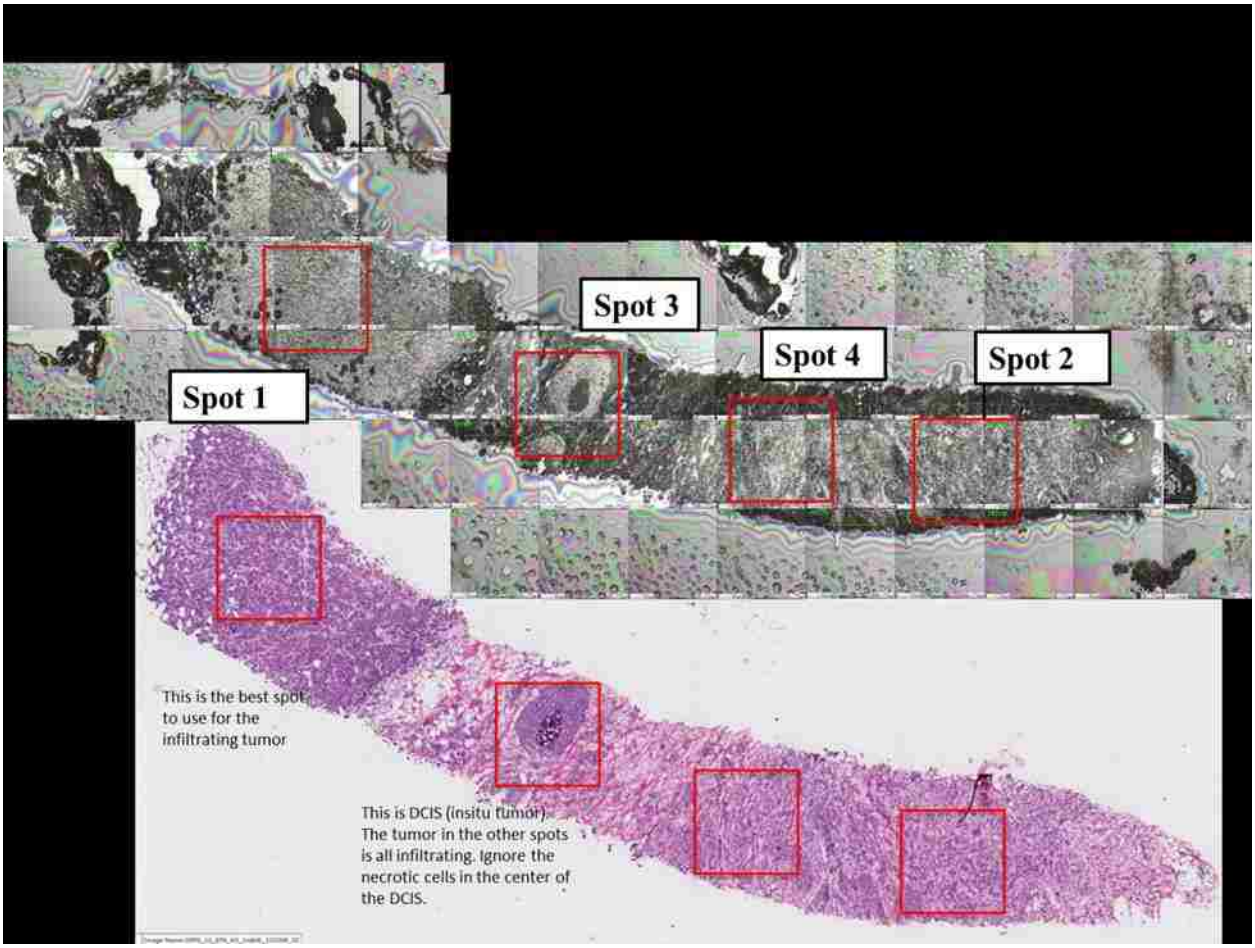


**Figure A.9.** H&E and corresponding ToF-SIMS camera stitch of tissue 120876 analysis areas.

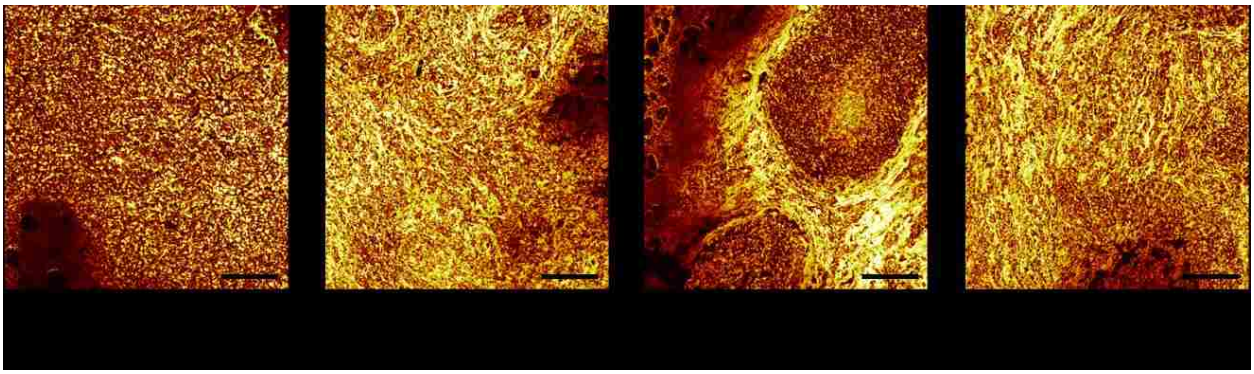

**Figure A.10.** High spatial resolution ToF-SIMS images of summed $CN^-$ and $CNO^-$ analysis areas from tissue 120876. Scale bars are 200 µm.

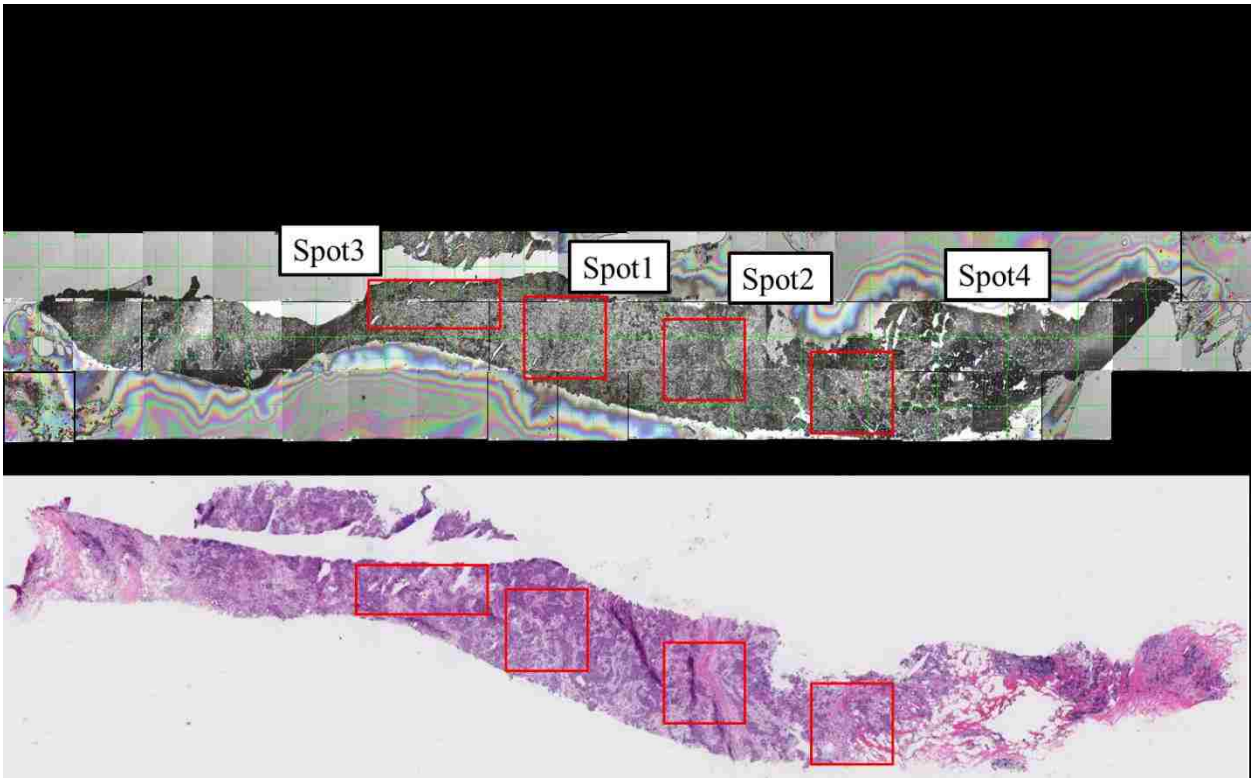


**Figure A.11.** H&E and corresponding ToF-SIMS camera stitch of tissue 120926 analysis areas.

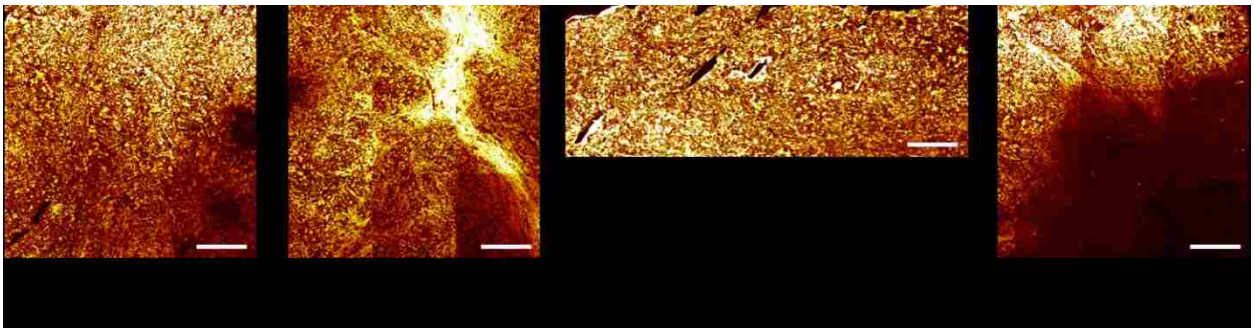

**Figure A.12.** High spatial resolution ToF-SIMS images of summed $CN^-$ and $CNO^-$ analysis areas from tissue 120926. Scale bars are 200 µm.

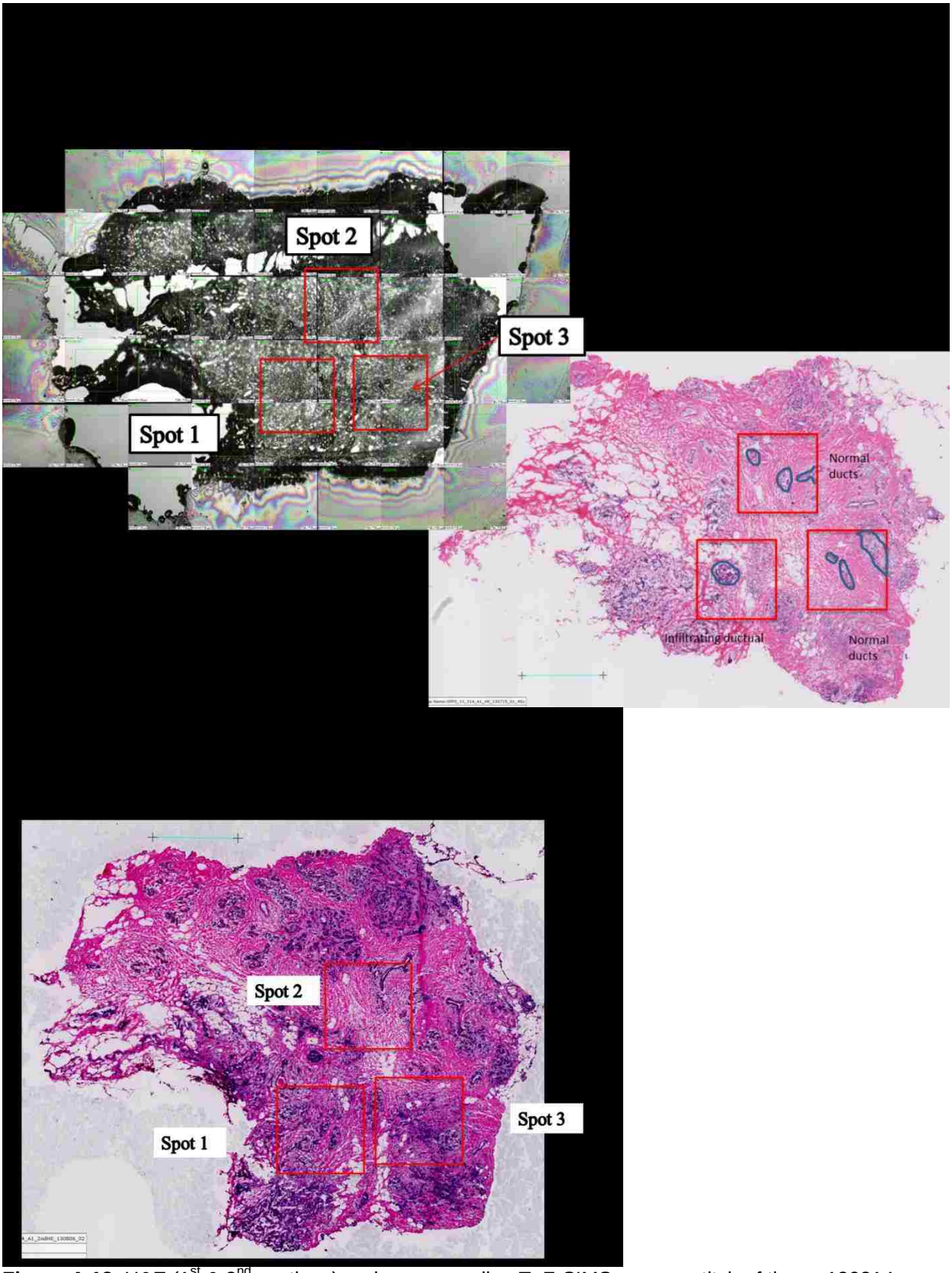


**Figure A.13.** H&E (1st & 2nd sections) and corresponding ToF-SIMS camera stitch of tissue 130314 analysis areas.

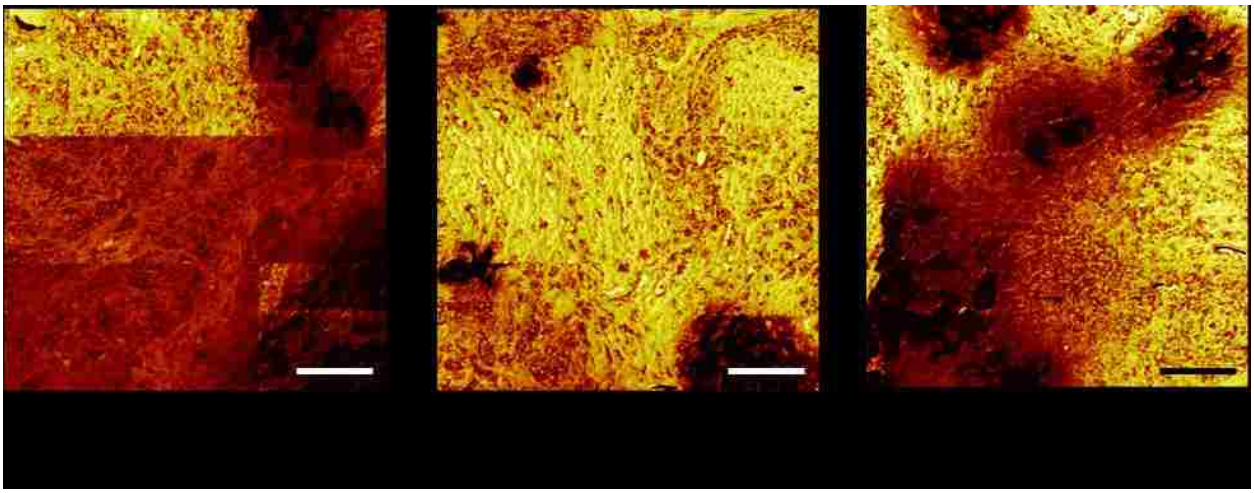

**Figure A.14.** High spatial resolution ToF-SIMS images of summed $CN^-$ and $CNO^-$ analysis areas from tissue 130314. Scale bars are 200 µm.

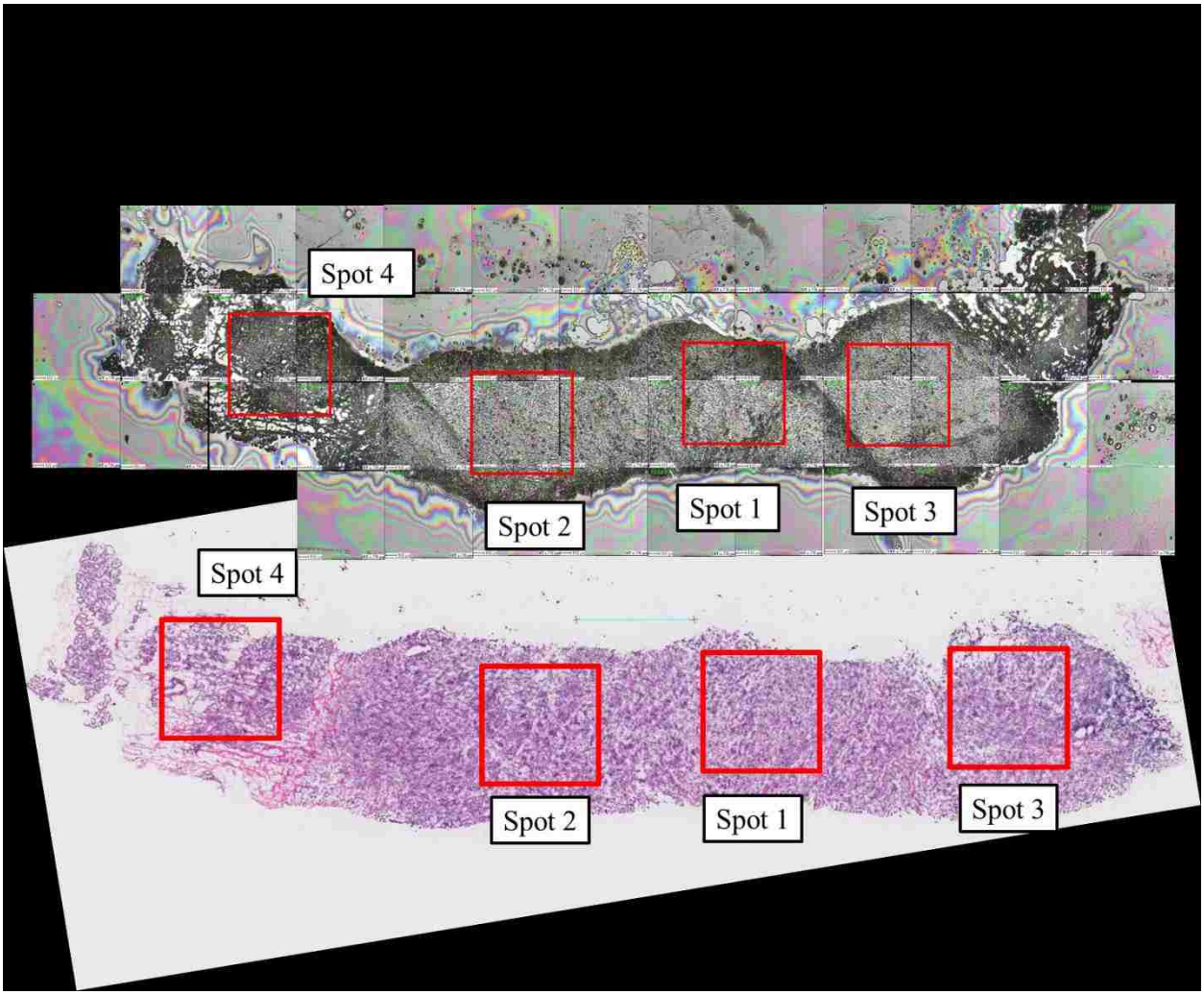


**Figure A.15.** H&E and corresponding ToF-SIMS camera stitch of tissue 130162 analysis areas.

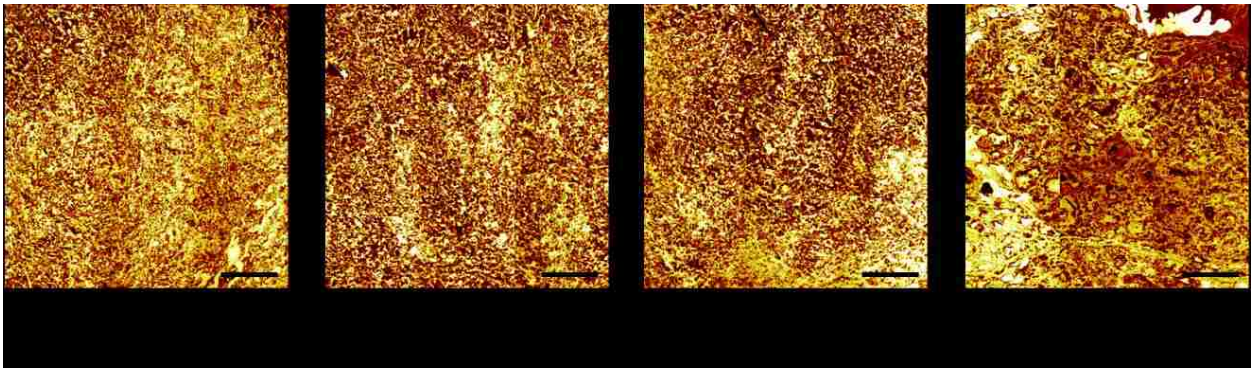

**Figure A.16.** High spatial resolution ToF-SIMS images of summed $CN^-$ and $CNO^-$ analysis areas from tissue 130162. Scale bars are 200 µm.

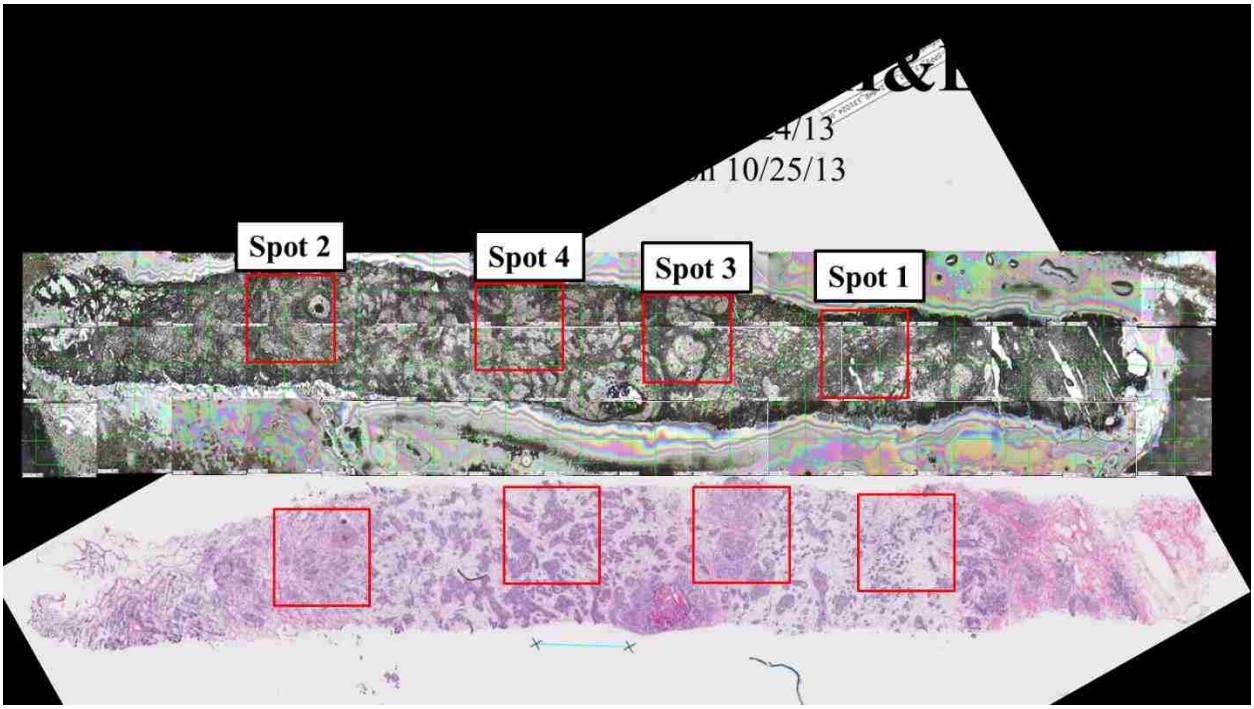


**Figure A.17.** H&E and corresponding ToF-SIMS camera stitch of tissue 130163 analysis areas.

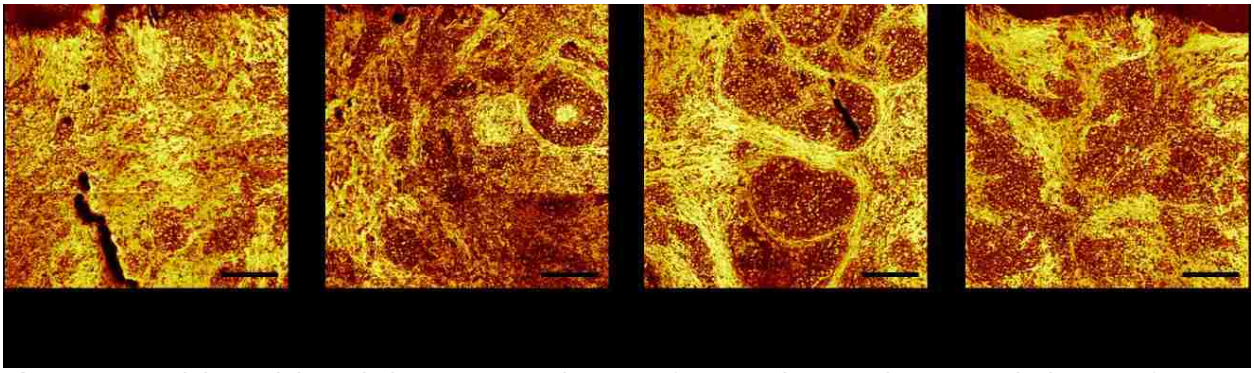

**Figure A.18.** High spatial resolution ToF-SIMS images of summed $CN^-$ and $CNO^-$ analysis areas from tissue 130163. Scale bars are 200 µm.

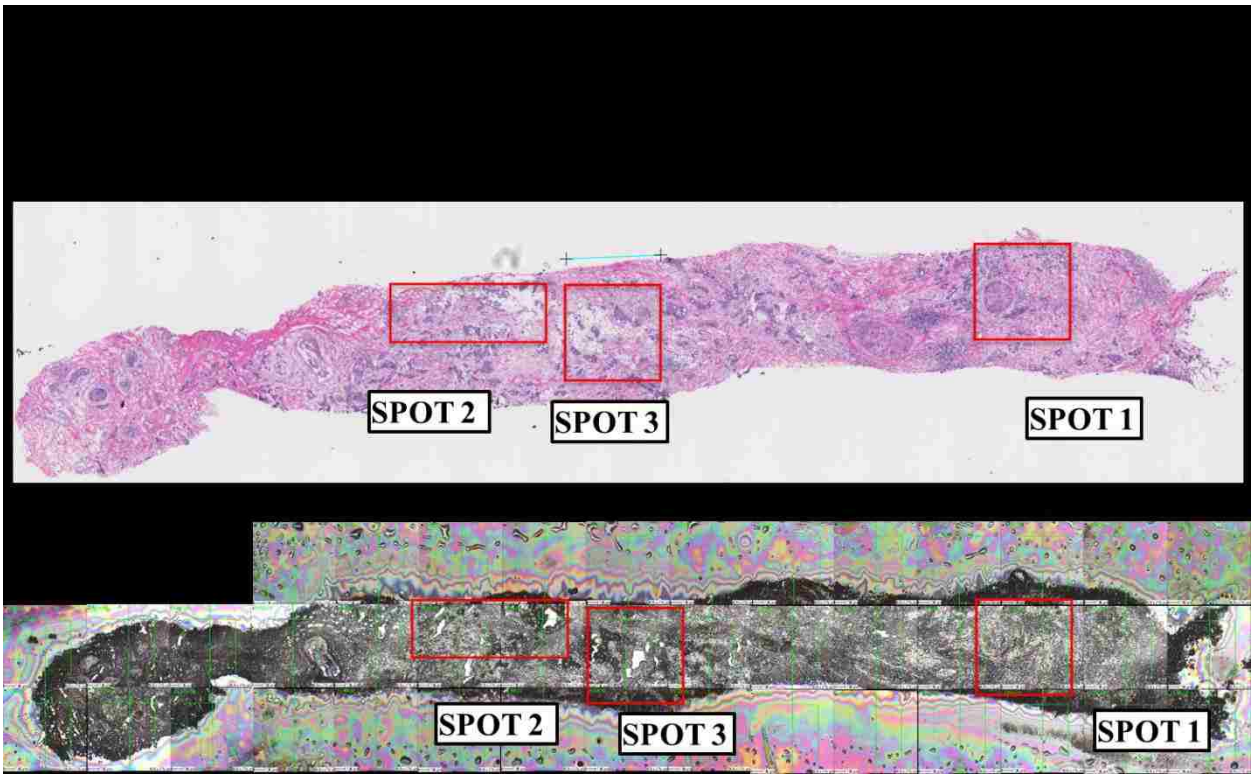


**Figure A.19.** H&E and corresponding ToF-SIMS camera stitch of tissue 130200 analysis areas.

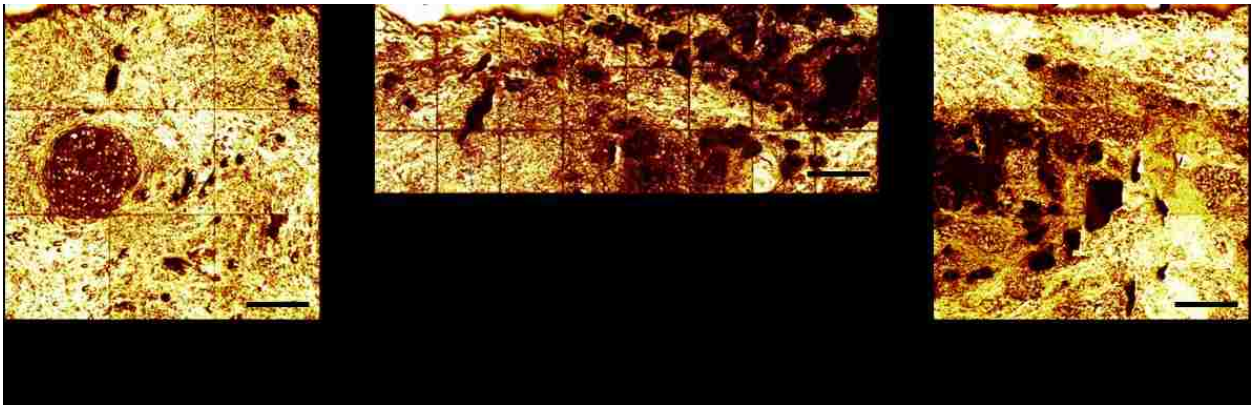

**Figure A.20.** High spatial resolution ToF-SIMS images of summed $CN^-$ and $CNO^-$ analysis areas from tissue 130200. Scale bars are 200 µm.

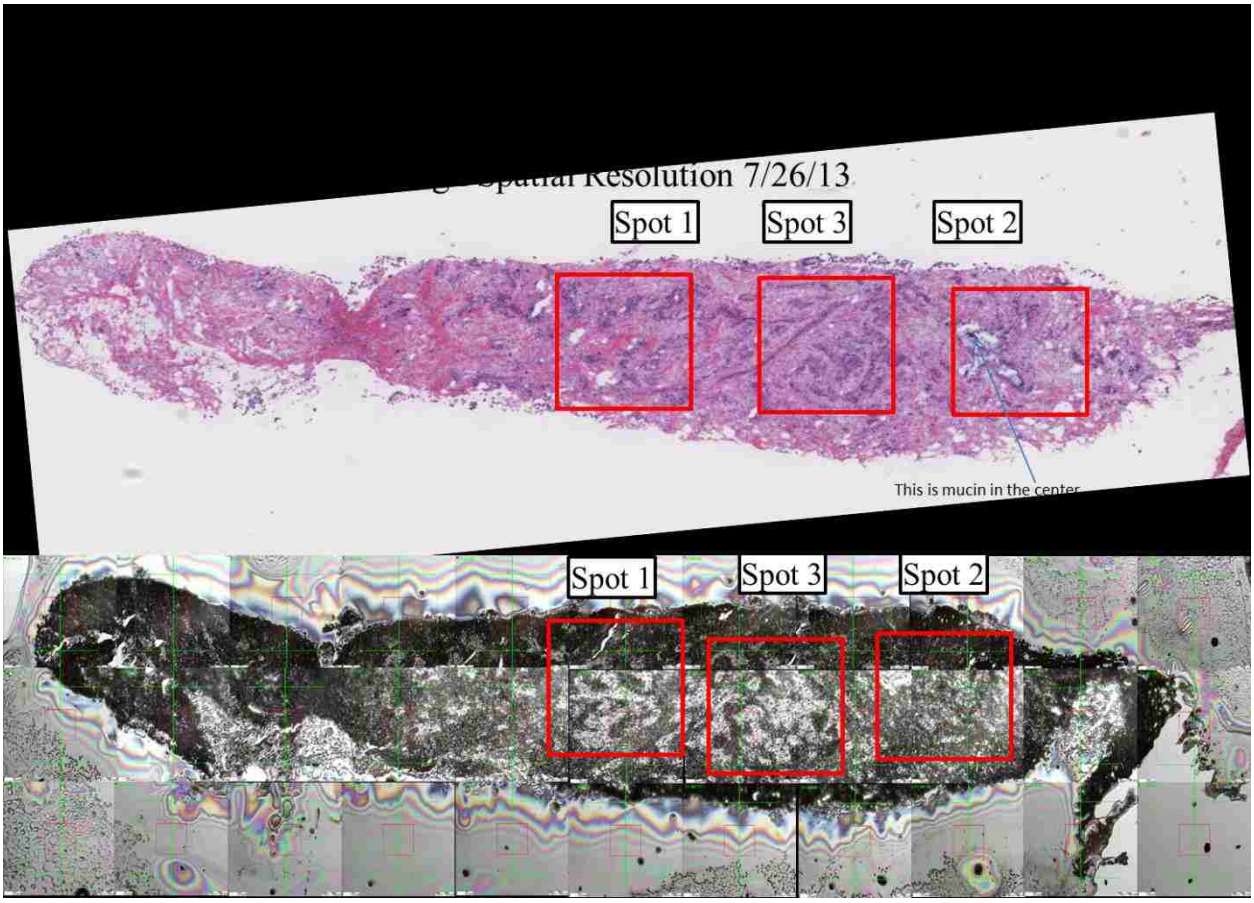


**Figure A.21.** H&E and corresponding ToF-SIMS camera stitch of tissue 130199 analysis areas.

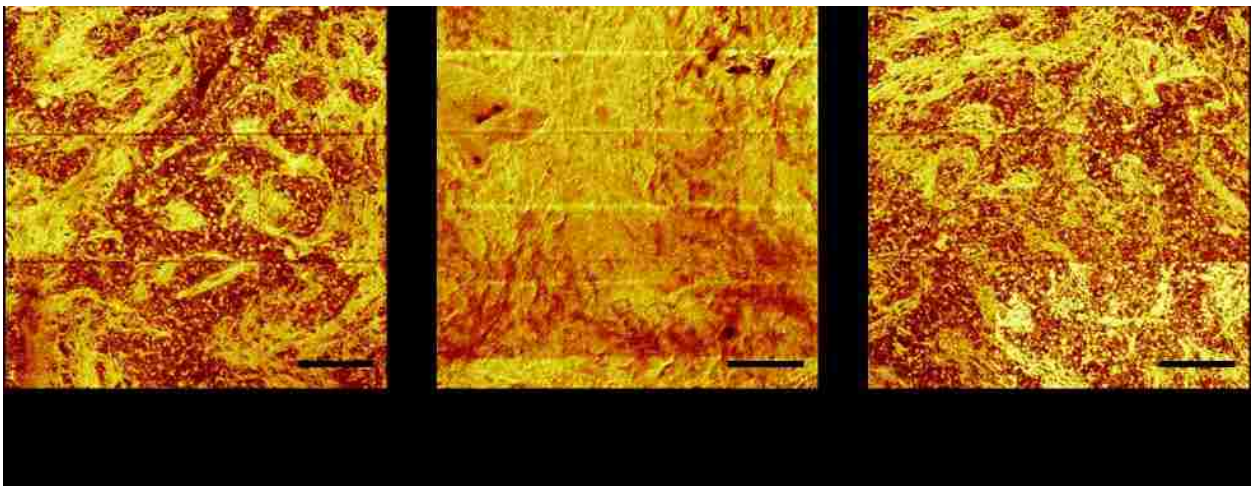

**Figure A.22.** High spatial resolution ToF-SIMS images of summed $CN^-$ and $CNO^-$ analysis areas from tissue 130199. Scale bars are 200 µm.

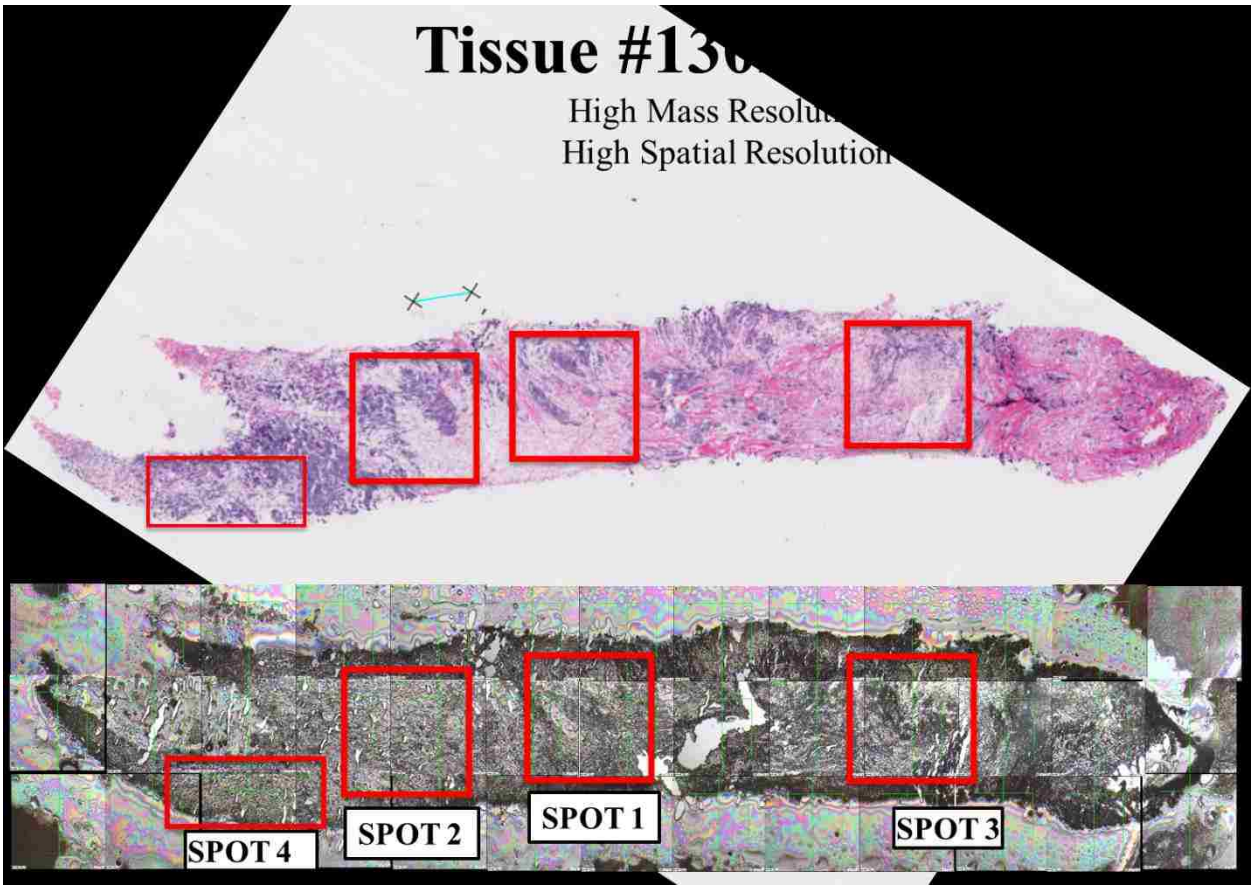


**Figure A.23.** H&E and corresponding ToF-SIMS camera stitch of tissue 130250 analysis areas.

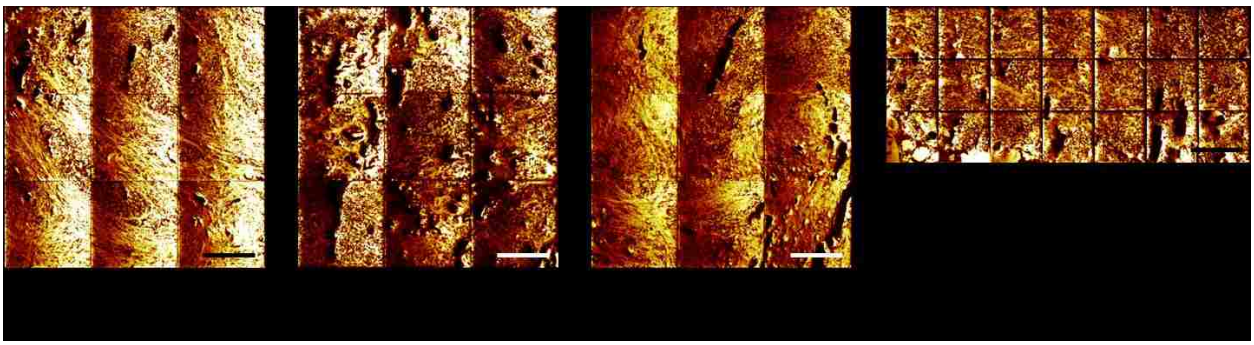

**Figure A.24.** High spatial resolution ToF-SIMS images of summed $CN^-$ and $CNO^-$ analysis areas from tissue 130250. Scale bars are 200 µm.

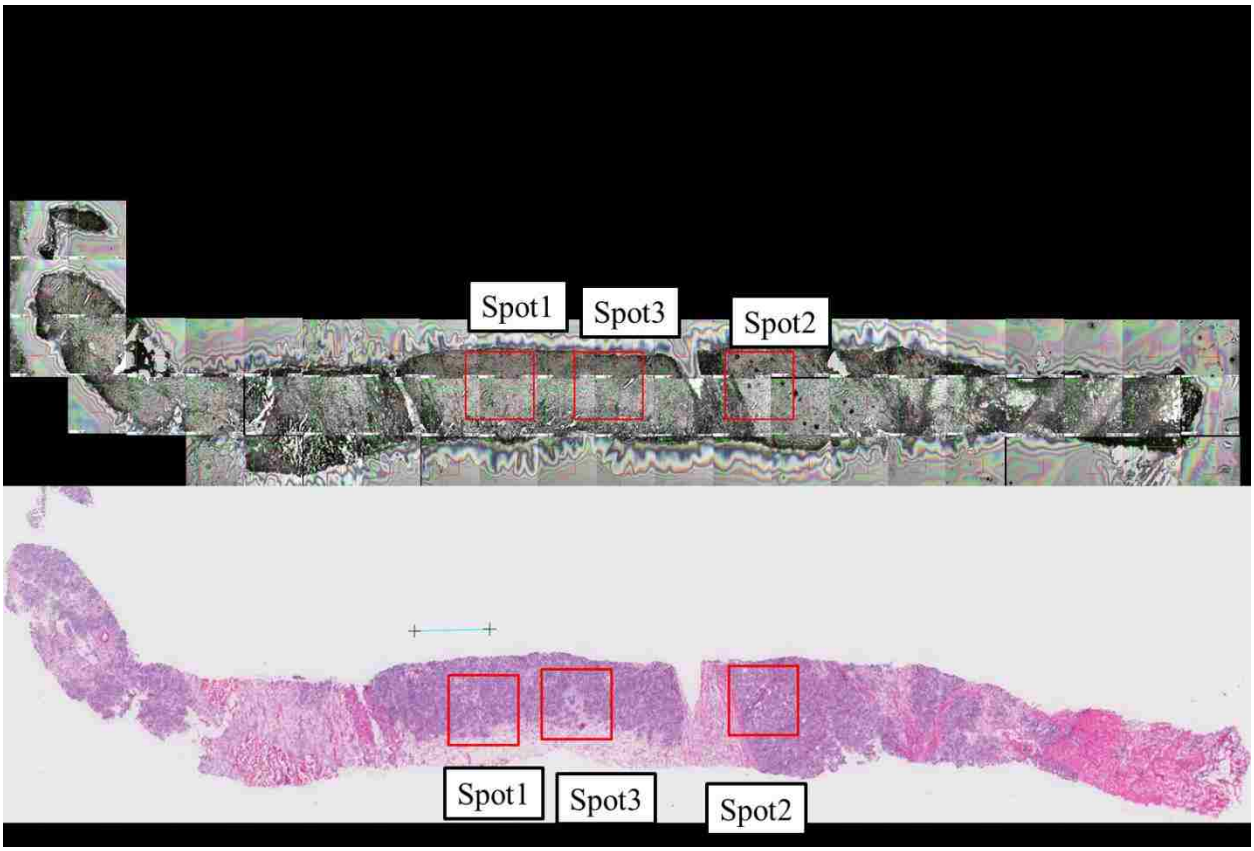


**Figure A.25.** H&E and corresponding ToF-SIMS camera stitch of tissue 130315 analysis areas.

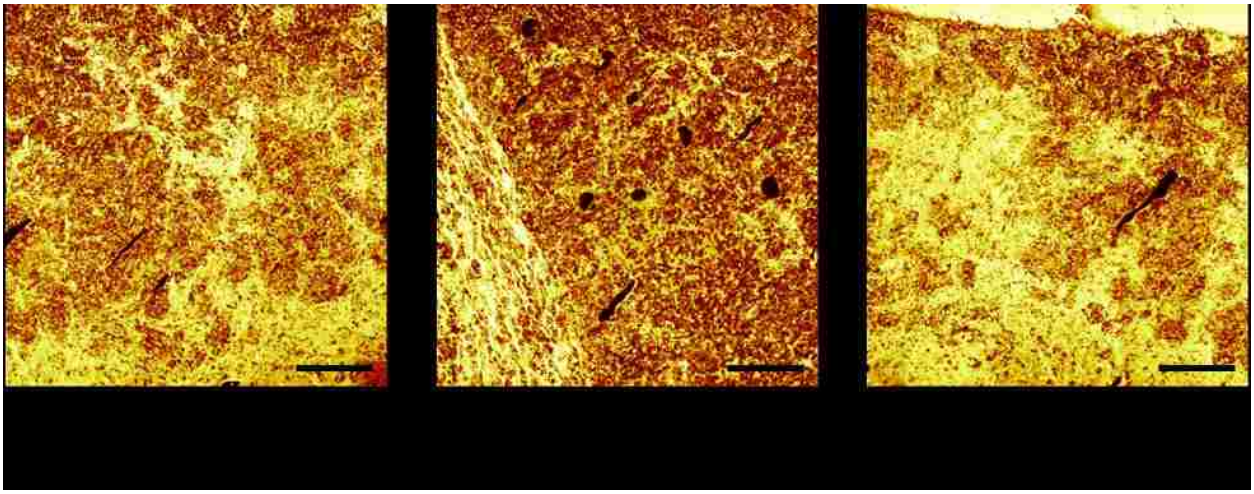

**Figure A.26.** High spatial resolution ToF-SIMS images of summed $CN^-$ and $CNO^-$ analysis areas from tissue 130315. Scale bars are 200 µm.

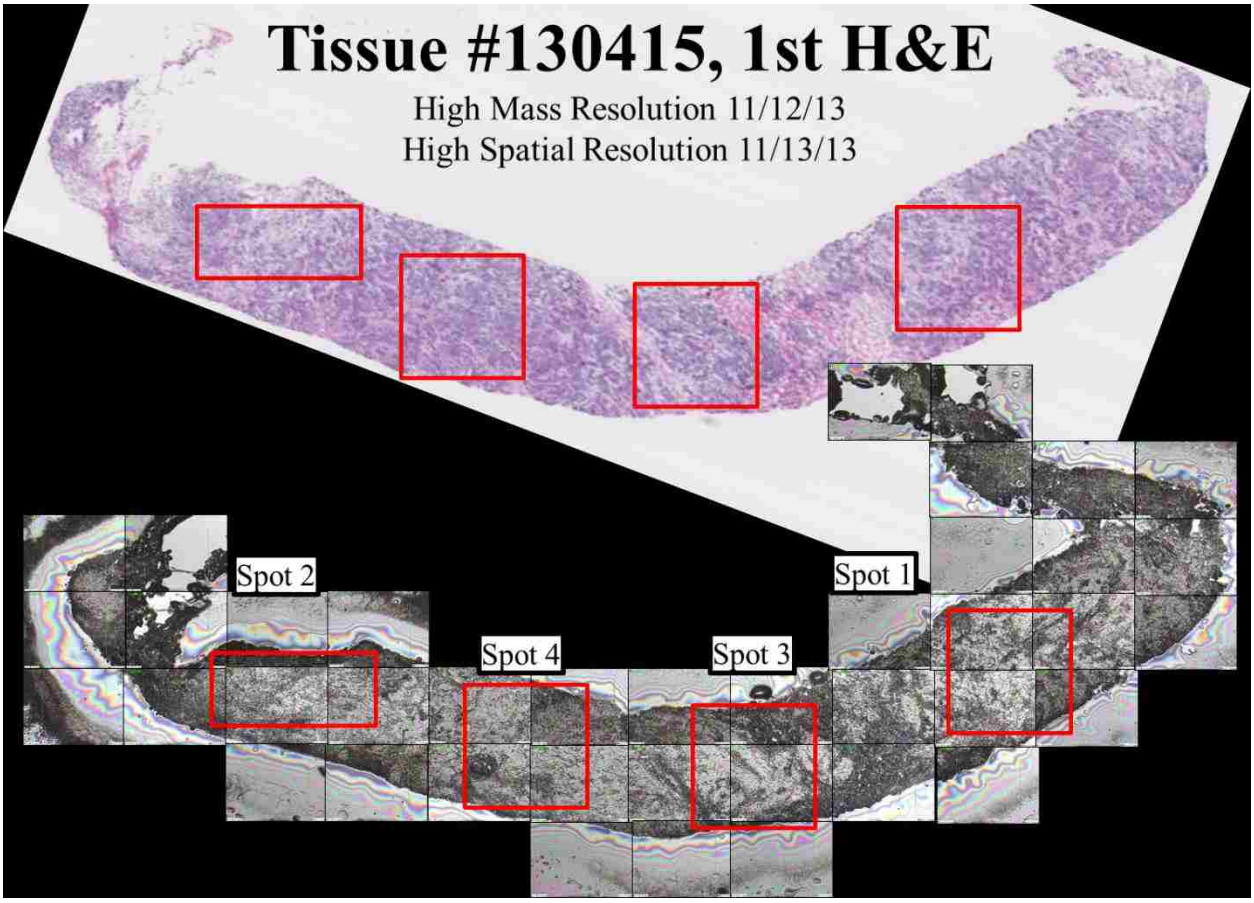


**Figure A.27.** H&E and corresponding ToF-SIMS camera stitch of tissue 130415 analysis areas.

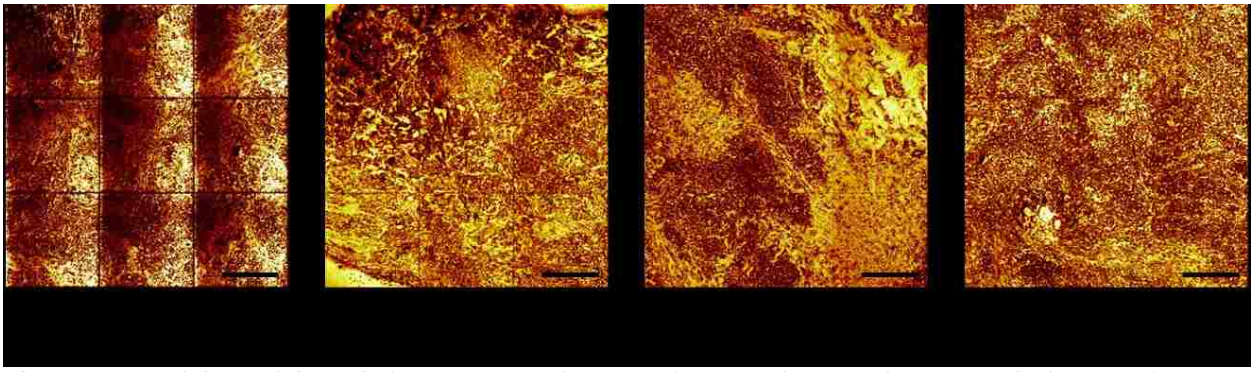

**Figure A.28.** High spatial resolution ToF-SIMS images of summed $CN^-$ and $CNO^-$ analysis areas from tissue 130415. Scale bars are 200 µm.

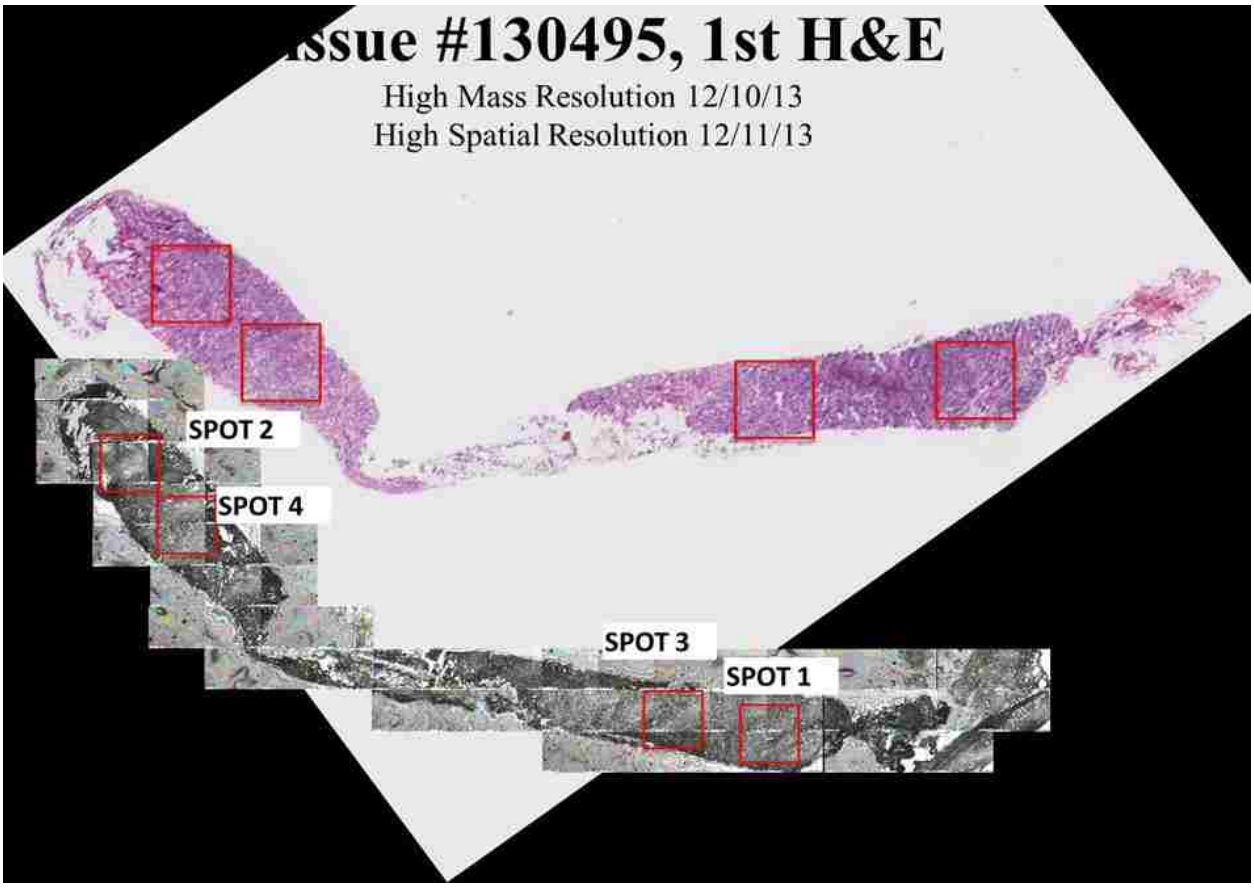


**Figure A.29.** H&E and corresponding ToF-SIMS camera stitch of tissue 130495 analysis areas.

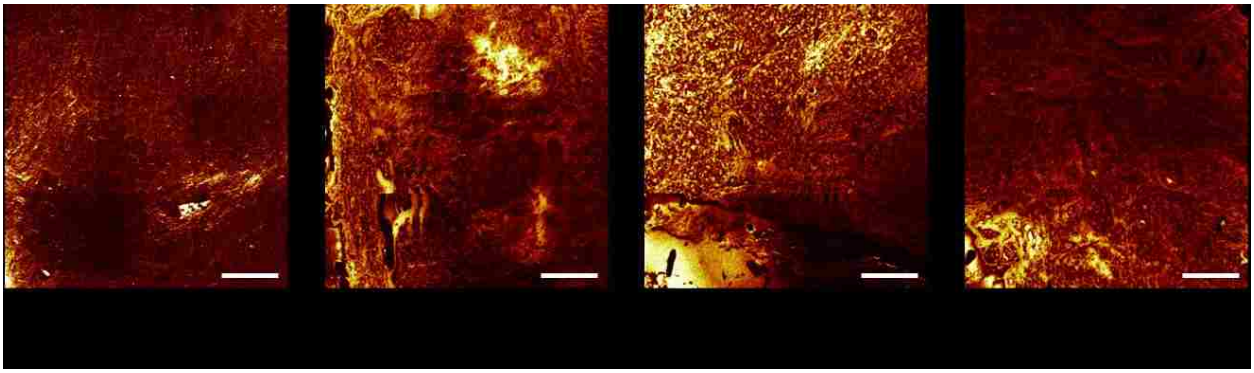

**Figure A.30.** High spatial resolution ToF-SIMS images of summed $CN^-$ and $CNO^-$ analysis areas from tissue 130495. Scale bars are 200 µm.

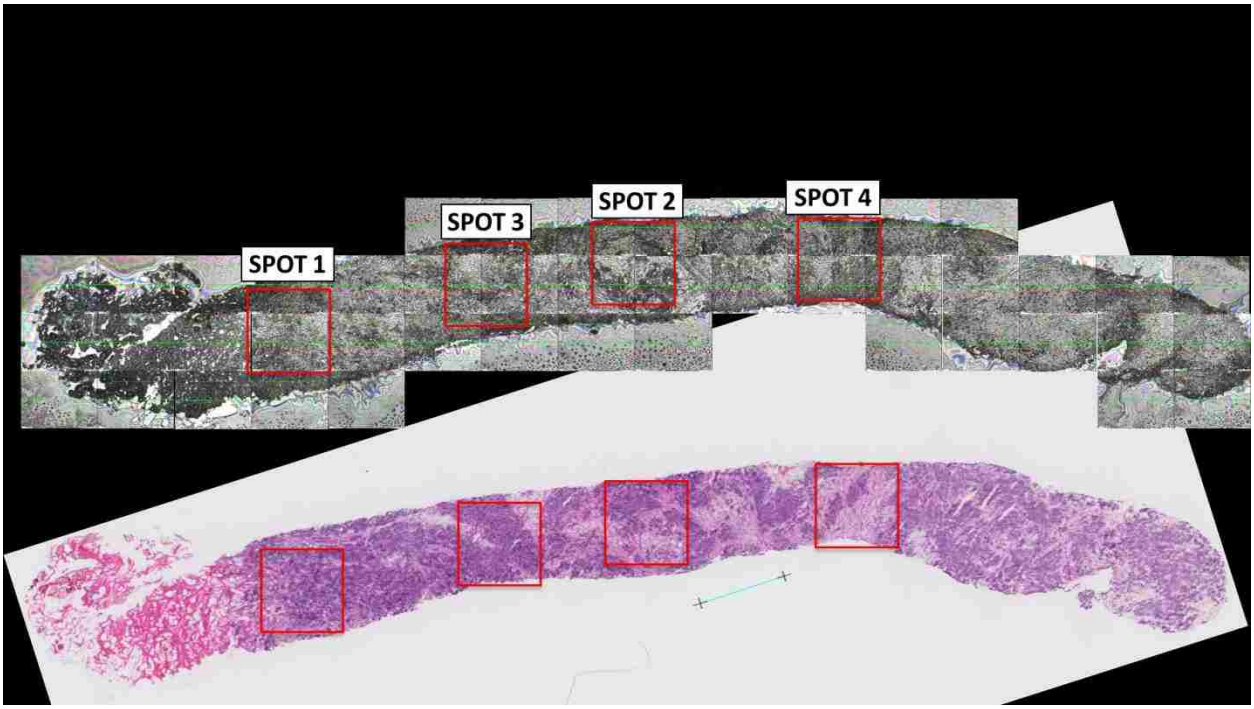


**Figure A.31.** H&E and corresponding ToF-SIMS camera stitch of tissue 130496 analysis areas.

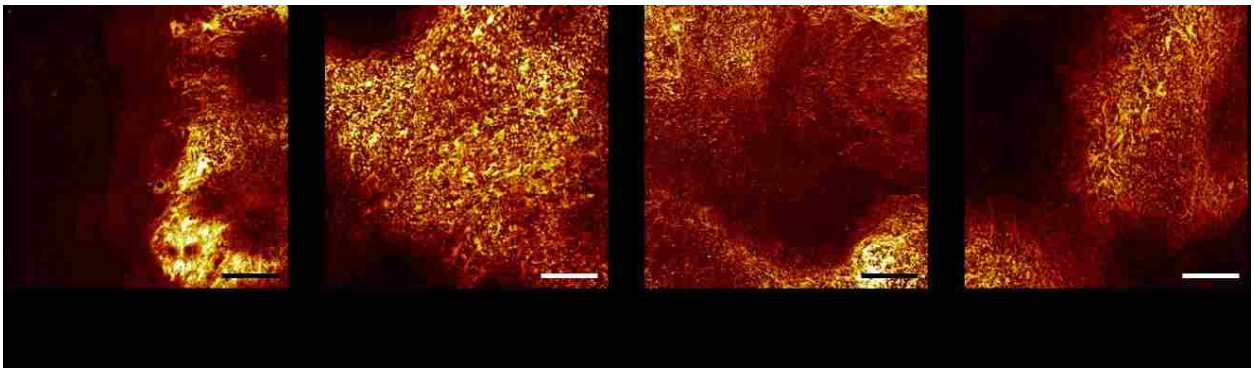

**Figure A.32.** High spatial resolution ToF-SIMS images of summed $CN^-$ and $CNO^-$ analysis areas from tissue 130496. Scale bars are 200 µm.

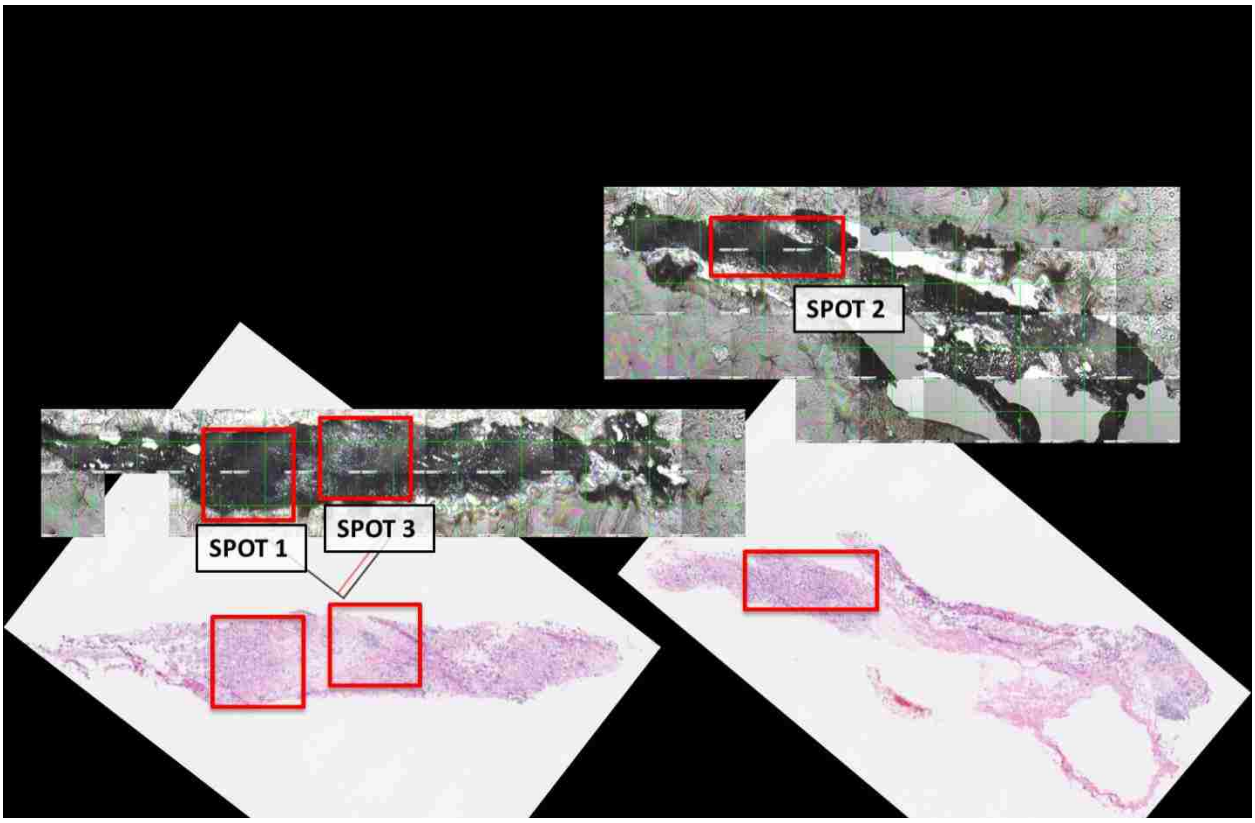


**Figure A.33.** H&E and corresponding ToF-SIMS camera stitch of tissue 130698 analysis areas.

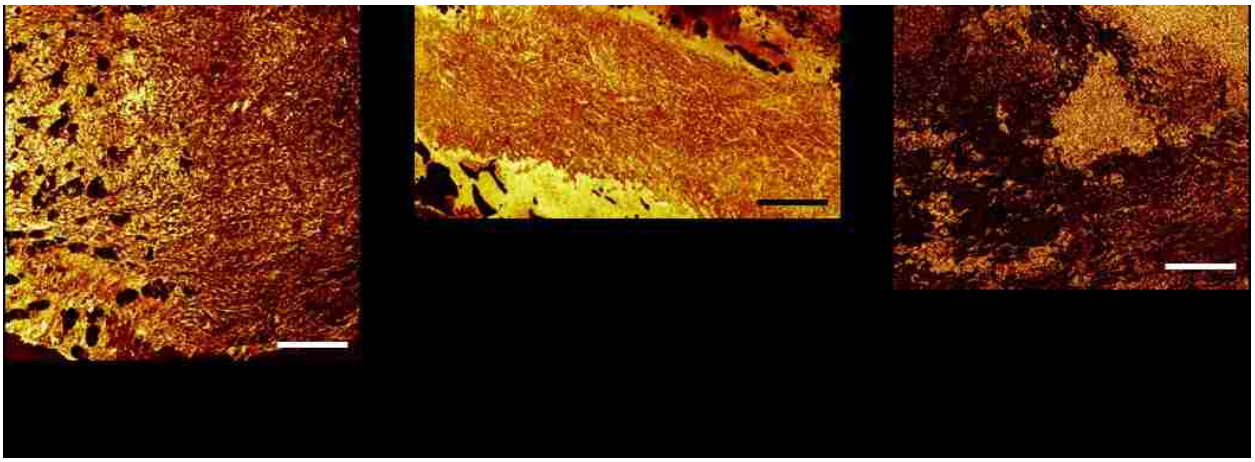

**Figure A.34.** High spatial resolution ToF-SIMS images of summed $CN^-$ and $CNO^-$ analysis areas from tissue 130698. Scale bars are 200 µm.

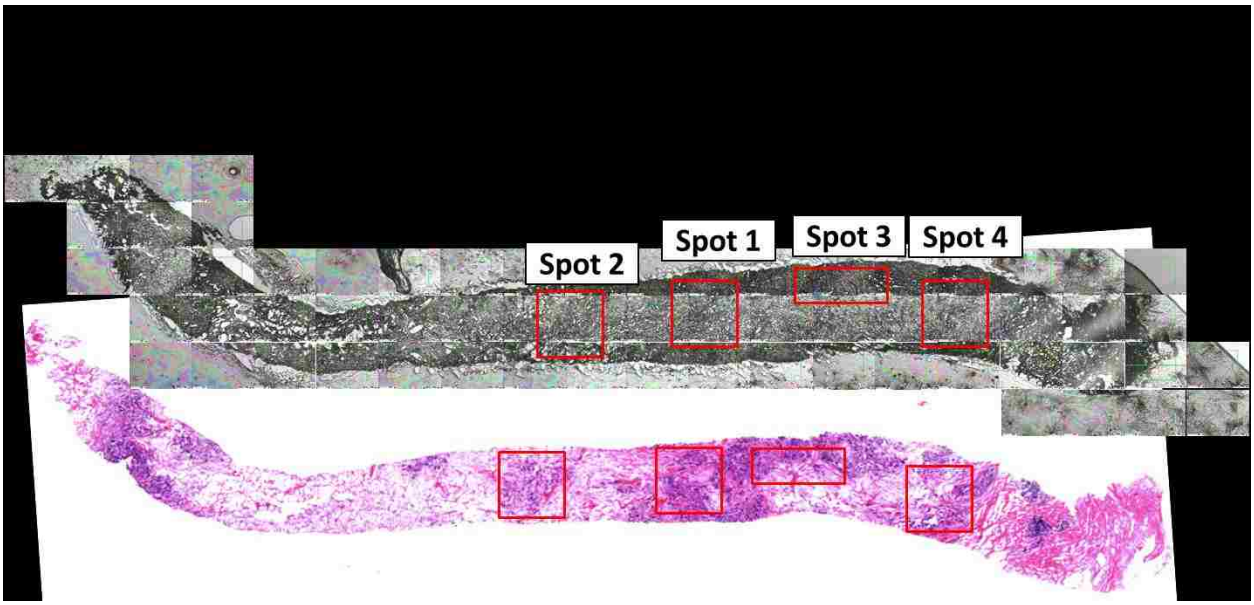


**Figure A.35.** H&E and corresponding ToF-SIMS camera stitch of tissue 130528 analysis areas.

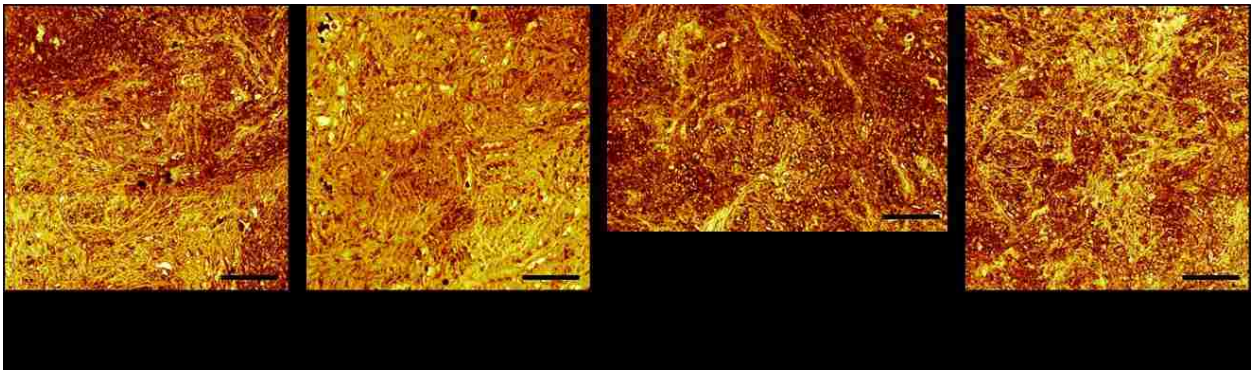

**Figure A.36.** High spatial resolution ToF-SIMS images of summed $CN^-$ and $CNO^-$ analysis areas from tissue 130528. Scale bars are 200 µm.

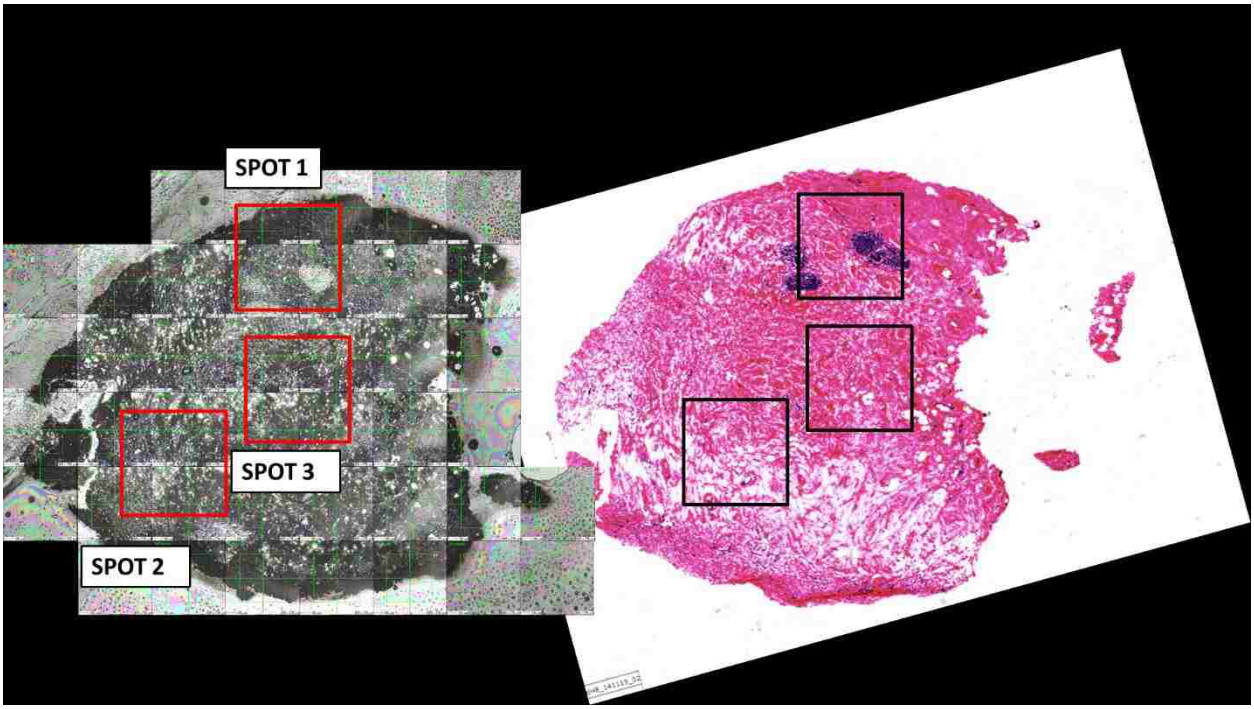


**Figure A.37.** H&E and corresponding ToF-SIMS camera stitch of tissue 140276 analysis areas.

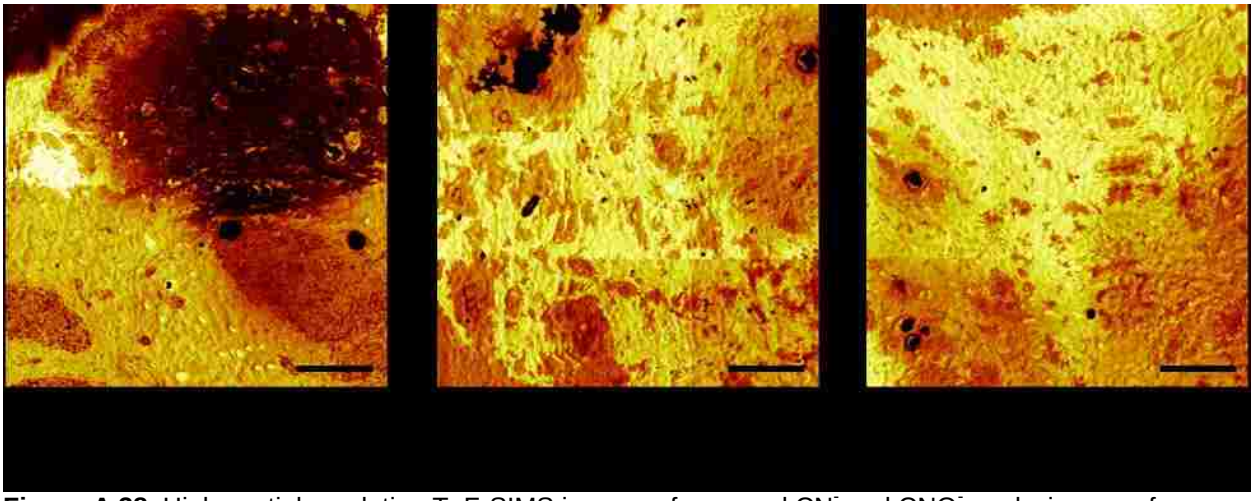

**Figure A.38.** High spatial resolution ToF-SIMS images of summed $CN^-$ and $CNO^-$ analysis areas from tissue 140276. Scale bars are 200 µm.

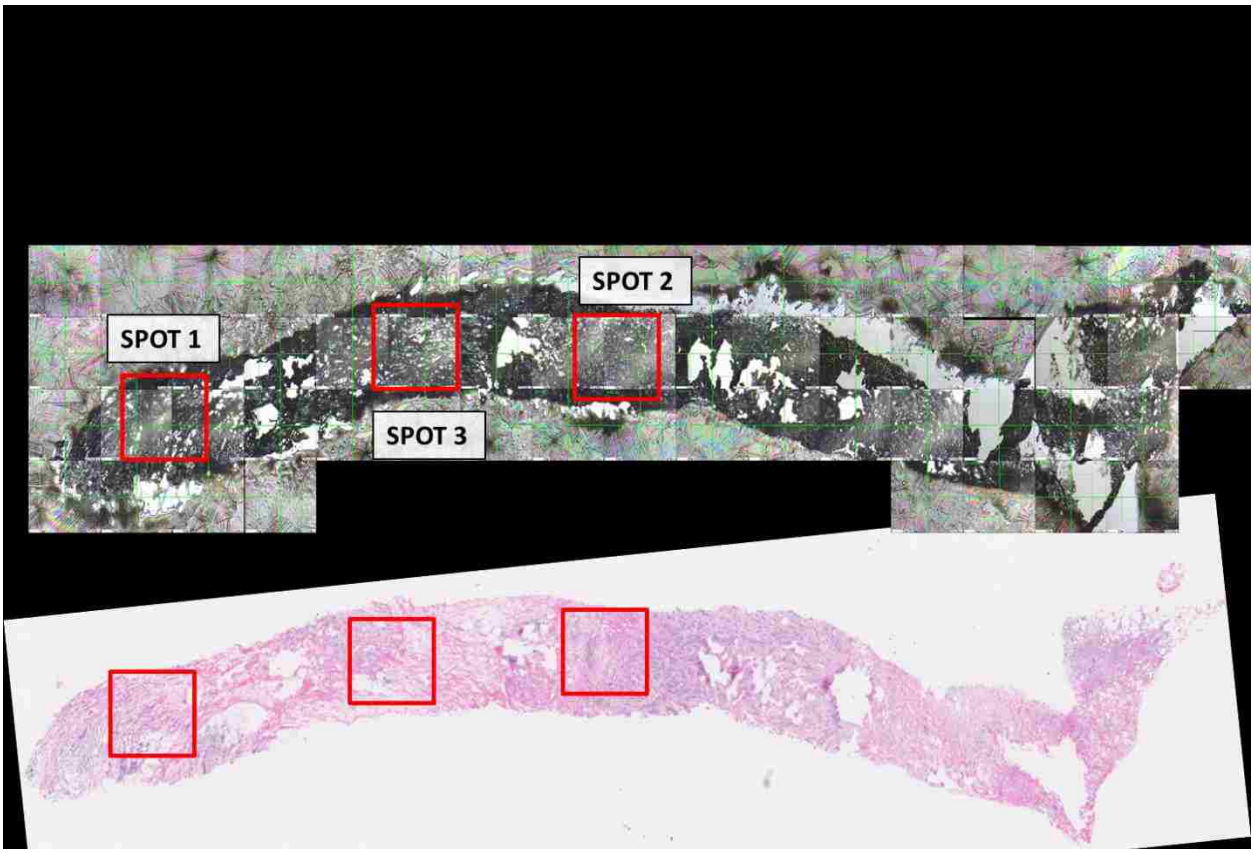


**Figure A.39.** H&E and corresponding ToF-SIMS camera stitch of tissue 130804 analysis areas.

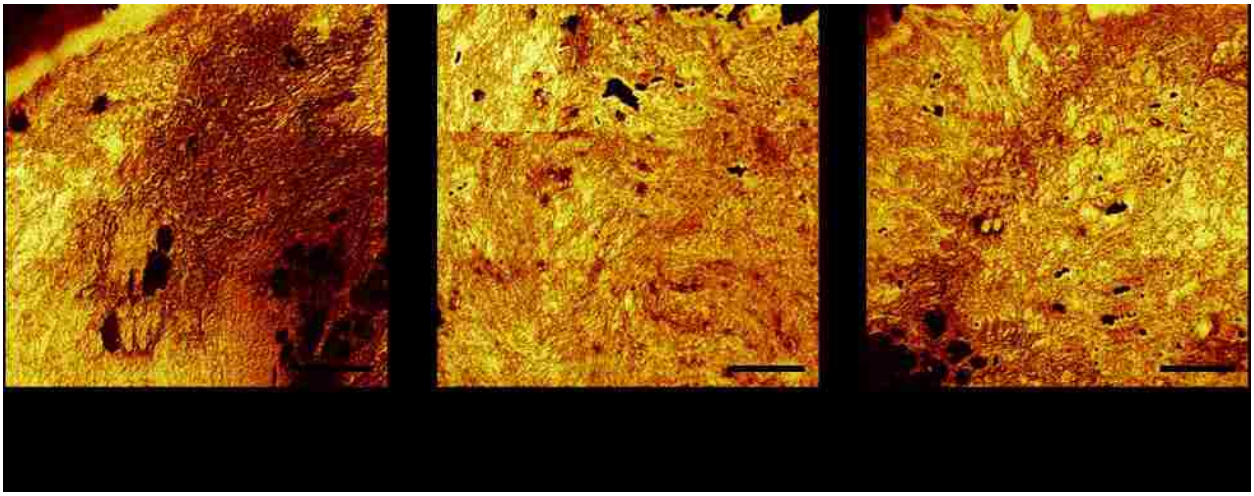

**Figure A.40.** High spatial resolution ToF-SIMS images of summed $CN^-$ and $CNO^-$ analysis areas from tissue 130804. Scale bars are 200 µm.

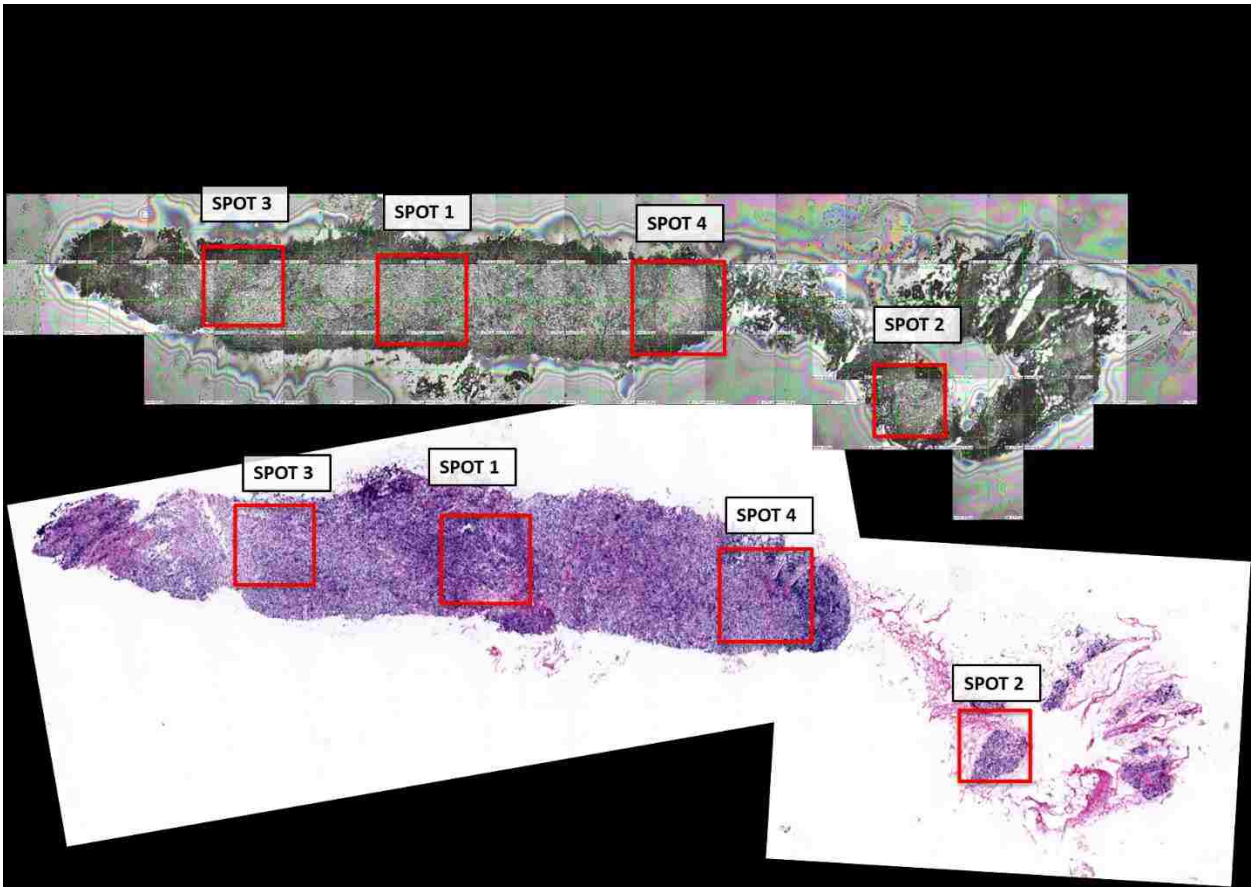


**Figure A.41.** H&E and corresponding ToF-SIMS camera stitch of tissue 130802 analysis areas.

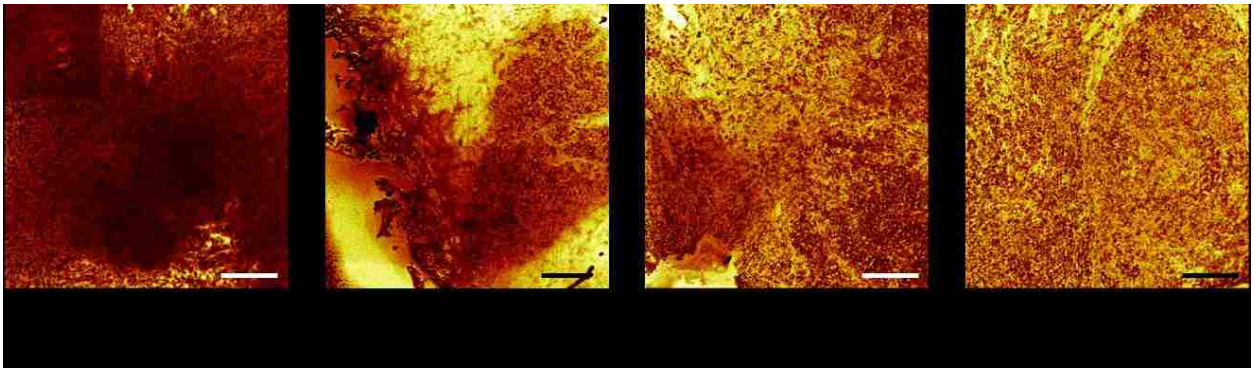

**Figure A.42.** High spatial resolution ToF-SIMS images of summed $CN^-$ and $CNO^-$ analysis areas from tissue 130802. Scale bars are 200 µm.

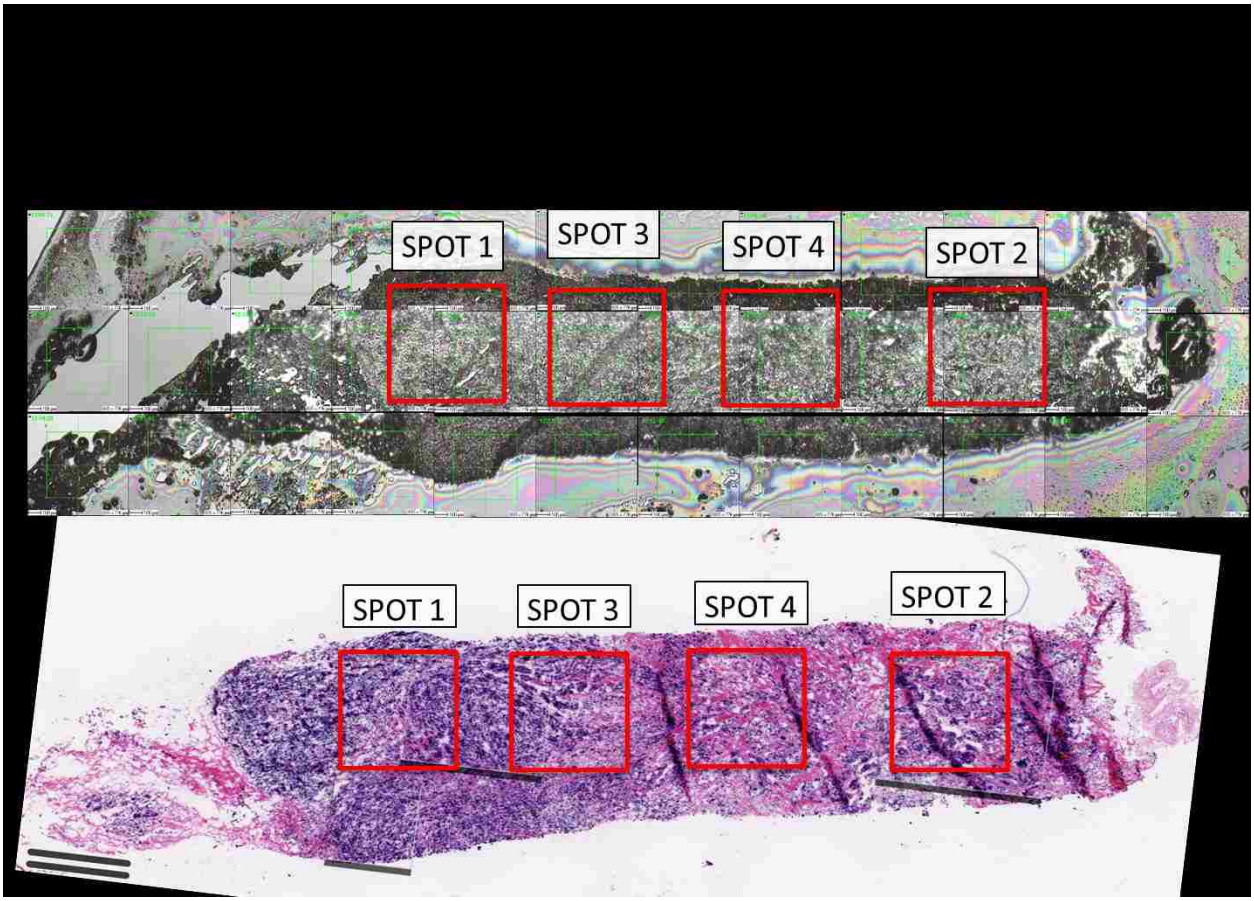


**Figure A.43.** H&E and corresponding ToF-SIMS camera stitch of tissue 130801 analysis areas.

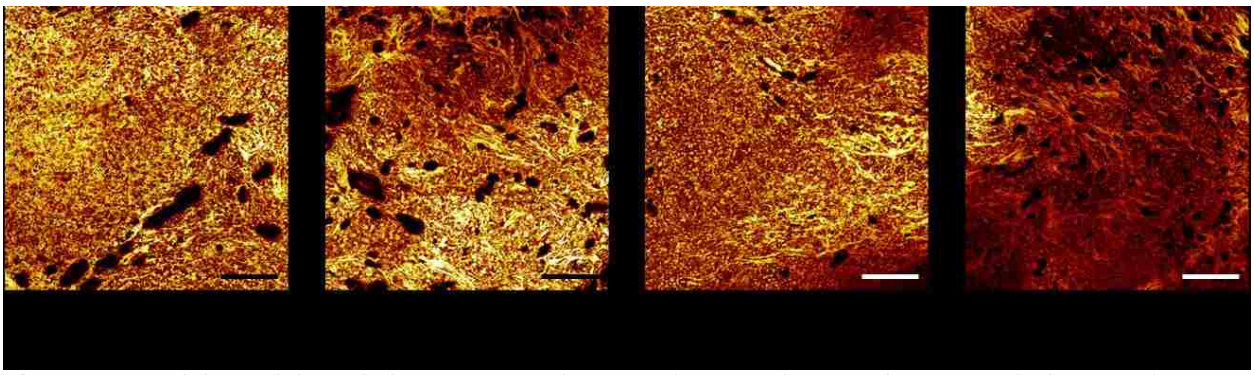

**Figure A.44.** High spatial resolution ToF-SIMS images of summed $CN^-$ and $CNO^-$ analysis areas from tissue 130801. Scale bars are 200 µm.

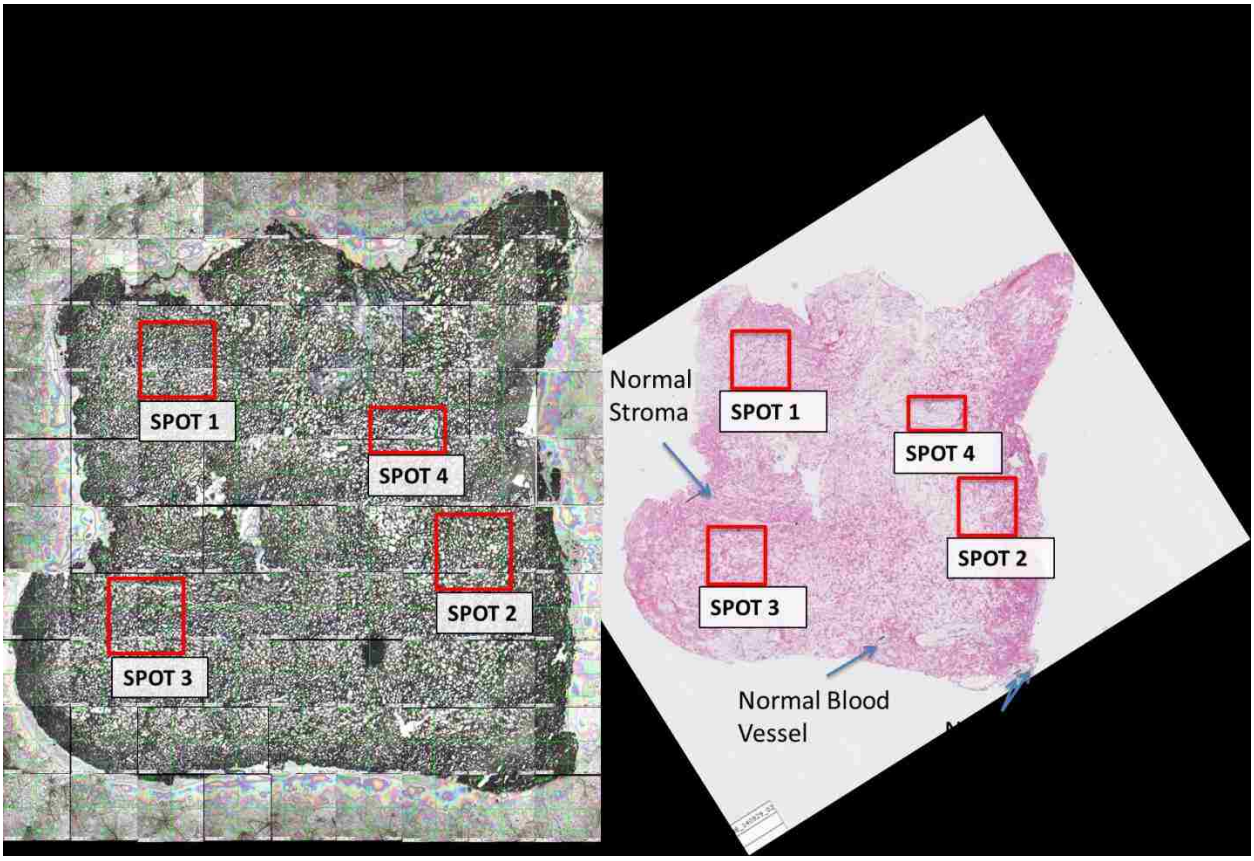


**Figure A.45.** H&E and corresponding ToF-SIMS camera stitch of tissue 140396 analysis areas.

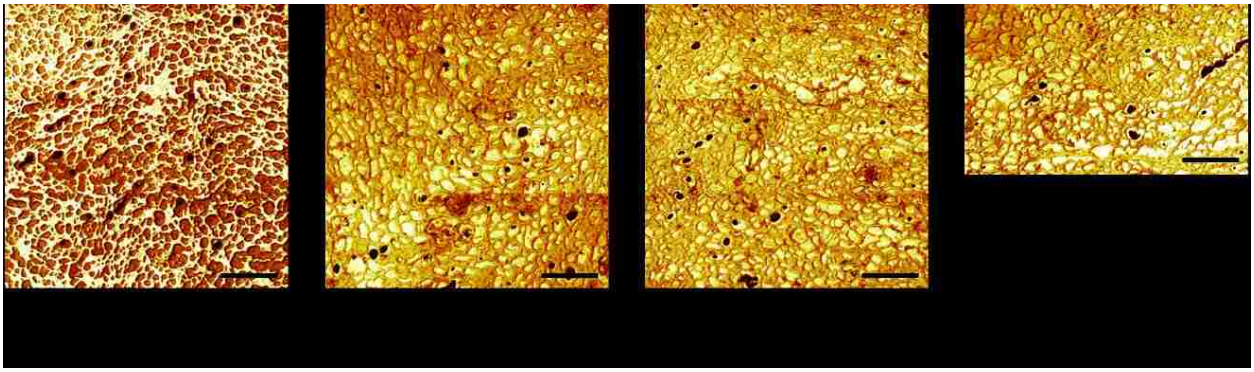

**Figure A.46.** High spatial resolution ToF-SIMS images of summed $CN^-$ and $CNO^-$ analysis areas from tissue 140396. Scale bars are 200 µm.

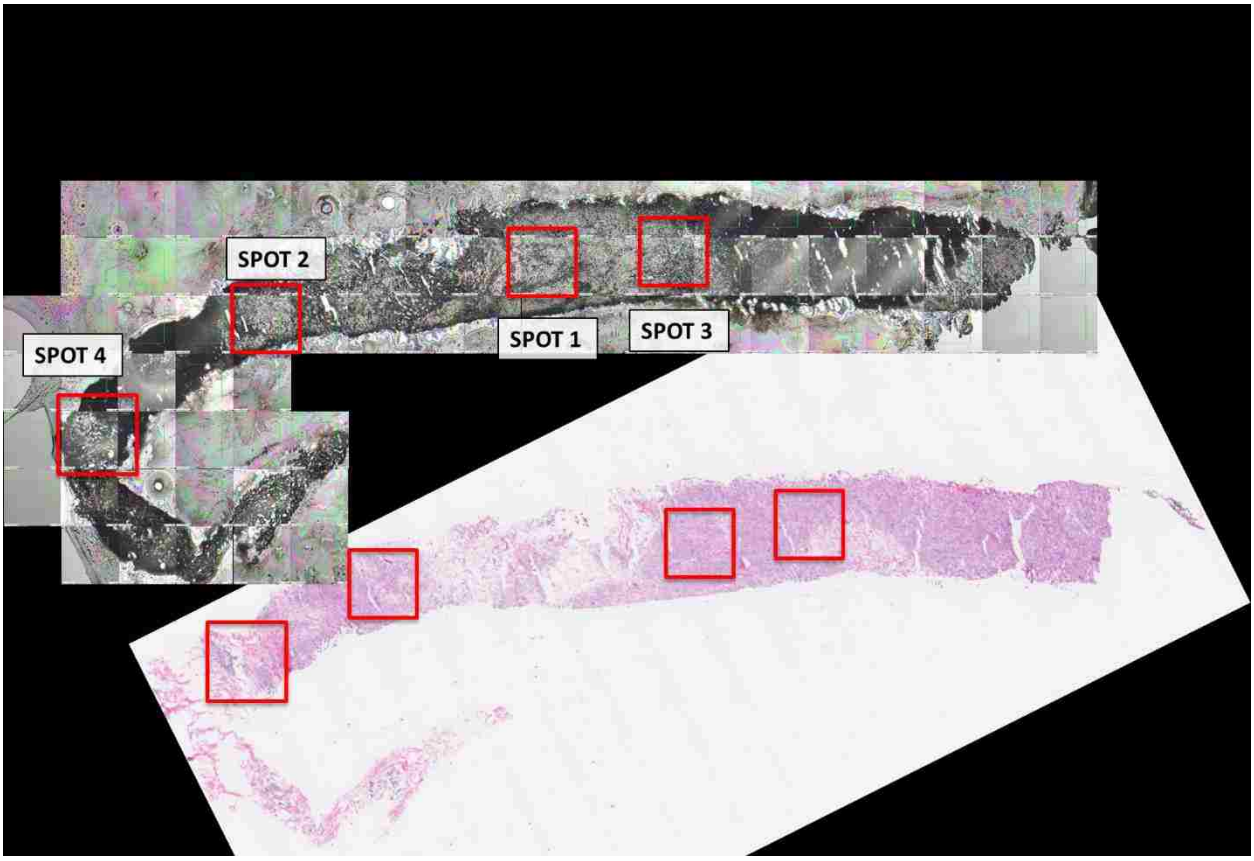


**Figure A.47.** H&E and corresponding ToF-SIMS camera stitch of tissue 140159 analysis areas.

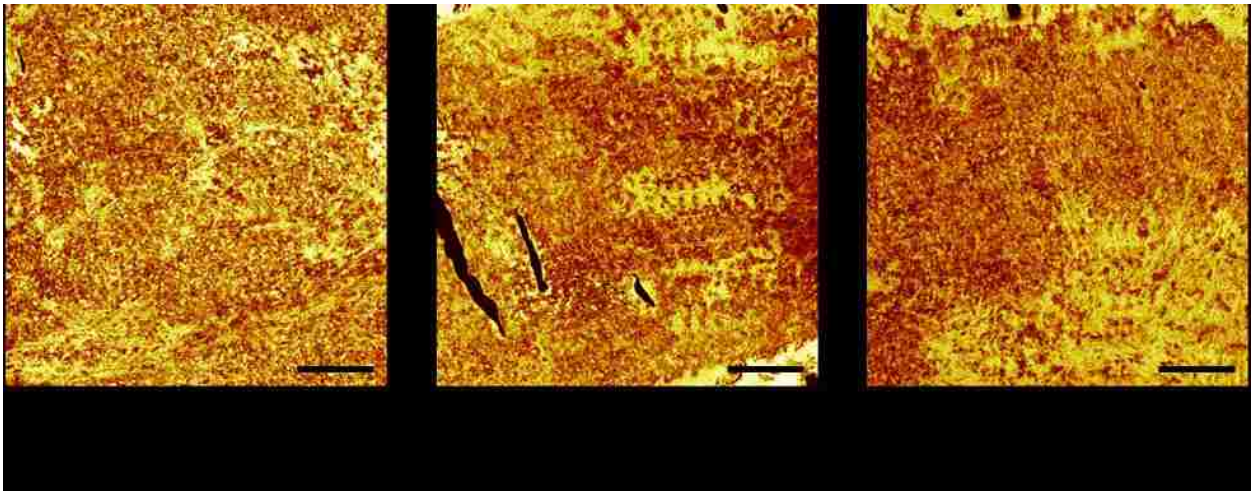

**Figure A.48.** High spatial resolution ToF-SIMS images of summed $CN^-$ and $CNO^-$ analysis areas from tissue 140159. Scale bars are 200 µm.

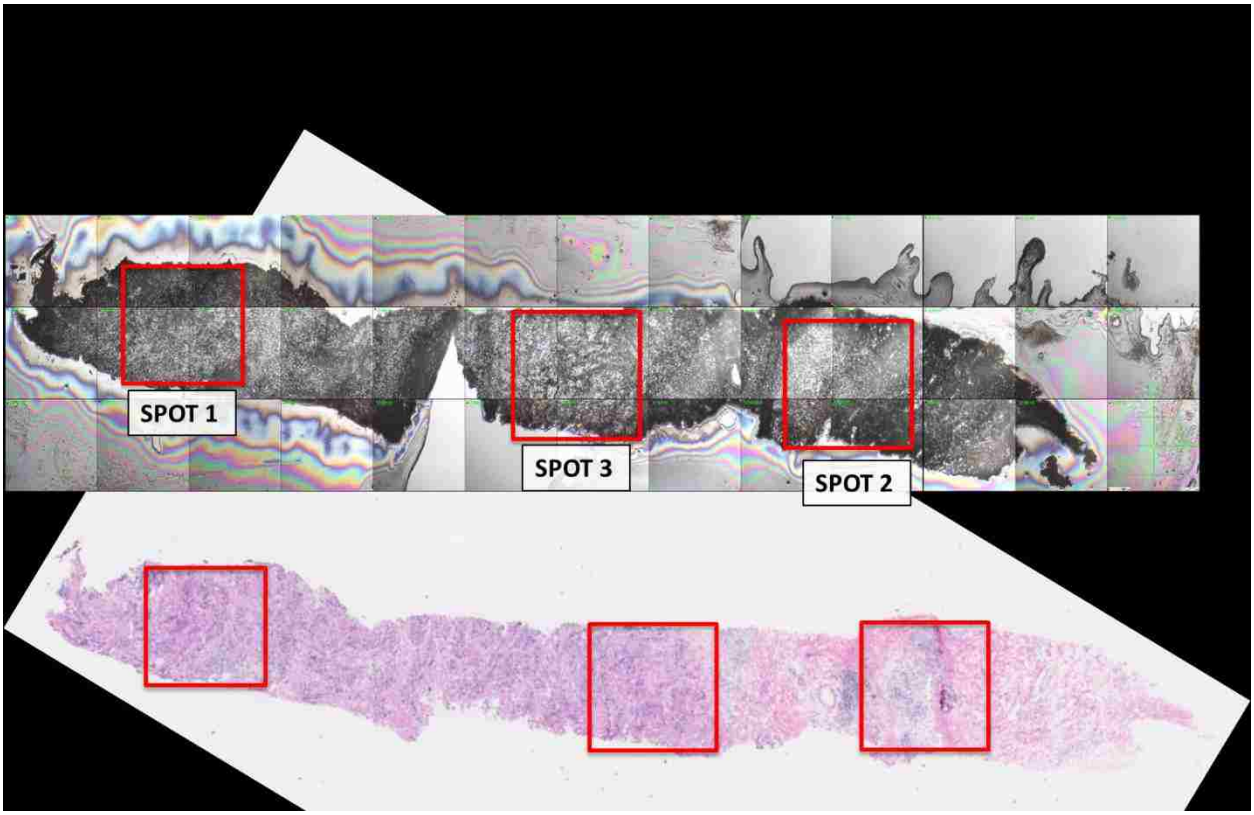


**Figure A.49.** H&E and corresponding ToF-SIMS camera stitch of tissue 140207 analysis areas.

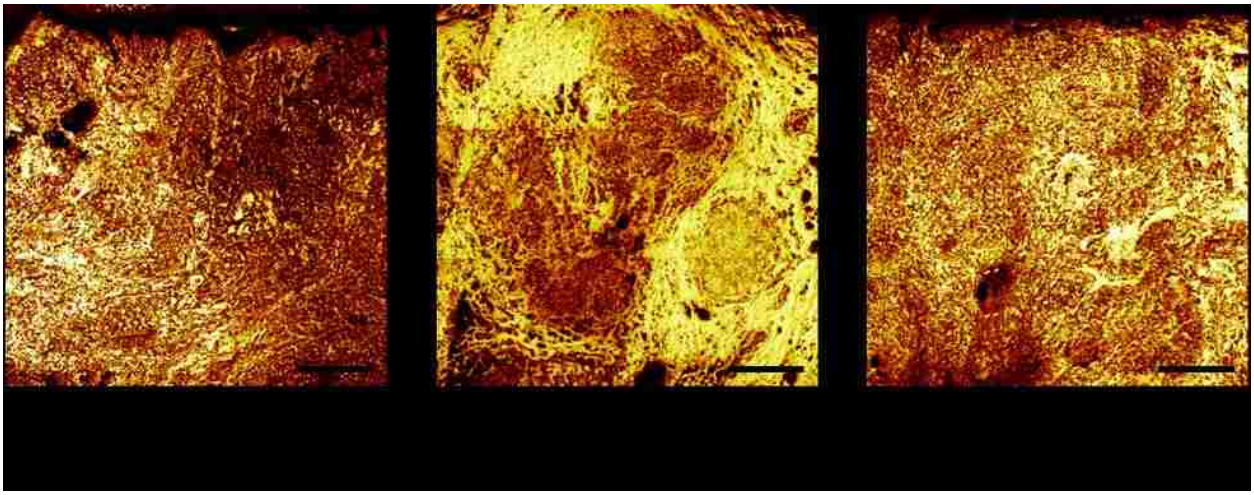

**Figure A.50.** High spatial resolution ToF-SIMS images of summed $CN^-$ and $CNO^-$ analysis areas from tissue 140207. Scale bars are 200 µm.

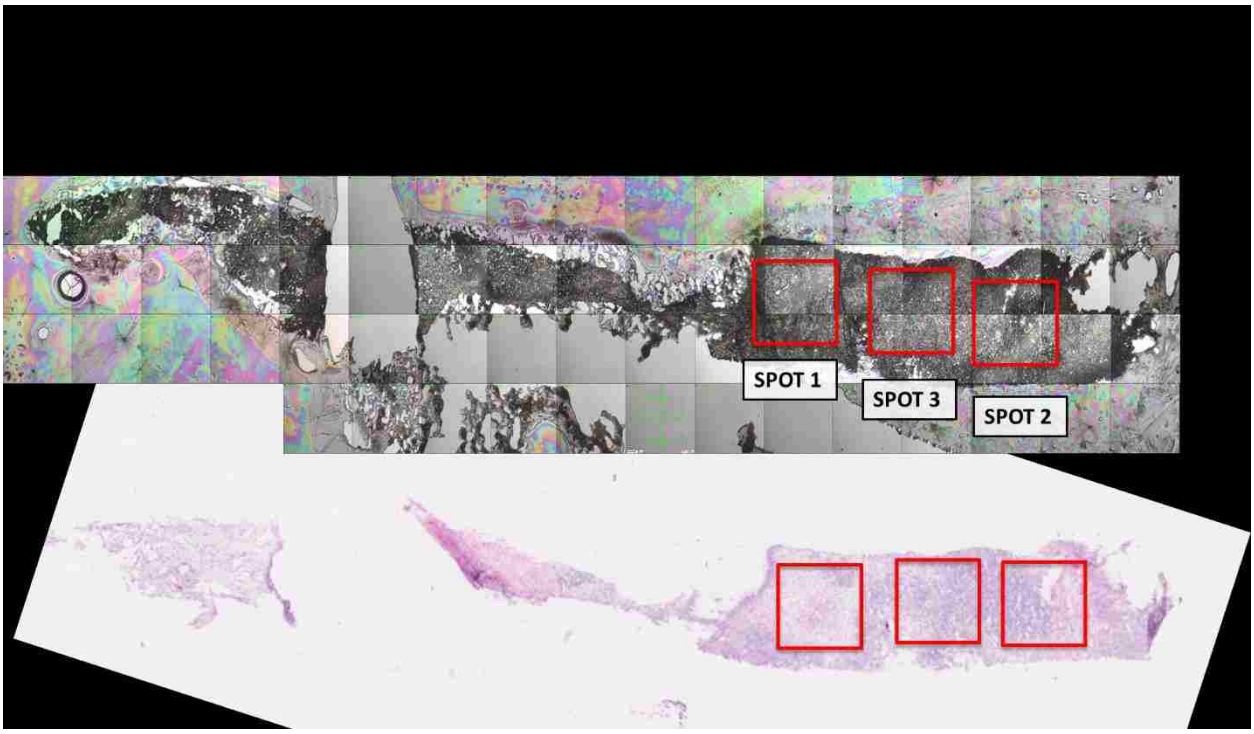


**Figure A.51.** H&E and corresponding ToF-SIMS camera stitch of tissue 140586 analysis areas.

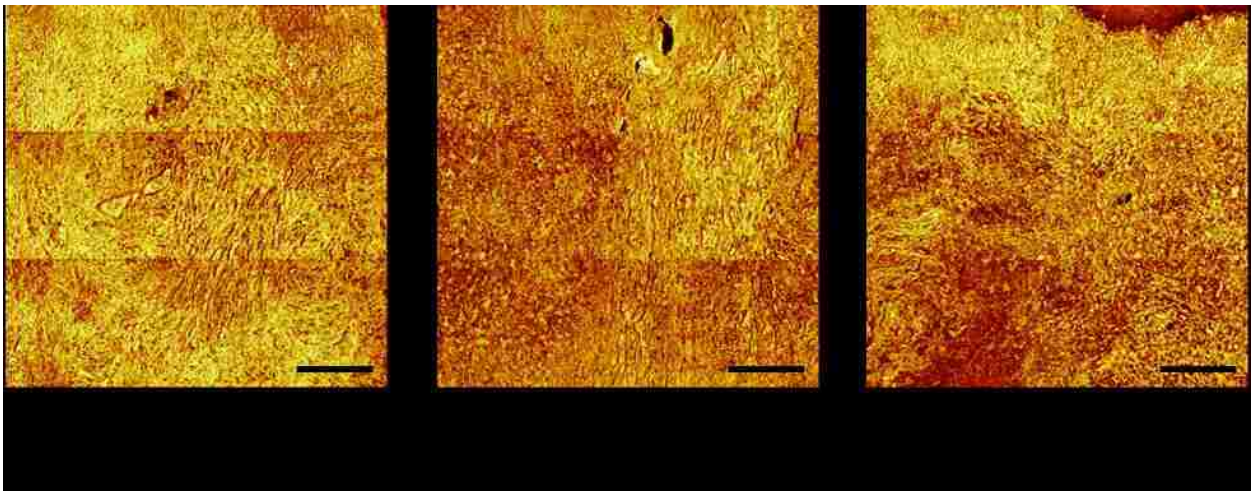

**Figure A.52.** High spatial resolution ToF-SIMS images of summed $CN^-$ and $CNO^-$ analysis areas from tissue 140586. Scale bars are 200 µm.

# APPENDIX B. TOF-SIMS OF TISSUES: 'LESSONS LEARNED' FROM MICE AND WOMEN

Lara J. Gamble[a) b)] , Daniel J. Graham[a)], Blake Bluestein[a)],
University of Washington, Department of Bioengineering, Molecular Engineering and Sciences Building, Box 351653, Seattle, Washington, 98195-1653, USA

Nicholas P. Whitehead,
University of Washington, Department of Physiology and Biophysics Box 357290, Seattle, Washington, 98195-1653, USA

David Hockenbery, Fionnuala Morrish, Peggy Porter
Fred Hutchinson Cancer Research Center, Seattle, Washington, 98109, USA

*Biointerphases*, 2015, Volume 10, Issue 1, Pages 019008

[a)]American Vacuum Society member

[b)]Electronic mail: lgamble@uw.edu

## Appendix B.1 ABSTRACT

The ability to image cells and tissues with chemical and molecular specificity could greatly expand our understanding of biological processes. The sub-cellular resolution mass spectral imaging capability of ToF-SIMS has the potential to acquire chemically detailed images. However the complexities of biological systems combined with the sensitivity of ToF-SIMS requires careful planning of experimental methods. Tissue sample preparation methods of formalin fixation followed by paraffin embedding (FFPE) and OCT embedding are compared. Results show that the FFPE can potentially be used as tissue sample preparation protocol for ToF-SIMS analysis if a cluster ion presputter is used prior to analysis and if non-lipid related tissue features are the features of interest. In contrast, embedding tissue in OCT is found to minimize contamination and maintains lipid signals. Various data acquisition methodologies and analysis options are discussed and compared using mouse breast and diaphragm muscle tissue. Methodologies for acquiring ToF-SIMS 2D images are highlighted along with applications of multivariate analysis to better identify specific features in a tissue sections when compared to H&E images of serial sections. Identification of tissue features is necessary for researchers to visualize a molecular map that correlates with specific biological features or functions. Finally, lessons learned from sample preparation, data acquisition, and data analysis methods developed using mouse models are applied to a preliminary analysis of human breast tumor tissue sections.

# REFERENCES


1. A. Brunelle, D. Touboul and O. Laprevote, *J Mass Spectrom*, 2005, **40**, 985-999.
2. D. Touboul, F. Kollmer, E. Niehuis, A. Brunelle and O. Laprevote, *J Am Soc Mass Spectrom*, 2005, **16**, 1608-1618.
3. C. M. Mahoney, *Cluster Secondary Ion Mass Spectrometry: Principles and Applications*, John Wiley & Sons, 2013.
4. R. N. Sodhi, *Analyst*, 2004, **129**, 483-487.
5. E. Niehuis, T. Heller, H. Feld and A. Benninghoven, *Journal of Vacuum Science & Technology A: Vacuum, Surfaces, and Films*, 1987, **5**, 1243-1246.
6. Y. K. Magnusson, P. Friberg, P. Sjovall, J. Malm and Y. Chen, *Obesity (Silver Spring)*, 2008, **16**, 2745-2753.
7. J.-W. Park, H. K. Shon, B. C. Yoo, I. H. Kim, D. W. Moon and T. G. Lee, *Applied Surface Science*, 2008, **255**, 1119-1122.
8. L. Wu, X. Lu, K. S. Kulp, M. G. Knize, E. S. F. Berman, E. J. Nelson, J. S. Felton and K. J. J. Wu, *International Journal of Mass Spectrometry*, 2007, **260**, 137-145.
9. P. Sjövall, B. Johansson and J. Lausmaa, *Applied Surface Science*, 2006, **252**, 6966-6974.
10. D. Touboul, A. Brunelle, F. Halgand, S. De La Porte and O. Laprevote, *J Lipid Res*, 2005, **46**, 1388-1395.
11. B. Cillero-Pastor, G. Eijkel, A. Kiss, F. J. Blanco and R. M. Heeren, *Anal Chem*, 2012, **84**, 8909-8916.
12. A. N. Lazar, C. Bich, M. Panchal, N. Desbenoit, V. W. Petit, D. Touboul, L. Dauphinot, C. Marquer, O. Laprevote, A. Brunelle and C. Duyckaerts, *Acta Neuropathol*, 2013, **125**, 133-144.
13. L. J. Gamble, D. J. Graham, B. Bluestein, N. P. Whitehead, D. Hockenbery, F. Morrish and P. Porter, *Biointerphases*, 2015, **10**, 019008.
14. P. Malmberg, H. Nygren, K. Richter, Y. Chen, F. Dangardt, P. Friberg and Y. Magnusson, *Microsc Res Tech*, 2007, **70**, 828-835.
15. Z. Takats, J. M. Wiseman and R. G. Cooks, *J Mass Spectrom*, 2005, **40**, 1261-1275.
16. D. R. Ifa, J. M. Wiseman, Q. Song and R. G. Cooks, *International Journal of Mass Spectrometry*, 2007, **259**, 8-15.
17. B. Spengler, *Anal Chem*, 2015, **87**, 64-82.
18. P. Van der Heide, *Secondary Ion Mass Spectrometry: An Introduction to Principles and Practices*, John Wiley & Sons, 2014.
19. E. R. Amstalden van Hove, D. F. Smith and R. M. Heeren, *J Chromatogr A*, 2010, **1217**, 3946-3954.
20. K. Chughtai and R. M. Heeren, *Chem Rev*, 2010, **110**, 3237-3277.
21. P. Chaurand, *J Proteomics*, 2012, **75**, 4883-4892.
22. H. R. Aerni, D. S. Cornett and R. M. Caprioli, *Anal Chem*, 2006, **78**, 827-834.
23. A. Rompp and B. Spengler, *Histochem Cell Biol*, 2013, **139**, 759-783.
24. Y. Schober, S. Guenther, B. Spengler and A. Rompp, *Anal Chem*, 2012, **84**, 6293-6297.
25. D. S. Cornett, M. L. Reyzer, P. Chaurand and R. M. Caprioli, *Nat Methods*, 2007, **4**, 828-833.
26. A. Zavalin, J. Yang, K. Hayden, M. Vestal and R. M. Caprioli, *Anal Bioanal Chem*, 2015, **407**, 2337-2342.
27. K. Chughtai, L. Jiang, T. R. Greenwood, K. Glunde and R. M. Heeren, *J Lipid Res*, 2013, **54**, 333-344.
28. S. Kang, H. S. Shim, J. S. Lee, D. S. Kim, H. Y. Kim, S. H. Hong, P. S. Kim, J. H. Yoon and N. H. Cho, *J Proteome Res*, 2010, **9**, 1157-1164.
29. K. S. Kulp, E. S. Berman, M. G. Knize, D. L. Shattuck, E. J. Nelson, L. Wu, J. L. Montgomery, J. S. Felton and K. J. Wu, *Anal Chem*, 2006, **78**, 3651-3658.
30. M. A. Robinson, D. J. Graham, F. Morrish, D. Hockenbery and L. J. Gamble, *Biointerphases*, 2015, **11**, 02A303.
31. M. J. Baker, M. D. Brown, E. Gazi, N. W. Clarke, J. C. Vickerman and N. P. Lockyer, *Analyst*, 2008, **133**, 175-179.
32. M. J. Baker, E. Gazi, M. D. Brown, N. W. Clarke, J. C. Vickerman and N. P. Lockyer, *Applied Surface Science*, 2008, **255**, 1084-1087.
33. J. Brison, M. A. Robinson, D. S. Benoit, S. Muramoto, P. S. Stayton and D. G. Castner, *Anal Chem*, 2013, **85**, 10869-10877.
34. F.-D. Mai, B.-J. Chen, L.-C. Wu, F.-Y. Li and W.-K. Chen, *Applied Surface Science*, 2006, **252**, 6809-6812.
35. J. N. Quong, M. G. Knize, K. S. Kulp and K. J. Wu, *Applied Surface Science*, 2004, **231-232**, 424-427.
36. T. B. Angerer, M. Dowlatshahi Pour, P. Malmberg and J. S. Fletcher, *Anal Chem*, 2015, **87**, 4305-4313.
37. N. T. Phan, J. S. Fletcher and A. G. Ewing, *Anal Chem*, 2015, **87**, 4063-4071.
38. Z. Takats, J. M. Wiseman, B. Gologan and R. G. Cooks, *Science*, 2004, **306**, 471-473.
39. L. S. Eberlin, C. R. Ferreira, A. L. Dill, D. R. Ifa, L. Cheng and R. G. Cooks, *Chembiochem*, 2011, **12**, 2129-2132.
40. C. Wu, A. L. Dill, L. S. Eberlin, R. G. Cooks and D. R. Ifa, *Mass Spectrom Rev*, 2013, **32**, 218-243.
41. V. Kertesz, G. J. Van Berkel, M. Vavrek, K. A. Koeplinger, B. B. Schneider and T. R. Covey, *Anal Chem*, 2008, **80**, 5168-5177.
42. J. Pol, V. Vidova, G. Kruppa, V. Kobliha, P. Novak, K. Lemr, T. Kotiaho, R. Kostiainen, V. Havlicek and M. Volny, *Anal Chem*, 2009, **81**, 8479-8487.
43. L. S. Eberlin, R. J. Tibshirani, J. Zhang, T. A. Longacre, G. J. Berry, D. B. Bingham, J. A. Norton, R. N. Zare and G. A. Poultsides, *P Natl Acad Sci USA*, 2014, **111**, 2436-2441.
44. C. C. Hsu, P. T. Chou and R. N. Zare, *Anal Chem*, 2015, **87**, 11171-11175.
45. L. S. Eberlin, I. Norton, A. L. Dill, A. J. Golby, K. L. Ligon, S. Santagata, R. G. Cooks and N. Y. Agar, *Cancer Res*, 2012, **72**, 645-654.
46. J. Laskin, B. S. Heath, P. J. Roach, L. Cazares and O. J. Semmes, *Analytical Chemistry*, 2011, **84**, 141-148.
47. D. Calligaris, D. Caragacianu, X. Liu, I. Norton, C. J. Thompson, A. L. Richardson, M. Golshan, M. L. Easterling, S. Santagata, D. A. Dillon, F. A. Jolesz and N. Y. Agar, *P Natl Acad Sci USA*, 2014, **111**, 15184-15189.
48. D. R. Ifa and L. S. Eberlin, *Clin Chem*, 2016, **62**, 111-123.
49. L. S. Eberlin, A. L. Dill, A. B. Costa, D. R. Ifa, L. Cheng, T. Masterson, M. Koch, T. L. Ratliff and R. G. Cooks, *Anal Chem*, 2010, **82**, 3430-3434.
50. A. L. Dill, L. S. Eberlin, A. B. Costa, C. Zheng, D. R. Ifa, L. Cheng, T. A. Masterson, M. O. Koch, O. Vitek and R. G. Cooks, *Chemistry*, 2011, **17**, 2897-2902.
51. L. S. Eberlin, I. Norton, D. Orringer, I. F. Dunn, X. Liu, J. L. Ide, A. K. Jarmusch, K. L. Ligon, F. A. Jolesz, A. J. Golby, S. Santagata, N. Y. Agar and R. G. Cooks, *P Natl Acad Sci USA*, 2013, **110**, 1611-1616.
52. N. J. Popczun, L. Breuer, A. Wucher and N. Winograd, *The Journal of Physical Chemistry C*, 2017, **121**, 8931-8937.

53. J. C. Vickerman and I. S. Gilmore, *Surface analysis: the principal techniques*, Wiley Online Library, 2009.
54. J. C. Cendan, D. L. Topping, J. Pruitt, S. Snowdy, E. M. Copeland, 3rd and D. S. Lind, *J Surg Res*, 1996, **60**, 284-288.
55. R. Castaing and G. Slodzian, *Cr Hebd Acad Sci*, 1962, **255**, 1893-1895.
56. A. Benninghoven, *Z Phys*, 1967, **199**, 141-156.
57. A. Benninghoven and E. Loebach, *Review of Scientific Instruments*, 1971, **42**, 49-52.
58. J. Griffiths, *Anal Chem*, 2008, **80**, 7194-7197.
59. H. F. Winters and P. Sigmund, *Journal of Applied Physics*, 1974, **45**, 4760-4766.
60. P. Sigmund and C. Claussen, *Journal of Applied Physics*, 1981, **52**, 990-993.
61. Z. Postawa, B. Czerwinski, M. Szewczyk, E. J. Smiley, N. Winograd and B. J. Garrison, *Analytical Chemistry*, 2003, **75**, 4402-4407.
62. B. J. Garrison, Z. Postawa, K. E. Ryan, J. C. Vickerman, R. P. Webb and N. Winograd, *Anal Chem*, 2009, **81**, 2260-2267.
63. R. Paruch, L. Rzeznik, M. F. Russo, B. J. Garrison and Z. Postawa, *The Journal of Physical Chemistry C*, 2010, **114**, 5532-5539.
64. A. Benninghoven, *Angewandte Chemie International Edition in English*, 1994, **33**, 1023-1043.
65. I. S. Gilmore and M. P. Seah, *Applied Surface Science*, 2003, **203-204**, 600-604.
66. R. Havelund, M. P. Seah, A. G. Shard and I. S. Gilmore, *J Am Soc Mass Spectrom*, 2014, **25**, 1565-1571.
67. M. Douglas and P. Chen, *Surface and Interface Analysis*, 1998, **26**, 984-994.
68. H. Hashimoto, K. Nakamura, H. Takase, T. Okamoto and N. Yamamoto, *Applied Surface Science*, 2004, **231-232**, 385-391.
69. F. Kollmer, *Applied Surface Science*, 2004, **231-232**, 153-158.
70. S. C. C. Wong, R. Hill, P. Blenkinsopp, N. P. Lockyer, D. E. Weibel and J. C. Vickerman, *Applied Surface Science*, 2003, **203-204**, 219-222.
71. J. S. Fletcher, X. A. Conlan, E. A. Jones, G. Biddulph, N. P. Lockyer and J. C. Vickerman, *Anal Chem*, 2006, **78**, 1827-1831.
72. H. K. Shon, S. Yoon, J. H. Moon and T. G. Lee, *Biointerphases*, 2016, **11**, 02A321.
73. S. Rabbani, A. M. Barber, J. S. Fletcher, N. P. Lockyer and J. C. Vickerman, *Anal Chem*, 2011, **83**, 3793-3800.
74. J. S. Fletcher, N. P. Lockyer, S. Vaidyanathan and J. C. Vickerman, *Anal Chem*, 2007, **79**, 2199-2206.
75. T. B. Angerer, P. Blenkinsopp and J. S. Fletcher, *International Journal of Mass Spectrometry*, 2015, **377**, 591-598.
76. J. S. Fletcher, S. Rabbani, A. Henderson, P. Blenkinsopp, S. P. Thompson, N. P. Lockyer and J. C. Vickerman, *Anal Chem*, 2008, **80**, 9058-9064.
77. I. Lanekoff, M. E. Kurczy, R. Hill, J. S. Fletcher, J. C. Vickerman, N. Winograd, P. Sjovall and A. G. Ewing, *Anal Chem*, 2010, **82**, 6652-6659.
78. I. Lanekoff, M. E. Kurczy, K. L. Adams, J. Malm, R. Karlsson, P. Sjövall and A. G. Ewing, *Surface and Interface Analysis*, 2011, **43**, 257-260.
79. N. T. N. Phan, M. Munem, A. G. Ewing and J. S. Fletcher, *Anal Bioanal Chem*, 2017, **409**, 3923-3932.
80. G. L. Fisher, A. L. Bruinen, N. Ogrinc Potocnik, J. S. Hammond, S. R. Bryan, P. E. Larson and R. M. Heeren, *Anal Chem*, 2016, **88**, 6433-6440.
81. M. K. Passarelli, C. F. Newman, P. S. Marshall, A. West, I. S. Gilmore, J. Bunch, M. R. Alexander and C. T. Dollery, *Anal Chem*, 2015, **87**, 6696-6702.
82. A. Pirkl, R. Moellers, H. Arlinghaus, F. Kollmer, E. Niehuis, A. Makarov, S. Horning, M. Passarelli, R. Havelund and P. Rakowska, *Microscopy and Microanalysis*, 2016, **22**, 340-341.
83. D. J. Graham, M. S. Wagner and D. G. Castner, *Applied Surface Science*, 2006, **252**, 6860-6868.
84. D. J. Graham and D. G. Castner, *Biointerphases*, 2012, **7**, 49.
85. M. S. Wagner, D. J. Graham and D. G. Castner, *Applied Surface Science*, 2006, **252**, 6575-6581.
86. S. Chandra, J. F. Chabot, G. H. Morrison and A. C. Leopold, *Science*, 1982, **216**, 1221-1223.
87. S. Chandra and G. H. Morrison, *Science*, 1985, **228**, 1543-1544.
88. S. Chandra, M. T. Bernius and G. H. Morrison, *Anal Chem*, 1986, **58**, 493-496.
89. R. Strick, P. L. Strissel, K. Gavrilov and R. Levi-Setti, *J Cell Biol*, 2001, **155**, 899-910.
90. R. Levi-Setti, J. M. Chabala, K. Gavrilov, R. Espinosa, 3rd and M. M. Le Beau, *Microsc Res Tech*, 1997, **36**, 301-312.
91. X. Zha, W. A. Ausserer and G. H. Morrison, *Cancer Research*, 1992, **52**, 5219.
92. P. Fragu, J. Clerc, C. Briancon, C. Fourre, J. Jeusset and S. Halpern, *Micron*, 1994, **25**, 361-370.
93. T. L. Colliver, C. L. Brummel, M. L. Pacholski, F. D. Swanek, A. G. Ewing and N. Winograd, *Analytical Chemistry*, 1997, **69**, 2225-2231.
94. M. C. Biesinger, D. J. Miller, R. R. Harbottle, F. Possmayer, N. S. McIntyre and N. O. Petersen, *Applied Surface Science*, 2006, **252**, 6957-6965.
95. A. G. Sostarecz, C. M. McQuaw, A. G. Ewing and N. Winograd, *J Am Chem Soc*, 2004, **126**, 13882-13883.
96. M. J. Baker, L. Zheng, N. Winograd, N. P. Lockyer and J. C. Vickerman, *Langmuir*, 2008, **24**, 11803-11810.
97. D. M. Cannon, M. L. Pacholski, N. Winograd and A. G. Ewing, *Journal of the American Chemical Society*, 2000, **122**, 603-610.
98. T. P. Roddy, D. M. Cannon, Jr., S. G. Ostrowski, N. Winograd and A. G. Ewing, *Anal Chem*, 2002, **74**, 4020-4026.
99. P. Sjovall, J. Lausmaa, H. Nygren, L. Carlsson and P. Malmberg, *Anal Chem*, 2003, **75**, 3429-3434.
100. S. G. Ostrowski, C. T. Van Bell, N. Winograd and A. G. Ewing, *Science*, 2004, **305**, 71-73.
101. J. S. Fletcher, N. P. Lockyer, S. Vaidyanathan and J. C. Vickerman, *Analytical Chemistry*, 2007, **79**, 2199-2206.
102. D. Breitenstein, C. E. Rommel, R. Mollers, J. Wegener and B. Hagenhoff, *Angew Chem Int Ed Engl*, 2007, **46**, 5332-5335.
103. D. Breitenstein, C. E. Rommel, J. Stolwijk, J. Wegener and B. Hagenhoff, *Applied Surface Science*, 2008, **255**, 1249-1256.
104. M. A. Robinson, D. J. Graham and D. G. Castner, *Anal Chem*, 2012, **84**, 4880-4885.
105. P. Sjovall, J. Lausmaa and B. Johansson, *Anal Chem*, 2004, **76**, 4271-4278.
106. F. Benabdellah, A. Seyer, L. Quinton, D. Touboul, A. Brunelle and O. Laprevote, *Anal Bioanal Chem*, 2010, **396**, 151-162.
107. E. A. Jones, N. P. Lockyer and J. C. Vickerman, *International Journal of Mass Spectrometry*, 2007, **260**, 146-157.
108. N. Tahallah, A. Brunelle, S. De La Porte and O. Laprevote, *J Lipid Res*, 2008, **49**, 438-454.
109. D. Debois, M. P. Bralet, F. Le Naour, A. Brunelle and O. Laprevote, *Anal Chem*, 2009, **81**, 2823-2831.
110. S. Mas, D. Touboul, A. Brunelle, P. Aragoncillo, J. Egido, O. Laprevote and F. Vivanco, *Analyst*, 2007, **132**, 24-26.
111. D. Touboul, O. Laprevote and A. Brunelle, *Curr Opin Chem Biol*, 2011, **15**, 725-732.
112. N. Desbenoit, E. Saussereau, C. Bich, M. Bourderioux, J. Fritsch, A. Edelman, A. Brunelle and M. Ollero, *Int J Biochem Cell Biol*, 2014, **52**, 77-82.

113. E. Gazi, J. Dwyer, N. Lockyer, P. Gardner, J. C. Vickerman, J. Miyan, C. A. Hart, M. Brown, J. H. Shanks and N. Clarke, *Faraday Discuss*, 2004, **126**, 41-59; discussion 77-92.
114. T. B. Angerer, Y. Magnusson, G. Landberg and J. S. Fletcher, *Anal Chem*, 2016, **88**, 11946-11954.
115. W. R. Zipfel, R. M. Williams, R. Christie, A. Y. Nikitin, B. T. Hyman and W. W. Webb, *P Natl Acad Sci USA*, 2003, **100**, 7075-7080.
116. L. A. McDonnell and R. M. Heeren, *Mass Spectrom Rev*, 2007, **26**, 606-643.
117. R. Van de Plas, J. Yang, J. Spraggins and R. M. Caprioli, *Nat Methods*, 2015, **12**, 366-372.
118. S. S. Rubakhin, J. C. Jurchen, E. B. Monroe and J. V. Sweedler, *Drug Discov Today*, 2005, **10**, 823-837.
119. D. S. Cornett, S. L. Frappier and R. M. Caprioli, *Anal Chem*, 2008, **80**, 5648-5653.
120. J. M. Wiseman, D. R. Ifa, Y. Zhu, C. B. Kissinger, N. E. Manicke, P. T. Kissinger and R. G. Cooks, *P Natl Acad Sci USA*, 2008, **105**, 18120-18125.
121. B. Prideaux and M. Stoeckli, *J Proteomics*, 2012, **75**, 4999-5013.
122. E. H. Seeley and R. M. Caprioli, *P Natl Acad Sci USA*, 2008, **105**, 18126-18131.
123. H. Nygren and P. Malmberg, *Proteomics*, 2010, **10**, 1694-1698.
124. N. Goto-Inoue, T. Hayasaka, N. Zaima and M. Setou, *Biochim Biophys Acta*, 2011, **1811**, 961-969.
125. M. K. Passarelli and N. Winograd, *Biochim Biophys Acta*, 2011, **1811**, 976-990.
126. J. W. Park, H. Jeong, B. Kang, S. J. Kim, S. Y. Park, S. Kang, H. K. Kim, J. S. Choi, D. Hwang and T. G. Lee, *Sci Rep*, 2015, **5**, 11077.
127. M. R. Junttila and F. J. de Sauvage, *Nature*, 2013, **501**, 346-354.
128. C. M. Perou, T. Sorlie, M. B. Eisen, M. van de Rijn, S. S. Jeffrey, C. A. Rees, J. R. Pollack, D. T. Ross, H. Johnsen, L. A. Akslen, O. Fluge, A. Pergamenschikov, C. Williams, S. X. Zhu, P. E. Lonning, A. L. Borresen-Dale, P. O. Brown and D. Botstein, *Nature*, 2000, **406**, 747-752.
129. T. Sorlie, C. M. Perou, R. Tibshirani, T. Aas, S. Geisler, H. Johnsen, T. Hastie, M. B. Eisen, M. van de Rijn, S. S. Jeffrey, T. Thorsen, H. Quist, J. C. Matese, P. O. Brown, D. Botstein, P. E. Lonning and A. L. Borresen-Dale, *P Natl Acad Sci USA*, 2001, **98**, 10869-10874.
130. S. Badve, D. J. Dabbs, S. J. Schnitt, F. L. Baehner, T. Decker, V. Eusebi, S. B. Fox, S. Ichihara, J. Jacquemier, S. R. Lakhani, J. Palacios, E. A. Rakha, A. L. Richardson, F. C. Schmitt, P. H. Tan, G. M. Tse, B. Weigelt, I. O. Ellis and J. S. Reis-Filho, *Mod Pathol*, 2011, **24**, 157-167.
131. K. R. Bauer, M. Brown, R. D. Cress, C. A. Parise and V. Caggiano, *Cancer*, 2007, **109**, 1721-1728.
132. B. Weigelt and J. S. Reis-Filho, *Nat Rev Clin Oncol*, 2009, **6**, 718-730.
133. M. L. Doria, C. Z. Cotrim, C. Simoes, B. Macedo, P. Domingues, M. R. Domingues and L. A. Helguero, *J Cell Physiol*, 2013, **228**, 457-468.
134. A. H. Beck, A. R. Sangoi, S. Leung, R. J. Marinelli, T. O. Nielsen, M. J. van de Vijver, R. B. West, M. van de Rijn and D. Koller, *Sci Transl Med*, 2011, **3**, 108ra113.
135. Y. Mao, E. T. Keller, D. H. Garfield, K. Shen and J. Wang, *Cancer Metastasis Rev*, 2013, **32**, 303-315.
136. J. A. Joyce and J. W. Pollard, *Nat Rev Cancer*, 2009, **9**, 239-252.
137. M. Egeblad, E. S. Nakasone and Z. Werb, *Dev Cell*, 2010, **18**, 884-901.
138. U. E. Martinez-Outschoorn, R. M. Balliet, D. B. Rivadeneira, B. Chiavarina, S. Pavlides, C. Wang, D. Whitaker-Menezes, K. M. Daumer, Z. Lin, A. K. Witkiewicz, N. Flomenberg, A. Howell, R. G. Pestell, E. S. Knudsen, F. Sotgia and M. P. Lisanti, *Cell Cycle*, 2010, **9**, 3256-3276.
139. G. Bonuccelli, A. Tsirigos, D. Whitaker-Menezes, S. Pavlides, R. G. Pestell, B. Chiavarina, P. G. Frank, N. Flomenberg, A. Howell, U. E. Martinez-Outschoorn, F. Sotgia and M. P. Lisanti, *Cell cycle (Georgetown, Tex.)*, 2010, **9**, 3506-3514.
140. P. Farmer, H. Bonnefoi, P. Anderle, D. Cameron, P. Wirapati, V. Becette, S. Andre, M. Piccart, M. Campone, E. Brain, G. Macgrogan, T. Petit, J. Jassem, F. Bibeau, E. Blot, J. Bogaerts, M. Aguet, J. Bergh, R. Iggo and M. Delorenzi, *Nat Med*, 2009, **15**, 68-74.
141. M. Verdonck, A. Denayer, B. Delvaux, S. Garaud, R. De Wind, C. Desmedt, C. Sotiriou, K. Willard-Gallo and E. Goormaghtigh, *Analyst*, 2016, **141**, 606-619.
142. C. R. Santos and A. Schulze, *FEBS J*, 2012, **279**, 2610-2623.
143. P. Du, W. A. Kibbe and S. M. Lin, *Bioinformatics*, 2008, **24**, 1547-1548.
144. J. S. Parker, M. Mullins, M. C. Cheang, S. Leung, D. Voduc, T. Vickery, S. Davies, C. Fauron, X. He, Z. Hu, J. F. Quackenbush, I. J. Stijleman, J. Palazzo, J. S. Marron, A. B. Nobel, E. Mardis, T. O. Nielsen, M. J. Ellis, C. M. Perou and P. S. Bernard, *J Clin Oncol*, 2009, **27**, 1160-1167.
145. D. M. Gendoo, N. Ratanasirigulchai, M. S. Schroeder and B. Haibe-Kains, *Journal*, 2015, R Package.
146. Y. Magnusson, P. Friberg, P. Sjovall, F. Dangardt, P. Malmberg and Y. Chen, *Clinical physiology and functional imaging*, 2008, **28**, 202-209.
147. P. Malmberg, K. Borner, Y. Chen, P. Friberg, B. Hagenhoff, J. E. Mansson and H. Nygren, *Biochim Biophys Acta*, 2007, **1771**, 185-195.
148. J. D. Brenton, L. A. Carey, A. A. Ahmed and C. Caldas, *J Clin Oncol*, 2005, **23**, 7350-7360.
149. M. L. Heien, P. D. Piehowski, N. Winograd and A. G. Ewing, in *Mass Spectrometry Imaging*, Springer, 2010, pp. 85-97.
150. G. Kroemer and J. Pouyssegur, *Cancer Cell*, 2008, **13**, 472-482.
151. S. Wang, X. Chen, H. Luan, D. Gao, S. Lin, Z. Cai, J. Liu, H. Liu and Y. Jiang, *Rapid Commun Mass Spectrom*, 2016, **30**, 533-542.
152. A. Kourtidis, R. Srinivasaiah, R. D. Carkner, M. J. Brosnan and D. S. Conklin, *Breast Cancer Res*, 2009, **11**, R16.
153. H. Liu, Y. Liu and J. T. Zhang, *Mol Cancer Ther*, 2008, **7**, 263-270.
154. Y. Ni and C. Eng, *Clin Cancer Res*, 2012, **18**, 4954-4961.
155. N. Weijl, F. Cleton and S. Osanto, *Cancer treatment reviews*, 1997, **23**, 209-240.
156. E. J. Ladas, J. S. Jacobson, D. D. Kennedy, K. Teel, A. Fleischauer and K. M. Kelly, *J Clin Oncol*, 2004, **22**, 517-528.
157. B. Kwon, H. K. Lee and H. W. Querfurth, *Biochim Biophys Acta*, 2014, **1843**, 1402-1413.
158. G. von Minckwitz, M. Untch, J. U. Blohmer, S. D. Costa, H. Eidtmann, P. A. Fasching, B. Gerber, W. Eiermann, J. Hilfrich, J. Huober, C. Jackisch, M. Kaufmann, G. E. Konecny, C. Denkert, V. Nekljudova, K. Mehta and S. Loibl, *J Clin Oncol*, 2012, **30**, 1796-1804.
159. F. C. Geyer, C. Marchio and J. S. Reis-Filho, *Pathology*, 2009, **41**, 77-88.

160. R. Nahta and F. J. Esteva, *Oncogene*, 2007, **26**, 3637-3643.
161. B. M. Bluestein, F. Morrish, D. J. Graham, J. Guenthoer, D. Hockenbery, P. L. Porter and L. J. Gamble, *Analyst*, 2016, **141**, 1947-1957.
162. M. P. Wymann and R. Schneiter, *Nat Rev Mol Cell Biol*, 2008, **9**, 162-176.
163. E. R. A. van Hove, T. R. Blackwell, I. Klinkert, G. B. Eijkel, R. M. Heeren and K. Glunde, *Cancer Research*, 2010, **70**, 9012-9021.
164. H. E. Canavan, D. J. Graham, X. Cheng, B. D. Ratner and D. G. Castner, *Langmuir*, 2007, **23**, 50-56.
165. C. J. May, H. E. Canavan and D. G. Castner, *Anal Chem*, 2004, **76**, 1114-1122.
166. D. Hanahan and L. M. Coussens, *Cancer Cell*, 2012, **21**, 309-322.
167. D. Carter, R. D. Pipkin, R. H. Shepard, R. C. Elkins and H. Abbey, *Am J Surg Pathol*, 1978, **2**, 39-46.
168. D. R. Green, *J Cell Biol*, 2000, **150**, F5-7.
169. B. Ogretmen and Y. A. Hannun, *Nat Rev Cancer*, 2004, **4**, 604-616.
170. M. He, S. Guo and Z. Li, *Sci Rep*, 2015, **5**, 11298.
171. Y. Ohno, S. Suto, M. Yamanaka, Y. Mizutani, S. Mitsutake, Y. Igarashi, T. Sassa and A. Kihara, *P Natl Acad Sci USA*, 2010, **107**, 18439-18444.
172. A. Jakobsson, R. Westerberg and A. Jacobsson, *Prog Lipid Res*, 2006, **45**, 237-249.
173. S. Grosch, S. Schiffmann and G. Geisslinger, *Prog Lipid Res*, 2012, **51**, 50-62.
174. Y. Cao, A. T. Pearman, G. A. Zimmerman, T. M. McIntyre and S. M. Prescott, *P Natl Acad Sci USA*, 2000, **97**, 11280-11285.
175. X. F. Wang, P. K. Witting, B. A. Salvatore and J. Neuzil, *Biochem Biophys Res Commun*, 2005, **326**, 282-289.
176. W. Yu, K. Israel, Q. Y. Liao, C. M. Aldaz, B. G. Sanders and K. Kline, *Cancer Res*, 1999, **59**, 953-961.
177. I. S. Fentiman, *BMJ : British Medical Journal*, 1992, **304**, 1261-1262.
178. D. N. Poller, A. Barth, D. J. Slamon, M. J. Silverstein, E. D. Gierson, W. J. Coburn, J. R. Waisman, P. Gamagami and B. S. Lewinsky, *The Lancet*, 1995, **345**, 1154-1157.
179. P. L. Jager, W. Vaalburg, J. Pruim, E. G. de Vries, K. J. Langen and D. A. Piers, *J Nucl Med*, 2001, **42**, 432-445.
180. M. G. Vander Heiden, L. C. Cantley and C. B. Thompson, *Science*, 2009, **324**, 1029-1033.
181. C. Juhasz, Z. Nahleh, I. Zitron, D. C. Chugani, M. Z. Janabi, S. Bandyopadhyay, R. Ali-Fehmi, T. J. Mangner, P. K. Chakraborty, S. Mittal and O. Muzik, *Nucl Med Biol*, 2012, **39**, 926-932.
182. J. Cai, Z. Mao, J. J. Hwang and S. C. Lu, *Cancer Res*, 1998, **58**, 1444-1450.
183. Z. Z. Huang, Z. Mao, J. Cai and S. C. Lu, *The American journal of physiology*, 1998, **275**, G14-21.
184. D. Hanahan and R. A. Weinberg, *Cell*, 2000, **100**, 57-70.
185. T. Hitosugi, S. Kang, M. G. Vander Heiden, T. W. Chung, S. Elf, K. Lythgoe, S. Dong, S. Lonial, X. Wang, G. Z. Chen, J. Xie, T. L. Gu, R. D. Polakiewicz, J. L. Roesel, T. J. Boggon, F. R. Khuri, D. G. Gilliland, L. C. Cantley, J. Kaufman and J. Chen, *Sci Signal*, 2009, **2**, ra73.
186. M. W. Conklin, J. C. Eickhoff, K. M. Riching, C. A. Pehlke, K. W. Eliceiri, P. P. Provenzano, A. Friedl and P. J. Keely, *The American Journal of Pathology*, 2011, **178**, 1221-1232.
187. X. Chen, O. Nadiarynkh, S. Plotnikov and P. J. Campagnola, *Nature protocols*, 2012, **7**, 654-669.
188. M. Han, G. Giese and J. Bille, *Opt Express*, 2005, **13**, 5791-5797.
189. T. L. Whiteside, *Oncogene*, 2008, **27**, 5904-5912.
190. O. Tredan, C. M. Galmarini, K. Patel and I. F. Tannock, *J Natl Cancer Inst*, 2007, **99**, 1441-1454.
191. A. Vazquez, J. J. Kamphorst, E. K. Markert, Z. T. Schug, S. Tardito and E. Gottlieb, *Journal of Cell Science*, 2016, **129**, 3367.
192. A. Finch, J. Prescott, K. Shchors, A. Hunt, L. Soucek, T. B. Dansen, L. B. Swigart and G. I. Evan, *Cancer Cell*, 2006, **10**, 113-120.
193. Z. E. Stine, Z. E. Walton, B. J. Altman, A. L. Hsieh and C. V. Dang, *Cancer discovery*, 2015, **5**, 1024-1039.
194. D. R. Wise, R. J. DeBerardinis, A. Mancuso, N. Sayed, X. Y. Zhang, H. K. Pfeiffer, I. Nissim, E. Daikhin, M. Yudkoff, S. B. McMahon and C. B. Thompson, *P Natl Acad Sci USA*, 2008, **105**, 18782-18787.
195. H. Zirath, A. Frenzel, G. Oliynyk, L. Segerstrom, U. K. Westermark, K. Larsson, M. Munksgaard Persson, K. Hultenby, J. Lehtio, C. Einvik, S. Pahlman, P. Kogner, P. J. Jakobsson and M. A. Henriksson, *P Natl Acad Sci USA*, 2013, **110**, 10258-10263.
196. L. R. Edmunds, L. Sharma, A. Kang, J. Lu, J. Vockley, S. Basu, R. Uppala, E. S. Goetzman, M. E. Beck, D. Scott and E. V. Prochownik, *J Biol Chem*, 2014, **289**, 25382-25392.
197. F. Morrish and D. Hockenbery, *Cold Spring Harb Perspect Med*, 2014, **4**, a014225.
198. F. Li, Y. Wang, K. I. Zeller, J. J. Potter, D. R. Wonsey, K. A. O'Donnell, J. W. Kim, J. T. Yustein, L. A. Lee and C. V. Dang, *Mol Cell Biol*, 2005, **25**, 6225-6234.
199. F. Morrish, J. Noonan, C. Perez-Olsen, P. R. Gafken, M. Fitzgibbon, J. Kelleher, M. VanGilst and D. Hockenbery, *J Biol Chem*, 2010, **285**, 36267-36274.
200. E. H. Shroff, L. S. Eberlin, V. M. Dang, A. M. Gouw, M. Gabay, S. J. Adam, D. I. Bellovin, P. T. Tran, W. M. Philbrick, A. Garcia-Ocana, S. C. Casey, Y. Li, C. V. Dang, R. N. Zare and D. W. Felsher, *P Natl Acad Sci USA*, 2015, **112**, 6539-6544.
201. Z. Hall, Z. Ament, C. H. Wilson, D. L. Burkhart, T. Ashmore, A. Koulman, T. Littlewood, G. I. Evan and J. L. Griffin, *Cancer Res*, 2016, **76**, 4608-4618.
202. S. Pelengaris, M. Khan and G. I. Evan, *Cell*, 2002, **109**, 321-334.
203. T. D. Littlewood, D. C. Hancock, P. S. Danielian, M. G. Parker and G. I. Evan, *Nucleic Acids Research*, 1995, **23**, 1686-1690.
204. V. Mazel, P. Richardin, D. Debois, D. Touboul, M. Cotte, A. Brunelle, P. Walter and O. Laprevote, *Anal Chem*, 2007, **79**, 9253-9260.
205. D. E. Greenwalt, Y. S. Goreva, S. M. Siljestrom, T. Rose and R. E. Harbach, *P Natl Acad Sci USA*, 2013, **110**, 18496-18500.
206. P. Petit and M. M. Loubatieres-Mariani, *Fundam Clin Pharmacol*, 1992, **6**, 123-134.
207. A. Kavishwar and A. Moore, *The journal of histochemistry and cytochemistry : official journal of the Histochemistry Society*, 2013, **61**, 910-919.
208. Y. Itoh, Y. Kawamata, M. Harada, M. Kobayashi, R. Fujii, S. Fukusumi, K. Ogi, M. Hosoya, Y. Tanaka, H. Uejima, H. Tanaka, M. Maruyama, R. Satoh, S. Okubo, H. Kizawa, H. Komatsu, F. Matsumura, Y. Noguchi, T. Shinohara, S. Hinuma, Y. Fujisawa and M. Fujino, *Nature*, 2003, **422**, 173-176.
209. R. Durrett, J. Foo, K. Leder, J. Mayberry and F. Michor, *Genetics*, 2011, **188**, 461-477.
210. B. M. Bluestein, F. Morrish, D. Hockenbery and L. J. Gamble, *Microscopy and Microanalysis*, 2015, **21**, 2065-2066.
211. P. Carmeliet and R. K. Jain, *Nature*, 2000, **407**, 249-257.

212. H. Hashizume, P. Baluk, S. Morikawa, J. W. McLean, G. Thurston, S. Roberge, R. K. Jain and D. M. McDonald, *The American Journal of Pathology*, 2000, **156**, 1363-1380.
213. L. S. Eberlin, M. Gabay, A. C. Fan, A. M. Gouw, R. J. Tibshirani, D. W. Felsher and R. N. Zare, *P Natl Acad Sci USA*, 2014, **111**, 10450-10455.
214. L. R. Edmunds, L. Sharma, H. Wang, A. Kang, S. d'Souza, J. Lu, M. McLaughlin, J. M. Dolezal, X. Gao, S. T. Weintraub, Y. Ding, X. Zeng, N. Yates and E. V. Prochownik, *PLoS One*, 2015, **10**, e0134049.
215. S. M. Jeon, *Exp Mol Med*, 2016, **48**, e245.
216. M. Subathra, A. Qureshi and C. Luberto, *PLoS One*, 2011, **6**, e23644.
217. I. Ischenko, J. Zhi, U. M. Moll, A. Nemajerova and O. Petrenko, *P Natl Acad Sci USA*, 2013, **110**, 3937-3942.
218. S. C. Robson, L. Ward, H. Brown, H. Turner, E. Hunter, S. Pelengaris and M. Khan, *BMC genomics*, 2011, **12**, 476.
219. C. Guerra, A. J. Schuhmacher, M. Canamero, P. J. Grippo, L. Verdaguer, L. Perez-Gallego, P. Dubus, E. P. Sandgren and M. Barbacid, *Cancer Cell*, 2007, **11**, 291-302.
220. S. Y. Gidekel Friedlander, G. C. Chu, E. L. Snyder, N. Girnius, G. Dibelius, D. Crowley, E. Vasile, R. A. DePinho and T. Jacks, *Cancer Cell*, 2009, **16**, 379-389.
221. E. R. Lawlor, L. Soucek, L. Brown-Swigart, K. Shchors, C. U. Bialucha and G. I. Evan, *Cancer Res*, 2006, **66**, 4591-4601.
222. M. Thai, S. K. Thaker, J. Feng, Y. Du, H. Hu, T. Ting Wu, T. G. Graeber, D. Braas and H. R. Christofk, *Nat Commun*, 2015, **6**, 8873.
223. F. Morrish, N. Isern, M. Sadilek, M. Jeffrey and D. M. Hockenbery, *Oncogene*, 2009, **28**, 2485-2491.
224. L. R. Edmunds, P. A. Otero, L. Sharma, S. D'Souza, J. M. Dolezal, S. David, J. Lu, L. Lamm, M. Basantani, P. Zhang, I. J. Sipula, L. Li, X. Zeng, Y. Ding, F. Ding, M. E. Beck, J. Vockley, S. P. Monga, E. E. Kershaw, R. M. O'Doherty, L. E. Kratz, N. A. Yates, E. P. Goetzman, D. Scott, A. W. Duncan and E. V. Prochownik, *Oncotarget*, 2016, **7**, 30379-30395.
225. H. Harizi, J. B. Corcuff and N. Gualde, *Trends Mol Med*, 2008, **14**, 461-469.
226. E. R. Greene, S. Huang, C. N. Serhan and D. Panigrahy, *Prostaglandins Other Lipid Mediat*, 2011, **96**, 27-36.
227. R. J. Konrad, C. D. Major and B. A. Wolf, *Biochemistry*, 2002, **33**, 13284-13294.
228. N. Mori, R. Delsite, K. Natarajan, M. Kulawiec, Z. M. Bhujwalla and K. K. Singh, *Mol Imaging*, 2004, **3**, 319-323.
229. C. V. Dang, *Cold Spring Harb Perspect Med*, 2013, **3**.
230. I. Amelio, F. Cutruzzola, A. Antonov, M. Agostini and G. Melino, *Trends Biochem Sci*, 2014, **39**, 191-198.
231. A. C. Newman and O. D. K. Maddocks, *Trends Cell Biol*, 2017, DOI: 10.1016/j.tcb.2017.05.001.
232. M. Yang and K. H. Vousden, *Nat Rev Cancer*, 2016, **16**, 650-662.
233. A. Vazquez, E. K. Markert and Z. N. Oltvai, *PLoS One*, 2011, **6**, e25881.
234. B. Anderton, R. Camarda, S. Balakrishnan, A. Balakrishnan, R. A. Kohnz, L. Lim, K. J. Evason, O. Momcilovic, K. Kruttwig, Q. Huang, G. Xu, D. K. Nomura and A. Goga, *EMBO Rep*, 2017, **18**, 569-585.
235. M. A. Nikiforov, S. Chandriani, B. O'Connell, O. Petrenko, I. Kotenko, A. Beavis, J. M. Sedivy and M. D. Cole, *Mol Cell Biol*, 2002, **22**, 5793-5800.
236. J. W. Locasale, *Nat Rev Cancer*, 2013, **13**, 572-583.
237. T. Chen and S. Y. Dent, *Nat Rev Genet*, 2014, **15**, 93-106.
238. K. Hayashi, P. Jutabha, H. Endou and N. Anzai, *Oncol Rep*, 2012, **28**, 862-866.
239. C. A. Elstad, G. G. Meadows and R. M. Abdallah, *Clin Exp Metastasis*, 1990, **8**, 393-416.
240. D. Schechter, G. A. Bachmann, J. Vaitukaitis, D. Phillips and D. Saperstein, *Psychosom Med*, 1989, **51**, 173-194.
241. V. E. Baracos and M. L. Mackenzie, *J Nutr*, 2006, **136**, 237S-242S.
242. N. Shyh-Chang, J. W. Locasale, C. A. Lyssiotis, Y. Zheng, R. Y. Teo, S. Ratanasirintrawoot, J. Zhang, T. Onder, J. J. Unternaehrer, H. Zhu, J. M. Asara, G. Q. Daley and L. C. Cantley, *Science*, 2013, **339**, 222-226.
243. C. V. Dang, *Cancer Res*, 2010, **70**, 859-862.

# VITA

Blake Bluestein was born in Albuquerque, New Mexico. He received his B.S. in Chemical Engineering from the University of New Mexico in 2011. He received his Ph.D. in Bioengineering from the University of Washington in 2017.